COMPTES RENDUS
DE L'ACADÉMIE DES SCIENCES

1878-1535 (electronic)

Physique

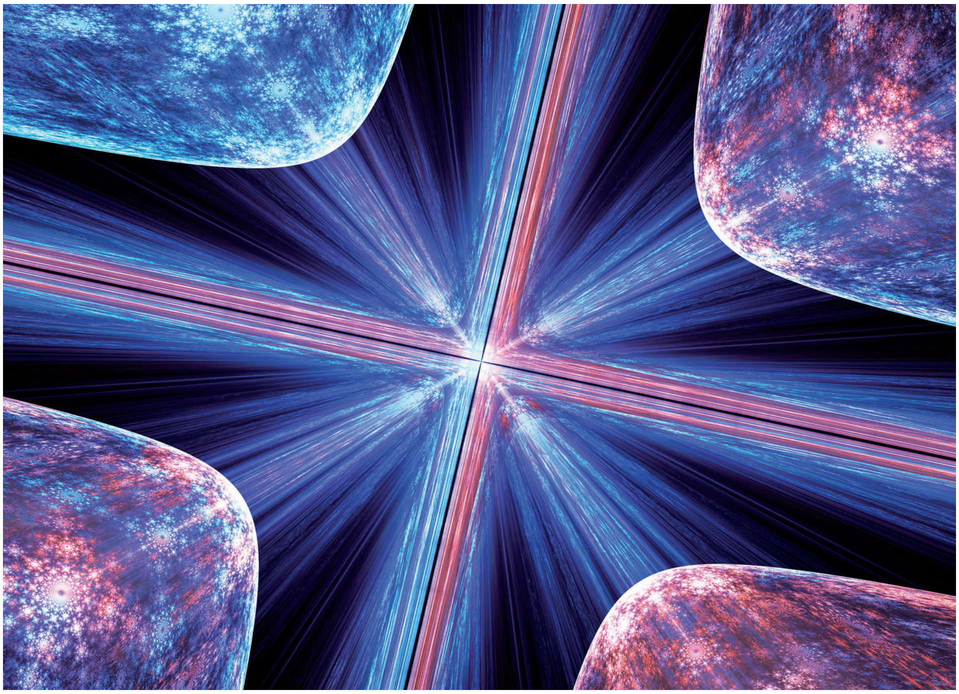

Volume 21, Special Issue 7-8, 2020

Special issue / *Numéro thématique*
Metamaterials 2 / *Métamatériaux 2*

Guest editors / *Rédacteurs en chef invités*
Boris Gralak, Sébastien Guenneau

Académie des sciences — Paris

INSTITUT DE FRANCE
Académie des sciences

CENTRE MERSENNE

Comptes Rendus

Physique

Objective of the journal

Comptes Rendus Physique is a peer-reviewed electronic journal of international standing, covering all fields of physics and astrophysics. It publishes mainly thematic issues, but also original research articles, preliminary announcements, review articles, historical perspectives, pedagogical texts or conference proceedings, without length limit, in English or in French. It also publishes special issues devoted to certain recent and/or significant aspects of the discipline, whose authors are chosen from among the most active researchers on the subject and whose coordination is assured by guest editors.

Comptes Rendus Physique is published according to a virtuous policy of diamond open access, free for authors (no publication fees) as well as for readers (immediate and permanent open access).

About the journal

All journal's information, including the text of published articles, which is fully open access, is available from the journal website at https://comptes-rendus.academie-sciences.fr/physique/.

Author enquiries

For enquiries relating to the submission of articles, please visit this journal's homepage at https://comptes-rendus.academie-sciences.fr/physique/.

Contact

Académie des sciences
23, quai de Conti, 75006 Paris, France
Tel: (+33) (0)1 44 41 43 72
CR-Physique@academie-sciences.fr

Comptes Rendus
Physique
2020, 21, nº 7-8

Contents / *Sommaire*

Comptes Rendus
Physique
2020, 21, nº 7-8, p. 619-623
`https://doi.org/10.5802/crphys.45`

Metamaterials 2 / *Métamatériaux 2*

Foreword

Avant-propos

Boris Gralak[*, a] **and Sébastien Guenneau**[b]

[a] CNRS, Aix Marseille Univ, Centrale Marseille, Institut Fresnel, Marseille, France
[b] UMI 2004 Abraham de Moivre-CNRS, Imperial College London, London SW7 2AZ, UK
E-mails: boris.gralak@fresnel.fr (B. Gralak), s.guenneau@imperial.ac.uk (S. Guenneau)

This double special volume of the Comptes Rendus Physique is the second part of a collection of fourteen articles which aim to draw an overview of the topic of metamaterials. This collection, carried out with the cooperation of leading international experts in the field of metamaterials, includes original research as well as more review-oriented contributions. The articles cover the topics of electromagnetic, acoustic, elastic, and seismic metamaterials and are organized in two double special volumes gathering on one side, articles more-oriented on concepts and models and on the other side, articles reporting results more related to promising potential applications. The two double special volume thus covers theoretical as well as experimental and fundamental as well as applied aspects in different areas of metamaterials from nanoscale (electrodynamics and plasmonics) to meter-scale (geophysics) media.

In this second double volume, the second set of seven articles, where promising applications are reported, is opened with a contribution on tunable metasurface-based waveplates by Nader Engheta and Nasim Estakhri. The authors propose an innovative type of waveplate, for full control on phase retardation and light polarization, consisting of two symmetric metasurfaces separated by a varying distance. The metastructures are designed by inverse design topology optimization. Several numerical examples are shown, including metastructures designed from a genetic algorithm and compatible with currently available fabrication techniques in the visible range.

The following article is a survey in the visible range of dispersion and efficiency engineering of metasurfaces by Benfeng Bai *et al.* Metasufaces allow the manipulation of electromagnetic waves from the strong resonant behaviors of varied meta-atoms arranged in a subwavelength lattice. After introducing metasurfaces, their advantages and drawbacks, the authors review the recent endeavors in solving the limitations of metasurfaces due to their dispersion and low efficiency. The dispersion and efficiency of metasurfaces are engineered according to the specific applications: ultra-highly sensitive sensing, field modulation, nonlinear interactions, full-color imaging, holographic display …

---

[*] Corresponding author.

Metasurfaces are again considered in the article on metasurfaces for thin antenna applications by Massimiliano Casaletti *et al.* In this contribution, metasurfaces are considered for microwaves, where standard circuit technologies can be used for easy fabrication and integration. The authors review the latest progress in metasurface antenna design, where metasurfaces are exploited to miniaturize the profile, increase the bandwidth, and control the radiation pattern in the near- and far-field regions.

The next article, by S. Anantha Ramakrishna *et al.*, focuses on the properties of waveguides filled with anisotropic metamaterials. The authors show how metamaterials based waveguides offer a whole new range of novel features exploiting anisotropic permittivity and permeability that can have vanishing or even sign-shifting eigenvalues. Zero-index and hyperbolic waveguides lead to modes with fractional and even imaginary orders. They may have potential applications in near-field optical microscopy, Laser amplification, harmonic generation, or self-phase modulation that can occur over short lengths of the waveguide.

The article by Vicent Romero-Garcia *et al.* initiates the series of contributions on classical waves other than electromagnetic with a survey on the design of acoustic metamaterials made of Helmholtz resonators for perfect absorption. The authors first report a robust technique for the design of acoustic metamaterials based on the analysis of the zeros and poles of the eigenvalues of the scattering matrix in the plane of complex frequencies. Then several examples of perfectly absorbing one-dimensional structures and membranes are reviewed. In particular, the possibility to obtain perfect absorption by some defined critical coupling conditions is discussed in detail.

That article on acoustic metamaterials is followed by the review article on the theory and design of metamaterials in mechanics by the metamaterial group of Muamer Kadic at FEMTO-ST. In this article, the authors present the general procedure of designing elastic metamaterials based on masses and springs. It is shown that using this simple approach, any set of effective properties can be designed, including linear elastic metamaterials—defined by bulk modulus, shear modulus, mass density—and nonlinear metamaterials—with instabilities or programmable parts. The designs and the corresponding numerical calculations to illustrate different constitutive behaviors are presented.

The last article of the second special double volume by Stéphane Brûlé at DGI-Ménard Inc and one of us is on the role of seismic metamaterials on soil dynamics. The article actually focuses its attention on control of soils structured by an array of boreholes (that are more akin to photonic crystals than metamaterials, as they essentially work in the Bragg regime), that have been shown to allow for shielding and focusing effects. Some previously unpublished experimental results show the potential for energy harvesting of ambient seismic noise of the array of boreholes. The authors further proposed to bridge the field of time-modulated media and seismic metamaterials in order to generate some new effects leading notably to a concept of analogue seismic computer and some internet of things using seismic ambient noise on a geophysics scale.

Boris Gralak is a 1997 graduate engineer of Ecole Polytechnique, received in 2001 the PhD degree of Université d'Aix-Marseille in *Mathematical physics and modelling*, and then worked for 3 years from 2001 to 2004 as researcher in Amsterdam at the research institute AMOLF of Nederlands organization for scientific research (NWO). He is presently Directeur de recherche at Centre national de la recherche scientifique (CNRS) and works at Institut Fresnel in Marseille, France. His main research interests include the mathematical analysis of equations of macroscopic electromagnetism, the modelling of electromagnetic metamaterials, and the design of optical devices.

Sébastien Guenneau is a Director of Research at the Centre National de la Recherche Scientifique who joined the CNRS-Imperial Abraham de Moivre Unité Mixte Internationale in 2019, after working as a lecturer in the Department of Mathematical Sciences at Liverpool University (2004–2005; 2007–2009) and as a CNRS researcher at the Institut Fresnel in Marseille (2006–2019). His main research interests lie in the physics of metamaterials for an enhanced control of wave and diffusion phenomena (including negative refraction and cloaking), in homogenization of multiscale periodic and quasi-periodic media, and in finite element models of acoustic, electromagnetic, hydrodynamic and elastodynamic waves.

Préface

Ce double volume spécial des Comptes Rendus Physique est la deuxième partie d'une collection de quatorze articles qui ont pour but de faire un tour d'horizon de la thématique des métamatériaux. Cet ensemble de quatorze articles, réalisé avec la coopération d'experts internationaux de premier plan dans le domaine des métamatériaux, comprend des recherches originales ainsi que des contributions plus orientées vers des revues de l'état de l'art. Les articles couvrent les sujets des métamatériaux électromagnétiques, acoustiques, élastiques et sismiques et sont organisés en deux doubles volumes rassemblant d'une part, des articles plus orientés sur les concepts et les modèles et, d'autre part, des articles rapportant des résultats plus liés à des applications potentielles prometteuses. Ces deux volumes doubles couvrent donc les aspects théoriques aussi bien qu'expérimentaux, et fondamentaux aussi bien qu'appliqués, dans différents domaines des métamatériaux, depuis les milieux à l'échelle nanométrique (électrodynamique et plasmonique) jusqu'aux milieux à l'échelle du mètre (géophysique).

Dans ce second volume double, la deuxième série de sept articles, où des applications prometteuses sont présentées, commence avec une contribution sur les lames d'onde accordables basées sur des métasurfaces, par Nader Engheta et Nasim Estakhri. Les auteurs proposent une classe de lames d'onde innovantes, pour un contrôle total du retard de phase et de la polarisation de la lumière, constituées de deux métasurfaces symétriques séparées par une distance variable. Les métastructures sont conçues par des méthodes inverses de type optimisation de topologie. Plusieurs exemples numériques sont présentés, dont des métastructures conçues à partir d'un algorithme génétique et compatibles avec les techniques de fabrication actuellement disponibles dans le domaine du visible.

L'article suivant est une étude dans le domaine visible de l'ingénierie de la dispersion et de l'efficacité des métasurfaces, par Benfeng Bai *et al.* Les métasufaces permettent la manipulation d'ondes électromagnétiques à partir du comportement fortement résonant de méta-atomes variés disposés sur un réseau sous-longueur d'onde. Après une introduction sur les métasurfaces, leurs avantages et leurs inconvénients, les auteurs passent en revue les efforts récents pour surmonter les limitations des métasurfaces en raison de leur dispersion et de leur faible efficacité. La dispersion et l'efficacité des métasurfaces sont contrôlées et adaptées en fonction des applications spécifiques : détection ultra-très sensible, modulation de champ, interactions non linéaires, image en couleur, affichage holographique …

Les métasurfaces sont à nouveau au cœur de l'article sur les métasurfaces pour les applications d'antennes de faible épaisseur, par Massimiliano Casaletti *et al.* Dans cette contribution, les métasurfaces sont considérées pour les micro-ondes, où les technologies standard des circuits imprimés peuvent être utilisées pour une fabrication et une intégration faciles. Les auteurs passent en revue les derniers progrès dans la conception d'antennes à métasurface, où les métasurfaces sont exploitées pour miniaturiser le profil, augmenter la bande passante et contrôler le diagramme de rayonnement dans les régions de champ proche et lointain.

L'article suivant, par S. Anantha Ramakrishna *et al.*, se concentre sur les propriétés des guides d'ondes remplis de métamatériaux anisotropes. Les auteurs montrent comment les guides d'ondes à base de métamatériaux offrent une toute nouvelle gamme de nouvelles fonctionnalités exploitant la permittivité et la perméabilité anisotropes qui peuvent avoir des valeurs propres de proches de zéro ou même avec changement de signe. Les guides d'ondes à indice proche de zéro et hyperboliques conduisent à des modes avec des ordres fractionnaires et même imaginaires. Ils peuvent avoir des applications potentielles dans la microscopie optique en champ proche, l'amplification laser, la génération d'harmoniques ou l'auto-modulation de phase qui peuvent se produire sur de courtes longueurs du guide d'ondes.

L'article de Vicent Romero-Garcia *et al.* est la première contribution sur les ondes classiques autres qu'électromagnétiques avec une étude sur la conception de métamatériaux acoustiques constitués de résonateurs de Helmholtz pour une absorption parfaite. Les auteurs présentent tout d'abord une technique robuste pour la conception de métamatériaux acoustiques basée sur l'analyse, dans le plan des fréquences complexes, des zéros et des pôles des valeurs propres de la matrice de diffraction. Ensuite, plusieurs exemples de structures et de membranes unidimensionnelles parfaitement absorbantes sont passés en revue. En particulier, la possibilité d'obtenir une absorption parfaite sous certaines conditions de couplage critiques spécifiques est discutée en détail.

Cet article sur les métamatériaux acoustiques est suivi de l'article de revue sur la théorie et la conception des métamatériaux en mécanique, par le groupe de recherche en métamatériaux de Muamer Kadic. Dans cet article, les auteurs présentent la procédure générale de conception de métamatériaux élastiques à partir de masses et de ressorts. Il est montré qu'en utilisant cette approche simple, tout un ensemble de propriétés effectives peut être conçu, y compris les métamatériaux élastiques linéaires — définis par le module de masse, le module de cisaillement et la densité de masse — et les métamatériaux non linéaires — avec des instabilités ou des éléments programmables. Les *designs* et les calculs numériques correspondants pour illustrer différents comportements constitutifs sont présentés.

Le dernier article de ce second double volume spécial, par Stéphane Brûlé de la société DGI-Ménard Inc et l'un de nous, porte sur le rôle des métamatériaux sismiques sur la dynamique des sols. L'article porte sur le contrôle des sols structurés par un réseau de trous de forage (qui s'apparentent plus à des cristaux photoniques qu'à des métamatériaux, car ils fonctionnent essentiellement dans le régime de Bragg), dont il a été démontré qu'ils permettent des effets de miroirs réfléchissants et de focalisation. Certains résultats expérimentaux inédits montrent le potentiel de récupération d'énergie du bruit sismique ambiant du réseau de forages. Les auteurs ont en outre proposé de jeter un pont entre le domaine des milieux modulés dans le temps et des métamatériaux sismiques afin de générer de nouveaux effets conduisant notamment à un concept d'ordinateur sismique analogique et d'Internet des objets utilisant le bruit sismique ambiant à l'échelle géophysique.

Boris Gralak est ingénieur de l'Ecole Polytechnique diplômé en 1997, a obtenu en 2001 le diplôme de doctorat de l'Université d'Aix-Marseille en *Physique mathématique et modélisation*, puis a travaillé pendant 3 ans de 2001 à 2004 comme chercheur à Amsterdam à l'institut de recherche AMOLF de l'organisation néerlandaise pour la recherche scientifique (NWO). Il est actuellement directeur de recherche au Centre national de la recherche scientifique (CNRS) et travaille à l'Institut Fresnel à Marseille en France. Ses principaux intérêts de recherche sont l'analyse mathématique des équations de l'électromagnétisme macroscopique, la modélisation des métamatériaux électromagnétiques et la conception de dispositifs optiques.

Sébastien Guenneau est directeur de recherche au Centre National de la Recherche Scientifique. Il a rejoint l'Unité Mixte Internationale CNRS-Impérial Abraham de Moivre en 2019, après avoir travaillé comme chargé de cours au Département des Sciences Mathématiques de l'Université de Liverpool (2004–2005 ; 2007–2009) et en tant que chercheur CNRS à l'Institut Fresnel de Marseille (2006–2019). Ses principaux axes de recherche résident dans la physique des métamatériaux pour un contrôle accru des phénomènes ondulatoires et des processus diffusifs (y compris la réfraction négative et le camouflage), dans l'homogénéisation de milieux périodiques et quasi-périodiques multi-échelles, et dans les modèles d'éléments finis en acoustique, électromagnétisme, hydrodynamique et élastodynamique.

Boris Gralak
CNRS, Aix Marseille Univ,
Centrale Marseille, Institut Fresnel,
Marseille, France
boris.gralak@fresnel.fr

Sébastien Guenneau
UMI 2004 Abraham deMoivre-CNRS
Imperial College London
London SW7 2AZ, UK
s.guenneau@imperial.ac.uk

Comptes Rendus
Physique
2020, 21, nº 7-8, p. 625-639
`https://doi.org/10.5802/crphys.5`

Metamaterials 2 / *Métamatériaux 2*

Tunable metasurface-based waveplates - A proposal using inverse design

Lames à retard d'onde accordables à base de métasurfaces - Une approche par conception inverse

Nasim Mohammadi Estakhri[a] **and Nader Engheta**[*, a]

[a] Department of Electrical and Systems Engineering, University of Pennsylvania,
Philadelphia, PA 19104, USA

E-mails: esmo@seas.upenn.edu (N. Mohammadi Estakhri), engheta@seas.upenn.edu
(N. Engheta)

Abstract. An approach to achieve tunable free-space waveplate operation based on a two-layer cascaded metastructure is proposed. Phase retardation is varied through changing the axial distance between the two layers. Full control on the ellipticity of the output wave is attained with wavelength-scale variations in the axial distance. The theoretically desired characteristics of the metastructures are presented and multiple physical implementations are suggested based on inverse design topology optimization.

Résumé. Une approche est proposée pour obtenir un retard de phase d'onde électromagnétique accordable en s'appuyant sur une méta-structure avec deux couches planes en regard l'une de l'autre. Le retard de phase est ajusté par l'intermédiaire de la variation de la distance axiale entre les deux couches. Un contrôle complet de l'ellipticité de l'onde en sortie de dispositif est atteint avec des variations de la distance axiale à l'échelle de la longueur d'onde. Les caractéristiques désirées des méta-structures sont présentées et plusieurs applications physiques sont suggérées, en s'appuyant sur des optimisations topologiques ou des algorithmes génétiques par conception inverse.

Keywords. Polarization, Waveplates, Tunability, Topology optimization, Inverse design, Metastructures.

Mots-clés. Polarisation, Lames d'onde, Accordabilité, Optimisation topologique, Conception inverse, Méta-matériau.

---

[*] Corresponding author.

1. Introduction

Generation of controllable ellipticity and tunable polarized light in a single device could enable a variety of applications in optical devices and set-ups, such as polarization cameras and material characterization. Waveplates are conventionally built using natural birefringent crystals which provide different effective indices depending on the polarization and direction of the incident wave. While propagating inside the crystal, a phase shift (retardation) is gradually created between two orthogonally polarized waves aligned with fast- and slow-axes of the crystal. Due to the small birefringence (e.g. $\Delta n \simeq 9\times 10^{-3}$ for quartz crystal at 633 nm [1]), such devices are typically multiple-wavelengths thick and less desirable for direct integration purposes. Alternatively, an approach that may provide potentially thinner solutions which are more suitable for integration purposes is to use metastructures (a general term we use hereafter referring to metasurfaces and metamaterials). Orientation, dimensions, material properties, and geometrical shape of surface elements in metastructures have been optimized to create the desired retardation between orthogonal polarizations, e.g. to create electromagnetically thin quarter-wave plates and halfwave plates [2–13], both in transmission and reflection modes. In addition to the smaller size, designer metastructures provide a platform to enforce application-based characteristics as the response is not anymore limited by the naturally available birefringent materials. For instance, attaining specific bandwidth of operation, angular dispersion, loss, etc. may be targeted using metastructure-based waveplates. In this article we propose a new scheme to attain phase shift "tunability" in a planar waveplate consisting of two cascaded metastructures and with close to ideal conversion efficiencies. One of the main advantages of our proposed platform resides in the fact that the controllable retardation is independent from the specifics of the employed metastructures. We show that by using a pair of metastructures as polarization-dependent beam splitters (anisotropic anomalous refraction), it is possible to achieve any amount of retardation simply through adjusting the distance between the two cascaded metastructures. Polarization sensitive anomalous refraction is implemented using the inverse topology optimization technique. These techniques have gained increasing amount of interest in the recent years due to relatively fast convergence and versatile range of applications [14–23]. The tunability can be expressed as a linear dependence between the retardation and the physical distance between the layers. Fast- and slow-axes of the structure are also automatically specified in the design and there is no need for additional steps to determine them, as required in conventional birefringent crystals. Previously reported tunable waveplates have relied on several reconfigurable elements to achieve some range of phase tunability, including incorporation of liquid crystals [24–26], phase change materials [27, 28], and electromechanically actuated capacitor arrays [29]. Our proposed waveplates, by contrast, are formed by two metasurfaces whose axial separation is the only movable part. In the following we will present the theoretical formulation of the transfer function of the waveplate in Section 2, followed by two sets of numerical examples in Sections 3 and 4. We will also look into several cases including oblique incidence and extreme refraction.

2. Theoretical formulation

2.1. *Idea and formulation: normal incidence*

Figure 1 illustrates the idea of the tunable free-space wave-plate configuration. Two planar metastructures (depicted with roman numbers I and II) are placed parallel to each other and with a finite distance "d" along the x-axis. Each metastructure has a thickness of "h" in the x-direction and it is periodic in the y-direction with fundamental periodicity of "L" (one period is shown in Figure 1). While the metastructures may be designed in the most general format, a two-dimensional (2D) configuration which is z-invariant in our arrangement is in principle sufficient

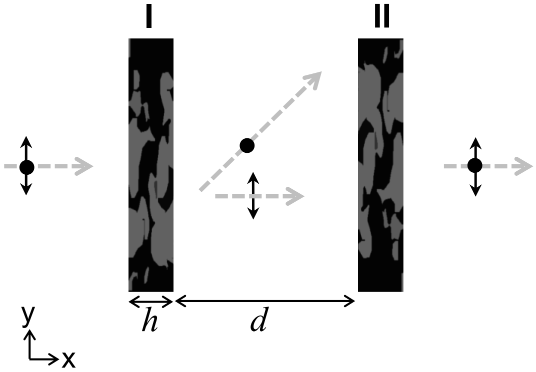

Figure 1. Polarization-dependent phase control. Schematic illustration of the idea of tunable waveplate metastructures. Two planar 2D (i.e. z-invariant) metastructures (I and II) are placed parallel to each other, each with thickness of "h" in the direction of wave illumination and period of "L" in y-direction. The two metastructures are identical in all aspects, except their placement orientation. Metastructure II is the mirror image of metastructure I in both x- and y-directions, i.e., it is rotated 180° around the z axis. In the example shown, metastructures only affect the momentum of TE waves (i.e. electric field polarized out-of-plane), but not the momentum of TM waves. Due to their arrangement, the change in the momentum imposed by the first structure is canceled out by the second one, creating a controllable phase retardation between the two polarizations.

to achieve polarization control and therefore it is not necessary to assume a 3D patterning. The distribution of the permittivity inside each metastructure is optimized according to the goal functions discussed in the following.

Waveplates (also known as wave retarders) operate based on creating a phase shift between two orthogonal polarizations whose orientations are specified based on the optical axis of the waveplate [30]. Although using metasurfaces have enabled a large variety of ultrathin polarizing elements, extensive parametric studies are typically required to attain the required phase shift (retardation) between the orthogonal polarization [5–13]. Quite contrary, here we rely on the difference in the imposed momentum on the Transverse Electric (TE) and Transverse Magnetic (TM) incident waves to attain controllable phase retardation [31]. As a result, once the core metastructure (as in Figure 1, metastructure I) is designed, the system can be tuned to create any desired phase shift between the two orthogonal incident waves. In other words, the retardation is determined by the arrangement (e.g. distance) of the two metastructures rather than intrinsic properties of each surface.

Assuming a monochromatic plane wave normally incident on the structure from left to right in Figure 1, the role of metastructure I is set to impose an abrupt, polarization-sensitive momentum change on the impinging wave. Upon refraction through the metastructure I, the TE incident wave is tilted by an angle of θ_{TE} which, as an example, is set at 45° throughout this article, and the TM incident wave is tilted by an angle of $\theta_{\mathrm{TM}} \neq \theta_{\mathrm{TE}}$ which we set at 0° hereafter. Metastructure I therefore operates similar to a polarization beam splitter, yet implemented with a planar and potentially thin structure. As the wave propagates beyond metastructure I, assuming $e^{j\omega t}$ time-harmonic convention, the total electric field may be written as,

$$\begin{aligned}\mathbf{E}_{\mathrm{total},1} = {} & \cos\theta_{\mathrm{TM}}{}^{-1/2}(\mathbf{y}\cdot\mathbf{E}_i)[\mathbf{y}\cos\theta_{\mathrm{TM}} - \mathbf{x}\sin\theta_{\mathrm{TM}}]e^{-jk_0(x\cos\theta_{\mathrm{TM}}+y\sin\theta_{\mathrm{TM}})+j\varphi_{\mathrm{TM},1}} \\ & + \cos\theta_{\mathrm{TE}}{}^{-1/2}(\mathbf{z}\cdot\mathbf{E}_i)\mathbf{z}e^{-jk_0(x\cos\theta_{\mathrm{TE}}+y\sin\theta_{\mathrm{TE}})+j\varphi_{\mathrm{TE},1}}\end{aligned} \tag{1}$$

indicating the polarization dependent beam splitting effect. Notably, the cumulative propagation phases of the two polarizations are different and depends on the refraction angles θ_{TM} and θ_{TE}. Note that in writing (1) we assume an ideal transmission response, meaning that reflected waves from metastructure I (for both co- and cross-polarizations) are negligible. Here, $\mathbf{E}_i$ is the incident electric field vector lying in the y–z-plane, k_0 is the free space wave number, and $\varphi_{\mathrm{TM},1}$ and $\varphi_{\mathrm{TE},1}$ are constant phases added to TM and TE waves upon traversing metastructure I. While the phase difference between the two polarizations varies upon propagation, the two waves are also angularly separated after metasurface I. In order to restore the original wavefront of the incident wave we use a second metastructure (as shown in Figure 1 with metastructure II), whose role is to restore the original momentum of both polarizations. This means that the TE and TM waves must be rotated by angles of $-\theta_{\mathrm{TE}}$ and $-\theta_{\mathrm{TM}}$, respectively. Interestingly, in order to restore the original momentum of the incident wave components it is not required to separately design a second metastructure from scratch. Indeed, investigating Figure 1, the trajectory of waves traversing metastructure II are identical to the trajectory of their interaction with metastructure I when they are time-reversed. As a result, it is sufficient to use an identical design for both metastructures, while the second structure is rotated 180° around the z-axis compared to the first one. Again, assuming ideal transmission with zero reflection by metastructure II, the total outgoing electric field beyond metastructure II then takes the following form,

$$\mathbf{E}_{\mathrm{total},2} = e^{-jk_0x}[(\mathbf{y}\cdot\mathbf{E}_i)\mathbf{y}e^{-jk_0d\cos\theta_{\mathrm{TM}}+j\varphi_{\mathrm{TM},2}} + (\mathbf{z}\cdot\mathbf{E}_i)\mathbf{z}e^{-jk_0d\cos\theta_{\mathrm{TE}}+j\varphi_{\mathrm{TE},2}}]. \tag{2}$$

Note that the full transmission of both polarizations from the second metastructure is guaranteed due to reciprocity [32, 33]. Investigating (2), it is clear that the phase difference $\Delta\Phi = \Phi_{zz} - \Phi_{yy}$ for the transmitted wave is controllable with the distance "d", as well as choice of θ_{TM} and θ_{TE}. For instance, if $\Delta\Phi$ is set at 90°, the metastructure in Figure 1 operates as a quarter waveplates, while for $\Delta\Phi$ of 180° we will have a half waveplate. This structure is analogous to a birefringent crystal, with the TE wave experiencing lower effective index (fast axis) and the TM wave is aligned with the slow axis with effective refractive index of 1 (assuming θ_{TE} of 45° and θ_{TM} of 0°). The waveplate is automatically "cut" in the right plate such that the fast and slow axes are parallel to the surface of the waveplate. In addition, note that we implicitly assume that if the metastructures are finite in the y-direction (i.e. a few periods of each surface are present), they are extended enough such that the waves will not spillover from the sides. As a rule of thumb, for Gaussian wave of waist w_0 focused on metastructure I, the structure must be extended at least to $y = (2w_0/\cos\theta)\sqrt{1+(\lambda_0 d/\pi w_0^2\cos\theta)^2} + d\tan\theta$, with $\theta = \max(\theta_{\mathrm{TM}}, \theta_{\mathrm{TE}})$.

Several techniques may be envisioned to attain polarization selective anomalous refraction. With electromagnetically thin surfaces, anomalous refraction can be created through carefully engineering the surface impedance profile to generate an effective constant momentum on the incident wave [34–36]. Along the same procedure, the surface profile maybe designed anisotropic (i.e. surface response depends on the polarization of the incident wave) to imprint a polarization dependent momentum on the wave [37, 38]. The choice of a specific technique to design such metastructures primarily depends on the wavelength of operation and the available computational resources. Here, we use optimization techniques (details in Sections 3 and 4) to create two sets of anisotropic metastructures complying with (2) and (4). While the performance of the system in Figure 1 is independent of the specifics of metastructures I and II (at the designed wavelength and angle of illumination), we note that several other properties of the system may strongly depend on the choice of platform. For instance, gradient metasurfaces have been shown to possess reasonably broadband behavior and angular stability [39,40]. Such properties may not be automatically given using other platforms such as inverse design, yet, they can be encoded into the optimization [19,22]. Here, we focused on narrowband optimization to demonstrate the concept. However, available broadband optimization techniques may be used to create broadband devices.

Prior to characterizing the system and providing numerical examples, as a side note it is also worth mentioning the case of Panchantram-Berry (PB) or geometrical phase metastructures [41, 42]. Through systematic rotation of a half-waveplate surface element, PB metastructures create a desired phase profile on their surface which is used to alter the properties of the transmitted wave. For instance, by creating a linear phase profile (when each surface element is rotated by a constant degree compared to its neighboring elements), the momentum of the transmitted wave can be altered according to the slope of the phase profile. PB phase operates on circularly polarized (CP) incident fields and the imprinted phase flips sign depending on the handedness of the incident light [41]. As a result, left-and right-hand CP waves experience opposite transformations along interaction with PB metastructures. While in this article we focus on waveplates for orthogonal linearly polarized waves, it is also possible to use PB surfaces to achieve polarization conversion in a system similar to Figure 1, as explained briefly in the following: Assume metastructure I implemented using PB surface elements to change the direction of normally incident right-handed CP (RCP) plane waves by an angle of θ_{RCP}. Therefore, the left-handed incident wave (LCP) will be rotated by an angle of $\theta_{\mathrm{LCP}} = -\theta_{\mathrm{RCP}}$. Metastructure II is a 180° rotated version of metasurface I (see Figure 1 caption), thus it will restore the trajectory of each CP wave to normal direction. We note that due to $|\theta_{\mathrm{LCP}}| = |\theta_{\mathrm{RCP}}|$ for the normal incidence, both waves will experience equal retardation even though they are first split and then re-combined in the system. Let us now consider an obliquely incident "linearly polarized" wave (angle of incidence $\theta_{\mathrm{oblique}}$, defined as the angle between the wave vector and the vector normal to the metastructure I interface), illuminating the system from left to right. The linearly polarized wave can be expressed as the summation of two CP waves with opposite handedness, each experiencing their corresponding surface momentum. Following momentum conservation, the refraction angles in the area between metastructures I and II can be written as,

$$\theta'_{\mathrm{RCP}} = \sin^{-1}(\sin\theta_{\mathrm{RCP}} + \sin\theta_{\mathrm{oblique}}); \quad \theta'_{\mathrm{LCP}} = \sin^{-1}(\sin\theta_{\mathrm{LCP}} + \sin\theta_{\mathrm{oblique}}). \tag{3}$$

Consequently, by breaking the symmetry of refraction through oblique illumination we achieve $\theta'_{\mathrm{RCP}} \neq -\theta'_{\mathrm{LCP}}$ and RCP and LCP waves experience different propagation phases as they traverse the system. When re-combined at Metastructure II, the polarization state of the outgoing wave may be designed at will, for instance the system can be fully transformed the input into the orthogonal linear polarization (i.e. TE to TM conversion or vice versa). This is especially appealing considering the straightforward design procedure of PB metasurfaces. While in the following we focus on linear polarization (i.e. the surface momentum is designed for two orthogonal linearly polarized waves), the above discussion shows that similar argument is also valid for PB metasurfaces with proper considerations.

Returning to our design, following (2), the phase difference $\Delta\Phi = \Phi_{zz} - \Phi_{yy}$ can be written as,

$$\Delta\Phi = -k_0 d(\cos\theta_{\mathrm{TE}} - \cos\theta_{\mathrm{TM}}) + \varphi_{\mathrm{cte}} \tag{4}$$

in which φ_{cte} is a constant phase enclosing the local properties of metastructure I. For instance, assuming θ_{TE} of 45° and θ_{TM} of 0°, the system can be tuned from quarter waveplate functionality to half waveplate functionality through changing the separation of the metastructures by $\lambda_0/(4-2\sqrt{2})$. At 633 nm, this is about 540 nm tuning in the distance between metastructures. The tuning might be achieved through several effects to create mechanical movement such as using MEMS, motorized stages, flexible substrates, thermal expansion, electrostatic forces, etc. [43–49]. For instance, MEMS tunable metasurface devices have been shown to offer micron-scale distance tunability [45], enough to achieve arbitrary retardation control in our example.

2.2. *Oblique incidence*

Equation (4) is written for the case of normal illumination on the system. Interestingly, the design in Figure 1 may also provide a platform for dual (or multiple) functionality under oblique incidence. Let us consider an incident angle of θ_{inc} (angle between the wave vector and the vector normal to the metastructure I interface, in the plane of incidence). Assuming θ_{inc} to be small enough such that the structure is still reflectionless, the imprinted momentum enforces the refracted angles of the TM and TE waves to be (in the region between metastructures I and II),

$$\theta'_{\mathrm{TE}} = \sin^{-1}(\sin\theta_{\mathrm{TE}} + \sin\theta_{\mathrm{inc}}), \quad \theta'_{\mathrm{TM}} = \sin^{-1}(\sin\theta_{\mathrm{TM}} + \sin\theta_{\mathrm{inc}}). \tag{5}$$

As a result, the phase shift between the orthogonal polarizations is a function of incidence angle following,

$$\Delta\Phi' = -k_0 d(\cos\theta'_{\mathrm{TE}} - \cos\theta'_{\mathrm{TM}}) + \varphi'_{\mathrm{cte}}. \tag{6}$$

There are several possibilities to use such form of dependence on the illumination angle. For example, one can imagine a structure specifically tuned to create half waveplate response for normal incidence and quarter waveplate response for oblique incidence. As another example, one can imagine a system correcting unwanted phase shifts depending on the angle of incidence. Clearly, exploiting the angular response of the system requires metastructures to be designed with reasonable angular stability. As mentioned, gradient metasurfaces typically maintain their performance over a wide range of incident angles [39, 40]. If other platforms are used, this property is to be built in the optimization procedure [19, 22].

3. Numerical results: Part I

In this section we present a set of numerical results to elucidate the principles of the operation of the proposed system, implementing a tunable waveplate. While the principles of the operation are similar, the same functionality may be implemented in several platforms and with distinct characteristics that maybe required for a specific application. Fabrication limitations, desired operational bandwidth and dispersion characteristics, availability of materials, desired angular response, and insertion loss are some of the main parameters that affect the choice of platform. Here, we start by an inverse-designed topology-optimized dielectric structures exploiting the entire design space (Section 3) and continue with topology-optimized complex multilayer structures with the goal of better compatibility with currently available fabrication techniques.

Figure 2 shows a set of four optimized geometries to achieve waveplate operation, following the schematic demonstration in Figure 1 (four separate examples are provided). The distribution of the permittivity inside each of the four metastructures is optimized such that the structure imprints zero momentum shift on the incident TM wave (θ_{TM} is 0°) and constant momentum shift on the incident TE waves (θ_{TE} is 45°). We exploit low-loss materials (e.g. $\mathrm{TiO_2}$ with permittivity of approximately 5.5 at 633 nm [50]) as shown in panel (a), as well as higher index materials (e.g. Silicon with approximate permittivity of 11.7 at 3000 nm [51]), as shown in panel (b). In each case, topology optimization [52] is used to find the distribution of permittivity, enforcing a quantized pattern as much as possible. In this regard, we are looking for patterns consisting of either air (blue) or dielectric (pink). This is especially clear in Figure 2b where we could achieve a bi-material pattern (Silicon and air) due to high refractive index of Silicon. We also note that the availability of materials play a crucial role on the size of the metastructures. In our examples shown in Figure 2, desired functionality was achieved over a thickness of approximately $0.8\lambda_0$ at 633 nm and $0.25\lambda_0$ at 3000 nm. Clearly, adding additional constraints on the optimization (such as angular stability, broadband operation, less granularity, etc. as discussed above) will entail larger structures. In the following, we will present the simulation results for the structure

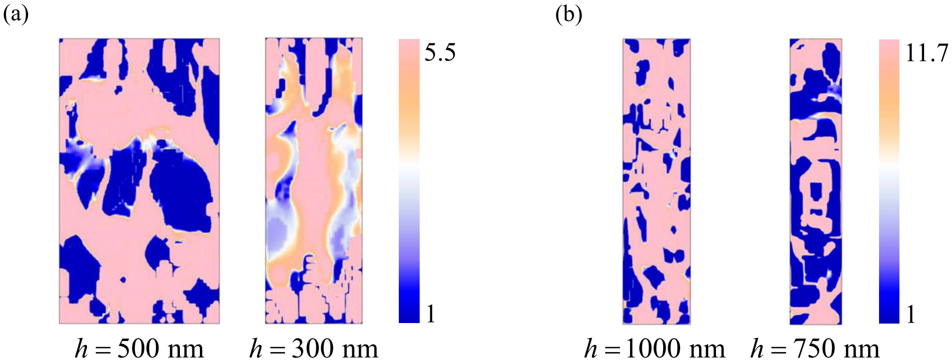

Figure 2. Inverse-design topology-optimized permittivity distributions to achieve polarization-dependent momentum control. The distribution of relative permittivity inside metastructure I in Figure 1 for θ_{TE} of 45° and θ_{TM} of 0°, optimized for two different thickness at (a) 633 nm when colors indicate TiO_2 and air at the extreme values, and (b) 3000 nm when colors indicate Si and SiO_2 at the extreme values. In each case, one unit cell in the y-direction is shown. The second case in panel (a) exhibits graded permittivity distribution, while the three other examples are approximately quantized.

shown in Figure 2a-left panel. The other three examples offer similar performances. The overall response of the system as shown in Figure 1, is indeed predominantly set based on the accuracy in the design of metastructure I. As a result, as long as efficient polarization-dependent beam splitting is achieved with metastructure I, the entire system operates efficiently following (4).

Enforcing θ_{TE} to be 45° (and θ_{TM} being 0°) requires a periodicity of $1.4\lambda_0$ for the structure in the y-direction [40]. This is approximately 900 nm at the design wavelength of 633 nm in the visible range. Optimization goals are set as simultaneous total transmission into zeroth order mode for the TM polarization and total transmission to the first order Floquet mode ($n = 1$) for the TE polarization. We note that the choice of θ_{TE} is arbitrary, and as it can be seen in Section 3.1, it merely affects the sensitivity of the waveplate operation to variations in the distance between the two metastructures. On the other hand, extreme angles of propagation in the area between metastructure I and II may be more difficult to achieve while maintaining full transparency. Figure 3 demonstrates the performance of the optimized structure shown in Figure 2a-left panel. Simulations are performed in COMSOL Multiphysics® using the frequency domain solver [52]. The optimized topology is capable of transforming more than 99% of the incident power into the desired diffraction modes for both polarization states of the incident wave. While the distribution of the wave inside the optimized layer exhibits complicated behavior, the evanescent decay is quite rapid and after a distance of approximately half a wavelength the desired scattering mode is dominant. This implies that when assembling the system in Figure 1, we can bring the surfaces as close as 300 nm for operation at 633 nm wavelength. Inspecting the field distributions in Figure 3, we note that the y-component of the electric field shown in the lower panel is not the tangential component of the field in the dielectric region. As a result, this component is mostly discontinuous across the dielectric region. This does not imply higher Q modes in the case of TM illumination. Indeed, one might look at the distribution of the z-component of the magnetic field in this case, which is continuous across all layers.

In the next step, two metastructures with the profile shown in Figure 2a-left panel are arranged cascaded (see Figure 1) with proper rotation of the second metastructure to achieve controllable retardation. The results are qualitatively portrayed in Figure 4 where we show time snapshot of the electric field distribution when the cascaded system is illuminated with TE and TM fields,

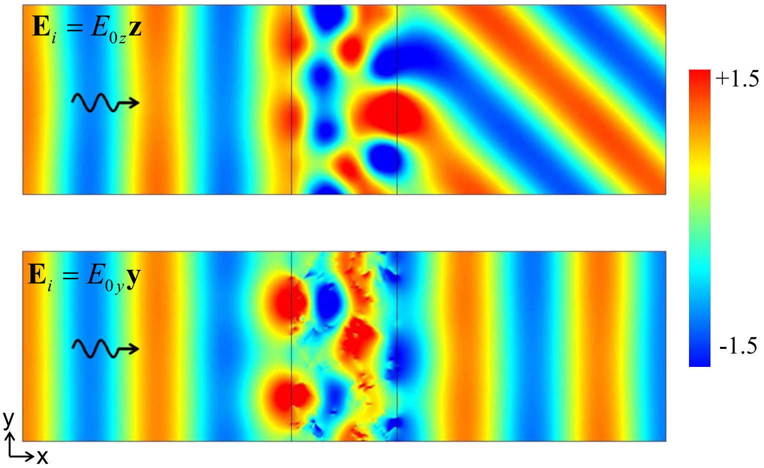

Figure 3. Polarization beam splitting metastructure. Snapshot in time of numerical simulation of electric field distribution when metastructure shown in Figure 2a-left panel is illuminated from left side with a plane wave (normal to the structure interface, i.e. $\theta_{\text{inc}} = 0$). The upper panel shows the distribution of the z-component of the electric field for TE illumination (i.e. $\mathbf{E}_i = E_{0z}\mathbf{z}$). The entire incident energy is funneled into the first order transmission Floquet mode, designed at θ_{TE} equal to 45°. The topology-optimized metastructure creates a complex near-field in the vicinity of the structure, however the evanescent waves decay rapidly. The lower panel shows the distribution of the y-component of the electric field for TM illumination (i.e. $\mathbf{E}_i = E_{0y}\mathbf{y}$). The entire incident energy is funneled into the zeroth-order transmission Floquet mode, indicating θ_{TM} equal to 0°. Note that in this case, the plotted component of the electric field (i.e. y-component) is not tangent to the metastructure pattern boundaries. As the result, the field distribution is discontinuous at the air-dielectric interfaces. Here, we have used COMSOL Multiphysics® frequency domain solver [52]. The structure is truncated with periodic boundaries at the top and bottom, linked to two periodic ports on the left (for excitation) and right. The polarization of the incident field is set at the ports and all incident waves are normal to the surface of the optimized structure, i.e. propagating in the x-direction.

respectively shown in the upper and lower panels. As expected, the wave experiences a different trajectory in the area between the two metastructures depending on the polarization of the incident wave. As viewed from the outside, normally incident waves experience polarization-dependent retardation as they traverse the system. Here we show four examples with the phase delay between the two polarizations changing between 0° (Figure 4a), 90° (Figure 4b), 180° (Figure 4c), and 270° (Figure 4d). Clearly, any other value of phase retardation can be achieved by adjusting the distance between the two layers in the values between such distances. Each degree of change in retardation requires a movement of approximately 6 nm in the distance between metastructures (see (4)).

The results are quantitatively studied in Figure 5 where we show the transmission amplitudes and phases as a function of the separation "d". As expected, the transmission amplitudes (Figure 5a) are very high for both polarizations and above 95% power transmission for TE wave and above 99% power transmission for the TM wave are achieved, independent of the spacing between metastructures. This is the direct result of enforcing zero reflection in the topology-optimized design of metastructure I, which ensures minimal Fabry–Pérot effects. The amplitude

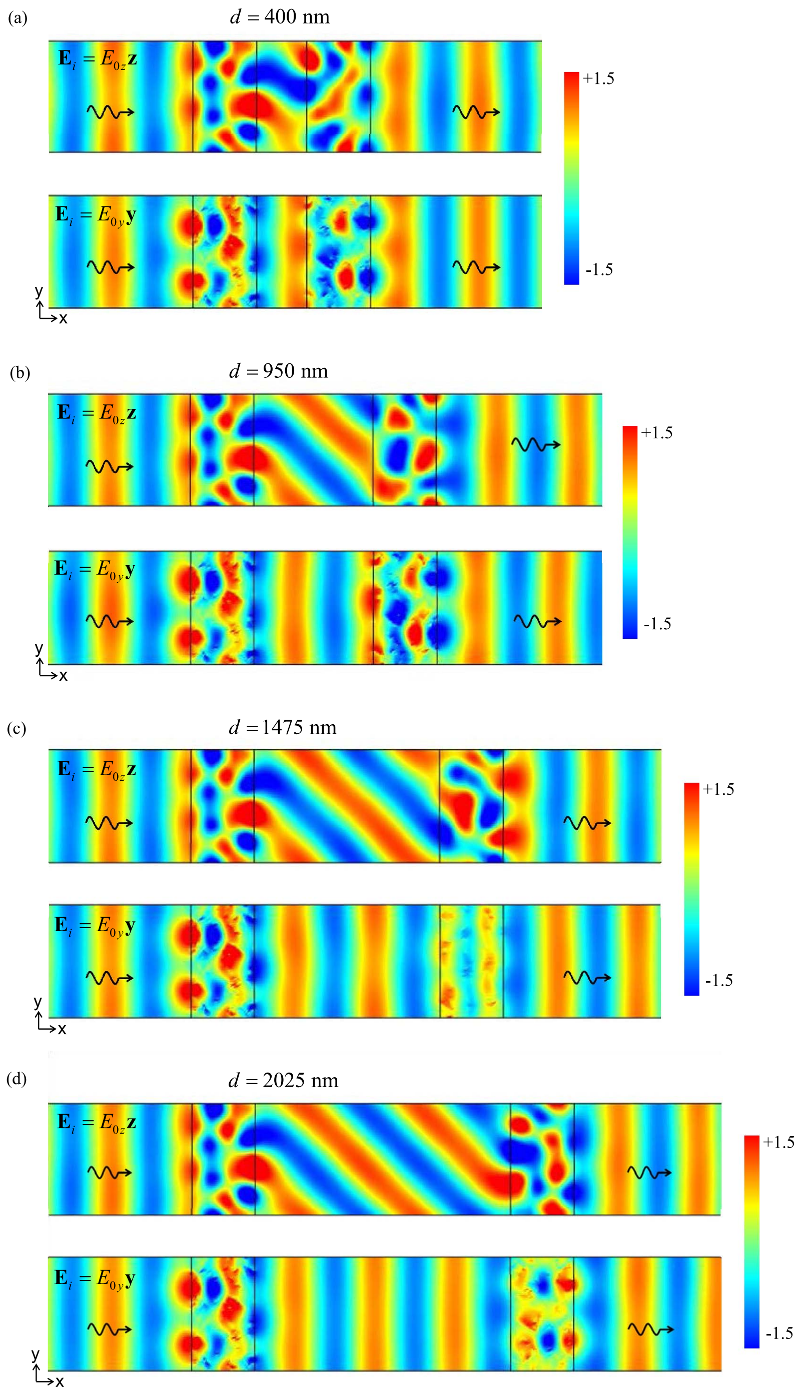

Figure 4. Tunable retardation. Snapshot in time of the numerical simulation of electric field distribution (both polarizations) for different values of "d" parameter, as shown in Figure 1. Metastructures I and II are identical and 180° rotated version of each other. Due to proper cascading, TE and TM waves experience different trajectories in the area between the two metastructures, but they merge after the second metastructure. The axial separation between metastructures (i.e. "d") is chosen such that the phase shift between two polarizations is (a) 0°, (b) 90°, (c) 180°, and (b) 270°. Details on the simulation setup are given in the caption of Figure 3.

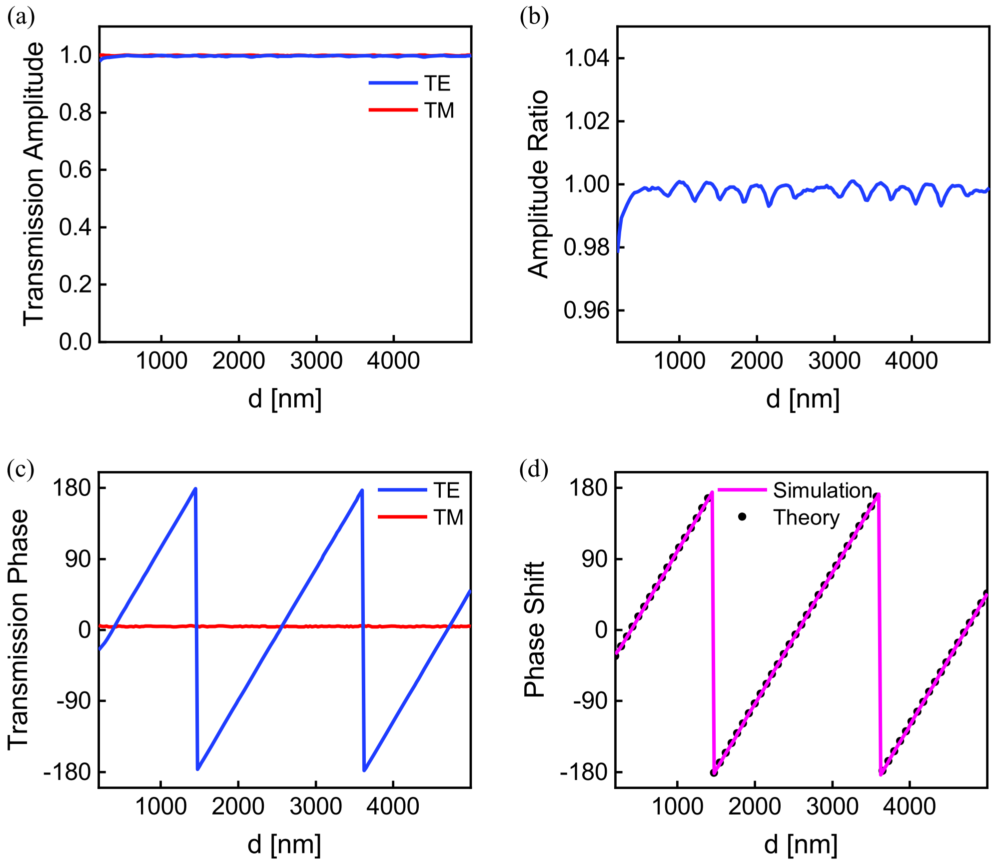

Figure 5. Tunable waveplate characterization. Simulation results for (a) Transmission amplitude of the TE (blue) and TM (red) normally incident plane waves from the waveplate system (shown in Figures 1 and 2a-left panel). Due to enforcing zero reflection in the optimization procedure, no resonance effect is observed. (b) Amplitude ratio defined as the ratio between the transmission amplitude of the TE wave divided by the transmission amplitude of the TM wave. (c) Transmission phase of the TE (blue) and TM (red) normally incident plane waves. Phases are recorded at constant positions regardless of the distance "d". Since the TM refraction angle is chosen at 0°, i.e. $\theta_{\mathrm{TM}} = 0$, the output phase is not a function of "d" for this polarization. (d) Phase difference between the outgoing waves, compared to the analytical expression given in (4).

ratio between the transmitted TE and TM waves is also shown in Figure 5b, maintaining approximate ratio of 1 across all values of "d". The transmission phase of the two polarization components versus the spacing "d" is shown in Figure 5c. Note that the inner refraction angles are set at $\theta_{\mathrm{TM}} = 0°$ and $\theta_{\mathrm{TE}} = 45°$. As a result, the outgoing phase of the TM wave is not a function of "d", merely maintaining a constant value due to the local constant phases added by metastructures. The transmission phase of the TE wave, on the other hand, follows a slope of $-k_0(\cos\theta_{\mathrm{TE}} - 1)$, as the sampling ports are positioned at fixed distances from each other. Figure 5d illustrated the simulated phase difference $\Delta\Phi = \Phi_{\mathrm{TE}} - \Phi_{\mathrm{TM}}$ compared with the expected linear variation calculated in (4), showing very good agreement.

3.1. *Extreme bending*

Figure 5d (along with the approximately constant amplitude ratio reported in Figure 5b) illustrates the tunable waveplate operation of the system. As mentioned before for our choice of refraction angles an axial distance variation of approximately 540 nm is required to change the retardation by 90° (6 nm change for each degree of retardation). More rigorously, this length can be expressed as a function of both refraction angles as,

$$\Delta d_{\pi/2} = \frac{\lambda_0}{4|\cos\theta_{\mathrm{TE}} - \cos\theta_{\mathrm{TM}}|}. \tag{7}$$

Evidently, by maximizing the denominator in (7) we can increase the sensitivity of the waveplate. As an example of this high sensitivity, we have used topology optimization to design metastructures with θ_{TM} of 0° and extreme θ_{TE} of 85°. Clearly, the extreme wave bending would entail a more sophisticated optimization procedure [36]. Here, we adhere to the same size and materials as used for the previous example to provide a sample design. The optimized metastructure couples approximately 98% of the incident TE wave power to the first Floquet mode and more than 99% of the incident TM wave to the zeroth order transmission mode. Figure 6a visually illustrates the performance of the waveplate when adjusted to create 180° phase shift between TE and TM waves (half-wave plate operation). Note the extreme bending in the area between the two metastructures under TE illumination. It is worth mentioning that power conservation requires that amplitude of the refracted wave to be inversely related to the incident normal wave [36]. For this reason, the wave in the area between the two metastructures shows a higher amplitude although it carries the same amount of power as the incident wave. There are no internal reflections or resonance behaviors involved and the wave smoothly propagates from left to right.

Due to high angle of refraction for the TE wave, cascading the two surfaces is quite challenging due to the possibility of internal reflections. This is quantified in Figure 6b, where the transmission amplitude of both polarizations is studied for different values of separation. Indeed, and in spite of the internal extreme bending, we are able to achieve a range with width of approximately 2000 nm where transmission amplitudes are approximately constant. The internal reflections create resonances beyond these points, which are to be avoided. In this range, as shown in Figure 6c, the phase shift between the two linear polarizations approximately follow the expected trajectory in (4). We note that the optimal phase trajectory is calculated for a reflectionless structure. As a result, when there is residual reflection from metastructures, or internal resonances are created, the phase shift differs from the optimal value reported in (4). Here, to switch from quarter-wave plate operation to half-wave plate operation at wavelength of 633 nm (i.e. 90° retardation change), the separation must be changed approximately 170 nm (less than 2 nm change for each degree of retardation). As discussed before, depending on the application, the sensitivity of the waveplate may be controlled through proper choice of θ_{TE} and θ_{TM}.

4. Numerical results: Part II

The results presented in Section 3 utilized the entire design space to provide topology-optimized metastructures for tunable waveplate operation. In this section we report another example designed using the genetic algorithm optimization technique and enforcing a multi-layer structure (similar to [22]), suitable for possible fabrication. Structure is designed at mid-infrared (3000 nm) in form of silicon posts embedded in alumina (shown in Figure 7a). Silicon posts are approximately 230 nm tall in x-direction and the minimum width of each post is more than 200 nm in y-direction. Genetic algorithm minimization [53] is used to define the optimum material in each pixel (total of 107 degrees of freedom). We assume θ_{TM} to be 0° and θ_{TE} of 45°. The corresponding transmission amplitudes and phase retardation between the two polarizations are shown in

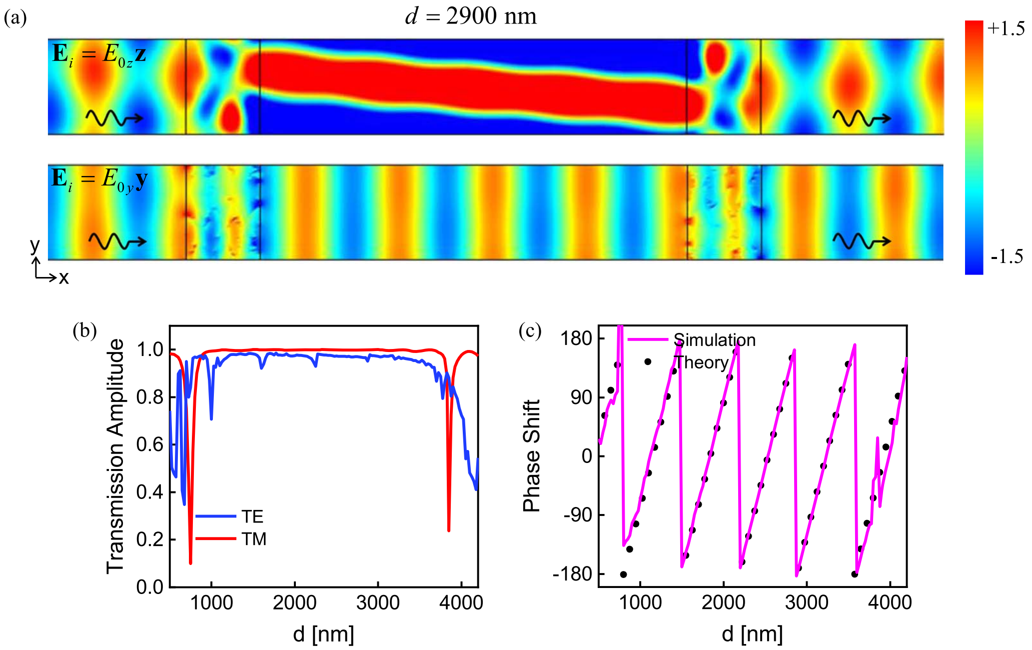

Figure 6. Tunable retardation with increased sensitivity. (a) Snapshot in time of numerical simulation of electric field distribution (both polarizations) for "d" parameter set at 2900 nm to provide a phase shift of 180° between two polarizations. Due to proper cascading, TE and TM waves experience different trajectories in the area between the two metastructures, but they merge after the second metastructure. (b) Transmission amplitude of the TE (blue) and TM (red) normally incident plane waves from the waveplate system when the internal angles are set to 85° for TE wave and 0° for the TM wave. (c) Phase difference between the outgoing waves, compared to the analytical expression given in (4), plotted versus separation "d". Details on the simulation setup are given in the caption of Figure 3. Here, due to the extreme bending angle and the enhanced sensitivity of response to the granularity of the metastructure, identical mesh profiles are used at the optimization and simulation stages. The response sensitivity may be controlled as a parameter in the optimization process.

Figures 7b and 7c, respectively. Here, there are residual unwanted scattering in metastructure I (which may be eliminated with further genetic algorithm optimization) around 14% for TE and 10% for TM waves. As a result, there is a fluctuation in the amplitude of the desired outgoing wave. The phase profile, however, is more resilient to such scatterings, as can be seen in Figure 7c.

5. Conclusions

We have numerically presented a new approach to achieve tunable waveplate operation using two cascaded metastructures. Metastructures are identical and designed to operate as polarization-sensitive beam splitters with designer refraction angles. It is shown that with proper arrangements, the phase delay between the two linearly polarized illuminating waves can be tuned by changing the distance between the metastructures. This can be envisioned through using MEMS, motorized stages, flexible substrates, or thermal expansion. The full retardation control (and hence control on the ellipticity of the outgoing wave) is attainable through wavelength-

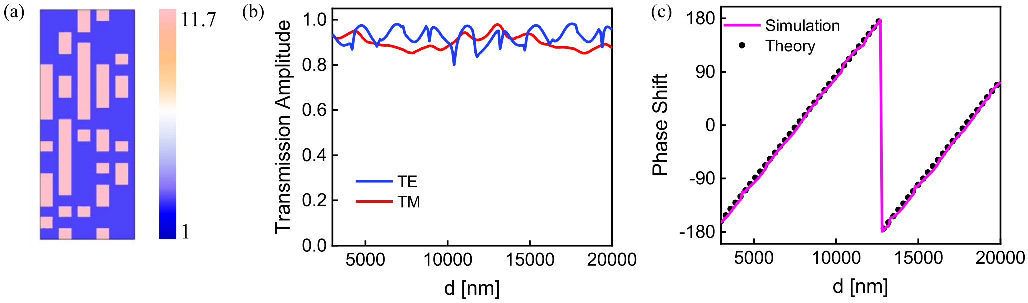

Figure 7. Multi-layer tunable waveplate. (a) Distribution of relative permittivity inside metastructure I. The pink color corresponds to silicon posts and the light blue background shows the alumina substrate. (b) Transmission amplitude of the TE (blue) and TM (red) normally incident plane waves from the waveplate system shown in panel a. (c) Phase difference between orthogonal polarizations of the outgoing wave, compared with the analytical expression given in (4), plotted versus separation "d".

scale axial distance variations. The internal refraction angles maybe used to control the sensitivity of the waveplate. Dual or multiple functionality is also possible by changing the incident angle. Implications of using geometrical phase (PB phase) to achieve linear polarization conversion is also discussed. Topology-optimized physical designs of waveplates for operation at visible and mid-infrared are presented. We consider both cases of full design space and restricted multi-layer optimizations using the commercial numerical solvers. In addition to tunable waveplate operation at typical cases of quarter and half-waveplate, the proposed structure is especially interesting to restore the desired polarization when unwanted phase shifts are created between orthogonal polarization components, in complex multi-elements setups. One of the key characteristics of the presented approach relies on the decoupling between the induced phase shift and the individual properties of the metastructure. We showed that the phase shift can be controlled with variation of a single physical parameter. This significantly reduces the complexity of the design procedure. With the growing interest in using metasurfaces in new realms (e.g. for non-electromagnetic waves [54–56] or non-classical waves [57–60]), our approach may find interesting applications in the broader metamaterial community.

Acknowledgements

This work is supported in part by the US Air Force Office of Scientific Research (AFOSR) Multidisciplinary University Research Initiative (MURI) grant # FA9550-17-1-0002.

References

[1] G. Ghosh, "Dispersion-equation coefficients for the refractive index and birefringence of calcite and quartz crystals", *Opt. Commun.* **163** (1999), no. 1–3, p. 95-102.

[2] N. Yu, F. Aieta, P. Genevet, M. A. Kats, Z. Gaburro, F. Capasso, "A broadband, background-free quarter-wave plate based on plasmonic metasurfaces", *Nano Lett.* **12** (2012), no. 12, p. 6328-6333.

[3] B. Yang, W. Ye, X. Yuan, Z. Zhu, C. Zeng, "Design of ultrathin plasmonic quarter-wave plate based on period coupling", *Opt. Lett.* **38** (2013), no. 5, p. 679-681.

[4] L. Cong, N. Xu, J. Gu, R. Singh, J. Han, W. Zhang, "Highly flexible broadband terahertz metamaterial quarter-wave plate", *Laser Photonics Rev.* **8** (2014), no. 4, p. 626-632.

[5] A. Roberts, L. Lin, "Plasmonic quarter-wave plate", *Opt. Lett.* **37** (2012), no. 11, p. 1820-1822.

[6] M. Mutlu, A. E. Akosman, G. Kurt, M. Gokkavas, E. Ozbay, "Experimental realization of a high-contrast grating based broadband quarter-wave plate", *Opt. Express* **20** (2012), no. 25, p. 27966-27973.

[7] A. Pors, S. I. Bozhevolnyi, "Efficient and broadband quarter-wave plates by gap-plasmon resonators", *Opt. Express* **21** (2013), no. 3, p. 2942-2952.

[8] Y. Zhao, A. Alu, "Tailoring the dispersion of plasmonic nanorods to realize broadband optical meta-waveplates", *Nano Lett.* **13** (2013), no. 3, p. 1086-1091.

[9] A. Pors, M. G. Nielsen, S. I. Bozhevolnyi, "Broadband plasmonic half-wave plates in reflection", *Opt. Lett.* **38** (2013), no. 4, p. 513-515.

[10] S. Jiang, X. Xiong, Y. Hu, Y. Hu, G. Ma, R. Peng, C. Sun, M. Wang, "Controlling the polarization state of light with a dispersion-free metastructure", *Phys. Rev. X* **4** (2014), no. 2, article no. 021026.

[11] Z. H. Jiang, L. Lin, D. Ma, S. Yun, D. H. Werner, Z. Liu, T. S. Mayer, "Broadband and wide field-of-view plasmonic metasurface-enabled waveplates", *Sci. Rep.* **4** (2014), p. 7511.

[12] F. Ding, Z. Wang, S. He, V. M. Shalaev, A. V. Kildishev, "Broadband high-efficiency half-wave plate: a supercell-based plasmonic metasurface approach", *ACS Nano* **9** (2015), no. 4, p. 4111-4119.

[13] D. Wang, Y. Gu, Y. Gong, C. Qiu, M. Hong, "An ultrathin terahertz quarter-wave plate using planar babinet-inverted metasurface", *Opt. Express* **23** (2015), no. 9, p. 11114-11122.

[14] P. I. Borel, A. Harpøth, L. H. Frandsen, M. Kristensen, P. Shi, J. S. Jensen, O. Sigmund, "Topology optimization and fabrication of photonic crystal structures", *Opt. Express* **12** (2004), no. 9, p. 1996-2001.

[15] J. S. Jensen, O. Sigmund, "Topology optimization for nano-photonics", *Laser Photonics Rev.* **5** (2011), no. 2, p. 308-321.

[16] C. M. Lalau-Keraly, S. Bhargava, O. D. Miller, E. Yablonovitch, "Adjoint shape optimization applied to electromagnetic design", *Opt. Express* **21** (2013), no. 18, p. 21693-21701.

[17] B. Shen, P. Wang, R. Polson, R. Menon, "An integrated-nanophotonics polarization beamsplitter with $2.4 \times 2.4\ \mu\text{m}^2$ footprint", *Nat. Photonics* **9** (2015), no. 6, p. 378.

[18] Y. Noguchi, T. Yamada, M. Otomori, K. Izui, S. Nishiwaki, "An acoustic metasurface design for wave motion conversion of longitudinal waves to transverse waves using topology optimization", *Appl. Phys. Lett.* **107** (2015), no. 22, article no. 221909.

[19] A. Y. Piggott, J. Lu, K. G. Lagoudakis, J. Petykiewicz, T. M. Babinec, J. Vuckovic, "Inverse design and demonstration of a compact and broadband on-chip wavelength demultiplexer", *Nat. Photonics* **9** (2015), no. 6, p. 374.

[20] F. Callewaert, V. Velev, P. Kumar, A. V. Sahakian, K. Aydin, "Inverse-designed broadband all-dielectric electromagnetic metadevices", *Sci. Rep.* **8** (2018), no. 1, p. 1358.

[21] Z. Lin, L. Christakis, Y. Li, E. Mazur, A. W. Rodriguez, M. Lončar, "Topology-optimized dual-polarization Dirac cones", *Phys. Rev. B* **97** (2018), no. 8, article no. 081408.

[22] Z. Lin, B. Groever, F. Capasso, A. W. Rodriguez, M. Loncar, "Topology-optimized multilayered metaoptics", *Phys. Rev. Appl.* **9** (2018), no. 4, article no. 044030.

[23] N. Mohammadi Estakhri, B. Edwards, N. Engheta, "Inverse-designed metastructures that solve equations", *Science* **363** (2019), no. 6433, p. 1333-1338.

[24] R. C. Sharp, D. P. Resler, D. S. Hobbs, T. A. Dorschner, "Electrically tunable liquid-crystal wave plate in the infrared", *Opt. Lett.* **15** (1990), no. 1, p. 87-89.

[25] L. Wang, X. W. Lin, W. Hu, G. H. Shao, P. Chen, L. J. Liang, B. B. Jin, P. H. Wu, H. Qian, Y. N. Lu, X. Liang, "Broadband tunable liquid crystal terahertz waveplates driven with porous graphene electrodes", *Light Sci. Appl.* **4** (2015), no. 2, article no. e253.

[26] L. Wang, S. Ge, W. Hu, M. Nakajima, Y. Lu, "Tunable reflective liquid crystal terahertz waveplates", *Opt. Mater. Express* **7** (2017), no. 6, p. 2023-2029.

[27] D. Wang, L. Zhang, Y. Gu, M. Q. Mehmood, Y. Gong, A. Srivastava, L. Jian, T. Venkatesan, C. Qiu, M. Hong, "Switchable ultrathin quarter-wave plate in terahertz using active phase-change metasurface", *Sci. Rep.* **5** (2015), p. 15020.

[28] T. Li, L. Huang, J. Liu, Y. Wang, T. Zentgraf, "Tunable wave plate based on active plasmonic metasurfaces", *Opt. Express* **25** (2017), no. 4, p. 4216-4226.

[29] X. Zhao, J. Schalch, J. Zhang, H. R. Seren, G. Duan, R. D. Averitt, X. Zhang, "Electromechanically tunable metasurface transmission waveplate at terahertz frequencies", *Optica* **5** (2018), no. 3, p. 303-310.

[30] B. E. Saleh, M. C. Teich, *Fundamentals of Photonics*, 3rd ed., John Wiley & Sons, 2019.

[31] N. Mohammadi Estakhri, N. Engheta, "Free-space optical Mach-Zehnder modulator based on two cascaded metasurfaces", in *CLEO: Applications and Technology*, Optical Society of America, 2018, p. JW2A-93.

[32] V. H. Rumsey, "Reaction concept in electromagnetic theory", *Phys. Rev.* **94** (1954), no. 6, p. 1483.

[33] G. Whitman, F. Schwering, "Reciprocity identity for periodic surface scattering", *IEEE Trans. Antennas Propag.* **27** (1979), no. 2, p. 252-254.

[34] N. Yu, P. Genevet, M. A. Kats, F. Aieta, J. Tetienne, F. Capasso, Z. Gaburro, "Light propagation with phase discontinuities: generalized laws of reflection and refraction", *Science* **334** (2011), no. 6054, p. 333-337.

[35] C. Pfeiffer, A. Grbic, "Metamaterial Huygens' surfaces: tailoring wave fronts with reflectionless sheets", *Phys. Rev. Lett.* **110** (2013), no. 19, article no. 197401.

[36] N. Mohammadi Estakhri, A. Alu, “Wave-front transformation with gradient metasurfaces”, *Phys. Rev. X* **6** (2016), no. 4, article no. 041008.

[37] S. Kruk, B. Hopkins, I. Kravchenko, A. Miroshnichenko, D. N. Neshev, Y. S. Kivshar, “Invited article: broadband highly efficient dielectric metadevices for polarization control”, *APL Photonics* **1** (2016), no. 3, article no. 030801.

[38] J. P. B. Mueller, N. A. Rubin, R. C. Devlin, B. Groever, F. Capasso, “Metasurface polarization optics: independent phase control of arbitrary orthogonal states of polarization”, *Phys. Rev. Lett.* **118** (2017), no. 11, article no. 113901.

[39] S. Sun, K. Yang, C. Wang, T. Juan, W. T. Chen, C. Y. Liao, Q. He, S. Xiao, W. T. Kung, G. Y. Guo, L. Zhou, “High-efficiency broadband anomalous reflection by gradient meta-surfaces”, *Nano Lett.* **12** (2012), no. 12, p. 6223-6229.

[40] N. Mohammadi Estakhri, A. Alu, “Manipulating optical reflections using engineered nanoscale metasurfaces”, *Phys. Rev. B* **89** (2014), no. 23, article no. 235419.

[41] E. Hasman, V. Kleiner, G. Biener, A. Niv, “Polarization dependent focusing lens by use of quantized Pancharatnam–Berry phase diffractive optics”, *Appl. Phys. Lett.* **82** (2003), no. 3, p. 328-330.

[42] X. Chen, L. Huang, H. Muhlenbernd, G. Li, B. Bai, Q. Tan, G. Jin, C. Qiu, S. Zhang, T. Zentgraf, “Dual-polarity plasmonic metalens for visible light”, *Nat. Commun.* **3** (2012), p. 1198.

[43] Y. Zou, W. Zhang, F. S. Chau, G. Zhou, “Miniature adjustable-focus endoscope with a solid electrically tunable lens”, *Opt. Express* **23** (2015), no. 16, p. 20582-20592.

[44] M. Baranski, S. Bargiel, N. Passilly, C. Gorecki, C. Jia, J. Fromel, M. Wiemer, “Micro-optical design of a three-dimensional microlens scanner for vertically integrated micro-opto-electro-mechanical systems”, *Appl. Opt.* **54** (2015), no. 22, p. 6924-6934.

[45] E. Arbabi, A. Arbabi, S. Kamali, Y. Horie, M. Faraji-Dana, A. Faraon, “MEMS-tunable dielectric metasurface lens”, *Nat. Commun.* **9** (2018), no. 1, p. 812.

[46] A. Zhan, S. Colburn, C. M. Dodson, A. Majumdar, “Metasurface freeform nanophotonics”, *Sci. Rep.* **7** (2017), no. 1, p. 1673.

[47] H.-S. Ee, R. Agarwal, “Tunable metasurface and flat optical zoom lens on a stretchable substrate”, *Nano Lett.* **16** (2016), no. 4, p. 2818-2823.

[48] S. Lee, H. Tung, W. Chen, W. Fang, “Thermal actuated solid tunable lens”, *IEEE Photonics Technol. Lett.* **18** (2006), no. 21, p. 2191-2193.

[49] J. Ou, E. Plum, J. Zhang, N. I. Zheludev, “An electromechanically reconfigurable plasmonic metamaterial operating in the near-infrared”, *Nat. Nanotechnol.* **8** (2013), no. 4, p. 252.

[50] R. C. Devlin, M. Khorasaninejad, W. T. Chen, J. Oh, F. Capasso, “Broadband high-efficiency dielectric metasurfaces for the visible spectrum”, *Proc. Natl Acad. Sci. USA* **113** (2016), no. 38, p. 10473-10478.

[51] H. W. Icenogle, B. C. Platt, W. L. Wolfe, “Refractive indexes and temperature coefficients of germanium and silicon”, *Appl. Opt.* **15** (1976), no. 10, p. 2348-2351.

[52] Comsol, Topology optimizations are performed with COMSOL optimization module, using SNOPT method. Forward simulations are performed using RF module in the frequency domain. www.comsol.com.

[53] Comsol, Genetic algorithm minimizations are performed in MATLAB (https://www.mathworks.com/) using LiveLink interface (https://www.comsol.com/livelink-for-matlab).

[54] Y. Jin, R. Kumar, O. Poncelet, O. Mondain-Monval, T. Brunet, “Flat acoustics with soft gradient-index metasurfaces”, *Nat. Commun.* **10** (2019), no. 1, p. 1-6.

[55] Z. Tian, C. Shen, J. Li, E. Reit, Y. Gu, H. Fu, S. A. Cummer, T. J. Huang, “Programmable acoustic metasurfaces”, *Adv. Funct. Mater.* **29** (2019), no. 13, article no. 1808489.

[56] S. Inampudi, J. Cheng, M. M. Salary, H. Mosallaei, “Unidirectional thermal radiation from a SiC metasurface”, *J. Opt. Soc. Amer. B* **35** (2018), no. 1, p. 39-46.

[57] S. I. Bozhevolnyi, “Shaping wavefronts of single photons with metasurfaces (Conference Presentation)”, in *Proc. SPIE 11344, Metamaterials XII, 113440O (1 April 2020)*, SPIE, 2020.

[58] N. M. Estakhri, T. B. Norris, “Controlling quantum interference using metamaterials”, in *Proc. SPIE 11091, Quantum Nanophotonic Materials, Devices, and Systems 2019, 110911D (3 September 2019)*, SPIE, 2019.

[59] P. Georgi, M. Massaro, K.-H. Luo, B. Sain, N. Montaut, H. Herrmann, T. Weiss, G. Li, C. Silberhorn, T. Zentgraf, “Metasurface interferometry toward quantum sensors”, *Light: Sci. Appl.* **8** (2019), no. 1, p. 1-7.

[60] R. Bekenstein, I. Pikovski, H. Pichler, E. Shahmoon, S. F. Yelin, M. D. Lukin, “Quantum metasurfaces with atom arrays”, *Nat. Phys.* (2020), p. 1-6.

Comptes Rendus
Physique
2020, 21, nº 7-8, p. 641-657
`https://doi.org/10.5802/crphys.18`

Metamaterials 2 / *Métamatériaux 2*

Dispersion and efficiency engineering of metasurfaces

Ingénierie de la dispersion et de l'efficacité des méta-surfaces

Xiaomeng Zhang [a], Benfeng Bai *, [a] and Hong-Bo Sun [a]

[a] State Key Laboratory of Precision Measurement Technology and Instruments,
Department of Precision Instrument, Tsinghua University, Beijing, China

E-mails: zhangxm16@mails.tsinghua.edu.cn (X. Zhang),
baibenfeng@mail.tsinghua.edu.cn (B. Bai), hbsun@mail.tsinghua.edu.cn (H.-B. Sun)

Abstract. Metasurfaces, ultrathin two-dimensional arrays of artificially engineered meta-atoms, can impart spatially varying changes towards the incident electromagnetic wave and provide versatile functionalities once unprecedented in sub-wavelength thick natural materials. The wavefront manipulation by metasurfaces usually arises from the strong resonant behaviors of varied meta-atoms in subwavelength lattice, which also brings some drawbacks like the unexpected dispersion due to separate resonances of the meta-atoms and the long concerned low efficiency problem. This paper reviews the recent surge of fruitful works on dispersion and efficiency engineering of metasurfaces and provides an overview of several effective methods to acquire metasurfaces with these distinctive features.

Résumé. Les méta-surfaces, des réseaux bi-dimensionnels ultra-fins de méta-atomes artificiels, peuvent transférer les variations spatiales de leur structure au champ électromagnétique et conférer ainsi des fonctionnalités jusqu'alors inégalées dans les matériaux naturels d'épaisseur sous-longueur d'onde. La manipulation du front d'onde par les méta-surfaces est généralement obtenue en exploitant le caractère fortement résonant des méta-atomes dans le réseau sous-longueur d'onde, qui conduit par ailleurs à des inconvénients tels qu'une dispersion inattendue en raison des résonances distinctes des méta-atomes et un problème d'efficacité qui a fait l'objet d'une attention de longue date. Cet article passe en revue les percées récentes des travaux sur ces problématiques de la dispersion et de l'efficacité des méta-surfaces et il donne un aperçu de plusieurs méthodes permettant d'obtenir des méta-surfaces avec des propriétés remarquables.

Keywords. Metasurface, Bound state in the continuum, Dispersion engineering, Material, Efficiency.

Mots-clés. Métasurface, État lié dans le continuum, Ingénierie de dispersion, Matériel, Efficacité.

2020 Mathematics Subject Classification. 00-01, 99-00.

---

* Corresponding author.

1. Introduction

Manipulating electromagnetic waves at will has long been a pursued goal since the establishment of electromagnetism. Numerous efforts have been made in this field and have brought abundant achievements in many areas, such as communication, energy, and entertainments. By applying electromagnetic field to a material, electric and magnetic responses are induced by the properties of the material, i.e. permittivity and permeability, which incur specific manipulation to the incident field. For natural materials, these properties have limited range in different frequency domains, which naturally set a limitation to the capability of engineering the field [1].

Metamaterials are a kind of artificial materials that can overcome the aforementioned impediment. This feature comes from its subwavelength artificial compositions, called meta-atoms. Permittivity and permeability describe the averaging polarized fields over a domain that occupies an area much larger than atom but smaller than wavelength. For natural materials, the composition over this domain is homogeneous. While metamaterials enable different geometries of meta-atoms in this domain, which may generate various artificial effective permittivity and permeability related not only to material but also to the geometry [2]. By means of this new paradigm, a lot of new phenomena have emerged, such as negative index [3], hyperbolic dispersion [4] and invisibility cloak [5]. However, the fabrication of three-dimensional subwavelength structures is quite challenging and the high loss due to the propagation in the material also hinders its potential applications.

In recent years, a type of ultra-thin planar metamaterials, called metasurfaces [6], are proposed to overcome these problems. Metasurfaces can exploit the well-developed standard semiconductor fabrication process and is easy to integrate due to its ultra-thin trait. Although metasurfaces are lack of field transformation in the direction along propagation, they can impart various manipulations to the incident field [7] and have been utilized to achieve control of many properties of light including the amplitude [8], frequency [9], phase [10], polarization [11] and momentum [12]. Despite the similar constructions of metamaterials and metasurfaces, they have essential differences [13]. The manipulation of field in metamaterials still relies on the optical path accumulation during propagation; while for metasurfaces, as its interactive length with field is extremely thin, the changes it imparts to the field can be seen as abrupt ones. Therefore, instead of concerning the bulk properties of metasurfaces, we can regard the metasurfaces as zero-thickness interfaces [14], whose surface susceptibilities or impedances are of great importance. By deliberately choosing the materials and geometries of the meta-atoms, metasurfaces may enable spatial-variant and multimode interactions [15], serving as efficient platforms for manipulating electromagnetic waves.

In order to obtain useful functionalities with metasurfaces, the meta-atoms need to interact strongly with the incident field, imparting a scattering field with a large difference from the incident one. This resonant state of meta-atom, however, often brings some drawbacks. The scattering spectrum of a single resonator is often represented by a Lorentzian curve [16] in the frequency domain, with the phase delay changing from 0 to π near the resonance. The width of the curve is related to the losses both from absorption and radiation. For an opening resonator and a continuum mode, this resonance width often lays in a certain range, so that the working wavelength of a metasurface can be neither too broad nor too narrow and the dispersion of a metasurface is also limited. This trait needs to be engineered for specific applications. For example, sharper resonances are preferred in ultra-highly sensitive sensing [16], field modulation [17] and nonlinear interactions [18]; while smoothly varied resonances are preferred in full-color imaging [19], holographic display [20] and other broadband applications. Hence, the dispersion of metasurfaces should be carefully engineered concerning specific applications in the interested frequency ranges. Besides, the power utilization efficiency of metasurfaces is also of great importance. From the earlier plasmonic structures working under cross-polarized condition with a maximal efficiency under 25% [21], the exploration in this field ranges from optimization of the materials [22] and the interference of different multipoles to match the impedance utterly, aiming to achieve 100% efficiency that is highly desired in many realistic applications. This requirement gets harsh when it comes to the gradient metasurfaces [23] to reroute all the power into the desired direction, where the impedance boundary condition has to be carefully satisfied to obtain perfect wave manipulation with unitary efficiency.

In this review, we have an overview on recent endeavors in solving the aforementioned limitations of metasurfaces. First, we review the ways of engineering the dispersion of metasurfaces, achieving either sharp resonances with high quality factors or smooth resonances working under broadband wavelength range. Then, the works exploring high efficiency metasurfaces are reviewed from both material and structural perspectives, by discussing the features of the structures that can achieve nearly unitary efficiency in both periodic and gradient quasi-periodic arrangements.

2. Dispersion engineering of metasurfaces

2.1. *Highly dispersive metasurfaces*

Highly dispersive metasurfaces, with strong resonances of high quality factors, have great importance in applications such as sensors, modulators like optical switches, slow-light devices [24] and nonlinear devices. To obtain such resonances, Fano resonance [25] with steep dispersion is usually exploited, which originates from the coupling between a discrete localized state and a continuum state.

Since the observation of an unusual sharp asymmetric line in the absorption spectra of noble gas, this resonance, bearing its explainer's name Fano, has attracted a lot of attentions due to its distinctive difference from the conventional Lorentzian resonance curve. This phenomenon was first discovered and explained in a quantum mechanical study of photoionization of atom [26]. The photoionization can go along two channels [27], direct ionization and autoionization, where the atom transits from the ground state to a continuum state directly or with an intermediate autoionization state, respectively. Fano resonance profile appears because of the interference between these two different paths. Among these two paths, intermediate autoionization state is of great importance. The autoionization state is a quasi-bound state and corresponds to a resonance with finite lifetime in scattering. This quasi-bound state can be regarded as the result of coupling between the bound state from one channel and the continuum state from the other channel. Hence, the coupling between a bound state and a continuum state is essential to obtain the so-called Fano resonance.

The formula for the scattering cross-section curve of Fano resonance with no absorption loss is expressed as [28]

$$\alpha = \frac{2\pi}{E(1+q^2)}\frac{(\Omega+q)^2}{1+\Omega^2}, \tag{1}$$

where E is the energy, Ω is defined by $2(E-E_F)/\Gamma$, q is the so-called Fano parameter (which is the ratio of the transition probabilities to the continuum state intermediately and directly), and E_F and Γ are the resonant energy and the width of the autoionization state, respectively. Equation (1) is applicable when the width of the resonance corresponding to this quasi-bound state is narrower enough than those of other resonances. According to (1), the curve has a minimum at $E = E_F - \Gamma q/2$ and a maximum at $E = E_F + \Gamma/(2q)$ and owns an asymmetric feature when q is neither 0 or infinity. This phenomenon appears when the scattering field corresponding to the autoionization undergoes a sharp phase change of π at the resonance, so that there will be constructive and destructive interferences between the two different paths, which can be located extremely close with an interval as $(q + 1/q)\Gamma/2$. This sharp variation from maximum to minimum in the profile could happen in a width nearly equal to that of the quasi-bound state, when the transition of the two paths are of the same strength, as shown in Figure 1(a).

There is another interesting discovery called bound state in the continuum (BIC) [29] in quantum system that also concerns the extremely high quality factor of the resonance. BIC is an exact bound state inside the continuum state and remains perfectly confined, which completely decouples with the radiating waves. It is quite different from the autoionization state in Fano resonance. In this sense, BIC can be regarded as a resonance with zero linewidth and infinitely high quality factor, which can only exist in structures with uniformity or periodicity in at least one dimensions to ensure the utter localization of the bound state. By considering the limited sample size and fabrication imperfections, the rigorous criteria on BIC make its practical realization impossible. But inspired by the requirements on BIC, a quasi-BIC with finite but quite high quality factor can be achieved, which can often be fulfilled by imparting a little perturbation to the ideal BIC system to turn the bound state in continuum into a leaky resonance. Recently, there is rigorous demonstration linking the transmission/reflection profile of quasi-BIC to the exact Fano formula [30], where the Fano parameter becomes ill-defined and the profile loses the features of Fano asymmetry. Thus, Fano resonance can be seen as a harbinger of BIC. Suppression of coupling between the bound state and the continuum state by tuning the parameter of structures or excitation conditions can transform them from one to the other.

Having the inspirations from Fano resonance and BIC in quantum systems, we focus on these phenomena in metasurfaces interacting with electromagnetic waves where interference is also ubiquitous. Metasurfaces provide particular platforms to obtain these phenomena, as they may support resonances of large diversity and favor experimental feasibility. Generally, the realization of BIC in mertasurfaces can be divided into three classes: symmetry protecting, total destructive interference of two resonances in the same cavity, and total destructive interference among different radiation channels. By introducing perturbations in these situations, quasi-BIC with Fano profile and high quality factor can be obtained.

The most prevalent method is through symmetry protecting. The complete prohibition of the outcoupling of the bound state can be realized by building different symmetry classes between the bound state and the continuum state. As the modes of different symmetry classes can be completely decoupled, this kind of symmetry-protected BIC can be quite robust even with varied structural parameters as long as the symmetry is not broken. Quasi-BIC originating from this symmetry-protected BIC comes from the slight breaking of the symmetry of the bound state, which directly results in its coupling with the continuum state. A resonance featured with Fano profile emerges, and moreover, its quality factor is directly related to the extent of symmetry breaking [30, 34]. Symmetry breaking relies on either the structures [35] or excitation conditions [36]. Considering different symmetry traits of different bound states, both in-plane [37–39] and out-of-plane symmetry [40] breaking have been explored. With the appropriate parameter tuning towards the critical point of symmetry, the change of quality factor from finity to infinity can be observed. In this way, quasi-BIC with extremely high quality factor can be acquired. Recently, with the help of a metasurface with subwavelength period of rod dimers varied from detuned to tuned, a transition from quasi-BIC to BIC was clearly exhibited [31], as shown in Figure 1(b). A coupled dipole analysis shows that the dimers support both symmetric and asymmetric modes. When the rod dimers are identical, the asymmetric mode is completely suppressed, which leads to symmetry-protected BIC with infinite quality factor. When the dimers are detuned, i.e. the dimers are different in geometry, the asymmetric mode turns into a leaky mode and the interference between symmetric and asymmetric mode contributes to the typical Fano profile in

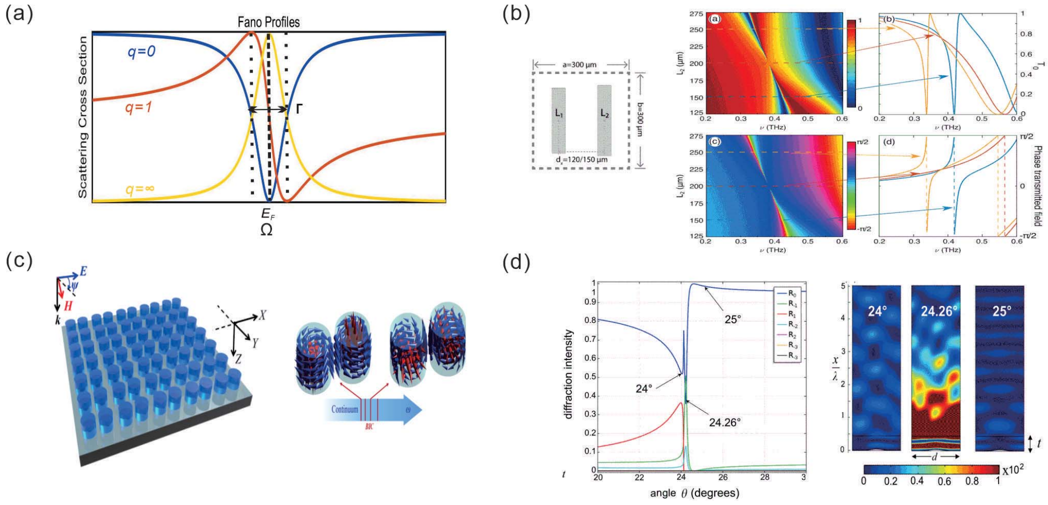

Figure 1. (a) The Fano profiles of different q. $q = 0$ corresponds to anti-resonance, $q = \infty$ corresponds to normal Lorentz resonance and $q = 1$ corresponds to the largest dispersion. (b) Symmetry-protected BIC. With the dimers varing from detuned to tuned status, a transition from Fano resonance to BIC is clearly exhibited from the reflectance diagrams. Reprinted with permission from [31] © The Optical Society. (c) Symmetry protected and unprotected toroidal dipole BIC. BIC originated from total destructive interference of toriodal and electronic dipoles are symmetry unprotected and can maintain relatively high quality factors when the symmetry is broken. Adapt with permission from [32] © The American Physical Society. (d) Quasi-BIC originated from a little deviation from destructive interference of Rayleigh and resonance anomalies. With a slight variation in the incident angle, the field intensity distribution changes utterly, indicating a high quality factor of the resonance anomaly. Adapt with permission from [33] © The Institute of Physics.

the transmission spectrum. Zigzag arrays [41] can also fulfill quasi-BIC with high quality factor under the same formalism. By making the resonant frequency of the coupled continuum mode far away from that of the bound state, there is no resonant background for quasi-BIC, which has been desired in applications like filtering.

The second method is the total destructive interference between two resonances in the same cavity and radiating into the same radiation channel, which is also called the Friedrich–Wintgen BIC [42]. In temporal coupled-mode theory [43], with these two resonances tuned, the eigenvalues of the resonator, as a function of its certain geometrical parameter, come near to crossing but then repel each other in the complex plane. When there is an avoided resonance crossing [44], either for real or imaginative part of eigenvalue, an important feature is generated, i.e., a state with a considerably increased lifetime and a simultaneous state with short lifetime. In order to turn the state with increased lifetime into a BIC, the two tuned resonances need to be coupled predominately in the far field with vanishing near-field coupling [32, 45], as shown in Figure 1(c), or own almost the same radiation rates [46]. Metasurfaces supporting this kind of BIC own some advantages compared to symmetry-protected BIC. As the divergence of the incident angle cannot be prevented in practical scene, the symmetry class of metasurface and its excitation condition cannot be pure. Thus, for a given quality factor, metasurfaces with Friedich–Wintgen BIC can achieve a smaller footprint than that of symmetry-protected BIC.

The third method for obtaining BIC needs only one resonance and the complete radiation vanishing comes from the destructive interference from two or more different radiation channels.

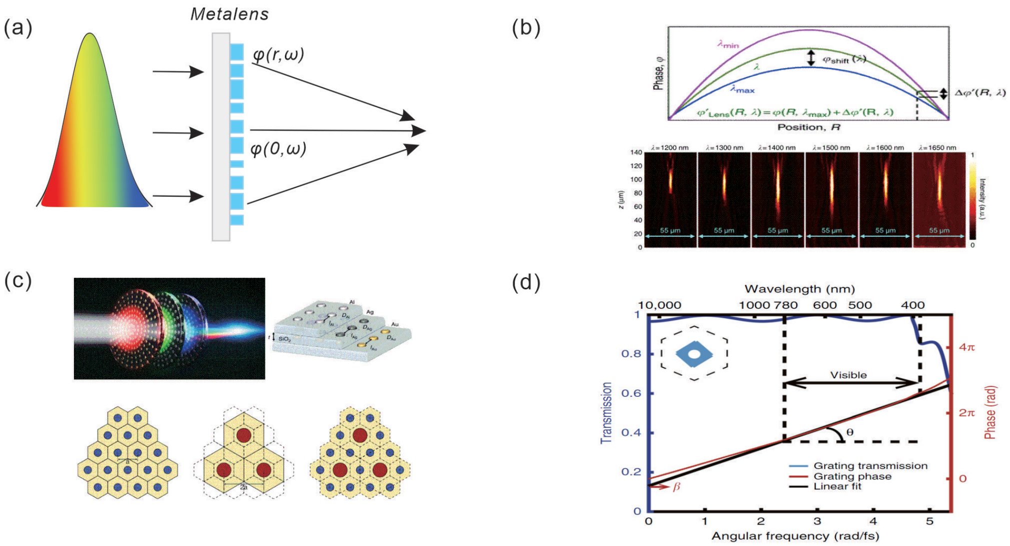

Figure 2. (a) A metalens without chromatic dispersion requires additional engineering of group delay, in order to maintain the identical shape of the incident pulse. (b) Achromatic focusing requires the phase delay profiles to change with the incident frequency. Adapted with permission from [47] © Springer Nature. (c) A stacked multilayer metasurface and an interleaved metasurface. Adapted with permission from [48] and [49] © Springer Nature. (d) The engineered dispersion of the resonator, which can offer the desired group delay with high efficiency. Reprinted with permission from [50] © Springer Nature.

A reflective grating with an extreme form of Wood's anomalies can support resonances with diverging quality factor [33]. This extreme form exists when two kinds of Wood's anomalies, i.e. Rayleigh anomaly and resonance anomaly, merge. Rayleigh anomaly occurs when a diffraction order emerges or vanishes, while resonance anomaly occurs when a diffraction order exciting the guided mode that the grating supports. The merge of these anomalies can be obtained by tuning the incident angle together and the period. This kind of BIC can be understood in the framework of leaky wave theory and can obtain quasi-BIC with relatively high quality factor in the vicinity of the critical tuning, as shown in Figure 1(d).

2.2. *Smoothly dispersive metasurface*

Metasurfaces with ordinary Lorentzian resonances often exhibit a dispersion changing too swiftly for broadband applications, due to the periodic lattice as diffractive device and the composed resonant meta-atoms. For a resonant meta-atom, its scattering field (both amplitude and phase) may undergo a large dynamic range near its resonance frequency. Although for some metasurfaces, whose phase profile is enabled by Pancharatnam–Berry (PB) phase [51], can provide exactly the same phase transformation to the incident field of different frequency, the amplitude cannot be held and the chromatic dispersion due to phase accumulation during the propagation of light cannot be eliminated. For this reason, most metasurfaces are designed under a particular working wavelength and usually exhibit negative chromatic dispersion [52] in the limited adjacent spectral range. Metasurfaces with smooth dispersion are especially desired for various applications in color imaging and display, such as the elimination of chromatic dispersion, where meta-atoms should impart smoothly varied phase delay at different frequencies to compensate the phase difference arising from propagation. Taking broadband metalens as an example, the phase delay should be engineered as [53]

$$\varphi(r,\omega) = \frac{\omega}{c}\left(-\sqrt{r^2+f^2}+f+\alpha\right)+\beta, \tag{2}$$

where ω is the angular frequency, r is the location on the metasurface, c is the light velocity, f is the focal length of the meta-lens, α is the spatial phase reference and β is the spectral phase reference. This equation can be directly get considering the Fermat principle in the scene depicted in Figure 2(a). When the angular frequency changes, the phase delay profile changes accordingly, as shown in Figure 2(b). Meta-atoms, which can accomplish the local phase delay defined by (3), impart different phase delays towards the impinging field of different frequency and can be immune from chromatic dispersion.

Eliminating chromatic dispersion at several discrete wavelengths were first addressed using metasurfaces, as shown in Figure 2(c). Stacked multilayer metasurfaces [48] are kind of approach conceptually simple yet powerful. Each layer is designed for one particular wavelength and the spectral crosstalk between each layer are set to be minimal. Interleaved metasurfaces [49] as another approach take a similar strategy. This aperture-shared method allows several metasurfaces designed for discrete wavelengths to assemble a hybrid single-layer metasurface. Comparing these two methods, the stacked metasurfaces allow meta-atoms of different materials for each layer, so that they can have lower crosstalk and higher efficiency. Instead of composing several ordinary metasurfaces together, there are also some endeavors of trying to engineer the dispersion at discrete frequencies of meta-atoms [54–56], so that they can naturally compensate the phase due to chromatic dispersion.

When it comes to continuous wavelength, wave manipulation enabled by metasurfaces without chromatic dispersion calls for more characteristics. Here we consider (3) again and get the derivative of φ with respected to ω,

$$\frac{\mathrm{d}\varphi(r,\omega)}{\mathrm{d}\omega} = \frac{1}{c}\left(-\sqrt{r^2+f^2}+f+\alpha\right), \tag{3}$$

which indicates that the structures we need in the metalens without chromatic dispersion should have certain group delay in their working wavelength range. And the absolute value of the group delay becomes larger with the positions of structures becoming farther from the center, which definitely sets limitations to the metalens on its working wavelength range and aperture. The device satisfying these requirements has shown exciting results especially on color imaging. Among them, achromatic metalens in the visible region from 400 nm to 660 nm with a numerical aperture (NA) of 0.106 in transmission mode was realized [57]. For plasmonic meta-atoms, large phase compensation can be achieved by adding more resonators in one unit cell [47]. With achromatic PB phase as the basic phase, the meta-atoms are deliberately designed, so that their own resonances compensate the phase differences arising from achromatic aberration and satisfy the group delay requirements. For dielectric meta-atoms, this method also works. While the field is usually localized inside the dielectric resonators, using field coupling among the dielectric resonators may not be as efficient as their plasmonic counterparts when compensating this phase difference. Therefore, resonators supporting higher multipoles [58] can be employed to achieve this goal. Using pillars with holes as the basic structures, 400 nm-thick silicon nitride structures can have outstanding dispersion properties [50], as shown in Figure 2(d). No matter what kind of meta-atoms are used, the selection of meta-atoms is a nontrivial job to assure the meta-atoms to offer the exact phase delays over the certain spectral range and suitable field intensity. Besides, when the working spectral range and the NA of the lens get larger, the requirement on the phase compensation becomes harsher and there would eventually be a tradeoff.

Generally, in order to have a smooth dispersion, meta-atoms are usually designed to support several modes. By tuning the parameters deliberately, these modes can work together to provide the required phase-frequency curves for different broadband applications.

3. Metasurfaces with high efficiency

Efficiency of metasurfaces has long been concerned for its importance in various device applications. Endeavors in this area ranges from the material choice to structural design, among which several methods, utilizing gap plasma resonance [59], Kerker effect [60] and waveguide-like resonance [61], have achieved great progress on metasurfaces with periodic meta-atoms. When metasurfaces come to a spatial-variant form, it calls for more delicate method to realize unitary efficiency, which is different from the common process of designing metasurfaces guided by the generalized Snell's Law [62]. Meta-gratings [63] and metasurfaces with spatial dispersion engineering [64] have been proposed to gain a higher efficiency for this kind of spatial-variant metasurfaces.

3.1. *Material choice of metasurfaces*

Meta-atoms made of noble metals, such as gold and silver, were first applied in metasurfaces due to its high conductivity and relatively low ohmic loss. The high conductivity makes the free electrons in meta-atoms strongly couple to the incident light and form the so-called local surface plasmon resonances [65]. This kind of resonances can increase the field density near the metal surfaces by orders of magnitude and localize the field into a sub-diffraction scale. But when the working wavelength comes to the near-infrared or visible range, the ohmic loss in metasurfaces severely increases because of the electron scattering and interband transitions [66]. Besides, noble metals are not compatible with the standard CMOS fabrication process (either chemical unstable or easily diffused) and cannot withstand high incident power or temperature. Considering these inherent drawbacks of noble metals, different materials have been explored to find the best substitution in near-infrared and visible frequency domain.

Materials, with comparatively large negative real part and relatively small imaginary part of permittivity compared to noble metals, are the best candidates to replace noble metals in plasmonic metasurfaces. However, nowadays alternatives of noble metals, like transparent conducting oxides (TCOs) and nitrides for near- or mid-infrared and visible spectral range [22, 67], can only obtain a tradeoff between these two requirements. TCOs can be heavily doped with a carrier concentration more than 10^{21} cm^{-3}, which is not possible for many semiconductors due to the solid-solubility limit. This carrier concentration guarantees the metallic feature of TCOs and a weaker electron scattering, together with a wide bandwidth that results in no inter-band loss. Hence, TCOs have much lower loss than noble metals at infrared frequency. However, the absolute value of the real part of their permittivity is much smaller than those of noble metals, as shown in Figure 3(a), indicating that noble metals still outperform TCOs for plasmonics [68]. The carrier concentration of typical metals can reach 10^{23} cm^{-3}, which results in a high plasma frequency and a high damping rate. Generally, TCOs can exhibit loss five times smaller than Ag in near-infrared frequency. Transition metal nitrides can be doped to an even higher carrier concentration as high as 10^{22} cm^{-3}, with the plasma frequency locating in the visible range similar to Au [69]. Transition metal nitrides are a kind of refractory materials with high chemical stability [70] and high damage threshold [71]. The loss in nitrides, however, are actually larger than that in bulk noble metals, due to both inter-band transition and Drude damping. For noble metals acquired upon evaporation, which are commonly used in plasmonic metasurfaces, the grain boundaries and roughness in metals cause additional scattering and result in higher loss. While

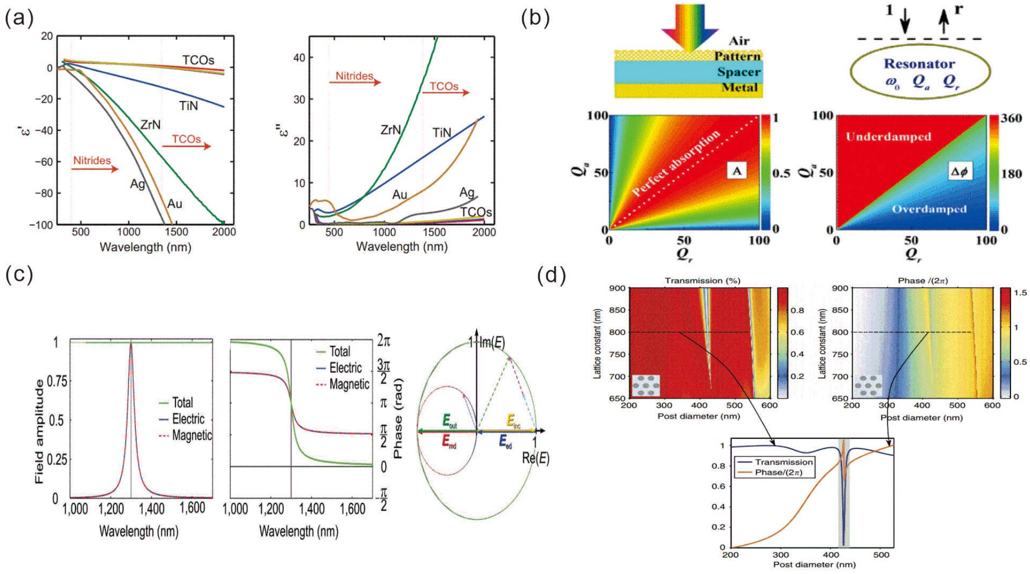

Figure 3. (a) Permittivity figures of noble metals, TCOs and transparent metal nitrides. Reprinted with permission from [67] © The Optical Society. (b) Gap-plasmon resonance calls for particular relationship between the absorption and radiation loss rates, in order to acquire unitary efficiency. Reprinted with permission from [76] © The American Physical Society. (c) Huygens' metasurface supports in-phase electric and magnetic dipoles of the same strength, which results in a unitary transmission and can be directly observed from Smith curves. Reprinted with permission from [77] © John Wiley and Sons. (d) Waveguide-like resonance, enabled by much thicker resonators than those in Huygens' metasurface, can also acquire high transmission at the resonant frequency by carefully engineering the resonant states in it. Reprinted with permission from [78] © Springer Nature.

for transition metal nitrides, a crystalline layer can be grown, so that in spectral range where inter-band loss can be neglected, transition metal nitrides can well replace noble metals. Furthermore, TCOs and nitrides also possess advantages such as property controlling via fabrication [72], CMOS fabrication compatibility, and high stability and tunability [73, 74], which make them popular replacements of noble metals in plasmonics applications. By tuning certain parameters in fabrication process, their plasma frequency can also be changed, which is not possible for noble metals. TCOs can also work as good epsilon-near-zero materials [75], with the real part of its permittivity crossing zero with fairly low loss. Besides, epitaxial silver, owning matched lattice with substrates such as alumina or mica can also refine the grain boundary defects.

In addition to the alternative plasmonic materials, dielectric materials with high refractive indices that support Mie-resonance [79] can also serve as good material candidates for metasurfaces. Dielectric materials have low optical loss and the induced displacement current inside the dielectric nanoparticles can support not only electric multipoles but also magnetic multipoles, which are featured by the circular displacement currents inside the particles [80]. While for plasmonic nanoparticles, magnetic multipoles can only appear with specific structural design, such as split-ring [81] and metal-insulator-metal (MIM) structures [82], due to the vanishing field inside the particles. Besides, Mie resonances can induce a local field enhancement inside the meta-atoms, compared to plasmonic resonance with near surface localization. For the aforementioned reasons, dielectric metasurfaces can exceed plasmonic metasurfaces in several applications, such as nonlinear devices [18] and directional scattering [83]. Despite all the advantages dielectric materials own compared with plasmonic materials, the size of the meta-atoms and the localized hot spot of the field are much larger due to the considerably smaller permittivity. Silicon [84] and titanium dioxide [85] are prevalently used in near-infrared and visible spectral domain with high and nearly pure real refractive index, which ensure the sufficient enhancement and localization of the field inside the meta-atoms to boost a resonance. Apart from these popular materials, some group IV and group III–V semiconductors, like Ge [86] or GaAs [87], also have the similar response under the incident field.

3.2. *Highly efficient metasurfaces with periodic arrangement*

Besides the inherent material properties, the structure of meta-atoms also plays an important role in efficiency. For metasurfaces with periodic arrangement, several special structures can obtain near unity efficiency at its resonant frequency. For example, metasurfaces supporting gap-plasmon resonance [88] can achieve near unity efficiency in reflection at the resonance frequency. This kind of metasurfaces consist of a thin dielectric spacer sandwiched between a thick metal film and an array of subwavelength metallic meta-atoms, which is also called the metal-insulator-metal structures [89]. This configuration has once attracted a lot of attention due to its simple fabrication yet huge capability of field transformation. This distinctive configuration supports asymmetrically induced conductive current in the upper metallic resonator and the metallic substrate, which can be seen as a transverse magnetic dipole. Different works concerning gap-plasmon resonances exhibited quite different functionalities, ranging from perfect absorber [90] to phase modulation with high reflection [91]. This difference has been clearly explained [76] using coupled-mode theory. When there is only one mode inside the interested spectral range, the periodic gap-plasmon metasurface can be regarded as a one-port single mode resonator. Unity transmission together with a 2π phase delay around resonance occurs as long as the absorptive quality factor is much larger than the radiative quality factor. Different geometrical parameters of MIM structures give different relationships between the absorption loss and radiation loss, which incur the aforementioned various performances from similar MIM structures. For a transmissive platform with two ports, a single mode resonator is not sufficient any more to achieve unitary efficiency at resonant frequency.

Dielectric transmission metasurfaces with periodic arrangement can acquire unity efficiency through two different methods, i.e. the directional scattering and the waveguide-like resonances. The scattering field in meta-atoms can be divided into the superposition of various multipoles [92], so that each meta-atom can be replaced by its equivalent multipoles. When the meta-atom can be regarded as a transverse electric dipole and a magnetic dipole with the same strength and phase, there will be no reflection because of the destructive interference between the scattering fields of these two dipoles. Meanwhile, if the material is lossless, all power will be transmitted and a so-called Kerker effect emerges. This kind of metasurfaces are called Huygens' metasurfaces [77]. The required relationships between the two dipoles are often achieved by embedding cylindrical meta-atoms in a medium with about 1.45 refractive index, which results in a stronger collective interaction in the periodic arrays. Therefore, with a slight change in period or incident angle of the Huygens' metasurface, a large difference in its performance may appear. Different from Huygens' metasurface, which only supports dipole resonances in its composing meta-atoms, metasurfaces with thicker meta-atoms can support waveguide-like resonances [78]. This kind of meta-atoms are usually seen as truncated waveguides supporting Fabry–Perot resonances, which interfere with each other and can lead to a high transmission. The multiple resonant states make it possible to direct all power into the transmitted channel.

3.3. *Highly efficient metasurfaces with spatially-variant meta-atoms*

One distinctive feature of metasurfaces is that they allow for spatial-variant transformation towards incident electromagnetic field [51]. When meta-atoms are arranged in a subwavelength lattice, deliberately design can impart abrupt transformation with subwavelength resolution. One important application of the spatially-variant metasurfaces is beam steering, such as focusing, deflecting, and imaging. The boost in this field occurs when the generalized Snell's law is proposed. Metasurface enables an unprecedented era of interface engineering. Its inhomogeneous trait brings phase delay variations depending on location to compensate the phase difference between incident and desired propagation phase profiles. Considering the conservation of momentum, the phase gradient incurred by the spatial-variant meta-atoms will endow extra terms in conventional Snell's law, which helps achieve extraordinary wave manipulation effects like anomalous refraction [93]. The generalized Snell's law implies the probability of arbitrary modulating of the reflected/transmitted light, where its propagating direction does not have to be located inside the incident-plane and can have nearly arbitrary angle. Enlightened by the generalized Snell's law, numerous work ranging from meta-lens, spin-orbital interaction to holograms, and polarizer have been exhibited. The common process of fulfilling a metasurface with spatially-variant properties starts from finding a set of meta-atoms, which ideally can yield different phase delays covering the full 2π range with unit efficiency in the concerned field (transmitted, reflected or scattered field depending on the specific scene). A simple arrangement of this set of meta-atoms satisfy the phase delay profile indicated by the generalized Snell's Law. Based on these methods, meta-lenses and holograms enabled by metasurfaces can all be obtained with efficiencies as high as 80% or so. However, when it comes to extreme wave manipulations like large angle steering, metasurfaces designed by this strategy is limited in efficiency and may eventually not exhibit the desired performance. This is because of the ignorance of impedance matching between the impinging and desired wave fronts, which is inevitable in beam deflecting and is expected to grow for steeper angles.

By considering the beam steering process, the required transformation imparted by a metasurface can be defined by the establishment of a transversely averaged yet inhomogeneous impedance boundary connecting both the impinging field and the desired field. When the induced currents in the metasurface form the exact impedance, perfect wave manipulation appears with unitary power efficiency. This ideal impedance boundary endowed by the metasurface is different from the phase compensation profile defined by the generalized Snell's Law [23, 64], which only considers the locally linear momentum conservation with the spatially-variant phase delay requirements. Impedance matching, however, provides a more comprehensive perspective and sets the ideal local profile in both phase and amplitude of the scattering field radiated from the metasurfaces. Furthermore, the difference of target profiles defined by these two methodologies not only lies in the absent amplitude profiles defined by the generalized Snell's Law, but also in the phase profiles. By taking reflected beam deflection performance as an example, the ideal phase profile defined by impedance matching calls for nonlinear distribution along the metasurface, while the generalized Snell's Law indicates a linear phase gradient, as shown in Figure 4(a). The difference of these two phase profiles becomes larger with the increase of the steering angle and the nonlinear gradient defined by the boundary conditions becomes steeper. This quickly varied nonlinear phase profile requires extremely small discretization and will eventually be limited by the resolution coming from both the size of meta-atoms and the fabrication. Besides, perfect impedance boundary conditions ask for an amplitude profile with both local power absorption and gain oscillations, which may bring tremendous difficulties in involving active meta-atoms. Luckily, these two barriers can be bypassed using merely passive lossless metasurfaces with deliberate consideration.

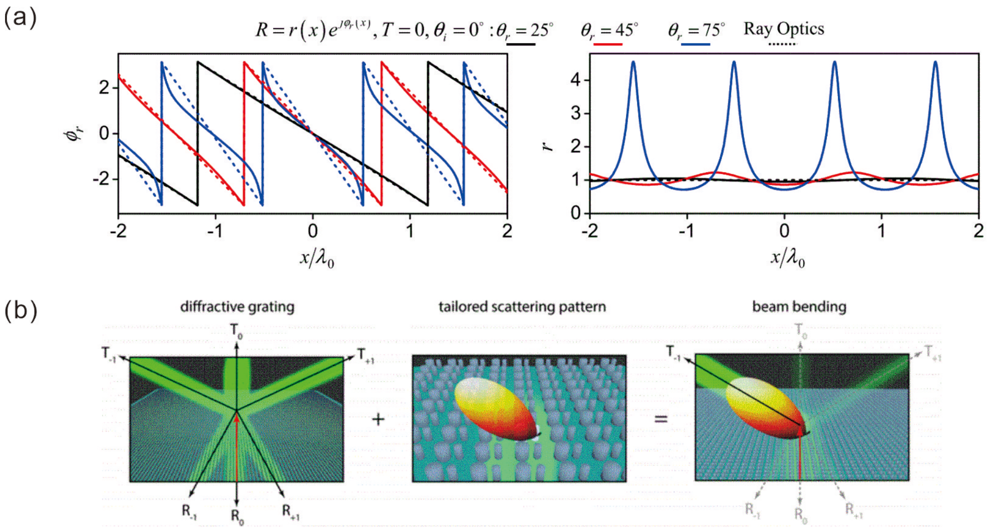

Figure 4. (a) The local reflectance deviation of the profiles defined by the generalized Snell's Law and the impedance boundary conditions in a reflective angle-deflecting metasurfaces, indicated by the dashed and solid lines, respectively. The differences become larger for steeper angle deflection and the unitary efficiency calls for local power absorption and gain oscillations. Reprinted with permission from [23] © The American Physical Society. (b) Concept of a meta-grating. The super lattice determines the diffraction angle, and the inclusions inside the super lattice determines the power rerouting directions. When the inclusions can reroute all the power into one diffraction order, a metasurface can acquire unitary efficiency even in steep angle steering. Reprinted with permission from [94] © The American Chemical Society.

Guided by the impedance boundary conditions, situations in reflection and refraction modes naturally bear large difference. Ideal transmission manipulation can be achieved by passive lossless metasurface, although there are still certain requirements on, for example, bianisotropy [95]. The transmission type metasurface should be reciprocal and allows bianisotropic response with the coupling between electric and magnetic polarizations in a unit cell. Moreover, the coupling coefficient has to be constant depending only on the incident and desired fields, while the electric and magnetic polarizabilities have to be spatially variant and satisfy certain relationships. For reflective metasurfaces, local power absorption and gain oscillations are required to achieve unitary efficiency, where spatial dispersion must be applied for passive metasurfaces [96]. Spatial dispersion makes the perfect reflection with unitary efficiency possible, by allowing periodic flow of power to enter the metasurface and then to launch back. However, this calls for strong nonlocal effect [64] to become locally absorptive and active yet overall passive and global lossless, which is a nontrivial work. A more preferable alternative may be a reflective metasurface allowing the discard of local active part at the cost of low power loss. People find that this part of energy loss is smaller when it reroutes to undesired reflection angle than being absorbed [23]. Therefore, the trade-off strategy is allowing suppressed reflection into undesired direction using lossless reflective metasurfaces. A much better efficiency is acquired in this circumstance than the passive lossy scene with only one desired deflected angle. This strategy also calls for both electric and magnetic polarization to obtain a higher efficiency.

In addition to the satisfactory local amplitude profile, the acquirement of the fast varying phase profile is inherently limited by the pixelate feature of metasurface, which is usually composed of subwavelength lattice. Methods that can surmount the small pixel barrier are highly desired. Meta-grating [63] is a new concept aiming at breaking the limited pixel resolution and offering an utterly continuous phase profile in the super lattice. By using the concept of grating to funnel power into specific channels, the super lattice is a fundamental periodic composition of metasurface and offers continuous transformation by regarding the structure inclusions as a whole. The super lattice selects the desired steering angle as a diffraction order and the complex inclusions inside the super lattice are tailored to reroute the incident power to the desired diffraction order and to suppress the other undesired diffraction orders. This strategy is distinguishable from discretization of the averaged continuous impedance profile, which is inherently limited by the subwavelength fabrication resolution. With meta-gratings, unitary efficiency can be achieved. Special attention should be paid to the complex inclusions in super lattice. For normal incidence, only one Floquet mode funneling power implies the asymmetric scattering by the inclusions, which might be obtained by directional scattering antennas. Various applications apply the metagrating concepts and yield high efficiency and great performance in high NA focusing [97], steep angle deflection [94, 98], etc.

4. Conclusion

Metasurfaces, featured with ultrathin thickness, subwavelength resolution transformation to the wavefront, and diverse interactions with the incident field, serve as a class of unprecedented compact and versatile platforms to modulate the incident electromagnetic waves. The resonances of meta-atoms guarantee their strong interactions with the impinging field, which results in desired transformation within a subwavelength scale. However, separate resonances may bring some inherent limitations, which results in certain restrictions on the properties of temporal dispersion and efficiency of metasurfaces. During the past decade, fruitful works have been done to break these limitations, which further broaden the capabilities of metasurfaces and endow more practical potentials for metasurface applications. These breakthroughs and improvements of metasurfaces come from the exploration and deeper comprehension of novel and multiplicate interactions between meta-atoms and the impinging field. The engineering and exploitation of different kinds of resonances and the control of coupling between them still need further exploration to acquire general guidelines for designing the inclusions and arrangements of metasurfaces.

Besides passive metasurfaces, tunable metasurfaces [99] enabling real-time modulation of both the transmittance/reflectance and phase are also worth being explored. Tunable metasurfaces have great potential in many practical applications such as beam steering in light detection and ranging (LIDAR) and holographic display, where the dispersion engineering and efficiency management are also essential. With these efforts, the capabilities and applications of metasurfaces may be further boosted.

Acknowledgements

National Natural Science Foundation of China (Projects No. 61775113 and No. 11474180).

References

[1] C. Tiejun, D. Smith, L. Ruopeng, *Metamaterials: Theory, Design and Applications*, Springer, New York, 2010.

[2] D. R. Smith, J. B. Pendry, M. C. Wiltshire, "Metamaterials and negative refractive index", *Science* **305** (2004), no. 5685, p. 788-792.

[3] V. M. Shalaev, "Optical negative-index metamaterials", *Nat. Photon.* **1** (2007), no. 1, p. 41.

[4] A. Poddubny, I. Iorsh, P. Belov, Y. Kivshar, “Hyperbolic metamaterials”, *Nat. Photon.* **7** (2013), no. 12, p. 948.

[5] D. Schurig, J. Mock, B. Justice, S. A. Cummer, J. B. Pendry, A. Starr, D. Smith, “Metamaterial electromagnetic cloak at microwave frequencies”, *Science* **314** (2006), no. 5801, p. 977-980.

[6] A. V. Kildishev, A. Boltasseva, V. M. Shalaev, “Planar photonics with metasurfaces”, *Science* **339** (2013), no. 6125, article no. 1232009.

[7] H. T. Chen, A. J. Taylor, N. Yu, “A review of metasurfaces: physics and applications”, *Rep. Prog. Phys.* **79** (2016), no. 7, article no. 076401.

[8] X. Song, L. Huang, C. Tang, J. Li, X. Li, J. Liu, Y. Wang, T. Zentgraf, “Selective diffraction with complex amplitude modulation by dielectric metasurfaces”, *Adv. Opt. Mater.* **6** (2018), no. 4, article no. 1701181.

[9] A. E. Minovich, A. E. Miroshnichenko, A. Y. Bykov, T. V. Murzina, D. N. Neshev, Y. S. Kivshar, “Functional and nonlinear optical metasurfaces”, *Laser Photon. Rev.* **9** (2015), no. 2, p. 195-213.

[10] S. Chen, Z. Li, Y. Zhang, H. Cheng, J. Tian, “Phase manipulation of electromagnetic waves with metasurfaces and its applications in nanophotonics”, *Adv. Opt. Mater.* **6** (2018), no. 13, article no. 1800104.

[11] R. Zhao, L. Huang, C. Tang, J. Li, X. Li, Y. Wang, T. Zentgraf, “Nanoscale polarization manipulation and encryption based on dielectric metasurfaces”, *Adv. Opt. Mater.* **6** (2018), no. 19, article no. 1800490.

[12] E. Karimi, S. A. Schulz, I. De Leon, H. Qassim, J. Upham, R. W. Boyd, “Generating optical orbital angular momentum at visible wavelengths using a plasmonic metasurface”, *Light: Sci. Appl.* **3** (2014), no. 5, article no. e167.

[13] C. L. Holloway, E. F. Kuester, J. A. Gordon, J. O’Hara, J. Booth, D. R. Smith, “An overview of the theory and applications of metasurfaces: the two-dimensional equivalents of metamaterials”, *IEEE Antennas Propag. Mag.* **54** (2012), no. 2, p. 10-35.

[14] E. F. Kuester, M. A. Mohamed, M. Piket-May, C. L. Holloway, “Averaged transition conditions for electromagnetic fields at a metafilm”, *IEEE Trans. Antennas Propag.* **51** (2003), no. 10, p. 2641-2651.

[15] Y. Yang, A. E. Miroshnichenko, S. V. Kostinski, M. Odit, P. Kapitanova, M. Qiu, Y. S. Kivshar, “Multimode directionality in all-dielectric metasurfaces”, *Phys. Rev. B* **95** (2017), no. 16, article no. 165426.

[16] M. A. Kats, N. Yu, P. Genevet, Z. Gaburro, F. Capasso, “Effect of radiation damping on the spectral response of plasmonic components”, *Opt. Express* **19** (2011), no. 22, p. 21748-21753.

[17] A. Forouzmand, M. M. Salary, S. Inampudi, H. Mosallaei, “A tunable multigate indium-tin-oxide-assisted all-dielectric metasurface”, *Adv. Opt. Mater.* **6** (2018), no. 7, article no. 1701275.

[18] Y. Yang, W. Wang, A. Boulesbaa, I. I. Kravchenko, D. P. Briggs, A. Puretzky, D. Geohegan, J. Valentine, “Nonlinear fano-resonant dielectric metasurfaces”, *Nano Lett.* **15** (2015), no. 11, p. 7388-7393.

[19] S. Colburn, A. Zhan, A. Majumdar, “Metasurface optics for full-color computational imaging”, *Sci. Adv.* **4** (2018), no. 2, article no. eaar2114.

[20] D. Wen, F. Yue, G. Li, G. Zheng, K. Chan, S. Chen, M. Chen, K. F. Li, P. W. H. Wong, K. W. Cheah, “Helicity multiplexed broadband metasurface holograms”, *Nat. Commun.* **6** (2015), p. 8241.

[21] X. Ding, F. Monticone, K. Zhang, L. Zhang, D. Gao, S. N. Burokur, A. de Lustrac, Q. Wu, C. Qiu, A. Alù, “Ultrathin Pancharatnam–Berry metasurface with maximal cross-polarization efficiency”, *Adv. Mater.* **27** (2015), no. 7, p. 1195-1200.

[22] G. V. Naik, V. M. Shalaev, A. Boltasseva, “Alternative plasmonic materials: beyond gold and silver”, *Adv. Mater.* **25** (2013), no. 24, p. 3264-3294.

[23] N. Mohammadi Estakhri, A. Alù, “Wave-front transformation with gradient metasurfaces”, *Phys. Rev. X* **6** (2016), no. 4, article no. 041008.

[24] Y. Yang, I. Kravchenko, D. P. Briggs, J. Valentine, “All-dielectric metasurface analogue of electromagnetically induced transparency”, *Nat. Commun.* **5** (2014), p. 5753.

[25] B. Luk’yanchuk, N. I. Zheludev, S. A. Maier, N. J. Halas, P. Nordlander, H. Giessen, C. T. Chong, “The fano resonance in plasmonic nanostructures and metamaterials”, *Nat. Mater.* **9** (2010), no. 9, p. 707-715.

[26] U. Fano, “Effects of configuration interaction on intensities and phase shifts”, *Phys. Rev.* **124** (1961), no. 6, p. 1866.

[27] A. E. Miroshnichenko, S. Flach, Y. S. Kivshar, “Fano resonances in nanoscale structures”, *Rev. Mod. Phys.* **82** (2010), no. 3, p. 2257.

[28] A. Rau, “Perspectives on the fano resonance formula”, *Phys. Scr.* **69** (2004), no. 1, article no. C10.

[29] C. W. Hsu, B. Zhen, A. D. Stone, J. D. Joannopoulos, M. Soljačić, “Bound states in the continuum”, *Nat. Rev. Mater.* **1** (2016), no. 9, article no. 16048.

[30] K. Koshelev, S. Lepeshov, M. Liu, A. Bogdanov, Y. Kivshar, “Asymmetric metasurfaces with high-q resonances governed by bound states in the continuum”, *Phys. Rev. Lett.* **121** (2018), no. 19, article no. 193903.

[31] D. R. Abujetas, N. van Hoof, S. ter Huurne, J. G. Rivas, J. A. Sánchez-Gil, “Spectral and temporal evidence of robust photonic bound states in the continuum on terahertz metasurfaces”, *Optica* **6** (2019), no. 8, p. 996-1001.

[32] Y. He, G. Guo, T. Feng, Y. Xu, A. E. Miroshnichenko, “Toroidal dipole bound states in the continuum”, *Phys. Rev. B* **98** (2018), article no. 161112.

[33] F. Monticone, A. Alù, “Bound states within the radiation continuum in diffraction gratings and the role of leaky modes”, *New J. Phys.* **19** (2017), no. 9, article no. 093011.

[34] M. Liu, D. Y. Choi, "Extreme Huygens' metasurfaces based on quasi-bound states in the continuum", *Nano Lett.* **18** (2018), no. 12, p. 8062-8069.

[35] S. Campione, S. Liu, L. I. Basilio, L. K. Warne, W. L. Langston, T. S. Luk, J. R. Wendt, J. L. Reno, G. A. Keeler, I. Brener, "Broken symmetry dielectric resonators for high quality factor fano metasurfaces", *ACS Photon.* **3** (2016), no. 12, p. 2362-2367.

[36] K. Fan, I. V. Shadrivov, W. J. Padilla, "Dynamic bound states in the continuum", *Optica* **6** (2019), no. 2, p. 169-173.

[37] C. Cui, C. Zhou, S. Yuan, X. Qiu, L. Zhu, Y. Wang, Y. Li, J. Song, Q. Huang, Y. Wang, C. Zeng, J. Xia, "Multiple fano resonances in symmetry-breaking silicon metasurface for manipulating light emission", *ACS Photon.* **5** (2018), no. 10, p. 4074-4080.

[38] S. Romano, G. Zito, S. Torino, G. Calafiore, E. Penzo, G. Coppola, S. Cabrini, I. Rendina, V. Mocella, "Label-free sensing of ultralow-weight molecules with all-dielectric metasurfaces supporting bound states in the continuum", *Photon. Res.* **6** (2018), no. 7, p. 726-733.

[39] Y. K. Srivastava, M. Manjappa, L. Cong, W. Cao, I. Al-Naib, W. Zhang, R. Singh, "Ultrahigh-qfano resonances in terahertz metasurfaces: strong influence of metallic conductivity at extremely low asymmetry", *Adv. Opt. Mater.* **4** (2016), no. 3, p. 457-463.

[40] A. S. Kupriianov, Y. Xu, A. Sayanskiy, V. Dmitriev, Y. S. Kivshar, V. R. Tuz, "Metasurface engineering through bound states in the continuum", *Phys. Rev. Appl.* **12** (2019), no. 1, article no. 014024.

[41] A. Tittl, A. Leitis, M. Liu, F. Yesilkoy, D.-Y. Choi, D. N. Neshev, Y. S. Kivshar, H. Altug, "Imaging-based molecular barcoding with pixelated dielectric metasurfaces", *Science* **360** (2018), no. 6393, p. 1105-1109.

[42] H. Friedrich, D. Wintgen, "Interfering resonances and bound states in the continuum", *Phys. Rev. A* **32** (1985), no. 6, p. 3231.

[43] S. Fan, W. Suh, J. D. Joannopoulos, "Temporal coupled-mode theory for the fano resonance in optical resonators", *JOSA A* **20** (2003), no. 3, p. 569-572.

[44] J. Wiersig, "Formation of long-lived, scarlike modes near avoided resonance crossings in optical microcavities", *Phys. Rev. Lett.* **97** (2006), no. 25, article no. 253901.

[45] A. Kodigala, T. Lepetit, Q. Gu, B. Bahari, Y. Fainman, B. Kante, "Lasing action from photonic bound states in continuum", *Nature* **541** (2017), no. 7636, p. 196-199.

[46] A. A. Bogdanov, K. L. Koshelev, P. V. Kapitanova, M. V. Rybin, S. A. Gladyshev, Z. F. Sadrieva, K. B. Samusev, Y. S. Kivshar, M. F. Limonov, "Bound states in the continuum and fano resonances in the strong mode coupling regime", *Adv. Photon.* **1** (2019), no. 01, article no. 016001.

[47] S. Wang, P. C. Wu, V. C. Su, Y. C. Lai, C. Hung Chu, J. W. Chen, S. H. Lu, J. Chen, B. Xu, C. H. Kuan, T. Li, S. Zhu, D. P. Tsai, "Broadband achromatic optical metasurface devices", *Nat. Commun.* **8** (2017), no. 1, p. 187.

[48] O. Avayu, E. Almeida, Y. Prior, T. Ellenbogen, "Composite functional metasurfaces for multispectral achromatic optics", *Nat. Commun.* **8** (2017), p. 14992.

[49] E. Arbabi, A. Arbabi, S. M. Kamali, Y. Horie, A. Faraon, "Multiwavelength metasurfaces through spatial multiplexing", *Sci. Rep.* **6** (2016), p. 32803.

[50] Z.-B. Fan, H.-Y. Qiu, H.-L. Zhang, X.-N. Pang, L.-D. Zhou, L. Liu, H. Ren, Q.-H. Wang, J.-W. Dong, "A broadband achromatic metalens array for integral imaging in the visible", *Light: Sci. Appl.* **8** (2019), no. 1, p. 67.

[51] D. Lin, P. Fan, E. Hasman, M. L. Brongersma, "Dielectric gradient metasurface optical elements", *Science* **345** (2014), no. 6194, p. 298-302.

[52] M. Khorasaninejad, W. T. Chen, R. C. Devlin, J. Oh, A. Y. Zhu, F. Capasso, "Metalenses at visible wavelengths: diffraction-limited focusing and subwavelength resolution imaging", *Science* **352** (2016), no. 6290, p. 1190-1194.

[53] W. T. Chen, A. Y. Zhu, V. Sanjeev, M. Khorasaninejad, Z. Shi, E. Lee, F. Capasso, "A broadband achromatic metalens for focusing and imaging in the visible", *Nat. Nanotechnol.* **13** (2018), no. 3, p. 220-226.

[54] M. Khorasaninejad, F. Aieta, P. Kanhaiya, M. A. Kats, P. Genevet, D. Rousso, F. Capasso, "Achromatic metasurface lens at telecommunication wavelengths", *Nano Lett.* **15** (2015), no. 8, p. 5358-5362.

[55] E. Arbabi, A. Arbabi, S. M. Kamali, Y. Horie, A. Faraon, "Multiwavelength polarization-insensitive lenses based on dielectric metasurfaces with meta-molecules", *Optica* **3** (2016), no. 6, p. 628-633.

[56] Y. Zhou, I. Kravchenko, H. Wang, J. R. Nolen, G. Gu, J. Valentine, "Multilayer noninteracting dielectric metasurfaces for multiwavelength metaoptics", *Nano Lett.* **18** (2018), no. 12, p. 7529-7537.

[57] S. Wang, P. C. Wu, V. C. Su, Y. C. Lai, M. K. Chen, H. Y. Kuo, B. H. Chen, Y. H. Chen, T. T. Huang, J. H. Wang, R. M. Lin, C. H. Kuan, T. Li, Z. Wang, S. Zhu, D. P. Tsai, "A broadband achromatic metalens in the visible", *Nat. Nanotechnol.* **13** (2018), no. 3, p. 227-232.

[58] E. Arbabi, A. Arbabi, S. M. Kamali, Y. Horie, A. Faraon, "Controlling the sign of chromatic dispersion in diffractive optics with dielectric metasurfaces", *Optica* **4** (2017), no. 6, p. 625-632.

[59] F. Ding, Y. Yang, R. A. Deshpande, S. I. Bozhevolnyi, "A review of gap-surface plasmon metasurfaces: fundamentals and applications", *Nanophotonics* **7** (2018), no. 6, p. 1129-1156.

[60] W. Liu, Y. S. Kivshar, "Generalized Kerker effects in nanophotonics and meta-optics", *Opt. Express* **26** (2018), no. 10, p. 13085-13105.

[61] A. Arbabi, Y. Horie, M. Bagheri, A. Faraon, "Dielectric metasurfaces for complete control of phase and polarization with subwavelength spatial resolution and high transmission", *Nat. Nanotechnol.* **10** (2015), no. 11, p. 937-943.

[62] N. Yu, P. Genevet, M. A. Kats, F. Aieta, J. P. Tetienne, F. Capasso, Z. Gaburro, "Light propagation with phase discontinuities: generalized laws of reflection and refraction", *Science* **334** (2011), no. 6054, p. 333-337.

[63] Y. Rad'i, D. L. Sounas, A. Alù, "Metagratings: beyond the limits of graded metasurfaces for wave front control", *Phys. Rev. Lett.* **119** (2017), no. 6, article no. 067404.

[64] A. Díaz-Rubio, V. S. Asadchy, A. Elsakka, S. A. Tretyakov, "From the generalized reflection law to the realization of perfect anomalous reflectors", *Sci. Adv.* **3** (2017), no. 8, article no. e1602714.

[65] E. Hutter, J. H. Fendler, "Exploitation of localized surface plasmon resonance", *Adv. Mater.* **16** (2004), no. 19, p. 1685-1706.

[66] P. B. Johnson, R.-W. Christy, "Optical constants of the noble metals", *Phys. Rev. B* **6** (1972), no. 12, p. 4370.

[67] G. V. Naik, J. Kim, A. Boltasseva, "Oxides and nitrides as alternative plasmonic materials in the optical range [invited]", *Opt. Mater. Express* **1** (2011), no. 6, p. 1090-1099.

[68] S. A. Gregory, Y. Wang, C. De Groot, O. L. Muskens, "Extreme subwavelength metal oxide direct and complementary metamaterials", *ACS Photon.* **2** (2015), no. 5, p. 606-614.

[69] U. Guler, G. V. Naik, A. Boltasseva, V. M. Shalaev, A. V. Kildishev, "Performance analysis of nitride alternative plasmonic materials for localized surface plasmon applications", *Appl. Phys. B* **107** (2012), no. 2, p. 285-291.

[70] U. Guler, A. Boltasseva, V. M. Shalaev, "Refractory plasmonics", *Science* **344** (2014), no. 6181, p. 263-264.

[71] L. Gui, S. Bagheri, N. Strohfeldt, M. Hentschel, C. M. Zgrabik, B. Metzger, H. Linnenbank, E. L. Hu, H. Giessen, "Nonlinear refractory plasmonics with titanium nitride nanoantennas", *Nano Lett.* **16** (2016), no. 9, p. 5708-5713.

[72] Y. Wang, A. Capretti, L. Dal Negro, "Wide tuning of the optical and structural properties of alternative plasmonic materials", *Opt. Mater. Express* **5** (2015), no. 11, p. 2415-2430.

[73] M. Z. Alam, I. De Leon, R. W. Boyd, "Large optical nonlinearity of indium tin oxide in its epsilon-near-zero region", *Science* **352** (2016), no. 6287, p. 795-797.

[74] J. Park, J. H. Kang, S. J. Kim, X. Liu, M. L. Brongersma, "Dynamic reflection phase and polarization control in metasurfaces", *Nano Lett.* **17** (2017), no. 1, p. 407-413.

[75] A. Howes, W. Y. Wang, I. Kravchenko, J. Valentine, "Dynamic transmission control based on all-dielectric Huygens metasurfaces", *Optica* **5** (2018), no. 7, p. 787-792.

[76] C. Qu, S. Ma, J. Hao, M. Qiu, X. Li, S. Xiao, Z. Miao, N. Dai, Q. He, S. Sun, L. Zhou, "Tailor the functionalities of metasurfaces based on a complete phase diagram", *Phys. Rev. Lett.* **115** (2015), no. 23, article no. 235503.

[77] M. Decker, I. Staude, M. Falkner, J. Dominguez, D. N. Neshev, I. Brener, T. Pertsch, Y. S. Kivshar, "High-efficiency dielectric Huygens' surfaces", *Adv. Opt. Mater.* **3** (2015), no. 6, p. 813-820.

[78] A. Arbabi, E. Arbabi, S. M. Kamali, Y. Horie, S. Han, A. Faraon, "Miniature optical planar camera based on a wide-angle metasurface doublet corrected for monochromatic aberrations", *Nat. Commun.* **7** (2016), p. 13682.

[79] A. I. Kuznetsov, A. E. Miroshnichenko, M. L. Brongersma, Y. S. Kivshar, B. Luk'yanchuk, "Optically resonant dielectric nanostructures", *Science* **354** (2016), no. 6314, p. 2956-2963.

[80] N. Papasimakis, V. A. Fedotov, V. Savinov, T. A. Raybould, N. I. Zheludev, "Electromagnetic toroidal excitations in matter and free space", *Nat. Mater.* **15** (2016), no. 3, p. 263-271.

[81] J. Zhou, T. Koschny, C. M. Soukoulis, "Magnetic and electric excitations in split ring resonators", *Opt. Express* **15** (2007), no. 26, p. 17881-17890.

[82] S. Alrasheed, E. Di, "Giant magnetic field enhancement in hybridized mim structures", *IEEE Photon. Technol. Lett.* **29** (2017), no. 24, p. 2151-2154.

[83] I. Staude, A. E. Miroshnichenko, M. Decker, N. T. Fofang, S. Liu, E. Gonzales, J. Dominguez, T. S. Luk, D. N. Neshev, I. Brener, "Tailoring directional scattering through magnetic and electric resonances in subwavelength silicon nanodisks", *ACS Nano* **7** (2013), no. 9, p. 7824-7832.

[84] I. Staude, J. Schilling, "Metamaterial-inspired silicon nanophotonics", *Nat. Photon.* **11** (2017), no. 5, p. 274-284.

[85] R. C. Devlin, M. Khorasaninejad, W. T. Chen, J. Oh, F. Capasso, "Broadband high-efficiency dielectric metasurfaces for the visible spectrum", *Proc. Natl. Acad. Sci. USA* **113** (2016), no. 38, p. 10473-10478.

[86] X. Zhu, W. Yan, U. Levy, N. A. Mortensen, A. Kristensen, "Resonant laser printing of structural colors on high-index dielectric metasurfaces", *Sci. Adv.* **3** (2017), no. 5, article no. e1602487.

[87] S. Liu, M. B. Sinclair, S. Saravi, G. A. Keeler, Y. Yang, J. Reno, G. M. Peake, F. Setzpfandt, I. Staude, T. Pertsch, "Resonantly enhanced second-harmonic generation using iii–v semiconductor all-dielectric metasurfaces", *Nano Lett.* **16** (2016), no. 9, p. 5426-5432.

[88] A. Pors, S. I. Bozhevolnyi, "Plasmonic metasurfaces for efficient phase control in reflection", *Opt. Express* **21** (2013), no. 22, p. 27438-27451.

[89] L. Zhang, S. Mei, K. Huang, C. Qiu, "Advances in full control of electromagnetic waves with metasurfaces", *Adv. Opt. Mater.* **4** (2016), no. 6, p. 818-833.

[90] C. M. Watts, X. Liu, W. J. Padilla, "Metamaterial electromagnetic wave absorbers", *Adv. Mater.* **24** (2012), no. 23, p. OP98-OP120.

[91] G. Zheng, H. Muhlenbernd, M. Kenney, G. Li, T. Zentgraf, S. Zhang, “Metasurface holograms reaching 80% efficiency”, *Nat. Nanotechnol.* **10** (2015), no. 4, p. 308-312.

[92] R. Alaee, C. Rockstuhl, I. Fernandez-Corbaton, “An electromagnetic multipole expansion beyond the long-wavelength approximation”, *Opt. Commun.* **407** (2018), p. 17-21.

[93] N. Yu, F. Capasso, “Flat optics with designer metasurfaces”, *Nat. Mater.* **13** (2014), no. 2, p. 139-150.

[94] E. Khaidarov, H. Hao, R. Paniagua-Dominguez, Y. F. Yu, Y. H. Fu, V. Valuckas, S. L. K. Yap, Y. T. Toh, J. S. K. Ng, A. I. Kuznetsov, “Asymmetric nanoantennas for ultrahigh angle broadband visible light bending”, *Nano Lett.* **17** (2017), no. 10, article no. 28898084.

[95] A. Serdiukov, I. Semchenko, S. Tertyakov, A. Sihvola, *Electromagnetics of Bi-anisotropic Materials—Theory and Application, Vol. 11*, Gordon and Breach Science Publishers, 2001.

[96] V. S. Asadchy, M. Albooyeh, S. N. Tcvetkova, A. Díaz-Rubio, Y. Ra’di, S. Tretyakov, “Perfect control of reflection and refraction using spatially dispersive metasurfaces”, *Phys. Rev. B* **94** (2016), no. 7, article no. 075142.

[97] R. Paniagua-Dominguez, Y. F. Yu, E. Khaidarov, S. Choi, V. Leong, R. M. Bakker, X. Liang, Y. H. Fu, V. Valuckas, L. A. Krivitsky, “A metalens with a near-unity numerical aperture”, *Nano Lett.* **18** (2018), no. 3, p. 2124-2132.

[98] D. Sell, J. Yang, S. Doshay, R. Yang, J. A. Fan, “Large-angle, multifunctional metagratings based on freeform multimode geometries”, *Nano Lett.* **17** (2017), no. 6, p. 3752-3757.

[99] T. Cui, B. Bai, H. Sun, “Tunable metasurfaces based on active materials”, *Adv. Funct. Mater.* **29** (2019), no. 10, article no. 1806692.

Comptes Rendus
Physique
2020, 21, nº 7-8, p. 659-676
`https://doi.org/10.5802/crphys.20`

Metamaterials 2 / *Métamatériaux 2*

An overview of metasurfaces for thin antenna applications

Application des métasurfaces aux antennes à faible épaisseur

Massimiliano Casaletti[*, a, b], **Guido Valerio**[a, b], **Oscar Quevedo-Teruel**[c]
and Paolo Burghignoli[d]

[a] Sorbonne Université, CNRS, Laboratoire de Génie Electrique et Electronique de Paris, 75252, Paris, France

[b] Université Paris-Saclay, CentraleSupélec, CNRS, Laboratoire de Génie Electrique et Electronique de Paris, 91192, Gif-sur-Yvette, France

[c] Division for Electromagnetic Engineering, School of Electrical Engineering and Computer Science, KTH Royal Institute of Technology, SE-100 44 Stockholm, Sweden

[d] Department of Information Engineering, Electronics and Telecommunications, Sapienza University of Rome, via Eudossiana 18, 00184 Rome, Italy

E-mails: massimiliano.casaletti@sorbonne-universite.fr (M. Casaletti), guido.valerio@sorbonne-universite.fr (G. Valerio), oscarqt@kth.se (O. Quevedo-Teruel), paolo.burghignoli@uniroma1.it (P. Burghignoli)

Abstract. In recent years, metasurfaces have become a rapidly growing domain of research in several fields of engineering and applied physics due to their ability to manipulate both phase and amplitude of electromagnetic fields. These artificial 2D-materials, usually composed of metallic elements printed on dielectric substrates, have the advantages of being low profile, lightweight as well as easy to fabricate and integrate with standard circuit technologies. In this context, this paper reviews the latest progress in metasurface antenna design, where metasurfaces are used to miniaturize the profile, increase the bandwidth, and control the radiation pattern in the near- and far-field regions.

Résumé. Ces dernières années, la thématique des métasurfaces est devenue un sujet de recherche en pleine expansion dans plusieurs domaines de l'ingénierie et de la physique appliquée, en raison de leur capacité à manipuler à la fois la phase et l'amplitude des champs électromagnétiques. Ces matériaux artificiels bidimensionnels, généralement composés d'éléments métalliques imprimés sur des substrats diélectriques, ont l'avantage d'être de très faible épaisseur, légers et faciles à fabriquer et à intégrer avec les circuits imprimés. Cet article passe en revue les dernières avancées dans la conception d'antennes à métasurface, où les métasurfaces sont utilisées pour minimiser l'épaisseur, augmenter la bande passante et contrôler le diagramme de rayonnement en champ proche et en champ lointain.

---

[*] Corresponding author.

ISSN (electronic) : 1878-1535

Keywords. Metasurface, Metasurface antennas, Artificial surfaces, Impedance surface, Fabry–Perot cavity, Leaky-wave antennas, Glide symmetry.

Mots-clés. Métasurface, Antennes à métasurface, Surfaces artificielles, Surface d'impédance, Cavité de Fabry–Pérot, Antennes à fuite, Symétrie de glissement.

1. Introduction

In the last years, metamaterials have become an appealing subject of research in applied physics and electrical engineering. They are synthetic materials that present unusual properties that cannot be found in nature such as double negative materials or negative index materials. Metasurfaces can be considered as the equivalent of metamaterials in 2D structures [1]. These synthetic surfaces are composed of periodic sub-wavelength elements. The special properties of metasurfaces, due to the electromagnetic scattering from the subwavelength elements, are controlled by the dimension and the specific shape of these scatterers. The properties of these surfaces are described in terms of surface impedances (or admittances) or dimensionless susceptibility tensors (analogous to the constitutive parameters for volumetric metamaterials). Using the first approach, the metasurface is described by the surface impedance tensor $\underline{\underline{\mathbf{Z_s}}}$ relating, for a particular wavevector $\mathbf{k^{sw}}$, the tangential electric ($\mathbf{E}_t$) and magnetic ($\mathbf{H}_t$) fields at the surface boundary S:

$$\mathbf{E}_t(\rho')|_{\rho'\in S} = \underline{\underline{\mathbf{Z_s}}}(\mathbf{k^{sw}}) \cdot \hat{\mathbf{n}} \times \mathbf{H}_t(\rho')|_{\rho'\in S} = \underline{\underline{\mathbf{Z_s}}} \cdot \mathbf{J}(\rho') \tag{1}$$

where $\hat{\mathbf{n}}$ is the unit vector normal to S, ρ' is a point on the metasurface and $\mathbf{J}(\rho') = \hat{\mathbf{n}} \times \mathbf{H}_t(\rho')|_{\rho'\in S}$ is the equivalent surface current density. For simple element geometries as circular or squared patch, TM and TE polarizations are decoupled (diagonal impedance tensor). These structures are known as *scalar impedance metasurfaces*, while geometries leading to full impedance matrices are known as *tensorial impedance metasurfaces*. The first implementations made use of simple printed geometries as dipoles for capacitive surfaces or rectangular slots for inductive ones [2] leading to diagonal impedance tensors. Later, with the availability of rigorous numerical simulation tools for periodic structures and the development of general impedance extraction methods [3, 4] more complicated geometries have been used to obtain full impedance tensors. It is important to stress the fact that only large metasurfaces (containing a large number of elements) could be homogenized with an effective impedance. In fact, under this hypothesis, each basic element will behave as inside an infinite periodic lattice. Then, using classical Floquet theory, an equivalent medium or impedance could be defined. In other words, the scattered field from the metasurface illuminated by a plane-wave is essentially a plane wave in the specular direction as for a homogeneous media. In small size metasurfaces, the edge effect becomes very strong (each basic element contribution depends on its physical position) and the scattered field under plane-wave illumination will be composed of several harmonics (plane-waves). As a result, the metasurface behaves as a passive array of elements and not as an effective medium. The analysis and the design of antennas using this latter kind of metasurfaces can only be done using numerical optimizations.

From the engineering point of view, these structures have several inherent advantages like low cost, low profile, low mass and easy fabrication/integration which are required in electrical engineering for applications from microwave to THz frequency regimes. Metasurfaces have been used mainly using three different approaches: as a passive element to improve already existing antennas; to develop new classes of antennas, and to develop new kinds of feeding networks for the antenna. For these reasons, different kind of metasurface antennas that perform better or differently than classical antennas were designed in the last years. As the interest in metasurfaces is rapidly expanding, several review articles or books can be found in the literature, as for example in [2, 5–8]. Here, we focus our attention on reviewing the recent progress of metasurface-based

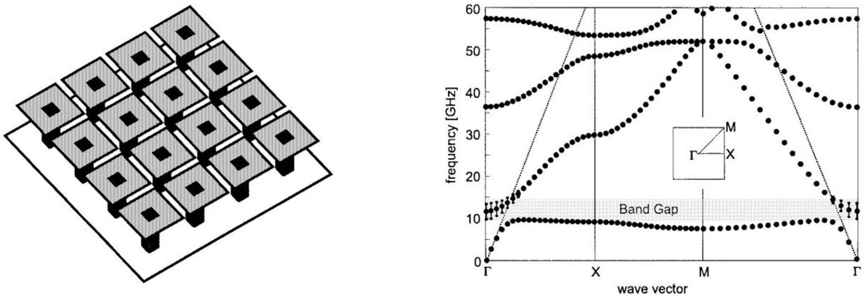

(a) (b)

Figure 1. AMC based on a 2-D array of metallic patches with vertical vias proposed in [9]. Brillouin diagram showing a band gap preventing surface waves to propagate along the metasurface. ©1999 IEEE. Reprinted, with permission, from [9].

antennas during the past few years presenting a compact profile and that cannot be included in well-known classical antenna theory as reflectarray, transmittarray, or Frequence Selective Surfaces (FSS).

The paper is organized as follows: Section 2 reviews the principle and the application of high-surface-impedance metasurfaces in antenna design. Adding a metasurface close to a classical planar antenna is possible to enhance some specific antenna parameters as bandwidth or gain. Section 3 discusses metasurface applications in Fabry–Perot cavities and 2-D leaky wave antennas. In this context, the metasurface is used as a semi-transparent wall to design resonant radiating cavities having some desired property. Section 4 describes recent developments in holographic antenna and aperture field wave-front engineering. The use of modulated metasurfaces allows the conversion of surface-waves into radiating waves having the desired direction and polarization leading to thin versable radiation diagram antennas. Section 5 highlights recent research work on parallel-plate metasurfaces to design planar lenses or control the dispersion properties in antenna structures. The use of multiple shifted metasurface layers (high order symmetries) allows the bandwidth enhancement of the beamforming network used in thin antennas. Conclusions are drawn in the final section.

2. High-impedance-surface antennas

Probably the most immediate way to enhance antenna properties by means of a metasurface is placing the antenna in the vicinity of the metasurface in order to enhance its performance. For exemple, metasurfaces can act as flat lenses if placed on the top of an antenna, thus modifying its radiation features [10]. A more common approach is the replacement of the perfect electric conductor (PEC) of the ground slab in a printed antenna with a high-impedance surface (HIS) approximating an artificial magnetic conductor (AMC) [9] (see Figures 1, 2). In other terms, the AMC enforces a dual boundary condition (null total *magnetic* tangential field) with respect to a PEC (null total *electric* tangential field). The AMC has then an ideally *infinite* surface impedance, while a PEC has a *null* surface impedance, which explains the term HIS commonly used in the literature for surfaces approximating AMC.

The different values of the surface impedances have an impact on both the reflective (plane-wave incidence) and the dispersive (surface-wave propagation) features of these surfaces. These two properties allow for complementary explanations of the performance of printed antennas close to HIS.

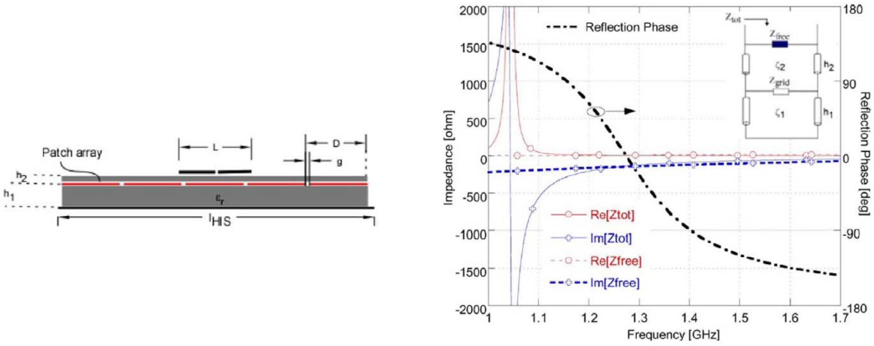

(a) (b)

Figure 2. (a) Printed antenna on an AMC. (b) Electric-field reflection coefficient of the AMC, showing a 0 phase at the resonant frequency around 1.25 GHz, and input impedance of a short dipole close and parallel to the metasurface. ©2011 IEEE. Reprinted, with permission, from [11].

Regarding its reflective behaviour, the AMC reflects plane waves with an electric-field reflection coefficient equal to 1, while the PEC has an electric-field reflection coefficient equal to -1. This is equivalent to a different sign of the images of currents placed near to the surface created by the two types of conductors: a tangential electric current is short circuited by a PEC, but not by a HIS.

For this reason, a HIS at the place of a PEC can lead to low-profile, larger bandwidth, and more compact designs. A radiating element close to a PEC should be at a distance of approximately $\lambda/4$ from the PEC (corresponding to the thickness of the dielectric slab, λ being the wavelength in the dielectric). A much thinner slab would short circuit the printed element, since the image of a planar electric current with respect to a PEC is opposed to the real current and cancels it out, thus reducing the gain of the antenna. Dense dielectrics can reduce this thickness, but will also reduce the bandwidth. An HIS removes this thickness limitation: the image of the planar electric current with respect to an AMC adds up to the real element without deteriorating the antenna gain and the input matching. For this reason, much thinner substrates can be used (but the thickness of the HIS itself should also be taken into account in the final design). Furthermore, the bandwidth limitation related to the frequency dispersion introduced by the electric thickness of the slab is overcome. Of course, the HIS synthesis relies on a resonant behaviour of the surface impedance, and the bandwidth can be limited by the practical HIS implementation. In [12] a circuit model including both the capacitance and the inductance of the metasurface is used to derive in closed form the fractional operational bandwidth of a HIS. In [11], a transverse-resonance method [13] is applied to take into account the spatial dispersion and the anisotropy of the surface, which should be considered when optimizing the full device. Degradation of the radiation pattern also plays a role in limiting the bandwidth of the complete device as discussed in [14]. Among other parameters, front-to-back radiation is reported to be enhanced when considering truncated structures [15]. A more general reactive surface condition has also been proposed, whose reactance can be optimized according to the device [16] in order to achieve a large bandwidth and antenna miniaturization.

The HIS can be then described by its electric-field reflection coefficient close to 1 when the surface is illuminated by a plane wave, usually with normal incidence. Of course, the printed antenna will be placed in proximity of the surface, so that the use of a far-field quantity for the design could be somehow questionable. However, starting from HIS designed under plane-wave illumination, an optimization of the complete device leads to the expected enhanced results.

A different interpretation of HIS, related to near-field quantities, is based on the dispersion behavior of these surfaces. As shown in [9, 17], HIS have usually an electromagnetic bandgap (EBG) behavior in the frequency band close to the impedance resonance. This means that surface waves cannot propagate along the HIS, and explains why HIS are also used to minimize surface-wave losses [18, 19] and inter-element coupling among elements in printed arrays [20, 21]. If surface-wave blockage is of interest, the EBG surface can also be printed on the same interface as the radiating element on the same grounded slab [22]. An in-depth treatment of these applications is presented in [23]. Other kinds of artificial surfaces can be used in order to enhance surface-wave contributions [11], thus obtaining a stronger excitation of the radiating element and a coherent radiation from the truncated edges of the device.

Different surface implementation methods have been proposed in the last two decades, based on patches with central vias [9, 24], or on purely planar realizations [18, 19, 25–27]. Via-less solutions may have weaker EBG behaviour and may be less robust with respect to the incidence angle, but are easier to fabricate [28]. However, via-less metasurfaces can be made more effective if placed in an embedded configuration [29].

Recently, different geometrical lattices have been proposed to realize the HIS, which could optimize the coupling with the antenna. Specifically, circular lattices have been investigated in [30–32] and have been found to be more effective in proximity of curvilinear radiating elements (circular slots, helicoidal antennas). In squared lattices, an interleaved texture enlarges the operational bandwidth and offers more angular and polarization stability [33]. If a multilayered configuration is allowed, a miniaturization of the cell size can be achieved through glide-symmetric configurations [34].

Applications to dual-band antennas have also been studied by using higher-order resonances of metasurfaces. In [35] fractal motives are used at first, and a more general genetic algorithm approach is also proposed. Different solutions have been designed more recently based on slotted patches [36] or angular-defined textures [37].

More complex implementations enable the tunability of the HIS in order to modify the central frequency of operation and to compensate for different environments (in [38] different kinds of human tissues are matched for on-body applications by reconfiguring the metasurface).

3. Fabry–Perot cavity antennas and other 2-d leaky wave antennas

The single refraction process that determines the aperture field in flat lenses or, more generally, transmitarrays (TAs), which locally involves a single uniform plane wave and a uniform homogenized interface, becomes a *multiple* refraction process in Fabry–Perot Cavity Antennas (FPCAs), structurally similar to TAs but based on highly reflecting screens, usually indicated in this context as Partially Reflecting Surfaces (PRSs). Such multiple refraction process increases the illuminated area of the aperture plane and hence the directivity of the primary pattern produced by the feeder, which is typically a simple, non-directive source like, e.g., a printed dipole, a slot on the ground plane, or a vertical coaxial probe.

Such a ray-optics radiation model was indeed adopted since the seminal paper of 1956 by von Trentini [39], where the very first FPCA was proposed, based on patterned metal PRSs, as well as in many of the more recent works on the subject [40–42]. Alternatively, the directive properties of FPCAs can be related to their resonant behavior when operated in reception under plane-wave illumination [43]. A third and very fruitful radiation model is based on recognizing that the extended illumination of the aperture plane is due to the excitation of dominant and weakly attenuated *leaky waves* that propagate radially along the FPCA [44–48], now seen as a partially open parallel-plate waveguide, in the form of cylindrical waves [49].

Metasurfaces have played an important role in the recent developments of FPCAs, providing different means of improving their overall antenna performance. A first example is the use of Artificial Magnetic Conductors (AMCs), like the HIS described in Section 2, as ground planes; this allows for *reducing the thickness* of the cavity, which is typically on the order of $\lambda/2$ for FPCAs with a standard uniform metal ground plane, to values on the order of a $\lambda/4$ [50, 51]; using more general metasurface ground planes, that exhibit a reflection phase between $-\pi$ and 0, the thickness can be furher reduced to $\lambda/6$ [52], or even $\lambda/16$ [53]. By employing an AMC-like metasurface also as a PRS further dramatic reductions in thickness can be achieved, down to $\lambda/64$ [54].

Other advanced designs employ metasurfaces with the aim of increasing the inherent small fractional pattern bandwidth of FPCAs. One approach is based on the observation, first made in [40], that *wideband* directive radiation can be obtained if the PRS has a reflection coefficient whose phase is a linearly increasing function of frequency. Such a non-Foster behavior is impossible to achieve using a single thin, passive, lossless PRS placed above an ordinary dielectric slab; therefore, more complex PRS structures have been proposed, e.g., based on two- or three-layer PRSs made from multiple dielectric slabs covered by metal screens and separated by air gaps [55–57]; on a single dielectric slab with periodic metal screens printed on both sides [58,59]; on Electromagnetic-BandGap (EBG) structures with defect layers, either metallized [60] or all-dielectric [61, 62]. A leaky-wave analysis of the broadband response of FPCAs based on a thick multilayer PRS with a double metallized side was proposed in [63] and, for general FPCAs with thick PRS, in [64].

Whereas most FPCAs are operated to radiate a narrow pencil beam at broadside, by increasing the operating frequency their leaky-wave nature allows for obtaining also *conical scanned patterns*. However, the degree of omnidirectionality of such patterns gradually decreases with the beam angle, due to the different dispersion features of the two cylindrical leaky waves, one TM and one TE with respect to the broadside direction, excited along the antenna. In [65] a simple metal strip grating is considered as a PRS, whose particular *spatially dispersive* nature allows for a single cylindrical leaky wave to propagate with the same radial wavenumber in all azimuthal directions; such wave is TM with respect to the strip axis, hence hybrid with respect to the broadside direction, and produces scanned patterns with improved omnidirectionality and high polarization purity. Alternatively, multilayer FPCAs with metal patch PRSs have been designed to support a pair of TM and TE leaky waves with *equalized wavenumbers* at a single frequency, whose independent excitation allows for designing narrow-band FPCAs with dual or even reconfigurable polarization [66].

The inherently dispersive nature of the leaky waves supported by FPCAs is responsible for their typical frequency scanning feature, i.e., the variation of the radiated beam angle with frequency. Since this may be undesirable in many applications, various designs have been proposed for achieving pattern-reconfigurable FPCAs at a *fixed frequency*. One of the first examples is that proposed in [67], based on a mechanically tunable impedance ground plane. More practical electronically tunable PRSs have been extensively investigated by many authors, typically including varactor diodes in the PRS structure [68–72]. In [73] beam steering is instead achieved through varactor-based phase-agile reflection cells placed on the antenna ground plane.

A different approach to electronic reconfigurability is based on the use of *tunable materials*, whose permittivity can be changed by applying suitable electrostatic bias fields. In [75], for instance, a tunable 2-D LWA was proposed, where a thin ferroelectric layer was inserted directly below the slot-type metal PRS inside the antenna cavity. In [76] a multistack PRS was instead considered, made of alternating layers of highly birefringent nematic liquid crystal and high-permittivity dielectric. The use of *graphene* has also been considered for achieving reconfigurable 2-D LWA operation since, as is well known, the conductivity of graphene can be tuned via electric-field effect by means of a suitable electrostatic bias. This has prompted in the last few years

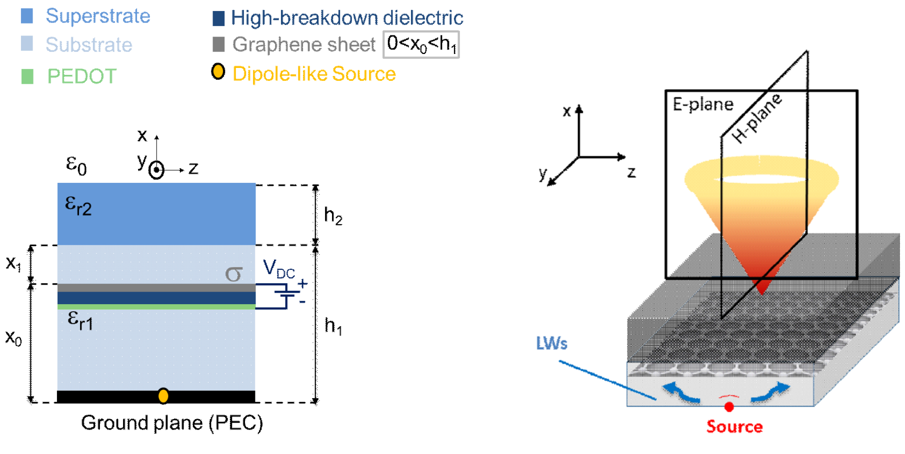

(a) (b)

Figure 3. Graphene-based FPCA in a substrate-superstrate configuration. (a) Transverse view of the multilayer, including the graphene biasing scheme. (b) 3-D view of the conical pattern. More information can be found in [74]. ©2017 IEEE. Reprinted, with permission, from [74].

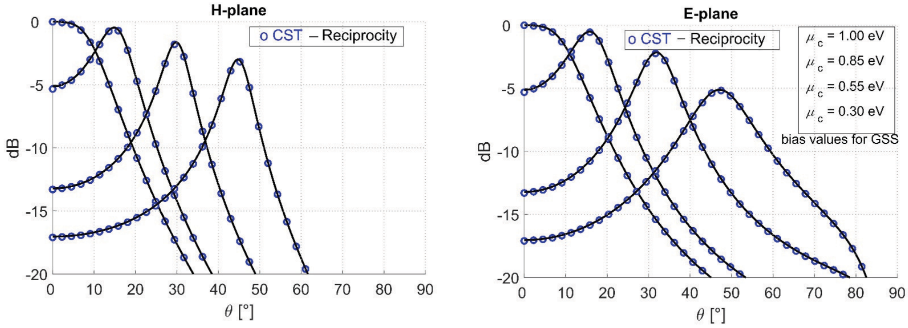

(a) (b)

Figure 4. Radiation patterns in the principal planes for the Graphene-based FPCA in Figure 3: scanning process at a fixed frequency by varying the graphene chemical potential μ_c via voltage bias in (a) the H-plane and (b) the E-plane. More information can be found in [74]. ©2017 IEEE. Reprinted, with permission, from [74].

a number of investigations on different kinds of graphene reconfigurable antennas. Recently, examples of graphene-based reconfigurable 2-D LWAs have also appeared, operating in the THz range and based on patterned graphene HISs [77] or unpatterned graphene sheets above a grounded slab [78] or in a substrate-superstrate configuration [74, 79] (see the structure in Figure 3 and the relevant radiation patterns in the principal planes in Figure 4).

In addition to producing directive far-field patterns, FPCAs can also generate near-feld distributions with *nondiffracting features*, such as Bessel beams, exploiting the radiating features of backward cylindrical leaky waves [80,81], on the basis of the approach originally proposed in [82] and based on standing-wave aperture distributions. Bessel beams can also be produced using *traveling-wave* aperture distributions [83], which can be synthesized, e.g., through radial-line slot antennas [84–86]. Alternatively, they can be synthesized by using 2-D LWAs not belonging to the

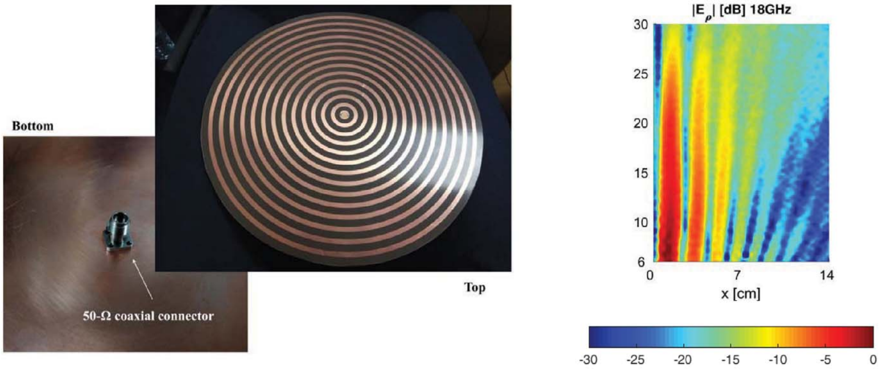

(a) (b)

Figure 5. (a) Bull-eye microstrip antenna for microwave Bessel-beam generation via backward cylindrical leaky waves. (b) Measured radial electric near field at $f = 18$ GHz in a longitudinal plane, showing the desired Bessel-like pattern inside the non-diffracting range. More information can be found in [88]. ©2018 IEEE. Reprinted, with permission, from [88].

class of FPCAs, based on radially periodic structures that cannot be homogenized (hence lack translational invariance) and support *backward* cylindrical leaky waves [87–89] (see Figure 5); similar structures also offer the possibility of *focusing* the radiation in the near field around a prescribed focal point [90,91]. These so-called "*bull-eye*" configurations were first proposed in [92] in the form of concentric microstrip rings for far-field operation in the microwave range; they were subsequently extensively studied by various groups, both at microwaves [93, 94] and, in variants based on metal corrugated structures, at millimeter-wave [95] and terahertz frequencies [96].

4. Holographic antennas

The present section reviews the research on using metasurfaces to transform guided waves into waves propagating in free space for the antenna design. This approach was firstly introduced by Sievenpiper's group at the microwave regime using the holographic concept to design the impedance surfaces [97]. Then, this concept has been used and extended by several other groups adding more physical insight [98–108]. The general geometry is shown in Figure 6a. A planar feeder is illuminating a metasurface composed by subwavelength metallic elements printed over a grounded dielectric slab. If the metasurface is spatially homogenous the structure is able to support eigen guided modes (TM modes for the scalar case or hybrid TM–TE mode for the tensorial one) with propagation constant $k_\rho^{sw} > k_0$. Since the spacing between adjacent elements is subwavelength, it is possible, using a slow variation of the impedance, to modify the wavevector of a guided wave adiabatically. Some techniques have been developed in order to study the propagation of the SW on such inhomogeneous metasurfaces [102–104].

In the scalar case the design is addressed considering as local tangent problem a sinusoidally modulated impedance of the form $Z(x) = jX_s[1 + M\cos(2\pi x/p)]$, where X_s represents the average reactance value, p the period, and $M < 1$ is the modulation index. The field over the metasurface can be expressed as the sum of Floquet modes. However, as demonstrated in [98, 100, 108], to the first order with respect to the small parameter M, only 3 modes contribute significantly to the field. If $k_\rho^{sw} - 2\pi/p < k_0$ one term radiates in free-space in the direction $\theta = \arcsin((k_\rho^{sw} - 2\pi/p)/k_0)$ with an amplitude proportional to M. The antenna is synthesized using an inhomogeneous modulation of the impedance (Figure 6c) obtained by varying the M and

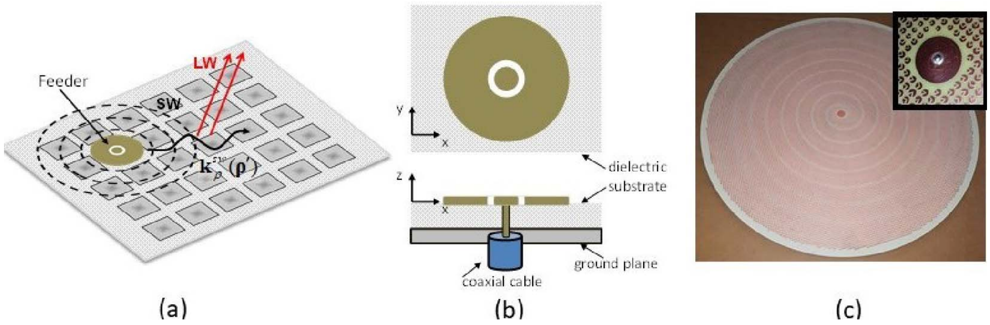

Figure 6. (a) General geometry. A propagating SW is transformed into a LW via impedance modulation. (b) Coaxial Feeder geometry. (c) A metasurface antenna geometry working at 12 GHz designed at Sorbonne Université.

p parameters of the modulation law. The entire metasurface is seen as an equivalent aperture surface magnetic current distribution whose phase and amplitude depend on the local modulation parameters, while the direction is dictated by the source. Using standard aperture antenna theory is it possible to optimize the parameters to obtain the desired radiation pattern. However, the range of different aperture field distributions achievable is limited by the inability to control the direction of the equivalent aperture surface current [100]. The most commonly used incident wave in the literature is the cylindrical SW generated by a coaxial probe (Figure 6b) placed at the center of the metasurface (equivalent magnetic current oriented along ϕ). Single beam circularly polarized antennas have been developed and experimentally validated (Figure 6a) using a spiral dependance of the impedance for the broadside direction [98] while an elongated spiral distribution is needed for tilted beams [100]. Linearly polarized beams have been achieved using some azimuthal phase discontinuity [100,109] in order to compensate in the opposite direction of symmetric current elements with respect to the origin. Multiple modulations have been used to generate beams at different frequencies [110]. Scalar metasurfaces have been also used to design near-field antennas as a Bessel beam [100]. From the scalar nature of the metasurface follows that the TM and TE polarization of the field could be designed separately. This aspect has been used to design polarization-insensitive antennas [111], dual-circularly polarized antenna [112], polarization reconfigurable antennas [113] and to generate different beams using multiple sources [114].

Tensorial metasurface antennas can be used to produce complex radiation patterns taking advantage of the ability to control the current orientation. Energy conservation and reciprocity imply that impedance tensor must be anti-Hermitian. Thus, physical impedances are described only by 3 real parameters. The antenna design is addressed considering as local tangent problem a modulated impedance tensor which elements have the form $Z_i(x) = jX_s^i[1 + M_i\cos(2\pi x/p_i)]$, where each component can have different period. As for the scalar case, the field above the metasurface can be seen as the sum of TM and TE Floquet modes. However, several terms now contribute to the radiated field as shown in [108]. In the first paper on the topic [97], the impedance tensor obtained from the holography principle was not anti-Hermitian, thus the impedance was synthesized using only the anti-Hermitian part of such tensor. This operation leads to non-sinusoidal modulations that can excite undesired radiating Floquet's modes [108]. Later, a different approach was successfully introduced by another group [103], where the SW-field is considered as quasi-TM mode, thus the design is performed using two independent tensor parameters. A third approach based on a local holography principle was introduced in [104], where the whole impedance parameters were used in order to implement a general aperture field distribution. More recently, a numerical optimization method based on the electric field integral

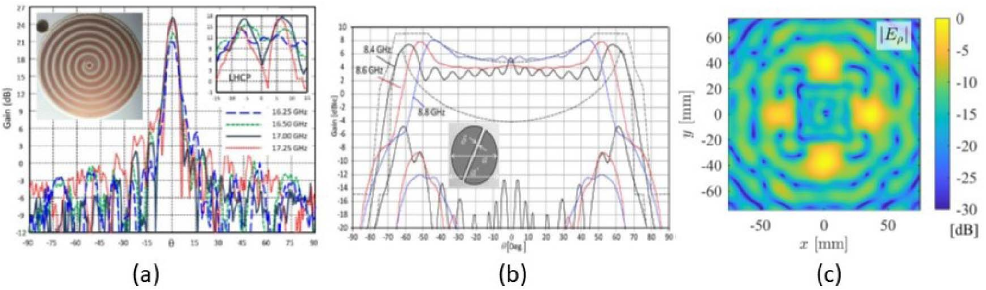

Figure 7. (a) Circularly polarized beam generated by a spiral scalar impedance metasurface. ©2011 IEEE. Reprinted, with permission, from [122]. (b) Isoflux antenna generated by tensorial metasuface. ©2012 IEEE. Reprinted, with permission, from [118]. (c) Near-field shaping and confinement using tensorial metasurface. ©2019 IEEE. Reprinted, with permission, from [121].

equation (EFIE) was successfully used in order to generate numerical results [115].

Single beam antennas have been experimentally validated in [116, 117] (Figure 7a). Numerical results of shaped beam configurations have been presented in [103]. More complex radiation pattern as isoflux [118] or flat-top [104] have been successfully designed (Figure 7b), while multibeam configurations have been presented in [104, 119], and experimentally validated in [120]. In addition, the near-field shaping capability of tensorial metasurface has been experimentally demonstrated in [121] where the energy has been confined in 4 beams (Figure 7c).

5. Parallel plate metasurfaces for antennas

Often, metasurfaces are not directly used in radiation, but rather that to control the propagation of confined waves. Commonly, these metasurfaces are embbeded between parallel plates to avoid any leakage. Once the desired distributions of both phase and amplitude are tailored, it is possible to produce high performance antennas [123]. The unit cells inside of the parallel plate must be adequately designed and distributed in order to produce the required equivalent refractive indexes (isotropic or anisotropic) and impedances [124, 125] that produce the desired phase and amplitude at the end of the metasurface. This type of metasurfaces can be classified as metallic and dielectric.

5.1. *Fully-metallic metasurfaces*

Fully-metallic metasurfaces are used to produce low-loss electromagnetic devices that can handle high power. Dielectric losses are typically high in the millimetre bands, above 30 GHz. Therefore, for high-frequency applications, such as 5G, fully-metallic solutions are preferred [126]. Fully-metallic configurations are also desired in radar systems and defense applications, where the systems must typically handle elevated amount of power [127].

There are two main types of metallic-configurations: bed-of-nails [128, 129] and holey structures [130]. These configurations are illustrated in Figure 8(a). Holey structures are more robust and cost-effective than pins. However, pin-type metasurfaces can achieve higher equivalent refractive indexes, and they do not require of thin air-gaps between layers [131]. The dispersion properties of these two type of structures are illustrated Figure 8(a).

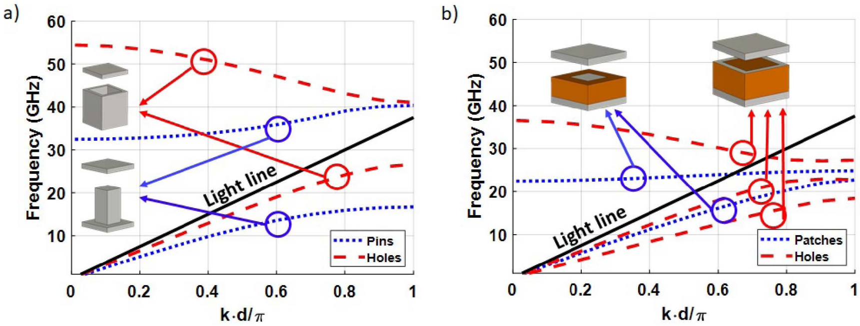

Figure 8. Dispersion diagrams of (a) pin-type and holey metallic metasurfaces, (b) patch- and holey-type dielectric metasurfaces.

5.2. *Dielectric metasurfaces*

For lower frequencies, dielectric metasurfaces are a preferred solution, since they are more cost-effective. Here again, there are two types of dielectric metasurfaces: patch- [132] and holey-type [133]. Patch-type metasurfaces are quite independent of the height between parallel plates. However, holey-type metasurfaces require thin plate gaps to produce high refractive indexes [134]. In general, holey-type structures provide lower losses than patch-type, since the waves will propagate mainly in the air. These two configurations and their dispersion diagrams are illustrated in Figure 8(b).

5.3. *Lens designs*

All these configurations have employed to produce a number of lenses, such as the Maxwell fish-eye lens [135] and its generalized version [136]. However, the most popular lens for antenna designs is the Luneburg lens. A Luneburg lens antenna typically needs a transformation from parallel plate to free-space. There are two methods to produce an efficient radiation: leaky-waves [137] or flares [138].

Among these two, the most used technique is the flare, since leaky-waves are dispersive, meaning that the angle of radiation changes with the frequency [139]. In the case of patch-type metasurfaces, it is difficult to reduce the reflections at the end of the structure since most of the fields are confined in the dielectric slab [140]. This problem does not exist in fully-metallic structures [131] and dielectric holey-type [134]. However, in the case of holey-type structures (metallic or dielectric), the flare may be long to achieve low-level of reflections. This is due to the fact that the air-gap between the metasurface and the ground plane must thin to achieve the required equivalent refractive index [141].

5.4. *Glide-symmetric metasurfaces*

Glide symmetry is a new degree of freedom that has been recently proposed to improve the properties of metasurfaces, for example, to increase the bandwidth and attenuation of stopbands created by periodic structures [142–144]. One periodic structure possesses glide symmetry if it is invariant after a translation and a mirroring [145, 146]. By adding glide symmetry to a metasurface, it is possible to increase its bandwidth of operation, i.e. to reduce its dispersion [147]. Additionally, glide symmetry can be used to increase the equivalent refractive index of periodic structures [131, 141], their anisotropy [148] and their magnetic response [149]. These

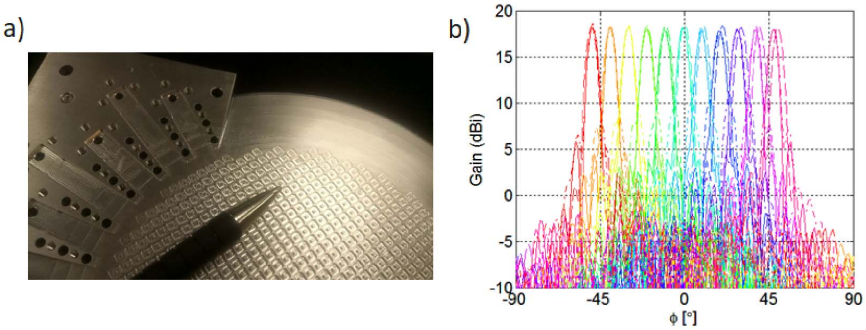

Figure 9. Glide-symmetric metasurface antenna in Ka-band: (a) Photo of the antenna, (b) Radiation patterns at 28 GHz. More information can be found in [141]. ©2018 IEEE. Reprinted, with permission, from [141].

features are beneficial to produce lens antennas. An example of a Luneburg lens antenna made of glide-symmetric metasurfaces is illustrated in Figure 9. This antenna operates in Ka-band and it designed for 5G communications. The antenna is able to produce a extreme angles of radiation with low scan-losses and high efficiency.

6. Conclusions

Metasurfaces have revolutionized the design of electromagnetic devices through tailoring subwavelength structures to shape the electromagnetic field. In this paper, we have reviewed the recent development in metasurface antenna design by introducing the fundamental concepts and presenting the actual state of the art of the physical realizations. Most of the presented examples operate at microwave but the same concept can be used up to visible light.

Starting from high impedance surface antennas, we have discussed how placing a planar antenna in the vicinity of a suitable metasurface could enhance its performances. We introduced how similar approaches could be used to improve the performances of Fabry–Perot cavity antennas and other 2-D leaky wave antennas. Furthermore, we discussed how the wave-front shaping ability of the metasurfaces can be used to design holographic aperture metasurface antennas (based on the conversion of a surface-wave into a radiated one) or to design planar lenses or control the dispersion properties in antenna structures.

With the level of advancements made already, there is a great prospect for the future. In recent years, research has been mainly conducted with the focus to improve the antenna performances using passive metasurfaces. Some active solutions have been presented (using control elements such as varactors, etc...), leading to bulky and expensive devices (complexity and cost proportional to the number of unit cells). The challenge for the next years will be the development of low-cost fully tunable or reconfigurable metasurfaces. This aspect will dramatically improve both antenna and optical beam-forming applications and open up new possibilities for electromagnetic devices.

References

[1] O. Quevedo-Teruel, H. Chen, A. Díaz-Rubio, G. Gok, A. Grbic, G. Minatti, E. Martini, S. Maci, G. V. Eleftheriades, M. Chen, N. I. Zheludev, N. Papasimakis, S. Choudhury, Z. A. Kudyshev, S. Saha, H. Reddy, A. Boltasseva, V. M. Shalaev, A. V. Kildishev, D. Sievenpiper, C. Caloz, A. Alù, Q. He, L. Zhou, G. Valerio, E. Rajo-Iglesias, Z. Sipus, F. Mesa, R. Rodríguez-Berral, F. Medina, V. Asadchy, S. Tretyakov, C. Craeye, "Roadmap on metasurfaces", *J. Opt.* **21** (2019), no. 7, article no. 073002.

[2] B. A. Munk, *Frequency Selective Surfaces Theory and Design*, Wiley Interscience, New York, 1995.

[3] N. Engheta, R. Ziolkowski, *Electromagntic Metamaterials: Physics and Engineering Aspects*, IEE-Wiley, New York, 2006.

[4] A. Patel, A. Grbic, "Effective surface impedance of a printed-circuit tensor impedance surface (pctis)", *IEEE Trans. Microw. Theory Tech.* **61** (2013), no. 4, p. 1403-1413.

[5] C. L. Holloway, E. F. Kuester, J. Gordon, J. O. Hara, J. Booth, D. R. Smith, "An overview of the theory and applications of metasurfaces: the two-dimensional equivalents metamaterials", *IEEE Trans. Antennas Propag.* **54** (2012), no. 2, p. 10-35.

[6] A. Li, S. Singh, D. Sievenpiper, "Metasurfaces and their applications", *Nanophotonics* **7** (2018), no. 6, p. 989-1011.

[7] H. H. Hsiao, C. H. Chu, D. P. Tsai, "Fundamentals and applications of metasurfaces", *Small Methods* **1** (2017), no. 4, article no. 1600064.

[8] S. Gaber, S. H. Zainud-Deen, H. A. E. Malhat, *Analysis and Design of Reflectarrays/Transmitarrays Antennas*, Lambert Academic Publishing, Saarbrücken, 2014.

[9] D. Sievenpiper, L. Zhang, R. F. J. Broas, N. G. Alexopolous, E. Yablonovitch, "High-impedance electromagnetic surfaces with a forbidden frequency band", *IEEE Trans. Microw. Theory Tech.* **47** (1999), no. 11, p. 2059-2074.

[10] A. O. Bah, P. Qin, R. W. Ziolkowski, Y. J. Guo, T. S. Bird, "A wideband low-profile tightly coupled antenna array with a very high figure of merit", *IEEE Trans. Antennas Propag.* **67** (2019), no. 4, p. 2332-2343.

[11] F. Costa, O. Luukkonen, C. R. Simovski, A. Monorchio, S. A. Tretyakov, P. M. de Maagt, "TE surface wave resonances on high-impedance surface based antennas: analysis and modeling", *IEEE Trans. Antennas Propag.* **59** (2011), no. 10, p. 3588-3596.

[12] F. Costa, S. Genovesi, A. Monorchio, "On the bandwidth of high-impedance frequency selective surfaces", *IEEE Antennas Wirel. Propag. Lett.* **8** (2009), p. 1341-1344.

[13] G. Valerio, D. R. Jackson, A. Galli, "Fundamental properties of surface waves in lossless stratified structures", *Proc. R. Soc. A* **466** (2010), no. 2120, p. 2447-2469.

[14] S. R. Best, D. L. Hanna, "Design of a broadband dipole in close proximity to an EBG ground plane", *IEEE Antennas Propag. Mag.* **50** (2008), no. 6, p. 52-64.

[15] G. Bianconi, F. Costa, S. Genovesi, A. Monorchio, "Optimal design of dipole antennas backed by a finite high-impedance screen", *Prog. Electromagn. Res. C* **18** (2011), p. 137-151.

[16] H. Mosallaei, K. Sarabandi, "Antenna miniaturization and bandwidth enhancement using a reactive impedance substrate", *IEEE Trans. Antennas Propag.* **52** (2004), no. 9, p. 2403-2414.

[17] F. Yang, Y. Rahmat-Samii, "Reflection phase characterizations of the EBG ground plane for low profile wire antenna applications", *IEEE Trans. Antennas Propag.* **51** (2003), no. 10, p. 2691-2703.

[18] R. Coccioli, F.-R. Yang, K.-P. Ma, T. Itoh, "Aperture-coupled patch antenna on UC-PBG substrate", *IEEE Trans. Microw. Theory Tech.* **47** (1999), no. 11, p. 2123-2130.

[19] F. Yang, Y. Rahmat-Samii, "Microstrip antennas integrated with electromagnetic band-gap (EBG) structures: a low mutual coupling design for array applications", *IEEE Trans. Antennas Propag.* **51** (2003), no. 10, p. 2936-2946.

[20] R. F. J. Broas, D. F. Sievenpiper, E. Yablonovitch, "An application of high-impedance ground planes to phased array antennas", *IEEE Trans. Antennas Propag.* **53** (2005), no. 4, p. 1377-1381.

[21] M. Li, S. Xiao, B. Wang, "Investigation of using high impedance surfaces for wide-angle scanning arrays", *IEEE Trans. Antennas Propag.* **63** (2015), no. 7, p. 2895-2901.

[22] E. Rajo-Iglesias, O. Quevedo-Teruel, L. Inclan-Sanchez, "Planar soft surfaces and their application to mutual coupling reduction", *IEEE Trans. Antennas Propag.* **57** (2009), no. 12, p. 3852-3859.

[23] F. Yang, Y. Rahmat-Samii, *Electromagnetic Band Gap Structures in Antenna Engineering*, Cambridge University Press, Cambridge, UK, 2009.

[24] Q. Zheng, Y. Fu, N. Yuan, "A novel compact spiral electromagnetic band-gap (EBG) structure", *IEEE Trans. Antennas Propag.* **56** (2008), no. 6, p. 1656-1660.

[25] M. F. Abedin, M. Z. Azad, M. Ali, "Wideband smaller unit-cell planar EBG structures and their application", *IEEE Trans. Antennas Propag.* **56** (2008), no. 3, p. 903-908.

[26] A. Vallecchi, J. R. De Luis, F. Capolino, F. De Flaviis, "Low profile fully planar folded dipole antenna on a high impedance surface", *IEEE Trans. Antennas Propag.* **60** (2012), no. 1, p. 51-62.

[27] N. Engheta, R. W. Ziolkowski, "Innovation and intellectual property rights", in *Metamaterials: Physics and Engineering Explorations*, Whiley, New York, USA, 2006, p. 377-402.

[28] P. Deo, A. Mehta, D. Mirshekar-Syahkal, P. J. Massey, H. Nakano, "Thickness reduction and performance enhancement of steerable square loop antenna using hybrid high impedance surface", *IEEE Trans. Antennas Propag.* **58** (2010), no. 5, p. 1477-1485.

[29] N. Capet, C. Martel, J. Sokoloff, O. Pascal, "Optimum high impedance surface configuration for mutual coupling reduction in small antenna arrays", *Prog. Electromagn. Res. B* **32** (2011), p. 283-297.

[30] J. Sarrazin, A. Lepage, X. Begaud, "Circular high-impedance surfaces characterization", *IEEE Antennas Wirel. Propag. Lett.* **11** (2012), p. 260-263.

[31] M. A. Amiri, C. A. Balanis, C. R. Birtcher, “Analysis, design and measurements of circularly symmetric high-impedance surfaces for loop antenna applications”, *IEEE Trans. Antennas Propag.* **64** (2016), no. 2, p. 618-629.

[32] M. A. Amiri, C. A. Balanis, C. R. Birtcher, “Gain and bandwidth enhancement of a spiral antenna using a circularly symmetric HIS”, *IEEE Antennas Wirel. Propag. Lett.* **16** (2017), p. 1080-1083.

[33] A. Vallecchi, R. J. Langley, A. G. Schuchinsky, “Metasurfaces with interleaved conductors: phenomenology and applications to frequency selective and high impedance surfaces”, *IEEE Trans. Antennas Propag.* **64** (2016), no. 2, p. 599-608.

[34] A. Presse, A. Tarot, “Circuit model of a double-layer artificial magnetic conductor”, *IEEE Antennas Wirel. Propag. Lett.* **15** (2016), p. 1061-1064.

[35] D. J. Kern, D. H. Werner, A. Monorchio, L. Lanuzza, M. J. Wilhelm, “The design synthesis of multiband artificial magnetic conductors using high impedance frequency selective surfaces”, *IEEE Trans. Antennas Propag.* **53** (2005), no. 1, p. 8-17.

[36] H.-H. Xie, Y.-C. Jiao, K. Song, Z. Zhang, “A novel multi-band electromagnetic band-gap structure”, *Prog. Electromagn. Res. Lett.* **9** (2009), p. 67-74.

[37] J. Sarrazin, A.-C. Lepage, X. Begaud, Z. Zhang, “Dual-band artificial magnetic conductor”, *Appl. Phys. A* **109** (2012), p. 1075-1080.

[38] D. Cure, T. M. Weller, F. A. Miranda, “Study of a low-profile 2.4-GHz planar dipole antenna using a high-impedance surface with 1-D varactor tuning”, *IEEE Trans. Antennas Propag.* **61** (2013), no. 2, p. 506-515.

[39] G. von Trentini, “Partially reflecting sheet arrays”, *IRE Trans. Antennas Propag.* **4** (1956), no. 4, p. 666-671.

[40] A. P. Feresidis, J. Vardaxoglou, “High gain planar antenna using optimised partially reflective surfaces”, *IEE Proc.-Microw. Antennas Propag.* **148** (2001), no. 6, p. 345-350.

[41] H. Boutayeb, K. Mahdjoubi, A.-C. Tarot, T. Denidni, “Directivity of an antenna embedded inside a Fabry–Perot cavity: analysis and design”, *Microw. Opt. Technol. Lett.* **48** (2006), no. 1, p. 12-17.

[42] A. Foroozesh, L. Shafai, “Investigation into the effects of the patch-type FSS superstrate on the high-gain cavity resonance antenna design”, *IEEE Trans. Antennas Propag.* **58** (2010), no. 2, p. 258-270.

[43] D. Jackson, N. Alexopoulos, “Gain enhancement methods for printed circuit antennas”, *IEEE Trans. Antennas Propag.* **33** (1985), no. 9, p. 976-987.

[44] D. R. Jackson, A. A. Oliner, “A leaky-wave analysis of the high-gain printed antenna configuration”, *IEEE Trans. Antennas Propag.* **36** (1988), no. 7, p. 905-910.

[45] T. Zhao, D. R. Jackson, J. T. Williams, H.-Y. Yang, A. A. Oliner, “2-d periodic leaky-wave antennas—Part I: metal patch design”, *IEEE Trans. Antennas Propag.* **53** (2005), no. 11, p. 3505-3514.

[46] T. Zhao, D. R. Jackson, J. T. Williams, “2-d periodic leaky-wave antennas—Part II: slot design”, *IEEE Trans. Antennas Propag.* **53** (2005), no. 11, p. 3515-3524.

[47] T. Zhao, D. R. Jackson, J. T. Williams, A. A. Oliner, “General formulas for 2-D leaky-wave antennas”, *IEEE Trans. Antennas Propag.* **53** (2005), no. 11, p. 3525-3533.

[48] G. Lovat, P. Burghignoli, D. R. Jackson, “Fundamental properties and optimization of broadside radiation from uniform leaky-wave antennas”, *IEEE Trans. Antennas Propag.* **54** (2006), no. 5, p. 1442-1452.

[49] A. Ip, D. R. Jackson, “Radiation from cylindrical leaky waves”, *IEEE Trans. Antennas Propag.* **38** (1990), no. 4, p. 482-488.

[50] S. Wang, A. Feresidis, G. Goussetis, J. Vardaxoglou, “Low-profile resonant cavity antenna with artificial magnetic conductor ground plane”, *Electron. Lett.* **40** (2004), no. 7, p. 405-406.

[51] A. P. Feresidis, G. Goussetis, S. Wang, J. C. Vardaxoglou, “Artificial magnetic conductor surfaces and their application to low-profile high-gain planar antennas”, *IEEE Trans. Antennas Propag.* **53** (2005), no. 1, p. 209-215.

[52] S. Wang, A. Feresidis, G. Goussetis, J. Vardaxoglou, “High-gain subwavelength resonant cavity antennas based on metamaterial ground planes”, *IEE Proc.-Microw. Antennas Propag.* **153** (2006), no. 1, p. 1-6.

[53] L. Zhou, H. Li, Y. Qin, Z. Wei, C. Chan, “Directive emissions from subwavelength metamaterial-based cavities”, *Appl. Phys. Lett.* **86** (2005), no. 10, article no. 101101.

[54] A. Ourir, A. de Lustrac, J.-M. Lourtioz, “All-metamaterial-based subwavelength cavities ($\lambda/60$) for ultrathin directive antennas”, *Appl. Phys. Lett.* **88** (2006), no. 8, article no. 084103.

[55] A. Feresidis, J. Vardaxoglou, “A broadband high-gain resonant cavity antenna with single feed”, in *2006 First European Conference on Antennas and Propagation*, IEEE, 2006, p. 1-5.

[56] C. Mateo-Segura, A. P. Feresidis, G. Goussetis, “Bandwidth enhancement of 2-D leaky-wave antennas with double-layer periodic surfaces”, *IEEE Trans. Antennas Propag.* **62** (2014), no. 2, p. 586-593.

[57] K. Konstantinidis, A. P. Feresidis, P. S. Hall, “Multilayer partially reflective surfaces for broadband Fabry–Perot cavity antennas”, *IEEE Trans. Antennas Propag.* **62** (2014), no. 7, p. 3474-3481.

[58] L. Moustafa, B. Jecko, “Broadband high gain compact resonator antennas using combined FSS”, in *2008 IEEE Antennas Propagation Society International Symposium*, IEEE, San Diego, CA, USA, 2008, p. 1-4.

[59] Y. Ge, K. P. Esselle, T. S. Bird, “The use of simple thin partially reflective surfaces with positive reflection phase

gradients to design, wideband, low-profile EBG resonator antennas", *IEEE Trans. Antennas Propag.* **60** (2012), no. 2, p. 743-750.

[60] L. Moustafa, B. Jecko, "EBG structure with wide defect band for broadband cavity antenna applications", *IEEE Antennas Wirel. Propag. Lett.* **7** (2008), p. 693-696.

[61] R. M. Hashmi, B. A. Zeb, K. P. Esselle, "Wideband high-gain EBG resonator antennas with small footprints and all-dielectric superstructures", *IEEE Trans. Antennas Propag.* **62** (2014), no. 6, p. 2970-2977.

[62] A. A. Baba, R. M. Hashmi, K. P. Esselle, A. R. Weily, "Compact high-gain antenna with simple all-dielectric partially reflecting surface", *IEEE Trans. Antennas Propag.* **66** (2018), no. 8, p. 4343-4348.

[63] A. Hosseini, F. Capolino, D. R. Jackson, "Leaky-wave explanation of gain-bandwidth-enhanced Fabry–Perot cavity antennas formed by a thick multilayer partially-reflective surface", in *2015 IEEE International Symposium on Antennas Propagation & USNC/URSI National Radio Science Meeting*, IEEE, Vancouver, BC, Canada, 2015, p. 1090-1091.

[64] A. T. Almutawa, A. Hosseini, D. R. Jackson, F. Capolino, "Leaky-wave analysis of wideband planar Fabry–Perot cavity antennas formed by a thick PRS", *IEEE Trans. Antennas Propag.* **67** (2019), no. 8, p. 5163-5175.

[65] P. Burghignoli, G. Lovat, F. Capolino, D. R. Jackson, D. R. Wilton, "Highly polarized directive radiation from a Fabry–Pérot cavity leaky-wave antenna based on a metal strip grating", *IEEE Trans. Antennas Propag.* **58** (2010), no. 12, p. 3873-3883.

[66] D. Comite, P. Baccarelli, P. Burghignoli, A. Galli, "Omnidirectional 2-D leaky-wave antennas with reconfigurable polarization", *IEEE Antennas Wirel. Propag. Lett.* **16** (2017), p. 2354-2357.

[67] D. Sievenpiper, J. Schaffner, J. Lee, S. Livingston, "A steerable leaky-wave antenna using a tunable impedance ground plane", *IEEE Antennas Wirel. Propag. Lett.* **1** (2002), p. 179-182.

[68] D. F. Sievenpiper, "Forward and backward leaky wave radiation with large effective aperture from an electronically tunable textured surface", *IEEE Trans. Antennas Propag.* **53** (2005), no. 1, p. 236-247.

[69] A. Ourir, S. Burokur, A. de Lustrac, "Electronically reconfigurable metamaterial for compact directive cavity antennas", *Electron. Lett.* **43** (2007), no. 13, p. 698-700.

[70] F. Costa, A. Monorchio, S. Talarico, F. M. Valeri, "An active high-impedance surface for low-profile tunable and steerable antennas", *IEEE Antennas Wirel. Propag. Lett.* **7** (2008), p. 676-680.

[71] F. Costa, A. Monorchio, "Design of subwavelength tunable and steerable Fabry–Perot/leaky wave antennas", *Prog. Electromagn. Res.* **111** (2011), p. 467-481.

[72] R. Guzmán-Quirós, A. R. Weily, J. L. Gómez-Tornero, Y. J. Guo, "A Fabry–Pérot antenna with two-dimensional electronic beam scanning", *IEEE Trans. Antennas Propag.* **64** (2016), no. 4, p. 1536-1541.

[73] A. R. Weily, T. S. Bird, Y. J. Guo, "A reconfigurable high-gain partially reflecting surface antenna", *IEEE Trans. Antennas Propag.* **56** (2008), no. 11, p. 3382-3390.

[74] W. Fuscaldo, P. Burghignoli, P. Baccarelli, A. Galli, "Graphene Fabry–Pérot cavity leaky-wave antennas: plasmonic versus nonplasmonic solutions", *IEEE Trans. Antennas Propag.* **65** (2017), no. 4, p. 1651-1660.

[75] G. Lovat, P. Burghignoli, S. Celozzi, "A tunable ferroelectric antenna for fixed-frequency scanning applications", *IEEE Antennas Wirel. Propag. Lett.* **5** (2006), p. 353-356.

[76] W. Fuscaldo, S. Tofani, D. C. Zografopoulos, P. Baccarelli, P. Burghignoli, R. Beccherelli, A. Galli, "Tunable Fabry–Pérot cavity THz antenna based on leaky-wave propagation in nematic liquid crystals", *IEEE Antennas Wirel. Propag. Lett.* **16** (2017), p. 2046-2049.

[77] X.-C. Wang, W.-S. Zhao, J. Hu, W.-Y. Yin, "Reconfigurable terahertz leaky-wave antenna using graphene-based high-impedance surface", *IEEE Trans. Nanotechnol.* **14** (2015), no. 1, p. 62-69.

[78] W. Fuscaldo, P. Burghignoli, P. Baccarelli, A. Galli, "Complex mode spectra of graphene-based planar structures for THz applications", *J. Infrared Millimeter Terahertz Waves* **36** (2015), no. 8, p. 720-733.

[79] W. Fuscaldo, P. Burghignoli, P. Baccarelli, A. Galli, "A reconfigurable substrate–superstrate graphene-based leaky-wave THz antenna", *IEEE Antennas Wirel. Propag. Lett.* **15** (2016), p. 1545-1548.

[80] M. Ettorre, A. Grbic, "Generation of propagating Bessel beams using leaky-wave modes", *IEEE Trans. Antennas Propag.* **60** (2012), no. 8, p. 3605-3613.

[81] W. Fuscaldo, G. Valerio, A. Galli, R. Sauleau, A. Grbic, M. Ettorre, "Higher-order leaky-mode Bessel-beam launcher", *IEEE Trans. Antennas Propag.* **64** (2016), no. 3, p. 904-913.

[82] S. Chávez-Cerda, "A new approach to Bessel beams", *J. Modern Opt.* **46** (1999), no. 6, p. 923-930.

[83] M. Albani, S. Pavone, M. Casaletti, M. Ettorre, "Generation of non-diffractive Bessel beams by inward cylindrical traveling wave aperture distributions", *Opt. Express* **22** (2014), no. 15, p. 18354-18364.

[84] A. Mazzinghi, M. Balma, D. Devona, G. Guarnieri, G. Mauriello, M. Albani, A. Freni, "Large depth of field pseudo–Bessel beam generation with a RLSA antenna", *IEEE Trans. Antennas Propag.* **62** (2014), no. 8, p. 3911-3919.

[85] M. Ettorre, S. C. Pavone, M. Casaletti, M. Albani, "Experimental validation of Bessel beam generation using an inward Hankel aperture distribution", *IEEE Trans. Antennas Propag.* **63** (2015), no. 6, p. 2539-2544.

[86] S. Pavone, M. Ettorre, M. Casaletti, M. Albani, "Transverse circular-polarized bessel beam generation by inward cylindrical aperture distribution", *Opt. Express* **24** (2016), no. 10, p. 11103-11111.

[87] B. G. Cai, Y. B. Li, W. X. Jiang, Q. Cheng, T. J. Cui, “Generation of spatial Bessel beams using holographic metasurface”, *Opt. Express* **23** (2015), no. 6, p. 7593-7601.

[88] D. Comite, W. Fuscaldo, S. K. Podilchak, P. D. Hílario-Re, V. Gómez-Guillamón Buendía, P. Burghignoli, P. Baccarelli, A. Galli, “Radially periodic leaky-wave antenna for Bessel beam generation over a wide-frequency range”, *IEEE Trans. Antennas Propag.* **66** (2018), no. 6, p. 2828-2843.

[89] W. Fuscaldo, D. Comite, A. Boesso, P. Baccarelli, P. Burghignoli, A. Galli, “Focusing leaky waves: a class of electromagnetic localized waves with complex spectra”, *Phys. Rev. A* **9** (2018), no. 5, article no. 054005.

[90] J. L. Gómez-Tornero, D. Blanco, E. Rajo-Iglesias, N. Llombart, “Holographic surface leaky-wave lenses with circularly-polarized focused near-fields—Part I: concept, design and analysis theory”, *IEEE Trans. Antennas Propag.* **61** (2013), no. 7, p. 3475-3485.

[91] D. Blanco, J. L. Gómez-Tornero, E. Rajo-Iglesias, N. Llombart, “Holographic surface leaky-wave lenses with circularly-polarized focused near-fields—Part II: experiments and description of frequency steering of focal length”, *IEEE Trans. Antennas Propag.* **61** (2013), no. 7, p. 3486-3494.

[92] P. Baccarelli, P. Burghignoli, G. Lovat, S. Paulotto, “A novel printed leaky-wave ‘bull-eye’ antenna with suppressed surface-wave excitation”, in *IEEE Antennas Propagation Society Symposium*, vol. 1, IEEE, Monterey, CA, USA, 2004, p. 1078-1081.

[93] S. Podilchak, Y. Antar, A. Freundorfer, P. Baccarelli, P. Burghignoli, S. Paulotto, G. Lovat, “Planar antenna for continuous beam scanning and broadside radiation by selective surface wave suppression”, *Electron. Lett.* **46** (2010), no. 9, p. 613-614.

[94] S. K. Podilchak, P. Baccarelli, P. Burghignoli, A. P. Freundorfer, Y. M. Antar, “Analysis and design of annular microstrip-based planar periodic leaky-wave antennas”, *IEEE Trans. Antennas Propag.* **62** (2014), no. 6, p. 2978-2991.

[95] U. Beaskoetxea, V. Pacheco-Peña, B. Orazbayev, T. Akalin, S. Maci, M. Navarro-Cía, M. Beruete, “77-GHz high-gain bull’s-eye antenna with sinusoidal profile”, *IEEE Antennas Wirel. Propag. Lett.* **14** (2015), p. 205-208.

[96] M. Beruete, U. Beaskoetxea, M. Zehar, A. Agrawal, S. Liu, K. Blary, A. Chahadih, X.-L. Han, M. Navarro-Cía, D. E. Salinas *et al.*, “Terahertz corrugated and bull’s-eye antennas”, *IEEE Trans. Terahertz Science and Technol.* **3** (2013), no. 6, p. 740-747.

[97] B. H. Fong, J. S. Colburn, J. J. Ottusch, J. L. Visher, D. F. Sievenpiper, “Scalar and tensor holographic artificial impedance surfaces”, *IEEE Trans. Antennas Propag.* **58** (2010), no. 10, p. 3212-3221.

[98] G. Minatti, F. Caminita, M. Casaletti, S. Maci, “Spiral leaky-wave antennas based on modulated surface impedance”, *IEEE Trans. Antennas Propag.* **59** (2011), no. 12, p. 4436-4444.

[99] A. M. Patel, A. Grbic, “A printed leaky-wave antenna based on a sinusoidally-modulated reactance surface”, *IEEE Trans. Antennas Propag.* **59** (2011), no. 6, p. 2087-2096.

[100] M. Casaletti, M. Śmierzchalski, M. Ettorre, R. Sauleau, N. Capet, “Polarized beams using scalar metasurfaces”, *IEEE Trans. Antennas Propag.* **64** (2016), no. 8, p. 3391-3400.

[101] A. M. Patel, A. Grbic, “The effects of spatial dispersion on power flow along a printed-circuit tensor impedance surface”, *IEEE Trans. Antennas Propag.* **62** (2014), no. 3, p. 1464-1469.

[102] E. Martini, M. Mencagli, D. Gonzalez-Ovejero, S. Maci, “Flat optics for surface waves”, *IEEE Trans. Antennas Propag.* **64** (2016), no. 1, p. 155-166.

[103] G. Minatti, F. Caminita, E. Martini, M. Sabbadini, S. Maci, “Synthesis of modulated-metasurface antennas with amplitude phase and polarization control”, *IEEE Trans. Antennas Propag.* **64** (2016), no. 9, p. 3907-3919.

[104] M. Teniou, H. Roussel, N. Capet, G. Piau, M. Casaletti, “Implementation of radiating aperture field distribution using tensorial metasurfaces”, *IEEE Trans. Antennas Propag.* **65** (2017), no. 11, p. 5895-5907.

[105] G. Minatti, F. Caminita, E. Martini, S. Maci, “Flat optics for leaky-waves on modulated metasurfaces: adiabatic floquet-wave analysis”, *IEEE Trans. Antennas Propag.* **64** (2016), no. 9, p. 3896-3906.

[106] G. Minatti, E. Martini, S. Maci, “Efficiency of metasurface antennas”, *IEEE Trans. Antennas Propag.* **65** (2017), no. 4, p. 1532-1541.

[107] G. Minatti, M. Faenzi, M. Sabbadini, S. Maci, “Bandwidth of gain in metasurface antennas”, *IEEE Trans. Antennas Propag.* **65** (2017), no. 6, p. 2836-2842.

[108] M. Casaletti, “Guided waves on scalar and tensorial reactance surfaces modulated by periodic functions: a circuital approach”, *IEEE Access* **7** (2019), p. 68823-68836.

[109] S. Pandi, C. A. Balanis, C. R. Birtcher, “Design of scalar impedance holographic metasurfaces for antenna beam formation with desired polarization”, *IEEE Trans. Antennas Propag.* **63** (2015), no. 7, p. 3016-3024.

[110] Y. Li, A. Li, T. Cui, D. F. Sievenpiper, “Multiwavelength multiplexing hologram designed using impedance metasurfaces”, *IEEE Trans. Antennas Propag.* **66** (2018), no. 11, p. 6408-6413.

[111] M. Li, S. Xiao, D. F. Sievenpiper, “Polarization-insensitive holographic surfaces with broadside radiation”, *IEEE Trans. Antennas Propag.* **64** (2016), no. 12, p. 5272-5280.

[112] A. T. Pereda, F. Caminita, E. Martini, I. Ederra, J. Teniente, J. C. Iriarte, R. Gonzalo, S. Maci, “Experimental validation

of a Ku-band dual-circularly polarized metasurface antenna", *IEEE Trans. Antennas Propag.* **66** (2018), no. 3, p. 1153-1159.

[113] M. Li, M. Tang, S. Xiao, "Design of a LP, RHCP and LHCP polarization-reconfigurable holographic antenna", *IEEE Access* **7** (2019), p. 82776-82784.

[114] S. Ramalingam, C. A. Balanis, C. R. Birtcher, H. N. Shaman, "Polarization-diverse holographic metasurfaces", *IEEE Antennas Wirel. Propag. Lett.* **18** (2019), no. 2, p. 264-268.

[115] M. Bodehou, C. Craeye, E. Martini, I. Huynen, "A quasi-direct method for the surface impedance design of modulated metasurface antennas", *IEEE Trans. Antennas Propag.* **67** (2019), no. 1, p. 24-36.

[116] M. Faenzi, F. Caminita, E. Martini, P. De Vita, G. Minatti, M. Sabbadini, S. Maci, "Realization and measurement of broadside beam modulated metasurface antennas", *IEEE Antennas Wirel. Propag. Lett.* **15** (2016), p. 610-613.

[117] M. Teniou, H. Roussel, M. Serhir, N. Capet, G.-P. Piau, M. Casaletti, "Tensorial metasurface antennas radiating polarized beams based on aperture field implementation", *Int. J. Microw. Wirel. Technol.* **10** (2018), no. 2, p. 161-168.

[118] G. Minatti, S. Maci, P. De Vita, A. Freni, M. Sabbadini, "A circularly-polarized isoflux antenna based on anisotropic metasurface", *IEEE Trans. Antennas Propag.* **60** (2012), no. 11, p. 4998-5009.

[119] D. Gonzalez-Ovejero, G. Minatti, G. Chattopadhyay, S. Maci, "Multibeam by metasurface antennas", *IEEE Trans. Antennas Propag.* **65** (2017), no. 6, p. 2923-2930.

[120] M. Teniou, H. Roussel, M. Serhir, N. Capet, G. Piau, M. Casaletti, "Experimental validation of tensorial metasurfaces for the implementation of radiating aperture field distributions", *IEEE Trans. Antennas Propag.* **67** (2019), no. 7, p. 4901-4906.

[121] I. Iliopoulos, M. Teniou, M. Casaletti, P. Potier, P. Pouliguen, R. Sauleau, M. Ettorre, "Near-field multi-beam generation by tensorial metasurfaces", *IEEE Trans. Antennas Propag.* **67** (2019), no. 9, p. 6068-6075.

[122] S. Maci, G. Minatti, M. Casaletti, M. Bosiljevac, "Metasurfing: addressing waves on impenetrable metasurfaces", *IEEE Antennas Wirel. Propag. Lett.* **10** (2011), p. 1499-1502.

[123] G. Peeler, D. Archer, "A two-dimensional microwave Luneberg lens", *Trans. IRE Professional Group on Antennas Propag.* **1** (1953), no. 1, p. 12-23.

[124] K. Sato, H. Ujiie, "A plate Luneberg lens with the permittivity distribution controlled by hole density", *Electron. Commun. Jpn. (Part I: Communications)* **85** (2002), no. 9, p. 1-12.

[125] L. Xue, V. F. Fusco, "24 ghz automotive radar planar Luneburg lens", *IET Microw. Antennas Propag.* **1** (2007), no. 3, p. 624-628.

[126] O. Quevedo-Teruel, M. Ebrahimpouri, F. Ghasemifard, "Lens antennas for 5G communications systems", *IEEE Commun. Mag.* **56** (2018), no. 7, p. 36-41.

[127] R. F. Rinehart, "A solution of the problem of rapid scanning for radar antennae", *J. Appl. Phys.* **19** (1948), no. 9, p. 860-862.

[128] M. G. Silveirinha, C. A. Fernandes, J. R. Costa, "Electromagnetic characterization of textured surfaces formed by metallic pins", *IEEE Trans. Antennas Propag.* **56** (2008), no. 2, p. 405-415.

[129] Y.-J. Park, W. Wiesbeck, "Angular independency of a parallel-plate luneburg lens with hexagonal lattice and circular metal posts", *IEEE Antennas Wirel. Propag. Lett.* **1** (2002), p. 128-130.

[130] C. Walter, "Surface-wave Luneberg lens antennas", *IRE Trans. Antennas Propag.* **8** (1960), no. 5, p. 508-515.

[131] O. Quevedo-Teruel, M. Ebrahimpouri, M. Ng Mou Kehn, "Ultrawideband metasurface lenses based on off-shifted opposite layers", *IEEE Antennas Wirel. Propag. Lett.* **15** (2016), p. 484-487.

[132] O. Luukkonen, C. Simovski, G. Granet, G. Goussetis, D. Lioubtchenko, A. V. Raisanen, S. A. Tretyakov, "Simple and accurate analytical model of planar grids and high-impedance surfaces comprising metal strips or patches", *IEEE Trans. Antennas Propag.* **56** (2008), no. 6, p. 1624-1632.

[133] L. Xue, V. F. Fusco, "Printed holey plate Luneburg lens", *Microw. Opt. Technol. Lett.* **50** (2008), no. 2, p. 378-380.

[134] C. D. Diallo, O. Quevedo-Teruel, G. Valerio, H. Legay, R. Sauleau, "Parallel-plate-waveguide Luneburg lens through a holey plate metasurface", in *2015 9th European Conference on Antennas Propagation (EuCAP)*, IEEE, 2015, p. 1-2.

[135] S. Maci, G. Minatti, M. Casaletti, M. Bosiljevac, "Metasurfing: addressing waves on impenetrable metasurfaces", *IEEE Antennas Wirel. Propag. Lett.* **10** (2011), p. 1499-1502.

[136] D. R. Prado, A. V. Osipov, O. Quevedo-Teruel, "Implementation of transformed lenses in bed of nails reducing refractive index maximum value and sub-unity regions", *Opt. Lett.* **40** (2015), no. 6, p. 926-929.

[137] M. Ettorre, R. Sauleau, L. Le Coq, "Multi-beam multi-layer leaky-wave SIW pillbox antenna for millimeter-wave applications", *IEEE Trans. Antennas Propag.* **59** (2011), no. 4, p. 1093-1100.

[138] C. Pfeiffer, A. Grbic, A. printed, "broadband Luneburg lens antenna", *IEEE Trans. Antennas Propag.* **58** (2010), no. 9, p. 3055-3059.

[139] L. Wang, J. L. Gomez-Tornero, E. Rajo-Iglesias, O. Quevedo-Teruel, "Low-dispersive leaky-wave antenna integrated in groove gap waveguide technology", *IEEE Trans. Antennas Propag.* **66** (2018), no. 11, p. 5727-5736.

[140] M. Bosiljevac, M. Casaletti, F. Caminita, Z. Sipus, S. Maci, "Non-uniform metasurface Luneburg lens antenna design", *IEEE Trans. Antennas Propag.* **60** (2012), no. 9, p. 4065-4073.

[141] O. Quevedo-Teruel, J. Miao, M. Mattsson, A. Algaba-Brazalez, M. Johansson, L. Manholm, "Glide-symmetric fully

metallic Luneburg lens for 5G communications at Ka-band", *IEEE Antennas Wirel. Propag. Lett.* **17** (2018), no. 9, p. 1588-1592.

[142] M. Ebrahimpouri, E. Rajo-Iglesias, Z. Sipus, O. Quevedo-Teruel, "Cost-effective gap waveguide technology based on glide-symmetric holey EBG structures", *IEEE Trans. Microw. Theory Tech.* **66** (2018), no. 2, p. 927-934.

[143] M. Ebrahimpouri, A. Algaba Brazalez, L. Manholm, O. Quevedo-Teruel, "Using glide-symmetric holes to reduce leakage between waveguide flanges", *IEEE Microw. Wirel. Components Lett.* **28** (2018), no. 6, p. 473-475.

[144] A. Monje-Real, N. J. G. Fonseca, O. Zetterstrom, E. Pucci, O. Quevedo-Teruel, "Holey glide-symmetric filters for 5G at millimeter-wave frequencies", *IEEE Microw. Wirel. Components Lett.* **30** (2020), no. 1, p. 31-34.

[145] G. Valerio, F. Ghasemifard, Z. Sipus, O. Quevedo-Teruel, "Glide-symmetric all-metal holey metasurfaces for low-dispersive artificial materials: modeling and properties", *IEEE Trans. Microw. Theory Tech.* **66** (2018), no. 7, p. 3210-3223.

[146] F. Ghasemifard, M. Norgren, O. Quevedo-Teruel, G. Valerio, "Analyzing glide-symmetric holey metasurfaces using a generalized Floquet theorem", *IEEE Access* **6** (2018), p. 71743-71750.

[147] M. Camacho, R. C. Mitchell-Thomas, A. P. Hibbins, J. R. Sambles, O. Quevedo-Teruel, "Mimicking glide symmetry dispersion with coupled slot metasurfaces", *Appl. Phys. Lett.* **111** (2017), no. 12, article no. 121603.

[148] M. Ebrahimpouri, O. Quevedo-Teruel, "Ultrawideband anisotropic glide-symmetric metasurfaces", *IEEE Antennas Wirel. Propag. Lett.* **18** (2019), no. 8, p. 1547-1551.

[149] M. Ebrahimpouri, L. F. Herran, O. Quevedo-Teruel, "Wide-angle impedance matching using glide-symmetric metasurfaces", *IEEE Microw. Wirel. Compon. Lett.* **30** (2020), no. 1, p. 8-11.

Comptes Rendus
Physique
2020, 21, nº 7-8, p. 677-711
`https://doi.org/10.5802/crphys.19`

Metamaterials 2 / *Métamatériaux 2*

Properties of waveguides filled with anisotropic metamaterials

Propriétés de guides d'ondes constitués d'un métamatériau anisotrope

Abhinav Bhardwaj[a], **Dheeraj Pratap**[b], **Mitchell Semple**[c], **Ashwin K. Iyer**[c],
Arun M. Jayannavar[d] **and S. Anantha Ramakrishna**[*, e, f]

[a] Department of Electrical Engineering, Indian Institute of Technology Kanpur, Kanpur, 208016, India

[b] Biomedical Instrumentation Division, CSIR — Central Scientific Instruments Organisation, Sector-30C, Chandigarh 160030, India

[c] Department of Electrical and Computer Engineering, University of Alberta Edmonton, Alberta T6G2V4, Canada

[d] Institute of Physics, Sachivalaya marg, Bhubaneswar, 751005, India

[e] CSIR — Central Scientific Instruments Organisation, Sector-30C, Chandigarh 160030, India

[f] Department of Physics, Indian Institute of Technology Kanpur, Kanpur, 208016, India

E-mails: Abhinavb@iitk.ac.in (A. Bhardwaj), dheeraj.pratap@csio.res.in (D. Pratap), msemple@ualberta.ca (M. Semple), iyer@ece.ualberta.ca (A. K. Iyer), jayan@iopb.res.in (A. M. Jayannavar), sar@iitk.ac.in (S. A. Ramakrishna)

Abstract. Metamaterials are artificially structured composite materials that show unusual properties not usually available in natural materials. In general, metamaterial structures and properties are anisotropic. A waveguide filled with an anisotropic metamaterial shows unique properties not achievable in conventional waveguides, such as propagation of backward waves and modes below the cut-off frequencies of the conventional fundamental mode, zero group velocity etc. The waveguide filler material can be anisotropic with the tensorial permittivity and permeability components having positive or negative values, and combinations thereof, giving rise to a rich variety of phenomena. Further, modes in a cylindrical waveguide filled with a hyperbolic metamaterial are described by unusual Bessel modes of complex orders. In many situations, the wave propagating region is isotropic, and it is enclosed by anisotropic metamaterials with different thicknesses and contrarily the propagating region is might be anisotropic that is enclosed by isotropic in some other situations. Various metamaterial waveguide geometries like a pair of parallel plates, waveguides with rectangular or cylindrical cross-section filled with anisotropic metamaterials as well as hollow-core waveguides with metamaterial claddings or linings have been demonstrated experimentally. The anisotropy can

---

[*] Corresponding author.

ISSN (electronic) : 1878-1535 `https://comptes-rendus.academie-sciences.fr/physique/`

be uniaxial or biaxial depending on the orientation of structure. Here we review the advances in the theory and applications of waveguides filled with subwavelength structured metamaterials with anisotropic or even hyperbolic properties across the electromagnetic spectrum. By examining the field behaviour in such waveguides, connection is made to the extraordinary transmission of light through arrays of subwavelength sized apertures in a metallic screen. Potential applications range from enhanced MRI imaging and electromagnetic shielding at radio frequencies to intriguing imaging applications and efficient coupling of the emitted radiation from small sources into waveguides at optical frequencies.

Résumé. Les métamatériaux sont des matériaux composites structurés de manière artificielle qui possèdent des propriétés que l'on ne trouve pas à l'état naturel. En général, les propriétés structurelles des métamatériaux sont anisotropes. Un guide d'ondes constitué d'un métamatériau possède des propriétés uniques inatteignables dans des guides d'ondes conventionnels, telles que la propagation d'onde rétrogrades et des modes sous les fréquences de coupure du mode fondamental d'un guide d'ondes conventionnel, une vitesse de groupe nulle etc. Le matériau constituant le guide d'ondes peut être anisotrope avec les éléments (ou des combinaisons d'éléments) des tenseurs de permittivité et perméabilité qui prennent des valeurs positives ou négatives, ce qui donne lieu à une riche variété de phénomènes. Par ailleurs, les modes d'un guide d'ondes cylindrique constitué d'un métamatériau hyperbolique sont décrits par des fonctions de Bessel inhabituelles présentant des ordres complexes. Dans de nombreuses situations, la région siège de la propagation d'ondes est isotrope, et est entourée de métamatériaux anisotropes avec différentes épaisseurs et inversement. Diverses géométries de guides d'ondes en métamatériaux tels que des paires de plaques parallèles, des guides rectangulaires et cylindriques constitués de milieux anisotropes, ainsi que des guides d'ondes à cœur creux avec une gaine en métamatériaux ou des *linings* ont été démontrés expérimentalement. L'anisotropie peut être uniaxe ou biaxe en fonction de l'orientation de la structure. Nous faisons un état de l'art sur les avancées dans la théorie et les applications des guides d'ondes constitués de métamatériaux avec une structuration sub-longueur d'onde dont les propriétés sont anisotropes ou même hyperboliques sur le spectre électromagnétique. En examinant le comportement du champ dans ce type de guides d'ondes, un lien est établi avec la théorie de la transmission extraordinaire de la lumière à travers des réseaux de trous sub-longueur d'onde dans un écran métallique. Les applications potentielles vont de l'imagerie médicale à résonance magnétique améliorée au bouclier électromagnétique aux fréquences radio en passant par des applications étonnantes en imagerie et au couplage efficace des émissions de petites sources avec des guides d'ondes aux fréquences optiques.

Keywords. Metamaterials, Structured waveguides, Anisotropic materials, Hyperbolic dispersion, Split ring resonator, Thin wire media.

Mots-clés. Métamatériaux, Guides d'ondes structurés, Matériaux anisotropes, Dispersion hyperbolique, Résonateur à anneau fendu, Matériaux en fils métalliques minces.

1. Introduction

Ever since Sir John Pendry gave recipes [1, 2] to generate composite media with negative effective parameters like dielectric permittivity and magnetic permeability at any given frequency, the electromagnetics and optics of structured composite media have been among the most popular topics in the past twenty years. These composite metal-dielectric materials, commonly called metamaterials, typically had small sub-wavelength sized units cells, and the composites could be described by effective medium theories. Veselago first proposed a negative refractive index medium as a material with simultaneously negative permittivity and permeability and treated it as an isotropic medium [3]. During the first decades of this century, many of the fundamental aspects of such media were understood and novel phenomena such as negative refraction [4], image resolution without any limit [5] and several novel effects were experimentally realised in structured composite media. Use of the most modern techniques of micro and nano fabrication enabled the demonstration of these effects from microwave frequencies up to optical frequencies [6, 7]. While much of the theory initially dealt with isotropic metamaterials (composite structure), almost all the fabricated metamaterials were anisotropic [8]. This was partially caused by the severe difficulty of assembling isotropic metamaterials, particularly at high frequencies, when the wavelength of radiation and the corresponding structural sizes become micrometric or even nanometrically small in size. Further, the requirement of an isotropic medium was not necessary for realizing many effects. It was further noted that anisotropic metamaterials could easily have one or two diagonal components of the permittivity or the permeability tensor becoming negative, while the others were positive. These tensors with indefinite signs resulted in the dispersion equations changing their form qualitatively from elliptic to hyperbolic equations [9, 10]. This was a new effect in optics and electromagnetism, where such dispersions lead to qualitatively new phenomena such as the hyperlens [10], and such media had infinities in the local density of states [11]. Thus, understanding the new possible effects possible in anisotropic media and hyperbolic media became imperative as metamaterials that had such properties became possible to fabricate.

Propagation of electromagnetic waves in a waveguide is well understood with the optical fiber becoming probably the most commonly used example of a waveguide. With the advent of metamaterials with exotic properties, researchers naturally investigated the properties of waveguides filled with metamaterials, particularly negative refractive index materials [12–16]. Waveguides filled with metamaterials could support propagation of electromagnetic modes with strange properties such as zero or negative group velocity, modes below the cutoff frequencies of the fundamental modes, and the absence of a fundamental mode [16–18]. These investigations naturally turned to the study of waveguides filled with anisotropic/hyperbolic metamaterials. Some interesting effects such as the propagation of modes well below the conventional cutoff were discovered, which were attractive for possibilities of miniaturization of radio frequency (RF) waveguide components, particularly in the context of magnetic resonance imaging (MRI) [17, 19].

At high frequencies such as optical and infrared frequencies, while there were a few theoretical studies [14, 16, 20], one was faced with the ostensibly impossible task of assembling millions or billions of micro/nano structures into microscopic volumes in an ordered fashion. Following the conventional techniques of drawing photonic crystal fibers [21], researchers attempted to draw fibers with embedded structural units such as metallic split ring resonators [22] or coaxial thin metallic wires [23, 24] for operation at THz frequencies. The first successful nanostructured metamaterial fiber for optical frequencies was realized by Pratap *et al.* [13], where they anodized an aluminum wire to successfully form a microtube of nanoporous alumina with radially emanating pores that could be filled electrolytically with plasmonic metals. This made waveguides filled with cylindrically symmetric anisotropic media realistically possible. Such waveguides were shown to support novel propagating modes described by unusual Bessel functions with complex orders [13]. Abhinav *et al.* have shown that light emanating from subwavelength-sized sources can be efficiently coupled into such waveguides [16]. Several novel effects appear possible, given the large variety of free parameters (components of the ε and μ tensor) that can be chosen here. Waveguides filled or lined with anisotropic metamaterials potentially have great utility in the context of guiding radio-waves in MRI applications where the anisotropic metamaterials play a major role in increasing throughput or coupling in the subwavelength sized waveguide. It was shown that anisotropy was a pre-requisite for negative refraction and focusing of guided surface plasmon waves on the interfaces of anisotropic negative-positive permittivity metamaterials [25].

We offer here a review of the advances in waveguides filled with anisotropic metamaterials. Our purpose is to introduce a young researcher to the new developments while logically developing the ideas behind the exciting advances. Starting with a quick introduction to the ideas of metamaterials and effective medium properties, we will introduce recent work carried out on metamaterial filled waveguides, particularly waveguides filled with negative refractive index materials and anisotropic metamaterials. We will then move on to describe the guided modes in these systems: first in rectangular and parallel plate waveguide geometries followed by cylindrical waveguides with cylindrically symmetry anisotropies. The behaviour of the propagating modes in various manifestations of these waveguides are discussed with a view to project out various kinds of applications for these waveguides at both optical and radio/microwave frequencies. A mapping of the waveguide phenomena to apertures in metallic screens, and subsequently periodic arrays of apertures that usually comprise metasurfaces, will also be described. Here, metamaterial liners have found application in the realization of compact aperture arrays demonstrating extraordinary free-space wave-manipulation properties that may be engineered to enable a multitude of functionalities. As such, these metamaterial-lined aperture arrays may be referred to as resonant metasurfaces. It is critical to appreciate that the description here, while being rigorous, cannot be comprehensive given the wide variety of phenomena possible. We will conclude with an outlook for future work in these areas.

2. General concept of metamaterial waveguides

An electrically neutral plasma has a dielectric permittivity given by

$$\varepsilon(\omega) = 1 - \frac{\omega_p^2}{\omega(\omega + \mathrm{i}\gamma)} \tag{1}$$

where $\omega_p^2 = ne^2/m_e\varepsilon_0$ is the plasma frequency determined by n, the number density of free charge carriers, e, is the charge, m_e, the mass of the charge carriers, and ε_0 is the vacuum permittivity. The γ is a phenomenological parameter that determines dissipation of the electromagnetic wave. There can be both positive and negative charges with different masses in a plasma, resulting in multiple plasma frequencies corresponding to each species.

2.1. *Metamaterials: thin wire medium and split ring resonator*

All good conductors are free electron plasmas that have $\varepsilon < 0$ for frequencies lower than the plasma frequency that typically lies at ultra-violet frequencies for metals like gold, silver, aluminium and copper. But, the large magnitude of $\mathrm{Re}(\varepsilon)$ parameters at the frequencies much lower than the plasma frequency does not allow plasmonic effects and applications to be easily realized in conductors [26]. Pendry *et al.* proposed that arrays of thin metallic wires as shown in Figure 1(a) behave as plasmas with much lowered plasma frequencies [27]. The radius of the wires can be sub-millimeter, micrometer and nanometer for radio, infrared and optical frequencies respectively [24]. The wire medium behaves as an effective medium if the radius of metal wire (r) is much smaller than the separation between wires (p) and both are much smaller than the wavelength the radiation (λ) ($r \ll p \ll \lambda$). Such as medium was shown to have a plasma-like dielectric permittivity with $\omega_p^2 = 2\pi c^2/p^2 \ln(p/r)$ that is seen to be determined merely by the geometric parameters of the structure. The large inductance of thin wires plays an important role in reducing the plasma frequency. The relative permittivity of a wire medium oriented only in one direction as shown in Figure 1(a) [27] has an uniaxial diagonal tensor $(\epsilon_t, \epsilon_t, \epsilon_z)$ with $\epsilon_z < 0$, where the axis of the wires is assumed parallel to the z-axis. A three-dimensional lattice of thin wires could behave as an isotropic low-frequency plasma.

Pendry *et al.* also first demonstrated the ability to obtain dynamic magnetic polarizability in metallic composites consisting of coupled split ring resonators (SRR), shown schematically in Figure 1(b) [2]. When the incident magnetic field vector is along the axis of the rings (SRR), an electromotive force is induced around the rings. The currents in the two rings get coupled through a distributed capacitance formed between the rings (due to the gap). This results in the structure acting as a resonant L-C circuit, driven by the magnetic field of the incident electromagnetic wave. The SRR medium forms a uniaxial magnetic medium if the axis of the ring

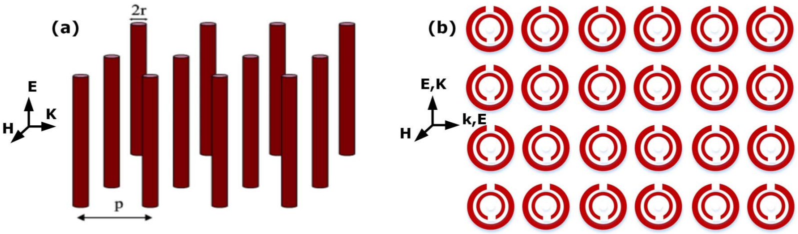

Figure 1. (a) Thin wire medium (b) 2D Image of a series of split ring resonators.

and the magnetic fields only along one direction. Smith *et al.* experimentally obtained negative refractive index media by combining thin wire and SRR structures with overlapping frequency ranges of negative permittivity and permeability [4].

2.2. *Effective medium theory*

In metamaterials, the composite (host and inclusion) materials are typically smaller than the wavelength of radiation, but much larger than the molecules or atoms. The periodic structure (unit cells) of these materials or their structural constituents can not be resolved by the wave and the material can be characterized by effective medium parameters such as relative permittivity and permeability. The effective medium parameters are obtained by appropriate averages of fields over the unit cell within the metamaterial [2].

The Maxwell–Garnett homogenization describes composites with small volume fraction of inclusion materials by incorporating the distortions due to the dipole fields of the inclusions on an average. Let us assume that a spherical particle having relative permittivity ε_i is embedded in a bulk host material of relative permittivity ε_h. The effective permittivity of this composite medium is

$$\epsilon_{\text{eff}} = \epsilon_h \frac{\epsilon_i(1+2f)+2\epsilon_h(1-f)}{\epsilon_i(1-f)+\epsilon_h(2+f)}, \tag{2}$$

where f is the volume filling fraction of the inclusions [26]. This method is valid for a fill-fraction up to about 0.3. An alternate process called the Bruggeman homogenization treats the inclusions and host constituents on equal footing and is valid for higher fill-fractions of inclusions also [28, 29]. The effective medium parameters can also be obtained from the modeling of the re-emission (reflection and transmittance) of light incident on the medium [8], a process that is often called the *Parameter retrieval procedure*.

Guenneau *et al.* homogenized three dimensional finite photonic crystals and waveguides filled with magneto-dielectric inclusions using a two-scale convergence to realize anisotropic effective media [30]. The problems of obtaining homogenized medium properties from emergent quantities using parameter retrieval methods for anisotropic media with aribitrarily oriented axes [31] and even bianisotropic metamaterials [32–35] have been addressed. Aspects of causality in such retrieval methods have been discussed [36, 37]. Usually, magneto-dielectric coupling or bianisotropy is not very strong in most metamaterials, although it is present in many, and most of the models do not explicitly include bianisotropy [38]. In our cases, most of the structures do not have much bianisotropy and it is not discussed here.

2.3. *Anisotropic, hyperbolic, zero permittivity and permeability*

Metamaterials, like thin wire array media, and SRR media can be modeled as anisotropic media characterized by permittivity and permeability tensors

$$\overline{\overline{\varepsilon}} = \begin{pmatrix} \epsilon_x & 0 & 0 \\ 0 & \epsilon_y & 0 \\ 0 & 0 & \epsilon_z \end{pmatrix}, \quad \overline{\overline{\mu}} = \begin{pmatrix} \mu_x & 0 & 0 \\ 0 & \mu_y & 0 \\ 0 & 0 & \mu_z \end{pmatrix}, \tag{3}$$

in a reference frame with appropriately oriented axes. As an example, consider an array of nanometrically thin long metallic wires, all oriented along the z-axis, at optical frequencies when the fields will completely penetrate across the nanometric wire. Such a system is realized by electrolytically deposited silver or copper wires in a nanoporous alumina template with oriented long nanoholes [39]. An electromagnetic wave polarized along the z-axis would experience an effective permittivity of $\varepsilon_z(\omega) = f\varepsilon_m(\omega)+(1-f)\varepsilon_h(\omega)$, where $\varepsilon_m(\omega)$ is the permittivity of the metal, $\varepsilon_h(\omega)$ is the host (alumina) permittivity, and f is the fill fraction of the metal. For the orthogonal polarization perpendicular to the axis of the cylindrical wires, one may derive an expression for the effective permittivity (similar to (2) for spherical inclusions). The material properties are different for different directions of the polarization of the wave. The dispersion relation of a plane wave propagating in an anisotropic metamaterial with the electric field polarized along the z-axis can be written as

$$\frac{k_y^2}{\epsilon_x} + \frac{k_x^2}{\epsilon_y} = \frac{\mu_z \omega^2}{c^2}, \tag{4}$$

where ω, k_x, k_y, c are the angular frequency of the wave, x component of the wave vector, y component of the wave vector, and speed of light in free space respectively. The material tensor components $(\varepsilon_x, \varepsilon_y, \mu_z)$ are experienced by the transverse magnetic polarized plane wave. The dispersion relation is an elliptical curve in the iso-frequency plane for metamaterials with all positive index diagonal tensors of relative permittivity and permeability. Waveguides filled with anisotropic materials have many unusual properties due to this elliptical dispersion, as demonstrated by Dheeraj *et al.* [13]. The diagonal components of the permittivity and permeability tensors may not have the same sign, in which case the dispersion relation (4) becomes a hyperbolic curve in the iso-frequency plane [9]. Such media are said to display “hyperbolic” (indefinite) dispersion and have capability to strongly enhance spontaneous emission due to the diverging density of states [11, 40], and can show negative refraction and enhanced perfect lensing effects [16,41]. Multilayered stacks of metal-dielectric thin films, multilayer fishnet structures and thin wire media are examples of hyperbolic media [41, 42]. With an anisotropic and hyperbolic cladding, Shaghik *et al.* analyzed that the hollow circular waveguides can guide modes with extremely subwavelength sized core diameters [14]. A circular waveguide filled with a hyperbolic metamaterial can support modes having upper but no lower cutoff frequency and enhance the power coupled from subwavelength sized sources [16].

Metamaterials exhibiting near-zero permittivities, known as epsilon-near-zero or ENZ metamaterials, have received a great deal of attention for their utility in the creation of compact resonators. One application is the homogeneous ENZ-filled metallic waveguide demonstrated by Alù and Engheta, which permits the transmission of power for arbitrarily small cross sections and waveguide geometries by way of a tunneling-like mechanism [15]. Transmission through such electrically small cross-sections is tantamount to an extreme reduction of the cutoff frequency of the fundamental waveguide mode. A generalization of this idea was put forth by Pollock and Iyer, who examined partially, or inhomogeneously, filled metallic waveguides—in particular, perfect electric conductor (PEC) circular waveguides lined using a thin coating of ENZ metamaterial [17]. It was determined that, for propagation through circular waveguides of arbitrarily small cross-section, the ENZ property was necessary but not sufficient: whereas a positive and near-zero permittivity drives the waveguide further into cutoff, a negative and near-zero permittivity is required to operate the waveguide well below cutoff. This is achieved through the introduction of a new low-frequency and backward-wave passband. This property was therefore termed epsilon-negative and near-zero, or ENNZ. The notion of thin, ENNZ liners was subsequently adapted to the creation of an array of compact resonant apertures demonstrating extraordinary transmission (EOT) well below their natural aperture resonances, but without reliance on diffraction anomalies related to the aperture period, as would be observed in more traditional EOT scenarios.

2.4. *Transmission-line metamaterial*

The thin wire and split ring resonator have limited practical applications because these structures are exhibit high loss and narrow bandwidth. A solution was identified by recognizing that the well-known transmission line (TL) theory models transverse electromagnetic wave propagation in a material using distributed lumped elements. In conventional materials, the use of per-unit-length series inductance and shunt capacitance represent positive permeability and permittivity respectively. It was observed by Iyer and Eleftheriades [43] and Caloz *et al.* [44, 45] that loading a host TL medium at subwavelength intervals in an inverted fashion, i.e. using discrete series capacitors and shunt inductors, would result in backward-wave (or left-handed) propagation over a finite, yet broad, bandwidth described by a negative phase velocity or, equivalently, a negative refractive index (NRI). As such, these TL metamaterials, which exhibited properties inherited from both the underlying TL and the periodic reactive loading, came to be known as NRI-TL metamaterials or composite right-/left-handed (CRLH) TL metamaterials.

3. Rectangular and parallel-plate waveguides

In this section, we first analyze the parallel-plate waveguide made of two infinitely extended PECs which are separated by a distance d $(= d_1 + d_2)$ as shown in Figure 2(a). The slab consisting of space in between can constitute different pairs of positive and negative relative permittivity and permeability. The transverse wave number is always imaginary for the propagating modes, when the slab is made of $\varepsilon_1 < 0, \mu_1 > 0$ and $\varepsilon_2 > 0, \mu_2 < 0$ materials or vice versa. But the transverse wavenumber can be real or imaginary depending on the wavenumber in the direction of wave of propagation, when the slab is made of a negative index material $(\varepsilon_1 < 0, \mu_1 < 0)$ and a positive index material $(\varepsilon_2 > 0, \mu_2 > 0)$ materials or vice versa. The dispersion relation for the TE and TM modes in the parallel-plate waveguide are

$$\frac{\mu_1}{k_1}\tan(k_1 d_1) = -\frac{\mu_2}{k_2}\tan(k_2 d_2); \quad \frac{\varepsilon_1}{k_1}\cot(k_1 d_1) = -\frac{\varepsilon_2}{k_2}\cot(k_2 d_2), \tag{5}$$

respectively. Where $k_i = \sqrt{(\omega^2 \varepsilon_i \mu_i - \beta^2)}$, for $i = 1, 2$ and β is the wave propagation constant in the direction of propagation of the wave (along the x-direction). From the dispersion relations (5), it is found that if the values of μ_1 and μ_2 have the same sign then the TE mode has no real value of the propagation constant. Similarly, for the TM mode with the same sign of value of ε_1 and ε_2, there is no propagation. The parallel-plate waveguide shows an interesting resonance when one slab of the parallel plate waveguide is made up with epsilon negative $(\varepsilon < 0, \mu > 0)$ (ENG) and the other slab has mu negative $(\varepsilon > 0, \mu < 0)$ (MNG) [15]. Here, it is also noted that no interface can support both TE and TM modes of propagation [15]. Due to the monotonic behaviour of the hyperbolic tangent function in the dispersion equation, for every pair of values of d_1 and the

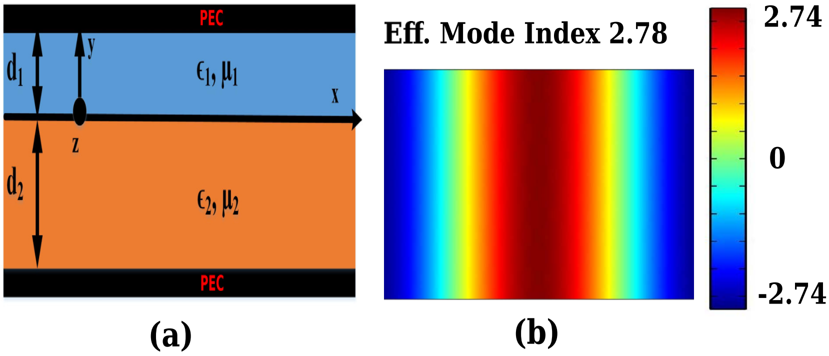

Figure 2. (a) Schematic diagram of a parallel plate waveguide filled with metamaterial slabs. (b) Axial magnetic field components showing the propagation of the $\mathrm{TE}_{0,1}$ mode in a homogeneously-filled rectangular waveguide (35 mm × 16 mm) at 3 GHz (below the cutoff frequency), where the permeability tensor is taken to be $(-1.2, 1.1, 1.1)$.

wave propagation constant, there is a unique value of d_2. In a double positive index material slab, multiple solutions of d_2 occur due to the periodic behaviour of fields. This is a unique characteristic of the parallel-plate waveguide made of ENG, and MNG materials. The detailed analysis of the parallel-plate slab waveguide is available in Refs. [15, 46, 47].

The conventional slab waveguide can act as a nonleaky waveguide for electromagnetic waves provided the refractive index of slab is higher than the surrounding dielectric medium. A slab waveguide made up of a negative refractive index material surrounded by a positive index medium has some novel properties such as the absence of fundamental modes [18]. The detailed analysis of an isotropic and an anisotropic slab waveguide is available in Refs. [18, 48–50].

3.1. *Anisotropic rectangular waveguide*

Xu *et al.* theoretically considered a rectangular waveguide filled with an anisotropic metamaterial and derived the general conditions for propagating TE and TM modes [51]. It was found that modes exist that propagate at low frequencies with cutoff at high frequencies [51]. Hrabar *et al.* demonstrated backward-wave propagation in miniaturized-transverse-dimension rectangular waveguides filled with an anisotropic metamaterial having a tensorial negative permeability [52]. All the walls of the rectangular waveguide are made up with PECs and the negative permeability is generated in by placing SRR structures parallel to the side walls of the waveguide. The distance between the SRRs is very small compared to the wavelength of radiation. We assume that the direction of propagation and the axis of waveguide are along the z-axis. The permeability tensor becomes (μ_t, μ_l, μ_l), where the values of μ_t and μ_l can be negative and positive, respectively, when the waveguide is filled with SRRs parallel to the side walls. This structure can support backward waves below the cutoff frequency of the dominant TE mode of the waveguide filled with a uniaxial material with negative permeability (other permittivity and permeability components are positive). All TE modes are backward waves below the natural cutoff frequency and exhibit low-pass behaviour. The transverse dimensions of this waveguide can be much smaller than the free space half-wavelength of the propagating wave. As the negative permeability only has a limited frequency band, this waveguide behaves as a band pass filter with central frequency located below the natural cutoff frequency of the waveguide [52, 53]. The propagation of the $\mathrm{TE}_{0,1}$ mode below the natural cutoff frequency is shown in Figure 2(b).

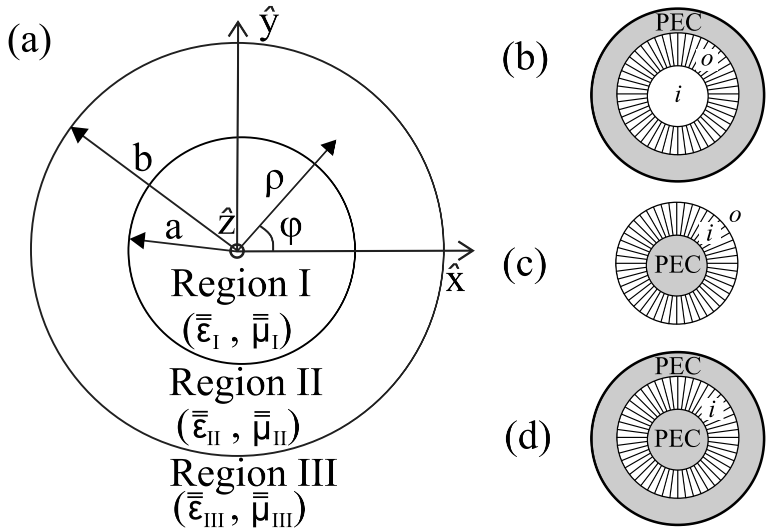

Figure 3. (a) Three-region waveguide setup for the following cases: (b) a metamaterial-lined PEC cylindrical waveguide, (c) a metamaterial-coated PEC rod, and (d) a metamaterial-filled coaxial waveguide. In all cases, the metamaterial region is represented using radial lines. Reprinted from [59], with the permission of AIP Publishing.

A similar planar/rectangular waveguide filled with SRRs was considered in Ref. [54], where modes with no cutoff were investigated. Slow-wave propagation of the guided modes was highlighted and the bianisotropy of SRR media was also considered. Meng *et al.* also theoretically considered an anisotropic metamaterial-filled rectangular waveguide and deduced the presence of both forward and backward propagation as well as forward-wave propagation below the conventional cutoff condition [55]. A giant modal birefringence was theoretically reported in Ref. [56] for a rectangular waveguide filled with a hyperbolic metamaterial at THz frequencies. Polarization effects and manipulation by using the large modal birefringence between the TE and TM modes was highlighted, and it was shown that the waveguide could act as a polarizer or a waveplate. A 50-fold enhancement of the spontaneous emission from molecules embedded in a slab of gold nanowire was reported in Ref. [57], where the emission coupled strongly to the waveguide modes and showed strong polarization effects due to preferential coupling. Ref. [58] presents a theoretical investigation of extraordinary transmission of light through a rectangular waveguide filled with an extreme uniaxial metamaterial having $\varepsilon_z \to \infty$ and $\mu_z \to \infty$, where z is the axis of the waveguide. It was concluded that a large number of higher-order guided modes propagate within the waveguide well below the conventional cutoff.

4. Cylindrical waveguides

In this section, we treat a class of anisotropic cylindrical waveguides consisting of 3 concentric regions (see Figure 3(a)): a central inner core region I of radius a, surrounded by an outer region II of radius b, embedded in a background medium III. Three distinct structures are considered: the metamaterial-lined PEC waveguide (Figure 3(b)), the metamaterial-coated PEC rod (Figure 3(c)), and the metamaterial-filled coaxial waveguide (Figure 3(d)).

Travelling-wave solutions along the axis of the waveguide are assumed. The metamaterial may be isotropic or anisotropic, but usually the cladding or core regions are taken to be isotropic. If an anisotropic core is considered, then at the centre the anisotropy can not be defined due to the geometrical singularity in the cylindrically symmetric medium. Hence we have to always exclude the centre of the anisotropic metamaterial waveguide by including a PEC boundary condition near the centre or by including an isotropic core at the centre.

4.1. *Analysis of the modes in a cylindrical waveguide*

Let's consider a cylindrically symmetric anisotropic medium whose permitivity and permeability are given by the diagonalised tensors $\bar{\bar{\varepsilon}} = (\varepsilon_r, \varepsilon_\phi, \varepsilon_z)$ and $\bar{\bar{\mu}} = (\mu_r, \mu_\phi, \mu_z)$, respectively. Travelling-wave solutions are considered in the cylindrically symmetric medium as,

$$\vec{E}(r,\phi,z,t) = \vec{E}(r,\phi)\mathrm{e}^{\mathrm{i}(\beta z-\omega t)}, \tag{6a}$$

$$\vec{H}(r,\phi,z,t) = \vec{H}(r,\phi)\mathrm{e}^{\mathrm{i}(\beta z-\omega t)}, \tag{6b}$$

where β is the propagation constant along the z-direction. Inserting these (6) in the Maxwell's equations, the transverse components of the electric and magnetic fields can be written in terms of the longitudinal components as,

$$E_r = \left\{\frac{\mathrm{i}\omega\mu_0\mu_\phi}{\omega^2\varepsilon_0\mu_0\varepsilon_r\mu_\phi - \beta^2}\right\}\left(\frac{\beta}{\omega\mu_0\mu_\phi}\frac{\partial E_z}{\partial r} + \frac{1}{r}\frac{\partial H_z}{\partial \phi}\right), \tag{7a}$$

$$E_\phi = \left\{\frac{\mathrm{i}\omega\mu_0\mu_r}{\omega^2\varepsilon_0\mu_0\varepsilon_\phi\mu_r - \beta^2}\right\}\left(-\frac{\partial H_z}{\partial r} + \frac{\beta}{\omega\mu_0\mu_r}\frac{1}{r}\frac{\partial E_z}{\partial \phi}\right), \tag{7b}$$

$$H_r = \left\{\frac{\mathrm{i}\beta}{\omega^2\varepsilon_0\mu_0\varepsilon_\phi\mu_r - \beta^2}\right\}\left(\frac{\partial H_z}{\partial r} - \frac{\omega\varepsilon_0\varepsilon_\phi}{\beta}\frac{1}{r}\frac{\partial E_z}{\partial \phi}\right), \tag{7c}$$

$$H_\phi = \left\{\frac{\mathrm{i}\beta}{\omega^2\varepsilon_0\mu_0\varepsilon_r\mu_\phi - \beta^2}\right\}\left(\frac{\omega\varepsilon_0\varepsilon_r}{\beta}\frac{\partial E_z}{\partial r} + \frac{1}{r}\frac{\partial H_z}{\partial \phi}\right). \tag{7d}$$

In general, the modes will be hybrid EH or HE. But for the special cases $H_z = 0$ the modes will be transverse magnetic (TM) and $E_z = 0$ the modes will be transverse electric (TE). This will happen in the case (3) of a coaxial waveguide.

By putting E_r and E_ϕ from (7a) and (7b) in the Maxwell's curl equation for electric field, we obtain

$$\frac{\omega\mu_0}{r}\frac{\partial}{\partial r}\left(\frac{\mu_r}{q}r\frac{\partial H_z}{\partial r}\right) + \chi\frac{\beta}{r}\frac{\partial^2 E_z}{\partial r\partial\phi} + \frac{\omega\mu_0\mu_\phi}{p}\frac{1}{r^2}\frac{\partial^2 H_z}{\partial\phi^2} - \frac{\beta}{r}\frac{\partial}{\partial r}\left(\frac{1}{q}\right)\frac{\partial E_z}{\partial\phi} + \omega\mu_0\mu_z H_z = 0. \tag{8}$$

Putting H_r and H_ϕ from (7c) and (7d) in the Maxwell's curl equation for magnetic field, we get

$$\frac{\omega\varepsilon_0}{r}\frac{\partial}{\partial r}\left(\frac{\varepsilon_r}{p}r\frac{\partial E_z}{\partial r}\right) + \chi\frac{\beta}{r}\frac{\partial^2 H_z}{\partial r\partial\phi} + \frac{\omega\varepsilon_0\varepsilon_\phi}{q}\frac{1}{r^2}\frac{\partial^2 E_z}{\partial\phi^2} + \frac{\beta}{r}\frac{\partial}{\partial r}\left(\frac{1}{p}\right)\frac{\partial H_z}{\partial\phi} + \omega\varepsilon_0\varepsilon_z E_z = 0. \tag{9}$$

In (8), and (9), we have defined

$$p = \frac{\omega^2}{c^2}\varepsilon_r\mu_\phi - \beta^2, \quad q = \frac{\omega^2}{c^2}\varepsilon_\phi\mu_r - \beta^2, \quad \chi = \left(\frac{1}{p} - \frac{1}{q}\right). \tag{10a}$$

Equations (8) and (9) are coupled to each other and are difficult to solve for an anisotropic and inhomogeneous case. For the anisotropic and homogeneous case, the problem is solvable. For the TE modes, the obtained solutions within the anisotropic medium defined entirely by the H_z component, are

$$H_z = [\mathrm{A}_{\mathrm{TE}}J_\nu(k_{\mathrm{TE}}r) + \mathrm{B}_{\mathrm{TE}}Y_\nu(k_{\mathrm{TE}}r)]\exp[\mathrm{i}(m\phi + \beta z)], \tag{11}$$

where J_ν and Y_ν are the Bessel and Neumann functions of order ν, and m is a non-zero integer. To simplify, if one considers only dielectric anisotropy with $\mu = 1$, and $\varepsilon_z = \varepsilon_\phi$, we have

$$k_{\mathrm{TE}}^2 = \varepsilon_\phi\frac{\omega^2}{c^2} - \beta^2, \quad \text{and} \quad \nu^2 = \frac{(\varepsilon_\phi\omega^2/c^2 - \beta^2)}{(\varepsilon_r\omega^2/c^2 - \beta^2)}m^2. \tag{12}$$

Table 1. Table showing the conditions on the material parameters and the propagation constant to obtain imaginary orders (ν or τ) for the Bessel functions that describe the modes for the TE and TM polarizations in the anisotropic fiber

Mode	k_{TE} or k_{TM}	Conditions for k_{TE} or k_{TM}	Requirements for $\nu^2 < 0$ or $\tau^2 < 0$
TE	Real	$\varepsilon_\phi > \beta^2/k_0^2$	$\varepsilon_r < \beta^2/k_0^2 < \varepsilon_\phi$
	Imag.	$\varepsilon_\phi < \beta^2/k_0^2$	$\varepsilon_\phi < \beta^2/k_0^2 < \varepsilon_r$
TM	Real	$\varepsilon_z/\varepsilon_r > 0$, $\varepsilon_r > \beta^2/k_0^2$	$\varepsilon_\phi/\varepsilon_r < 0$, $\varepsilon_r > \beta^2/k_0^2$, $\varepsilon_\phi > \beta^2/k_0^2$
			$\varepsilon_\phi/\varepsilon_r > 0$, $\varepsilon_\phi < \beta^2/k_0^2 < \varepsilon_r$
		$\varepsilon_z/\varepsilon_r < 0$, $\varepsilon_r < \beta^2/k_0^2$	$\varepsilon_\phi/\varepsilon_r < 0$, $\varepsilon_r < \beta^2/k_0^2$, $\varepsilon_\phi < \beta^2/k_0^2$
			$\varepsilon_\phi/\varepsilon_r > 0$ and $\varepsilon_r < \beta^2/k_0^2 < \varepsilon_\phi$

Note that $k_0^2 = \omega^2/c^2$.

An analogous expression is obtained for the TM modes, defined entirely by the E_z component, are

$$E_z = [\mathrm{A}_{\mathrm{TM}} J_\tau(k_{\mathrm{TM}} r) + \mathrm{B}_{\mathrm{TM}} Y_\tau(k_{\mathrm{TM}} r)] \exp[\mathrm{i}(m\phi + \beta z)], \tag{13}$$

where J_τ and Y_τ are the Bessel and Neumann functions of order τ,

$$k_{\mathrm{TM}}^2 = \frac{\varepsilon_z}{\varepsilon_r}(\varepsilon_r \omega^2/c^2 - \beta^2), \quad \text{and} \quad \tau^2 = \frac{\varepsilon_\phi}{\varepsilon_r}\left(\frac{\varepsilon_r \omega^2/c^2 - \beta^2}{\varepsilon_\phi \omega^2/c^2 - \beta^2}\right) m^2. \tag{14}$$

The properties of the modes critically depend on ν, τ, k_{TE} and k_{TM}. A few conditions for the TE and TM modes are summarised in Table 1. It is well known in literature of hyperbolic metamaterials [10] that when k_{TE} or k_{TM} is imaginary, modal solutions take the form of the modified Bessel functions. We should note that, in such cases, the anisotropic nature of the waveguide allows the order, ν or τ, of the Bessel function to be fractional and sometimes even imaginary ($\nu^2 < 0$ or $\tau^2 < 0$) [60, 61], which is not possible in the conventional isotropic waveguide. We consider only a propagating (β is real) TE mode with real k_{TE} (implying that $\varepsilon_\phi > \beta^2 c^2/\omega^2$). If $\varepsilon_r < \beta^2 c^2/\omega^2 < \varepsilon_\phi$, then $\nu^2 < 0$ and the order of the mode becomes an imaginary number. This occurs straightforwardly in a medium with $\varepsilon_r < 0$ and $\varepsilon_\phi > 0$, whereas in a medium with $\varepsilon_r = \varepsilon_\phi$, such a situation would not occur. Note that the inequalities become reversed if we seek a TE mode with imaginary k_{TE} described by the modified Bessel functions. The requirements for an imaginary order of the TM modes represents slightly more cases due to several possibilities of the material permittivity, and Table 1 summarizes these conditions for $\tau^2 < 0$. Some simplifications may occur when $\varepsilon_z = \varepsilon_\phi$ because of the reduced number of constraints in the mathematical expressions.

4.2. *Experimental realizations and applications*

In practice, it has been complicated to organize metamaterial structures within the small confines of a waveguide. When the waveguide size is large, such as in the case of structures at tens of MHz for MRI, it is possible to organize such structures. For high frequency solutions, such as at optical IR frequencies, the small micro and nanosizes demand approaches involving self-organization processes. Very few such metamaterial waveguides have been experimentally realised and many are yet to be properly explored. In general, we can categorize the waveguides into three kinds: axial structuring, radial structuring and metamaterial-clad waveguides. Here we will discuss a few cases of cylindrical waveguides that have been experimentally realized.

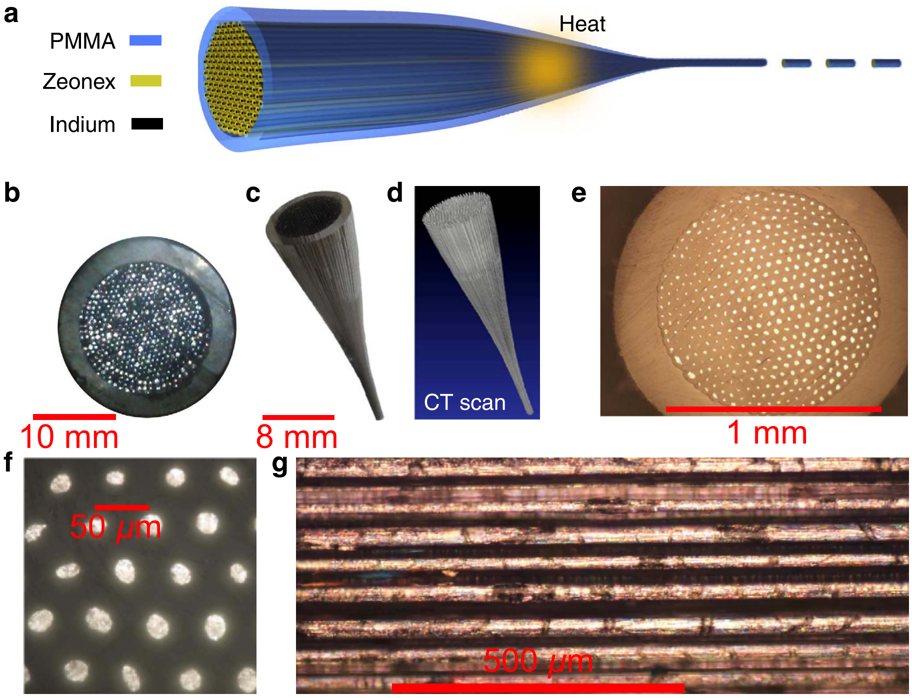

Figure 4. (a) Schematic plan and drawing of the fiber, (b) Optical photograph of the cross-section. (c) Optical and (d) Computed Tomography (CT) scan image of the tapered region. (e) 10 times zoomed optical microscope image of the cross-section, (f) 40 times zoomed image and (g) longitudinal optical microscope image of the waveguide. Figure reproduced from [64]; Licensed under Creative Commons Attribution-NonCommercial-ShareAlike 3.0 Unported License (CC BY-NC-SA 3.0).

4.2.1. *Axially structured waveguide*

This type of waveguide is typically axially invariant and usually has an axially continuous structure. These waveguides also show anisotropy of the type $\varepsilon_r = \varepsilon_\phi \neq \varepsilon_z$. Such metamaterial waveguides are typically fabricated by fiber-drawing techniques [62, 63]. Figure 4 shows the schematic and optical microscope images of such an example. By stacking indium metal wires in a low-absorption polymer Zeonex, a preform of 1 cm is created in a polymethyl methacrylate (PMMA) tube [64]. This assembly is heated whereby the polymer becomes viscous and metal becomes liquid, so that the preform can be drawn from a tapered die into a uniform fiber. The choice of indium here is to match the low-temperature softening behaviour of PMMA. The cross-section of the waveguide and its optical microscope images are shown in other sub-figures.

These waveguides have been used for imaging and focusing of terahertz (THz) radiation at the below the diffraction limit. Figure 5 shows the experimental and simulated results of the intensity from the two apertures made of 50-μm-thick brass discs. The diameter, separated inner-edge, and length of this metamaterial waveguide are 200 μm, 100 μm, and 3.4 mm, respectively. Here the intensity is a function of the position and frequency averaged at the centre plane ($y = 0$). The direct near-field measurement of the apertures without the waveguide is also shown for comparison. Panels 5(a–d) show the output intensity measurement of the apertures without the waveguide. It is clear that even measuring just after the apertures at a 125 μm distance from the apertures there is diffraction in the images. Panels 5(e–h) show the aperture output intensity after

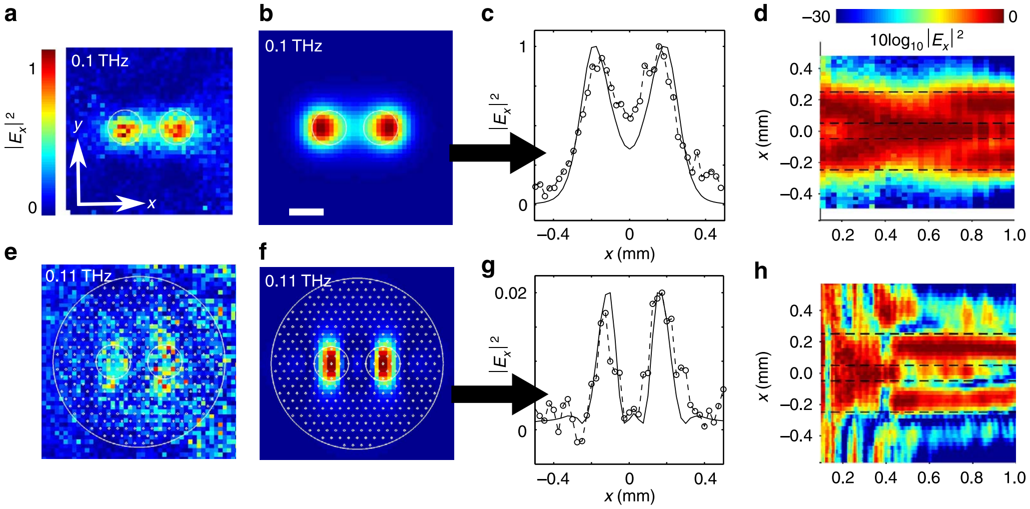

Figure 5. (a) Measured and (b) simulated intensity of two apertures of 200 μm diameter with separated inner-edge of 100 μm at 0.1 THz frequency was calculated at 125 μm from the output of the aperture, (c) intensity distribution along x-direction at $y = 0$ μm, and (d) the logarithmic intensity distribution with respect to the incident frequencies along the x-direction averaged over $y = 0 \pm 50$ μm. (e) Measured and (f) simulated intensity of the same apertures propagating through the 3.4 mm long metamaterial waveguide, calculated at 50 μm output from the waveguide, (g) intensity distribution along the x-direction, averaged over $y = 0 \pm 100$ μm, and (h) the logarithmic intensity distribution with respect to the incident frequencies along the x-direction averaged over $y = 0 \pm 100$ μm. Figure reproduced from [64]; Licensed under Creative Commons Attribution-NonCommercial-ShareAlike 3.0 Unported License (CC BY-NC-SA 3.0).

light travels through the 3.4-mm-long metamaterial waveguide and were measured at a 50 μm distance from the waveguide. Here there is clear evidence that the images are diffraction-free and that resolution is increased. This happens since the wired metamaterial shows hyperbolic dispersion and along the z-direction and very large propagation vectors are achieved [9, 10], which focuses both the near-field as well as the far-field. Therefore, diffraction-free images become possible using the metamaterial waveguide.

Another example that can be used is the hollow-core metamaterial waveguide. Min Yan and co-workers theoretically show that a hollow-core metamaterial waveguide made of silver-silica multilayered metamaterial can transport TM IR light 100 times more effectively than a simple hyperbolic metamaterial waveguide [65]. Such a hollow-core waveguide exhibits lower losses than the non-hollow hyperbolic metamaterial fiber. These waveguides can be used for IR applications.

4.2.2. *Radially structured waveguide*

In this type of waveguide, the structuring is perpendicular to the waveguide axis, althrough the invariance along the axis is preserved in a coarsely grained metamaterial description. For example, there can be nanopores or nanowires oriented along the radial direction of the waveguide, in which case the anisotropy is of the type $\varepsilon_r \neq \varepsilon_\phi = \varepsilon_z$. Such a waveguide was first realized by a nanoporous alumina metamaterial waveguide [13, 59, 66, 67]. This nanoporous alumina waveguide consists of an inner impermeable alumina nano layer near the centre from which nanopores

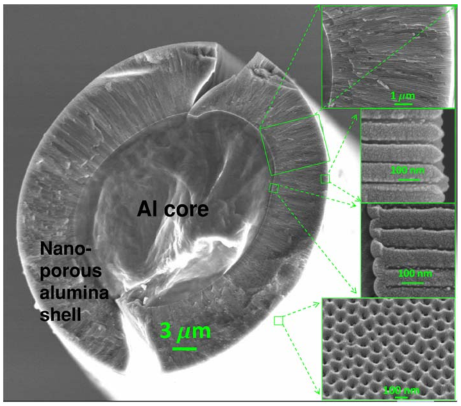

Figure 6. Scanning electron microscope (SEM) image of the nanoporous alumina waveguide. The presence of the radially oriented non-branching nanopores are clearly shown. The nanoporous outer surface and the impermeable barrier pure alumina oxide layer at the inner tubular surface are shown in the insets. Brittle alumina waveguides crack when cleaved for SEM imaging. Reprinted with permission from [13] © The Optical Society.

radially emanate and terminate at the outer nanoporous surface formed by the nanopores, as shown in Figure 6. The nanopores of this waveguide may be filled with a plasmonic metal like silver, gold etc. by electrodeposition techniques [24]. This results in an extremely large anisotropy in the waveguide. In this case, the centre of the waveguide has an aluminum core (PEC) or an impermeable alumina core (isotropic medium). A local Maxwell–Garnett or Bruggeman homogenization process can be adopted to describe the effective medium permittivity at each point locally. This has also been validated by a geometric mapping of the cylindrical system to a planar system [13].

The guiding of light through a bent section of a nanoporous anisotropic waveguide and an aluminium core is shown in Figures 7(a,b). The scattering from the structure and other defects is strong, but the evidence for the light confinement and guidance is very clear. Because of the large scattering, most of the modes get coupled, and it was not possible to image the mode structure of the propagating modes. The propagation losses will also be very large due to the structured nature. Figures 7(c,d) show the variation in the anisotropic material effective permittivity with radial distance calculated for air nanopores in the cylindrical nanoporous alumina, and silver nanowires in nanoporous alumina where a Drude dielectric permittivity model for silver was used, given by $\varepsilon_{\mathrm{Ag}} = \varepsilon_\infty - \omega_p^2/[\omega(\omega + \mathrm{i}\gamma)]$ with $\varepsilon_\infty = 5.7$, $\omega_p = 9.2$ eV and $\gamma = 0.021$ eV [68]. The host alumina data is available in Ref. [69]. The imaginary part of the effective permittivity for the silver-nanowires-filled nanoporous structure is also small due to the small fill fractions. Because of the radial variation of the nanopores, the nanoporous alumina waveguides are actually spatially inhomogenous, which will affect the nature of the modes. Figures 7(e, f) show the normalized electric field (E_z) plots of two TM modes for homogeneously filled metamaterial waveguides. The modes of the plots intentionally used high m value (40) to show the effect of the imaginary order (τ). If the effective order τ value is real but fractional then for high m, the field is pushed outwards from the centre of waveguide, but when the effective τ is imaginary then the field is concentrated towards the centre of the waveguide.

Another good example of a radially structured metamaterial waveguide is a hybrid-glass metamaterial fiber, which was reported for nonlinear effects [70]. This waveguide is fabricated by a laser-based fiber drawing technique [71, 72]. To fabricate such a waveguide, sapphire ($\alpha - \mathrm{Al_2O_3}$)

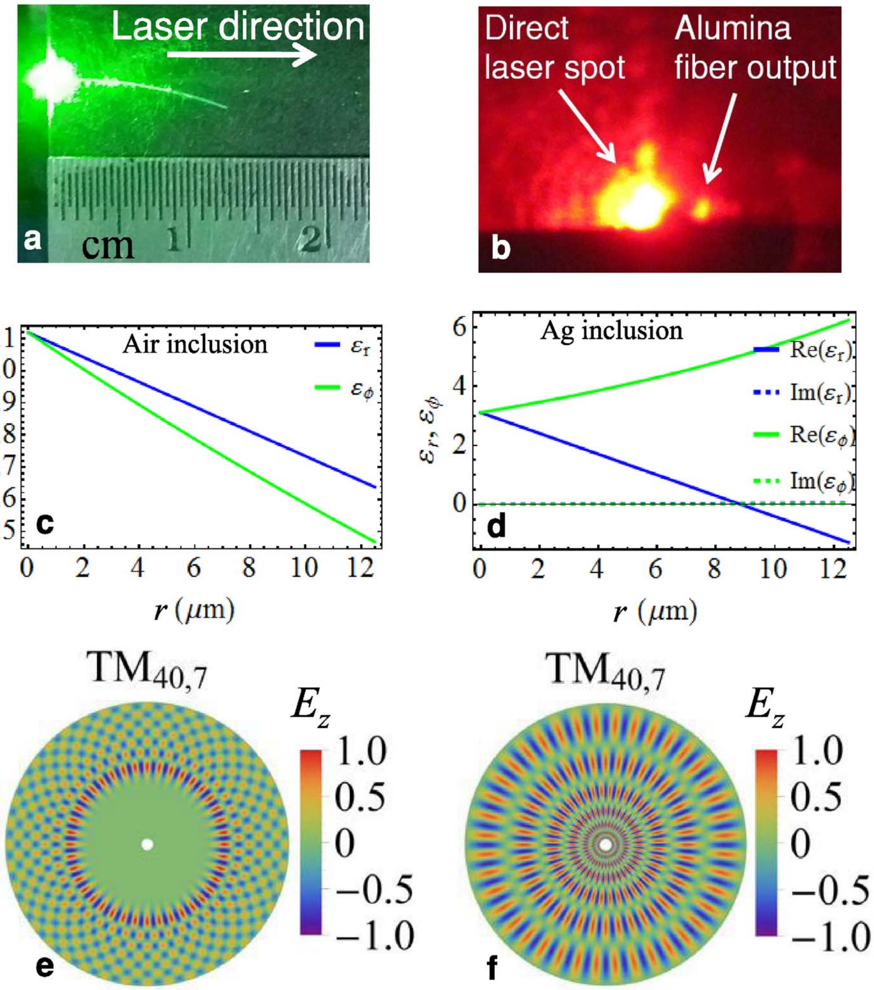

Figure 7. (a) Picture of light (λ = 532 nm) propagating across a bent nanoporous alumina waveguide with an aluminum core (Aluminium core diameter—10 μm, nanoporous alumina shell diameter—80 μm, length—1.3 cm, nanopore diameter is 30 nm and nanopore periodicity is 100 nm at outer surface). (b) The light output from the waveguide at λ = 633 nm. Plots of the variation of the effective dielectric permittivity components with the radial distance in a nanoporous alumina waveguide for (c) air inclusion, and (d) when the nanopores of the waveguide are filled with silver nanowires for nanopore radius $q = 25$ nm at outer surface and $f = 0.23$. The bottom: Calculated normalized electric field (E_z) plots of TM modes for homogeneously filled coaxial metamaterial waveguides at λ = 633 nm, (e) for fractional order modes when $\varepsilon_r = 2.467$ and $\varepsilon_\phi = \varepsilon_z = 2.638$, and (f) for imaginary order modes when $\varepsilon_r = 2.638$ and $\varepsilon_\phi = \varepsilon_z = 2.467$. Reprinted with permission from [13] © The Optical Society.

was taken as a seed dielectric core and dendrite crystalline $\gamma - Al_2O_3$ was deposited on it. A silica layer is coated on the outside as a cladding. Such a waveguide is used for second harmonic generation (SHG) using nonlinear effects. This waveguide has monolithically integrated dendrites for intracavity and resonant SHG. Similar to the nanoporous fiber developed by anodization and

Table 2. Table showing the dependence of the axial propagation constant (β), cutoff frequency and order of the propagating modes with the material parameters

Mode	Material permittivity ($\mu = 1$)	Axial propagation constant (β)	Remarks about modes and cutoff frequencies
TE	$\epsilon_r < 0; \epsilon_\phi > 0; \epsilon_z > 0$	$\sqrt{k_0^2\,\lvert\epsilon_\phi\rvert - k_{\mathrm{TE}}^2}$	Finite cutoff, solutions similar to positive index fibers, Modes may be fractional order or Imaginary order
TE	$\epsilon_\phi < 0; \epsilon_r > 0; \epsilon_z > 0$	$i\sqrt{k_0^2\,\lvert\epsilon_\phi\rvert + k_{\mathrm{TE}}^2}$	No propagation
TE	$\epsilon_z < 0; \epsilon_r > 0; \epsilon_\phi > 0$	$\sqrt{k_0^2\epsilon_\phi - k_{\mathrm{TE}}^2}$	Finite cutoff, solutions similar to positive index fibers, Modes may be fractional order or Imaginary order
TM	$\epsilon_r < 0; \epsilon_\phi > 0; \epsilon_z > 0$	$i\sqrt{k_0^2\,\lvert\epsilon_r\rvert - \frac{\lvert\epsilon_r\rvert}{\epsilon_z}k_{\mathrm{TM}}^2}$	Upper cutoff, Mode has upper limitation of frequencies for propagation, modes may be imaginary order
TM	$\epsilon_\phi < 0; \epsilon_r > 0; \epsilon_z > 0$	$\sqrt{k_0^2\epsilon_r - \frac{\epsilon_r}{\epsilon_z}k_{\mathrm{TM}}^2}$	Finite cutoff, solutions similar to positive index fibers, modes may be fractional order or imaginary order
TM	$\epsilon_z < 0; \epsilon_r > 0; \epsilon_\phi > 0$	$\sqrt{k_0^2\epsilon_r + \frac{\epsilon_r}{\lvert\epsilon_z\rvert}k_{\mathrm{TM}}^2}$	No cutoff frequency, modes may be fractional order or imaginary order

electrodeposition techniques, the laser-based fiber drawing technique also results in a volumetric metamaterial waveguide that can be rapidly fabricated over large lengths.

4.3. *Modes and applications of hyperbolic waveguides*

The waveguide filled with hyperbolic metamaterials has advantageous propagation properties. The axial propagation constant, cutoff frequencies and the order of propagating modes are shown in Table 2 for different hyperbolic permittivity tensors by using the dispersion equations (14). It is seen that the radial and axial hyperbolic metamaterial waveguides have no cutoff frequencies for the transverse magnetic modes. The propagation of modes much below the cutoff frequency was verified by an explicit calculation using the COMSOL® Multiphysics Simulation Suite based on the finite element method. The fields of these eigenmodes are shown in Figure 8 for a waveguide with $\epsilon_r = -1$, $\epsilon_\phi = \epsilon_z = 3.2883$, and inner and outer diameters of 200 nm and 500 nm, respectively. The real positive values of effective mode indices are evidence of forward propagating modes at 200 THz, much below the natural cutoff frequency (the minimum cutoff frequency to propagate the TM_{11} mode in an equally size waveguide filled with an isotropic medium is 567.8 THz), as shown in Figure 8.

This can be advantageously used to couple the near-field evanescent modes associated with large transverse wavevectors of small sources to these high-angular-momentum waveguide modes, well below the conventional cutoff frequencies [16]. Such waveguides can couple light very efficiently from small sources into the propagating modes of the waveguide, which can then

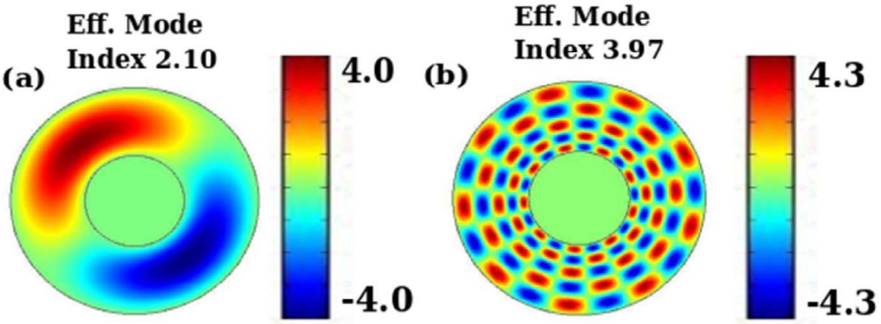

Figure 8. Electric fields (E_z) in an anisotropic hyperbolic fiber, when the annular region ($R_1 < r < R_2$) has $\epsilon_r^{\text{eff}} = -1, \epsilon_\phi^{\text{eff}} = \epsilon_z^{\text{eff}} = 3.2883$, $R_1 = 100$ nm and $R_2 = 500$ nm. The propagating TM$_z$ modes are (a) TM$_{1,1}$ and (b) TM$_{9,5}$ at a frequency of 200 THz.

be adiabatically coupled into a conventional waveguide or fiber. Abhinav *et al.* studied the capability of such a hyperbolic waveguide to transmit power from the near field of subwavelength sources, where the inner and outer surfaces of the annular region of the waveguide (as shown in region II of Figure 3(a)) is covered with air and PEC respectively [16]. They found that the average power at the output port is higher for the radial hyperbolic case ($\epsilon_r < 0; \epsilon_\phi \simeq \epsilon_z > 0$) by several orders of magnitude compared to the angular hyperbolic ($\epsilon_\phi < 0; \epsilon_r \simeq \epsilon_z > 0$) and the axial hyperbolic ($\epsilon_z < 0; \epsilon_r \simeq \epsilon_\phi > 0$) cases from a point dipole source at 200 THz. The coupling efficiencies with such an anisotropic waveguide coupler, measuring a few wavelengths long, can exceed the coupling efficiencies with a conventional coupler by a factor of 10^7 [16, 73]. Coupling efficiencies of the radial hyperbolic waveguides are higher when compared with the tapered nanofibers [16]. The radial hyperbolic waveguide can be used as a near-field coupler or an imaging probe, and it has the convenience of butt-coupling, which results in better spatial accuracy.

4.4. *Metamaterial-clad waveguide*

The cladding of a waveguide affects the properties of the waveguide and directly controls the wave propagation within. By changing the cladding, one can vary the electromagetic properties of the waveguide. In the conventional waveguide the cladding is isotropic, but by using an anisotropic metamaterial cladding some unusual properties can be achieved. Metamaterial-clad waveguides show properties like backward propagation below the cut-off frequency with respect to the un-clad waveguide, field collimation [17], miniaturization and resonant tunnelling [74, 75], transport of large amounts of power [76], and slow light propagation [12]. Several metamaterial-clad waveguides have been reported. These claddings are made of many kinds of metamaterial-like subwavelenth layered structures [77], split-ring-resonators [17, 74, 75], microwires or nanowires [65, 67], liquid crystals, or a combinations of these [76, 78]. Metamaterial-clad waveguides are more popular because they are easy to fabricate compared to volume-filled metamaterial waveguides. Due to the large dissipation in metamaterials, metamaterial-clad waveguides may offer better propagation characteristics.

4.5. *Metamaterial-lined PEC waveguide*

First, the practical realization of an ENNZ-metamaterial-lined waveguide is discussed. To realize the ENNZ-metamaterial liner, TL-metamaterials are used.

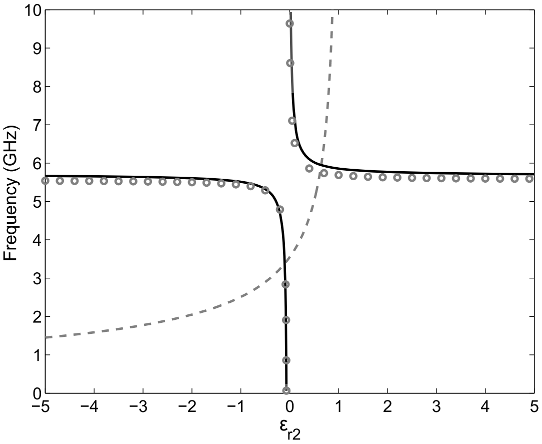

Figure 9. HE_{11} mode cutoff frequency versus liner permittivity. Full, anisotropic dispersion (black curve), approximate isotropic dispersion (empty grey circles), and Drude permittivity model (dashed grey curve). © 2013 IEEE. Reprinted, with permission, from [17].

Experimentally, metamaterials have been incorporated into many devices, including antennas, lenses, couplers, and waveguides. Of interest here is the ENNZ-lined cylindrical waveguide. The ENNZ-lined cylindrical waveguide consists of a metamaterial-lined (and otherwise hollow) PEC cylinder, where the metamaterial is designed to exhibit ENNZ properties, see Figure 3(b). In this case, the ENNZ metamaterial is designed specifically to interact with the HE_{11} mode of the inhomogeneously filled waveguide system as this mode exhibits many desirable properties: below-cutoff propagation and collimated central fields, to name just two. To design a metamaterial that responds in the expected way, consider just the liner region of the waveguide. For the desired HE_{11} mode, the liner exhibits longitudinally directed H-fields and radially directed E-fields. The transverse fields resemble an azimuthal TL-mode standing-wave field distribution. As such, the TL-metamaterial is an ideal metamaterial technology with which to imbue the liner region with ENNZ properties. This can be achieved using the plasma-like properties of an array of thin, highly inductive wires, which exhibits a Drude-like permittivity response near its resonance (plasma) frequency. Thin-wire metamaterials, or equivalently, inductively loaded TL-metamaterials, are generally anisotropic, however, the theoretical analysis above has shown that for a thin liner, the HE_{11} modal cutoff frequency is only weakly dependent on liner properties other than the radial permittivity ϵ_ρ. A representative Drude dispersion curve is plotted against the HE_{11} mode cutoff frequency in Figure 9. Note that the two curves cross at two points: the first at $f = 3.381$ GHz, and second at $f = 5.958$ GHz. The first corresponds to the designed ENNZ region with $\epsilon_{r2} = -0.09$ and is well below the natural TE_{11} cutoff frequency of $f = 5.864$ GHz, while the second corresponds to a nearly homogeneous waveguide with $\epsilon_{r2} = 0.644$, and a cutoff frequency only marginally above the homogeneous waveguide cutoff. A suitable TL-metamaterial to realize the above properties employs an azimuthally directed coplanar-strip (CPS) TL loaded at 45° intervals using discrete inductors to create the ENNZ response. The EH_{01} mode also necessarily exists in the frequency-reduced regime below the liner's plasma frequency, but is orthogonal to the HE_{11} mode and may therefore be suppressed through proper excitation. In addition, higher-order azimuthal resonances may be suppressed by loading the series branch of the CPS TL using a small series capacitance.

The experimental setup used two shielded-loop antennas to feed a closed cylindrical waveguide, which was either unloaded, or loaded with several printed circuit board rings of the TL-

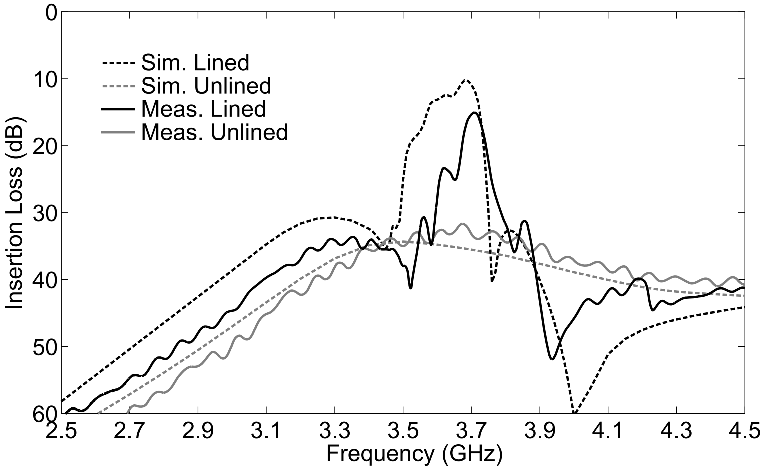

(a)

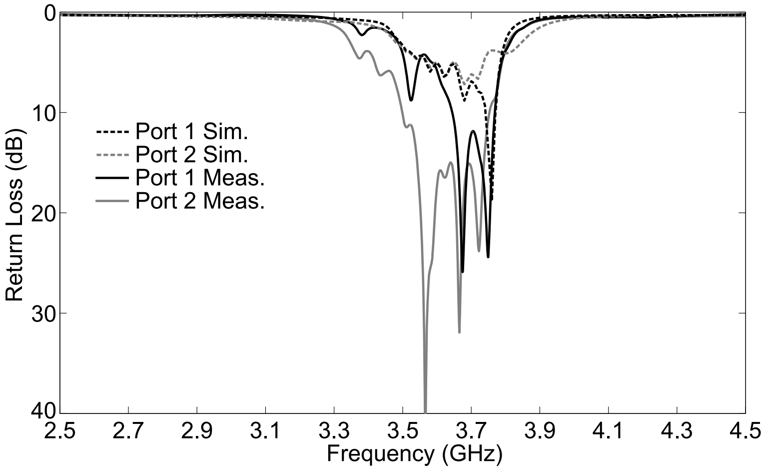

(b)

Figure 10. (a) Insertion loss and (b) return loss obtained from simulation and measurements of the practical ENNZ-lined metamaterial waveguide. © 2016 IEEE. Reprinted, with permission, from [79].

metamaterial described previously. A comparison of the insertion loss and return loss of the full-wave Ansys high frequency structure simulator (HFSS) simulation to the fabricated structure (see Figure 10) show good agreement and any discrepancies are attributed to fabrication tolerances.

4.5.1. *Applications*

Travelling-wave MRI is a sensing paradigm where the bore of the MRI scanner is treated as a cylindrical waveguide, and the RF signal may be generated/detected by way of externally placed antennas, freeing up space within the bore and also mitigating the problem of standing waves on coils placed within the bore, which can contribute to image dark spots at very high RF frequencies/static field strengths. However, typical human-sized scanners have bore diameters that cause the fundamental TE_{11} mode to be well below cutoff at operating frequencies corresponding to clinical field strengths, such as 1.5 T or 3 T. In order to restore propagation in such clinical MRI machines and employ the traveling-wave method, it is necessary to somehow reduce the natural cutoff frequency of the bore. Lining the bore of an MRI with an ENNZ-metamaterial liner allows the excitation of the below-cutoff HE_{11} mode to propagate the signal, but the HE_{11} mode also has very homogeneous fields in the central bore, which improves image quality while occupying less space than the conventional birdcage coils that may otherwise induce claustrophobia.

A second application of the ENNZ-lined metamaterial waveguide is particle-beam studies [59]. Specifically, particle-beam studies use the TM_{01} mode of an air-filled cylindrical waveguide to accelerate charged particles to relativistic speeds. Unfortunately, the fundamental mode of a cylindrical waveguide is the TE_{11} mode, thus monomodal operation is impossible and efficiency is degraded. A waveguide lined with a metamaterial that exhibits anisotropic negative and near-zero permittivity supports a spectrum of backward-wave modes, of which the EH_{01} mode has the highest cutoff frequency and hence supports monomodal propagation. This mode also shares many properties with the TM_{01} mode of the unlined cylindrical waveguide, which makes it ideal for the described particle-beam studies. These studies could benefit from increasing the monomodal bandwidth of the EH_{01} mode by reducing the cutoff frequency of the HE_{n1} modes (the first being HE_{11}). The cutoff frequency of the EH_{01} mode occurs at the plasma frequency ω_p of ϵ_ρ of the liner, independent of the other tensor components of ϵ. Further, the cutoff frequency of the HE_{11} mode is reduced for thicker liners. In an illustrative example, it has been shown that the monomodal bandwidth of the EH_{01} mode can be increased by greater than 38.5% over the isotropic case by introducing anisotropy and increasing the liner thickness.

A third application that has been explored is open-ended waveguide probe antennas [74]. Open-ended waveguide (OEWG) probes have many applications, but those that can benefit the most from miniaturization are antenna near-field measurements and material characterization. It was proven that lining an OEWG probe operating below cutoff with an ENNZ-metamaterial liner can improve the gain of the highly miniaturized antenna by over 60 dB.

4.6. *Metamaterial-coated PEC rod*

A PEC rod may be seen as the inverse of the hollow PEC waveguide (Figure 3(c)). The guided modes supported by this structure are tightly bound surface modes referred to as Sommerfeld modes. Recently, these rods have been used as probes in THz-endoscopy methods to sense small quantities of material. These applications use the EH_{01} mode of the rod as it has no cutoff in this geometry and is circularly symmetric. Subwavelength sensing resolution is achieved by tapering the rod to a fine tip. As the field confinement limits the ultimate resolution, the slow-wave, high-β regime is used near the surface plasmon resonance. For smooth metal rods, this occurs at $\omega_{ep}/\sqrt{2}$, where ω_{ep} is the plasma frequency of the bulk metal. Hence, for regular metals, this is a constant frequency range that is often in the UV. At lower frequencies, the required field confinement can be achieved by modifying the plasma frequency through corrugations on the surface of the metal, or by coating the rod in high-permittivity dielectrics. Surface corrugations have been modeled in other contexts using anisotropic surface impedance or by thin layers of anisotropic permittivity and permeability. Here, the EH_{01} mode dispersion is engineered for a rod coated in a thin, practical anisotropic metamaterial [59].

First, consider the case of a metamaterial coating with isotropic permittivity, but chosen plasma frequency ω_{ep}. The dispersion of the EH_{01} mode of this structure closely resembles that of the smooth PEC rod, with field confinement increasing towards ω_{ep}, but the loss introduced by the metamaterial also leads to higher attenuation. Further reduction of the plasma frequency of the metamaterial requires stronger loading components, but this generally increases losses and fabrication difficulty. The dispersion of the EH_{01} mode with anisotropy introduced to the metamaterial model closely mimics the dispersion of an isotropic EH_{01} with half the plasma frequency, meaning the simple addition of anisotropy effectively halves the lumped component values required to realize the metamaterial. Further, the losses are significantly reduced, and the radial field confinement is improved.

4.7. *Metamaterial-filled coaxial waveguide*

The following section focuses on exploring interesting dispersion phenomena in the THz regime in the recently realized alumina metamaterial-filled coaxial waveguide discussed above, a case of Figure 3(d). The structure consists of an alumina tube embedded with radially emanating micropores, with an aluminum microwire core and finally a thin aluminum outer coating [59].

The dispersion profile of the permittivity tensor for a structure with air-filled pores is weakly anisotropic, and shows strong dispersion where the phonon resonances occur for alumina between 10 and 25 THz. More extreme degrees of anisotropy may be observed by filling the holes with a plasmonic metal such as silver. This frequency regime is well below silver's bulk plasma frequency, hence it exhibits large, negative permittivity. Due to the radial orientation of the nanopores, ϵ_ρ is dominated by the response of the silver, and ϵ_ϕ is marginally affected. Losses are substantially increased.

Next, consider the TM_{11} mode of the coaxial waveguide loaded with the above air-filled porous metamaterial [59]. Above the plasma frequency of 28 THz, the permittivity of the alumina is positive and modal dispersion for the TM_{11} mode approaches what it would be for an isotropic alumina-filled coaxial waveguide, and a low-loss passband occurs. For the isotropic alumina case, near the phononic resonances, (i.e. 13 THz and 17.2 THz), several lossy bands with negative group velocity exist. The introduction of air-filled pores creates a small but lossy backward-wave band between 24 and 25 THz. Finally, the addition of silver into the nanopores severely impacts the mode's dispersion: generally, losses are increased by an order of magnitude, however, a small, low-loss backward-wave band is introduced at 4.3 THz, which may be useful for backward-wave propagation. As the nanopores are hydrophilic, they may be filled with all sorts of materials, such as dye molecules, quantum dots, and dispersed nanoparticles whose resonant features could be used to modify the anisotropic effective permittivity of the waveguide from THz to visible frequencies. The large surface area of the nanopores may also prove beneficial in sensing.

5. From waveguides to apertures

A waveguide may be transformed into an aperture in a few simple steps. Consider again an inhomogeneously filled PEC cylindrical waveguide, as shown in Figure 11: a PEC shell of radius $\rho = b$ is lined with a metamaterial (ϵ_{r2}, μ_{r2}, $a < \rho < b$) and finally filled with air (ϵ_{r1}, μ_{r1}, $\rho < a$) [17]. The PEC condition on the surface of the waveguide enforces that all fields outside the waveguide be zero, thus the PEC wall's thickness may be extended to infinity in the transverse (x–y) plane. This system, of course, supports the same spectrum of modes as the original metamaterial-lined PEC waveguide. Next, shorten the waveguide's extent in the propagation (z-) direction to be infinitesimally small. In this limit, the waveguide becomes an aperture in a PEC sheet, as shown in Figure 12. Apertures in an infinitesimally thin metallic screen support resonances analogous to waveguide modal cutoffs, but do not support guided-wave propagation.

In this section, we begin by exploring the salient features of lining apertures with non-magnetic, epsilon-negative and near-zero (ENNZ) metamaterials by comparing them to equivalent ENNZ-metamaterial-lined waveguides, with examples in both the microwave and optical regimes: the Fano-shape resonant transmission, the waveguide modal cutoff frequency's relation

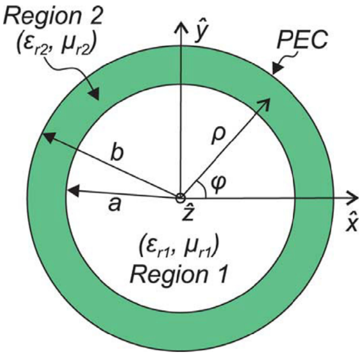

Figure 11. Cross-section of a metamaterial-lined waveguide. Region 1 ($\rho < a$) is filled with vacuum (but may generally take on any ϵ_{r1}, μ_{r1}), region 2 ($a < \rho < b$) is filled with a metamaterial that has arbitrary ϵ_{r2} and μ_{r2}, and the outer boundary at b is a PEC. © 2013 IEEE. Reprinted, with permission, from [17].

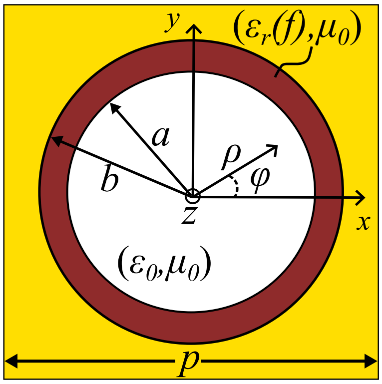

Figure 12. Planar view if an metamaterial-lined aperture. Region 1 ($\rho < a$) is filled with vacuum (but may generally take on any ϵ_{r1}, μ_{r1}), region 2 ($a < \rho < b$) is filled with a metamaterial that has arbitrary ϵ_{r2} and μ_{r2}, and the outer region ($b < \rho$) is a PEC. Reprinted with permission from [80] © The Optical Society.

to the aperture resonance frequency, and the practical implementation. We continue the discussion with an extension into resonant metasurfaces (MTSs), where the ENNZ-metamaterial-lined apertures are arrayed in the transverse plane with period p. This necessitates a discussion on diffraction anomalies, interaperture coupling, and excitation mechanisms. Finally, we conclude with metamaterial-lined aperture MTS applications and outlook.

5.1. *Theory of operation*

Although Bethe's well-known aperture theory predicts that an empty aperture will transmit poorly when it is electrically small (below what would be the cutoff frequency of the equivalent fundamental unlined-waveguide mode), the below-cutoff modes introduced by the metamaterial lining create resonant transmission for subwavelength apertures [80, 81]. This resonance is unlike those most commonly produced by larger apertures as it exhibits a characteristic Fano lineshape, which is a strong enhancement followed by strong extinction of the transmission, as seen in the transmission/reflection parameters plotted in Figure 13.

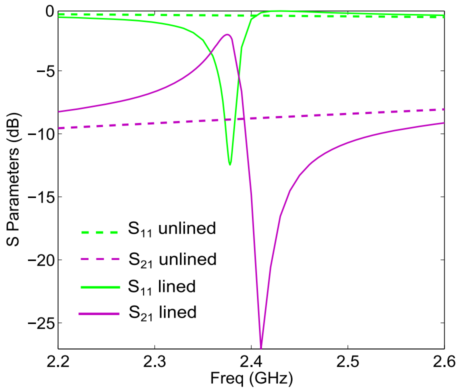

Figure 13. Transmission and reflection parameters of an ENNZ-metamaterial-lined aperture array with $b = 15.65$ mm, $a = 13.69$ mm and $p = 40$ mm (solid). Also plotted is the transmission for an array of apertures with no liner (radius $b = 15.65$ mm and spacing $p = 40$ mm, dashed). Reprinted with permission from [80] © The Optical Society.

The Fano response is well-described by a dual resonator model, under the conditions where a high-Q resonator (i.e. sharp or discrete resonance) interacts with a low-Q resonator spectrum (i.e. wide or continuous spectral response) in the weak-coupling regime [82]. The high-Q resonator has a 180-degree phase shift at resonance, and the wide spectrum follows a continuous phase response. The two constructively then destructively interfere near the discrete resonance frequency to produce the Fano resonance. In the case of the apertures described here, the sharp, frequency-reduced HE_{11} resonance interacts with the low, wide-band background transmission of an unlined aperture predicted by Bethe's theory (the −10-dB unlined transmission shown in Figure 13) to produce a Fano lineshape.

The aperture resonance frequency is very sensitive to the metamaterial liner properties. To find the resonance frequencies, the Helmholtz equation is solved in cylindrical coordinates subject to appropriate boundary conditions, in a similar way to finding the dispersion relation of the equivalent waveguide system, as was done in [79]. The dispersion relation is as follows:

$$A = \Big[\frac{\mu_{z1}}{\gamma^{\mu}_{\rho 1}} \frac{J'_{\tau 1}(\gamma^{\mu}_{\rho 1} a)}{J_{\tau 1}(\gamma^{\mu}_{\rho 1} a)} - \frac{\mu_{z2}}{\gamma^{\mu}_{\rho 2}} \frac{G'_{\tau 2}(\gamma^{\mu}_{\rho 2} a)}{G_{\tau 2}(\gamma^{\mu}_{\rho 2} a)} \Big] \tag{15a}$$

$$B = \Big[\frac{\epsilon_{z1}}{\gamma^{\epsilon}_{\rho 1}} \frac{J'_{\nu 1}(\gamma^{\epsilon}_{\rho 1} a)}{J_{\tau 1}(\gamma^{\epsilon}_{\rho 1} a)} - \frac{\epsilon_{z2}}{\gamma^{\epsilon}_{\rho 2}} \frac{G'_{\nu 2}(\gamma^{\epsilon}_{\rho 2} a)}{G_{\nu 2}(\gamma^{\epsilon}_{\rho 2} a)} \Big], \tag{15b}$$

where $\gamma = \alpha + \mathrm{j}\beta$ is the complex wave propagation constant in the axial direction of the waveguide, $\gamma_{\rho_1} = \sqrt{\gamma^2 + k_0^2}$, and $G_{\nu_\mu} = Y'_{\nu_\mu}(\gamma^{\mu}_{\rho_2} b) J'_{\nu_\mu}(\gamma^{\mu}_{\rho_2} \rho) - J'_{\nu_\mu}(\gamma^{\mu}_{\rho_2} b) Y'_{\nu_\mu}(\gamma^{\mu}_{\rho_2} \rho)$ is a combination of Bessel (J_ν) and Neumann (Y_ν) functions. The roots of (15a) and (15b) correspond to the EH mode and HE mode cutoff frequencies, respectively. Plotting the cutoff frequency with respect to liner permittivity for each mode leads to an interesting result for the HE_{11} mode: the cutoff frequency is strongly reduced for negative and near-zero values of permittivity. This mode shows weak, collimated fields in the centre region and strong fields in the liner. Consider a thin liner similar to the case studied in [79]. For an aperture with $b = 140$ nm and $a = 120$ nm, the cutoff frequency of the HE_{11} mode is plotted with respect to the anisotropic ϕ and ρ liner permittivity components in Figure 14(a). Clearly, for a thin liner, the ϕ component has very little effect on the frequency-reduced HE_{11} modal cutoff frequency.

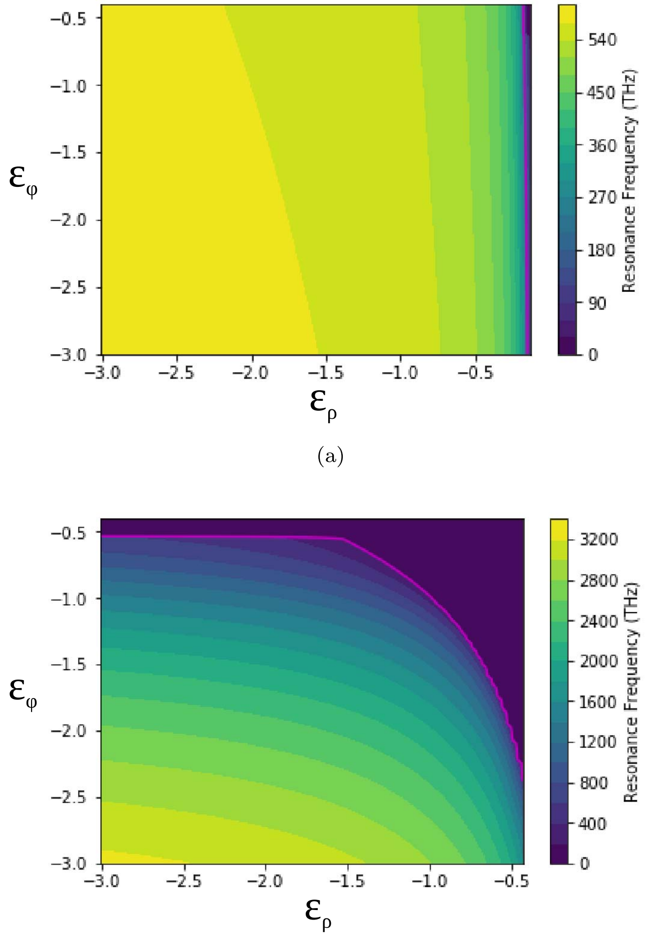

(a)

(b)

Figure 14. Surface plot of HE_{11} cutoff frequency with respect to anisotropic liner permittivity parameters for (a) a thin liner ($b = 140$ nm, $a = 120$ nm), and (b) a thick liner ($b = 140$ nm, $a = 14$ nm). The magenta line denotes 193 THz, or 1.55 μm, the wavelength of optical telecommunications.

If the inner radius is reduced to $a = 14$ nm, as plotted in Figure 14(b), the contribution from ϵ_ϕ is as important as the ϵ_ρ component given the higher filling factor of the aperture. As permittivity nears zero, the resonance frequency is reduced to the electrostatic condition (DC), as was observed for the metamaterial-lined PEC waveguide. Frequency-reduced resonance occurs for either ϵ_ρ or ϵ_ϕ, whereas the isotropic case required ϵ_ρ be near zero. A slice taken from the lower left to the top right of the plot extracts the response for an isotropic liner permittivity, and it can be seen that for a thick, isotropic liner, the resonance frequency saturates at DC for a much higher absolute value of permittivity (i.e. near $(-1,-1)$) than for either anisotropic parameter, and is thus more sensitive to very small changes in permittivity.

The interested reader may find more information on other 3D spherical and cylindrical core-shell structures that support compact resonances with arbitrary anisotropic permittivities and permeabilities in some of the following references: [13, 59, 79, 83–87].

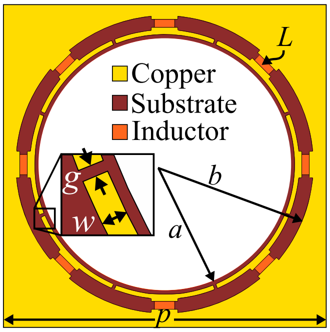

Figure 15. Practical implementation of the ENNZ-metamaterial lined aperture from [80], Figure 1(c). a, b, and p are borrowed from Figure 12. L refers to discrete radial inductors, w is the azimuthal trace width, and g is the azimuthal capacitive gap width. Reprinted with permission from [80] © The Optical Society.

5.2. *Microwave implementation*

The practical implementation of the ENNZ-lined aperture takes on a very similar geometry to the practical ENNZ-lined waveguide, but rather than a cascade of identical liner rings, includes only a single liner layer, as shown in Figure 15 [80]. If the liner (Figure 16(a)) is straightened out and viewed as an azimuthally directed CPS TL (Figure 16(b)), the well-known TL-metamaterial theory prescribes that a positive susceptance placed in shunt leads to a homogenized negative effective permittivity (Figure 16(c)) [43, 79]. The positive susceptance is created using shunt discrete inductors (L), and series capacitors are used to suppress any azimuthal resonances. Eight unit-cells are arranged around the azimuth to create an effective medium that is polarization insensitive.

Printed components may also be used, and offer many advantages. They are simpler to fabricate, can be made conformal, are easy to modify/tune, and can be more accurately modeled in simulation. The fabricated ENNZ-lined aperture shown in Figure 17(a) uses printed dual-arm spiral inductors and small gap capacitors. This structure was patterned with an LPKF ProtoMat S62 mechanical milling machine, which uses a digitally controlled mechanical routing bit to remove the copper cladding from a microwave substrate with up to 100 μm precision, as shown in Figure 17(b). The experimental results match full-wave electromagnetic simulations performed in Ansys HFSS. The resonance frequency of the aperture can be tuned in the same way the waveguide cutoff frequency is tuned: stronger inductive loading or larger aperture size reduce the resonance frequency, while weaker inductive loading or smaller apertures increase the resonance frequency.

Compact resonance may also be achieved in a similar manner on a solid metallic "patch" that is the dual of the aperture case. The ENNZ-liner becomes a coating with strong series capacitive loading instead of shunt inductive loading, which leads to an MNNZ response. This structure, however, has less in common with the equivalent waveguide as the patch may support longitudinal electric fields on the surface of the central disc, whereas the fields inside the core of the waveguide must be zero.

5.3. *Optical implementation*

ENNZ-metamaterial-lined apertures can be translated from the microwave to the optical domain, where inductors can no longer be made from coiled wires and copper no longer acts as

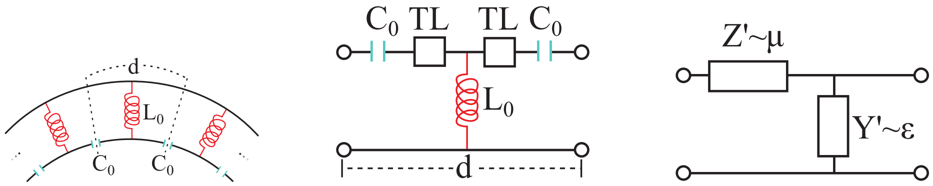

(a) (b) (c)

Figure 16. TL model for the ENNZ liner. (a) is the circuit equivalent of the liner with lumped components, (b) is the equivalent transmission-line model, and (c) is the homogenized TL-metamaterial model. © 2016 IEEE. Reprinted, with permission, from [79].

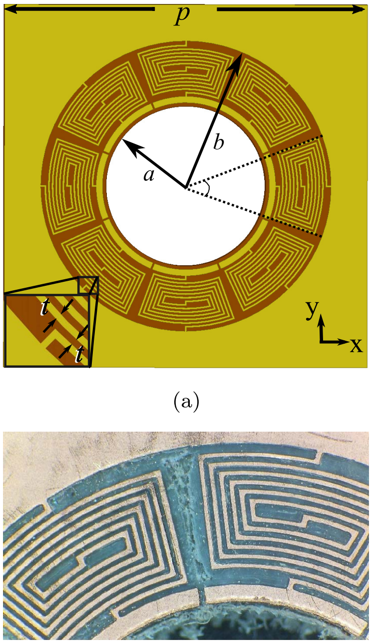

(a)

(b)

Figure 17. Printed ENNZ-metamaterial-lined aperture, (a) full aperture design, and (b) fabricated structure. © 2018 IEEE. Reprinted, with permission, from [88].

a perfect metal [89]. To implement an ENNZ liner, the concept of optical nanocircuits is invoked [90–94]. Optical nanocircuits generalize lumped circuit elements to apply not only to conduction currents (dominant at lower frequencies), but also to displacement currents (dominant at optical frequencies). Effectively, chains of nanoparticles with positive permittivity act as lumped optical capacitors, and nanoparticles with negative permittivity act as lumped optical inductors. It is well known that metals exhibit negative permittivity near and below their plasmonic resonance frequency, hence lumped inductors can be replaced with metallic nanoparticles, and lumped capacitors can be replaced with dielectric nanoparticles or air gaps. Notice that this is very similar to printed microwave components, however, the inductors no longer need to be meandered, hence an optical implementation of the ENNZ-lined aperture can be created by simply replacing the printed lumped inductors with nanowires.

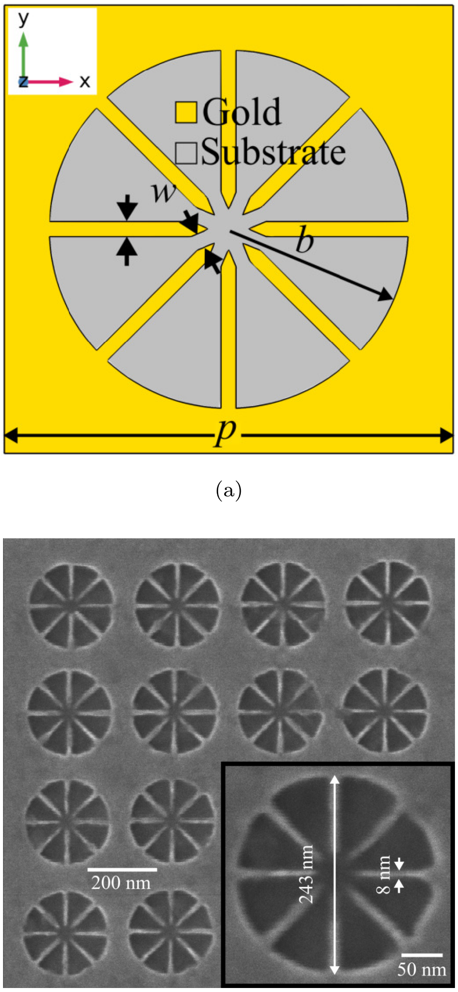

(a)

(b)

Figure 18. Optical implementation of the thick-liner ENNZ-metamaterial-lined apertures: (a) designed structure, (b) fabricated structure using helium ion milling. © 2019 IEEE. Reprinted, with permission, from [89].

The properties of a printed inductor are much easier to control than those of a nanowire, thus a new mechanism was introduced to control the resonance frequency of the optical ENNZ-lined aperture: the liner thickness. As the size of the liner increases, the liner fields move further from the PEC boundary and may have both radial and azimuthal components. Hence the anisotropic model for the liner permittivity must be incorporated, as explained above. In fact, increasing the liner thickness allows a greater degree of miniaturization to be achieved than the isotropic liner for a given liner dispersion. The thickest possible liner extends nearly to the centre of the aperture, and is used for the optical implementation shown in Figure 18(a). This structure exhibits another interesting feature: the liner fields are strongly enhanced at the centre of the aperture. Plasmonic field enhancement of this nature is used to encourage low-probability scattering events such as Raman scattering, to increase sensor sensitivity, to encode information at a subwavelength scale, and more.

The structure was patterned into a 50 nm gold layer (which has low loss and is optically opaque) on a transparent glass substrate. A minimum feature size of 10 nm was chosen for maximum control over the nanowire plasmonic resonance frequency. Fabrication of such small features with large aspect ratios in metal films is an extreme challenge, and can only be accomplished by helium focused ion beam milling. The Zeiss Orion Nanofab Helium Ion Microscope was used to pattern the structure shown in Figure 18(b). Characterization efforts are ongoing.

Individually, metamaterial-loaded resonators can be used as subwavelength sensors in much the same way as the waveguides they are based on can be used as probes, however, because they are flat, another degree of freedom is available: 2D, flat arrays of subwavelength resonators, i.e., metasurfaces.

6. Periodic arrays (metasurfaces)

Expanding the scope of metamaterial-loaded resonators to 2D grids introduces a host of features not present for a single aperture or waveguide, some of which include: diffraction anomalies, interaperture coupling and excitation angles.

6.1. *Extraordinary optical transmission*

Recent interest in diffraction anomalies was sparked by Ebbesen's observation of extraordinary optical transmission (EOT) in 1998 [95]. Ebbesen *et al.* patterned a silver film with a square array of nanoholes and measured the optical transmission. They were surprised to find that when the period of the array was exactly one wavelength, near-perfect transmission was observed, counter to the classical Bethe theory of diffraction by subwavelength holes [81]. Although this was initially interpreted using concepts of surface plasmons, and later spoof surface plasmons, the current more rigorous understanding is on the basis of diffraction anomalies and the generation of a leaky-wave field that couples to the incoming and outgoing free-space modes [96–99]. Modern work on the subject consists of generalizing diffraction anomalies to new structures with cartesian, polar and spherical periodicity. Generally, diffraction anomalies occur for periodic structures with wavelength-scale spacings.

The current understanding of EOT clearly establishes that diffraction anomalies are not responsible for the increased transmission seen in arrays of metamaterial-lined apertures as the spacing between apertures/resonators is much too small.

6.2. *Inter-aperture coupling*

Another complication introduced by the arraying of apertures is the ability to couple apertures. This effect makes the design of arrays significantly more challenging, as individually designed elements may act very differently in combination. For electrically large elements, such as those used in frequency-selective surfaces (FSS), the coupling is generally low and the resonator's interaction can be well-modeled with antenna array theory or coupled-line theory [100, 101]. In the case of closely spaced, electrically small elements (i.e. resonant metasurfaces), however, the energy stored by the resonator in the near-field will generally lead to strong coupling with adjacent elements [102, 103]. The ENNZ-metamaterial-lined aperture avoids this issue by strongly confining the fields at resonance (plotted in Figure 19) to the liner area, which allows both uniform and nonuniform arrays to be designed from individual unit cells.

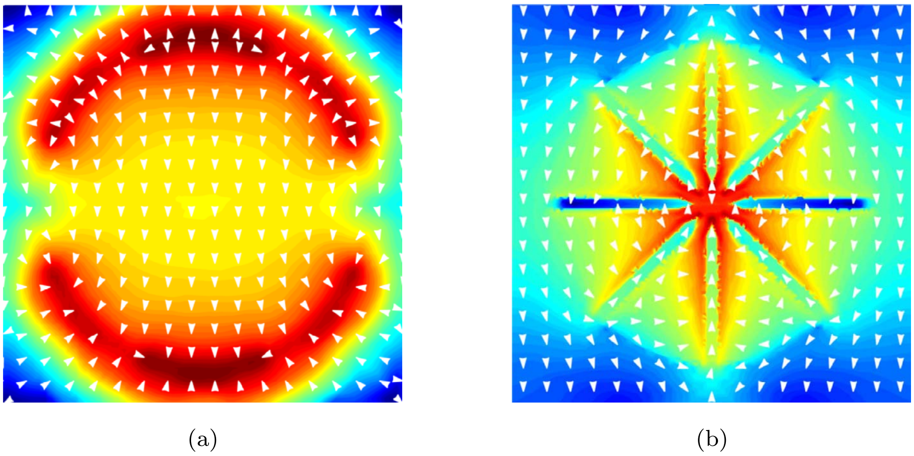

(a) (b)

Figure 19. Complex electric-field magnitude and vector direction for (a) the microwave, thin-liner case, where fields are confined to the liner region, and (b) the optical, thick-liner case, where fields are confined to the centre of the aperture. © 2019 IEEE. Reprinted, with permission, from [89].

6.3. *Excitation polarization and angle*

Although complications exist for periodic arrays, there are also many advantages over waveguides. The in-plane periodicity makes fabrication much simpler than the multilayer fabrication required for waveguides. Rather than using different waveguide excitations, metasurfaces are studied under the effect of incident plane waves. These plane waves can be arbitrarily polarized and incident from any angle. TE and TM plane waves are degenerate for normal incidence, but lead to very different excitation conditions off-normal. For example, assuming no bianisotropy, the z-component (x–y periodicity) of the magnetic field for a TE polarized wave can excite a planar magnetic dipolar resonance, whereas the TM polarized wave cannot. Furthermore, off-normal incidence effectively changes the period of the metasurface with respect to the wavelength of the incoming wave. This emphasizes the need for extremely subwavelength and decoupled unit cells, as the effective periodicity variation changes the response less, and hence gives a stable response for wide angles of incidence.

The incident polarization that the ENNZ-metamaterial-lined aperture metasurface responds to may be controlled by changing the azimuthal periodicity. At first, 8 unit cells per azimuthal period was chosen in part to be polarization insensitive and better comparable to the waveguide case, but if only 2 unit cells are used, the resonance only occurs for one incident linear polarization. An array of polarization-sensitive apertures can be used as a polarization splitter or shield. The resonance is largely independent of elements placed on the opposing axis, and dual-band or dual-polarization metasurfaces with independently controllable bands can be made on a single layer.

Any fully planar MTS cannot produce a magnetic dipole resonance for normal incidence as a loop must be formed longitudinally in the current path. Unfortunately, imparting the full 2π transmission phase shift required for phase-gradient MTSs to an incoming plane wave requires the excitation of both a magnetic- and an electric-dipolar resonance, and normal incidence is often the most practical setup [104]. For this reason, many modern metasurface designers have moved towards multilayer systems. Recall that the practical implementation of the metamaterial-lined waveguide required essentially cascading metamaterial-lined apertures, hence the theory

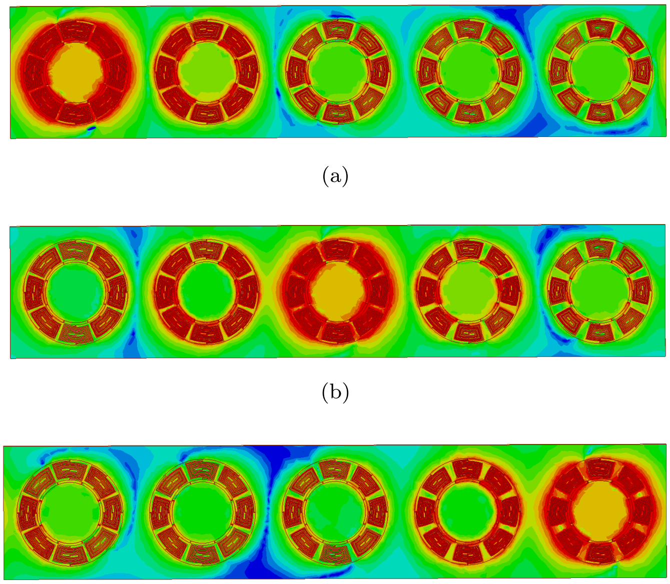

(a)

(b)

(c)

Figure 20. Complex electric-field magnitudes at successive resonance frequencies for a 5 × 1 nonuniform array of ENNZ-metamaterial-lined apertures. (a) 2.695 GHz. (b) 2.965 GHz. (c) 3.30 GHz. © 2018 IEEE. Reprinted, with permission, from [88].

lends well to creating multilayer metamaterial-lined aperture metasurfaces, but further study will be required to fully develop the required design procedures.

7. Applications

ENNZ-lined aperture metasurfaces share some applications with the equivalent waveguide. Sensing of dielectric materials may be done in both cases by passing liquids through the empty centre, where shifts in resonance or cutoff frequency can be associated with changes in permittivity. The metasurface, however, may improve this device due to its added ability to parallelize a process with many adjacent apertures under different sensing conditions at a subwavelength scale. For example, Baladi *et al.* showed that by creating a nonuniform array of 5 ENNZ-lined apertures with different inductors, obstacles can be detected in front of each aperture individually by examining the disappearance of each corresponding resonance in the transmitted spectrum, at a resolution better than $\lambda/6$ [88]. Figure 20 shows the electric-field magnitude at three of the resonance frequencies. It can clearly be seen that only one aperture reacts at each frequency.

In fact, the resonance frequency of an ENNZ-lined aperture is most sensitive to the permittivity of the liner, which may make an optical implementation where an analyte may also pass through the liner much more sensitive. The metasurface may be made tunable by the introduction of varactors or active elements, which can allow for flexibility in shielding, filtering, and sensing. Furthermore, introducing nonlinear optical materials into the optical ENNZ-metamaterial-lined apertures can allow for high-speed optical switching phenomena to occur. The strong field enhancement at the centre of the optical ENNZ-metamaterial-lined metasurface can be used to strongly excite optical nonlinearities for frequency conversion and its subwavelength nature could be used to increase the density of optical storage media.

8. Outlook

There are many future directions for metamaterial-liner-loaded metasurfaces. Immediate work on adapting the already proven structures to exhibit polarization sensitivity will open many options in polarizing and shielding devices, and exploring the response of the complementary metafilm structure will allow control over both reflection and transmission. Further, multilayer metasurfaces with robust design methods are very active, but will take some development to allow for non-uniform liners in the axial direction.

For the optical case, once the characterization problem is solved, polarization-sensitive structures will allow the resonance frequency to be shifted to the visible, where subwavelength apertures may cheaply increase the resolution of conventional photolithography or qualitatively sense analyte concentration in fluids by changing transmission colour.

The nanostructured fibers presented here, even though the structure is at a subwavelength size, will always create some scattering of light and will have high throughput losses. Hence it is never envisaged that metamaterial filled waveguides will be utilized for long distance propagation, for example, in optical communications. Instead, these waveguides possess unique properties that make them suitable for other applications. For example, end-coupling or butt-coupling of the fiber to the near-field modes of a source has been shown to be easily possible for these anisotropic or hyperbolic fibers. These have potential applications as high throughput probes for near-field optical microscopy. Further, as the fields of the higher-order modes tend to spread out throughout the cross-section of the optical fiber, there are distinct advantages against spatial hole-burning and bleaching processes due to large localized fields. Such processes may provide support for applications such as laser amplification, parametric amplification, harmonic generation, or self-phase modulation that can occur over short lengths of the waveguide.

In another manifestation, where the central core region is empty or filled with a dielectric material and the cladding consists of an anisotropic metamaterial, modes concentrated near the centre may be effectively coupled to other materials placed in the central core region. Behaviour of emitting molecules in such regions will be drastically affected due to the large field enhancements as well as the modified density of modes available. Such optical fibers may also be effectively controlled by microfluidic flows in the central core region of the optical fibers. The hollow-core waveguide may be utilized for sensing applications, where a solution is pumped through the central core and the molecules or bacteria, if present, will scatter the light in fiber and modify the transmittance to enable their sensing.

The nanoporous-alumina-based fibers make available an immensely large porous volume which may be utilized for adsorption processes. The presence of adsorbed molecules on the optical fiber will result in an effective refractive index change of the optical fiber and selectively change the transmission or reflection of certain modes of the optical fiber, making them good candidates for sensor purposes. Incorporation of any other media, such as a liquid or a polymer in the nanopores of the optical fiber may be easily carried out by immersing of a portion of the optical fiber in the liquid or the polymer melt. Due to capillary action, the liquid or the polymer would be strongly drawn into the nanopores of the optical fiber. Embedding laser amplifying media, such as laser dyes, into the nanopores of the alumina microtubes would make them potential candidates for fiber amplifiers.

Further, it should be noted that deeply subwavelength and decoupled unit cells are a necessity here for the effective medium approximation to hold, particularly for waves with large transverse wave-vectors such as those that occur at large oblique angles of incidence or become evanescent in the waveguide. Having highly subwavelength structure to form the metamaterial is also very beneficial to reduce the scattering and wave-guide losses. This is very important for large transverse order waveguide modes in the indefinite permittivity/permeability waveguides, where the fields rapidly vary along the angular or transverse directions in the interior of the waveguide.

We conclude by noting that in almost all reports on this topic, the axes of the anisotropic medium and the waveguide coincide, while the metamaterial axes could be arbitrarily oriented. The very large parameter space made available for exploration by anisotropic and hyperboic metamaterials in the context of waveguides makes it certain that many important new phenomena and applications await us in the future.

Acknowledgements

AMJ thanks Department of Science and Technology, India for support with the J.C. Bose National Fellowship. AKI and MS thank the Natural Sciences and Engineering Research Council (NSERC) of Canada, the Canada Foundation for Innovation (CFI), Alberta Innovates, and the Province of Alberta for financial support.

References

[1] J. B. Pendry, A. Holden, W. Stewart, I. Youngs, "Extremely low frequency plasmons in metallic mesostructures", *Phys. Rev. Lett.* **76** (1996), no. 25, article no. 4773.

[2] J. B. Pendry, A. J. Holden, D. J. Robbins, W. Stewart *et al.*, "Magnetism from conductors and enhanced nonlinear phenomena", *IEEE Trans. Microw. Theory Tech.* **47** (1999), no. 11, p. 2075-2084.

[3] V. G. Veselago, "The electrodynamics of substances with simultaneously negative values of ϵ and μ", *Phys.-Usp.* **10** (1968), no. 4, p. 509-514.

[4] D. R. Smith, W. J. Padilla, D. Vier, S. C. Nemat-Nasser, S. Schultz, "Composite medium with simultaneously negative permeability and permittivity", *Phys. Rev. Lett.* **84** (2000), no. 18, article no. 4184.

[5] J. B. Pendry, "Negative refraction makes a perfect lens", *Phys. Rev. Lett.* **85** (2000), no. 18, article no. 3966.

[6] N. M. Litchinitser, A. I. Maimistov, I. R. Gabitov, R. Z. Sagdeev, V. M. Shalaev, "Metamaterials: electromagnetic enhancement at zero-index transition", *Opt. Lett.* **33** (2008), no. 20, p. 2350-2352.

[7] S. Zhang, W. Fan, N. Panoiu, K. Malloy, R. Osgood, S. Brueck, "Experimental demonstration of near-infrared negative-index metamaterials", *Phys. Rev. Lett.* **95** (2005), no. 13, article no. 137404.

[8] D. Smith, D. Vier, T. Koschny, C. Soukoulis, "Electromagnetic parameter retrieval from inhomogeneous metamaterials", *Phys. Rev. E* **71** (2005), no. 3, article no. 036617.

[9] D. Smith, D. Schurig, "Electromagnetic wave propagation in media with indefinite permittivity and permeability tensors", *Phys. Rev. Lett.* **90** (2003), no. 7, article no. 077405.

[10] Z. Jacob, L. V. Alekseyev, E. Narimanov, "Optical hyperlens: far-field imaging beyond the diffraction limit", *Opt. Express* **14** (2006), no. 18, p. 8247-8256.

[11] H. N. Krishnamoorthy, Z. Jacob, E. Narimanov, I. Kretzschmar, V. M. Menon, "Topological transitions in metamaterials", *Science* **336** (2012), no. 6078, p. 205-209.

[12] Q. Zhang, T. Jiang, Y. Feng, "Slow-light propagation in a cylindrical dielectric waveguide with metamaterial cladding", *J. Phys. D: Appl. Phys.* **44** (2011), no. 47, article no. 475103.

[13] D. Pratap, S. A. Ramakrishna, J. G. Pollock, A. K. Iyer, "Anisotropic metamaterial optical fibers", *Opt. Express* **23** (2015), no. 7, article no. 9074.

[14] S. Atakaramians, A. Argyros, S. C. Fleming, B. T. Kuhlmey, "Hollow-core waveguides with uniaxial metamaterial cladding: modal equations and guidance conditions", *J. Opt. Soc. Am. B* **29** (2012), no. 9, p. 2462-2477.

[15] A. Alù, N. Engheta, "Guided modes in a waveguide filled with a pair of single-negative (sng), double-negative (dng), and/or double-positive (dps) layers", *IEEE Trans. Microw. Theory Tech.* **52** (2004), no. 1, p. 199-210.

[16] A. Bhardwaj, K. V. Srivastava, S. A. Ramakrishna, "Enhanced coupling of light from subwavelength sources into a hyperbolic metamaterial fiber", *J. Lightwave Technol.* **37** (2019), no. 13, p. 3064-3072.

[17] J. G. Pollock, A. K. Iyer, "Below-cutoff propagation in metamaterial-lined circular waveguides", *IEEE Trans. Microw. Theory Tech.* **61** (2013), no. 9, p. 3169-3178.

[18] I. V. Shadrivov, A. A. Sukhorukov, Y. S. Kivshar, "Guided modes in negative-refractive-index waveguides", *Phys. Rev. E* **67** (2003), no. 5, article no. 057602.

[19] A. Bhardwaj, K. V. Srivastava, S. A. Ramakrishna, "Propagation of wave in a cylindrical waveguide filled with hyperbolic negative index medium", *Microw. Opt. Technol. Lett.* **62** (2020), no. 11, p. 3385-3390.

[20] K. Porsezian, V. C. Kuriakose, *Optical Solitons: Theoretical and Experimental Challenges, Vol. 613*, Springer Science & Business Media, Heidelberg, Germany, 2003.

[21] P. Russell, "Photonic crystal fibers", *Science* **299** (2003), no. 5605, p. 358-362.

[22] N. Singh, A. Tuniz, R. Lwin, S. Atakaramians, A. Argyros, S. C. Fleming, B. T. Kuhlmey, "Fiber-drawn double split ring resonators in the terahertz range", *Opt. Mater. Express* **2** (2012), no. 9, p. 1254-1259.

[23] M. G. Silveirinha, C. A. Fernandes, "Nonresonant structured material with extreme effective parameters", *Phys. Rev. B* **78** (2008), no. 3, article no. 033108.

[24] C. R. Simovski, P. A. Belov, A. V. Atrashchenko, Y. S. Kivshar, "Wire metamaterials: physics and applications", *Adv. Mater.* **24** (2012), no. 31, p. 4229-4248.

[25] M. Kadic, S. Guenneau, S. Enoch, S. A. Ramakrishna, "Plasmonic space folding: focusing surface plasmons via negative refraction in complementary media", *ACS Nano* **5** (2011), no. 9, p. 6819-6825.

[26] S. A. Ramakrishna, T. M. Grzegorczyk, *Physics and Applications of Negative Refractive Index Materials*, CRC Press, Bellingham, Washington, USA, 2008.

[27] J. B. Pendry, A. Holden, D. Robbins, W. Stewart, "Low frequency plasmons in thin-wire structures", *J. Phys.: Condens. Matter* **10** (1998), no. 22, article no. 4785.

[28] D. J. Bergman, "The dielectric constant of a composite material—a problem in classical physics", *Phys. Rep.* **43** (1978), no. 9, p. 377-407.

[29] T. G. Mackay, A. Lakhtakia, "Bruggeman formalism versus", *J. Nanophoton.* **6** (2012), no. 1, article no. 069501.

[30] S. Guenneau, F. Zolla, A. Nicolet, "Homogenization of 3d finite photonic crystals with heterogeneous permittivity and permeability", *Waves Random Complex Media* **17** (2007), no. 4, p. 653-697.

[31] A. Castanié, J.-F. Mercier, S. Félix, A. Maurel, "Generalized method for retrieving effective parameters of anisotropic metamaterials", *Opt. Express* **22** (2014), no. 24, p. 29937-29953.

[32] W. S. Weiglhofer, A. Lakhtakia, "On electromagnetic waves in biaxial bianisotropic media", *Electromagnetics* **19** (1999), no. 4, p. 351-362.

[33] X. Chen, B.-I. Wu, J. A. Kong, T. M. Grzegorczyk, "Retrieval of the effective constitutive parameters of bianisotropic metamaterials", *Phys. Rev. E* **71** (2005), no. 4, article no. 046610.

[34] C. E. Kriegler, M. S. Rill, S. Linden, M. Wegener, "Bianisotropic photonic metamaterials", *IEEE J. Sel. Top. Quantum Electron.* **16** (2009), no. 2, p. 367-375.

[35] T. G. Mackay, A. Lakhtakia, *Electromagnetic Anisotropy and Bianisotropy: A Field Guide*, World Scientific, Singapore, 2010.

[36] B. Gralak, M. Lequime, M. Zerrad, C. Amra, "Phase retrieval of reflection and transmission coefficients from Kramers–Kronig relations", *J. Opt. Soc. Am. A* **32** (2015), no. 3 (ts), p. 456-462.

[37] Y. Liu, S. Guenneau, B. Gralak, "Causality and passivity properties of effective parameters of electromagnetic multilayered structures", *Phys. Rev. B* **88** (2013), article no. 165104.

[38] A. Serdiukov, I. Semchenko, S. Tertyakov, A. Sihvola, *Electromagnetics of Bi-anisotropic Materials-Theory and Application, Vol. 11*, Gordon and Breach Science Publishers, Norwich, UK, 2001.

[39] G. Sauer, G. Brehm, S. Schneider, K. Nielsch, R. Wehrspohn, J. Choi, H. Hofmeister, U. Gösele, "Highly ordered monocrystalline silver nanowire arrays", *J. Appl. Phys.* **91** (2002), no. 5, p. 3243-3247.

[40] R. Kumar, F. A. Inam, A. Ly, C. Bradac, S. A. Ramakrishna, "Silver columnar thin-film-based half-wavelength antennas for bright directional emission from nanodiamond nitrogen-vacancy centers", *Phys. Rev. Appl.* **11** (2019), no. 3, article no. 034002.

[41] A. Poddubny, I. Iorsh, P. Belov, Y. Kivshar, "Hyperbolic metamaterials", *Nat. Photon.* **7** (2013), no. 12, article no. 948.

[42] L. Ferrari, C. Wu, D. Lepage, X. Zhang, Z. Liu, "Hyperbolic metamaterials and their applications", *Prog. Quantum Electron.* **40** (2015), p. 1-40.

[43] G. V. Eleftheriades, A. K. Iyer, P. C. Kremer, "Planar negative refractive index media using periodically LC loaded transmission lines", *IEEE Trans. Microw. Theory Tech.* **50** (2002), no. 12, p. 2702-2712.

[44] C. Caloz, T. Itoh, "Novel microwave devices and structures based on the transmission line approach of metamaterials", in *IEEE MTT-S International Microwave Symposium Digest, 2003*, vol. 1, IEEE, 2003, p. 195-198.

[45] A. Lai, C. Caloz, T. Itoh, "Transmission line based metamaterials and their microwave applications", *Microw. Mag.* **5** (2004), no. 3, p. 34-50.

[46] I. Nefedov, S. Tretyakov, "Waveguide containing a backward-wave slab", *Radio Sci.* **38** (2003), no. 6, p. 9-1.

[47] A. Alù, N. Engheta, "Pairing an epsilon-negative slab with a mu-negative slab: resonance, tunneling and transparency", *IEEE Trans. Antennas Propag.* **51** (2003), no. 10, p. 2558-2571.

[48] Y. Satomura, M. Matsuhara, N. Kumagai, "Analysis of electromagnetic-wave modes in anisotropic slab waveguide", *IEEE Trans. Microw. Theory Tech.* **22** (1974), no. 2, p. 86-92.

[49] I. V. Lindell, S. Ilvonen, "Waves in a slab of uniaxial bw medium", *J. Electromagn. Waves Appl.* **16** (2002), no. 3, p. 303-318.

[50] B.-I. Wu, T. M. Grzegorczyk, Y. Zhang, J. A. Kong, "Guided modes with imaginary transverse wave number in a slab waveguide with negative permittivity and permeability", *J. Appl. Phys.* **93** (2003), no. 11, p. 9386-9388.

[51] Y. Xu, "A study of waveguides filled with anisotropic metamaterials", *Microw. Opt. Technol. Lett.* **41** (2004), no. 5, p. 426-431.

[52] S. Hrabar, J. Bartolic, Z. Sipus, "Waveguide miniaturization using uniaxial negative permeability metamaterial", *IEEE Trans. Antennas Propag.* **53** (2005), no. 1, p. 110-119.

[53] R. Marques, J. Martel, F. Mesa, F. Medina, "Left-handed-media simulation and transmission of EM waves in subwavelength split-ring-resonator-loaded metallic waveguides", *Phys. Rev. Lett.* **89** (2002), no. 18, article no. 183901.

[54] R. Yang, Y. Xie, X. Yang, R. Wang, B. Chen, "Fundamental modal properties of srr metamaterials and metamaterial based waveguiding structures", *Opt. Express* **17** (2009), no. 8, p. 6101-6117.

[55] F.-Y. Meng, J.-H. Fu, G.-H. Yang, Q. Wu, L.-W. Li, "Backward and forward waves in a uniaxial anisotropic metamaterial waveguide", in *2008 International Conference on Microwave and Millimeter Wave Technology*, vol. 1, IEEE, 2008, p. 54-57.

[56] H. Zhu, X. Yin, L. Chen, Z. Zhu, X. Li, "Manipulating light polarizations with a hyperbolic metamaterial waveguide", *Opt. Lett.* **40** (2015), no. 20, p. 4595-4598.

[57] D. J. Roth, A. V. Krasavin, A. Wade, W. Dickson, A. Murphy, S. Kéna-Cohen, R. Pollard, G. A. Wurtz, D. Richards, S. A. Maier *et al.*, "Spontaneous emission inside a hyperbolic metamaterial waveguide", *ACS Photon.* **4** (2017), no. 10, p. 2513-2521.

[58] H. Ruan, Y. Shuang, L. Li, T. Cui, "Extraordinary optical transmission through a rectangular hole filled with extreme uniaxial metamaterials", *Opt. Lett.* **42** (2017), no. 12, p. 2386-2389.

[59] J. G. Pollock, A. K. Iyer, D. Pratap, S. A. Ramakrishna, "A class of circular waveguiding structures containing cylindrically anisotropic metamaterials: Applications from radio frequency/microwave to optical frequencies", *J. Appl. Phys.* **119** (2016), no. 8, article no. 083103.

[60] T. Dunster, "Bessel functions of purely imaginary order, with an application to second-order linear differential equations having a large parameter", *SIAM J. Math. Anal.* **21** (1990), no. 4, p. 995-1018.

[61] C. Chapman, "The asymptotic theory of dispersion relations containing Bessel functions of imaginary order", *Proc. R. Soc. A* **468** (2012), no. 2148, p. 4008-4023.

[62] A. Tuniz, B. Kuhlmey, R. Lwin, A. Wang, J. Anthony, R. Leonhardt, S. Fleming, "Drawn metamaterials with plasmonic response at terahertz frequencies", *Appl. Phys. Lett.* **96** (2010), no. 19, article no. 191101.

[63] A. Tuniz, R. Lwin, A. Argyros, S. C. Fleming, B. T. Kuhlmey, "Fabricating metamaterials using the fiber drawing method", *J. Vis. Exp.* **68** (2012), article no. e4299.

[64] A. Tuniz, K. J. Kaltenecker, B. M. Fischer, M. Walther, S. C. Fleming, A. Argyros, B. T. Kuhlmey, "Metamaterial fibres for subdiffraction imaging and focusing at terahertz frequencies over optically long distances", *Nat. Commun.* **4** (2013), article no. 2706.

[65] M. Yan, N. A. Mortensen, "Hollow-core infrared fiber incorporating metal-wire metamaterial", *Opt. Express* **17** (2009), no. 17, p. 14851-14864.

[66] D. Pratap, A. Bhardwaj, S. A. Ramakrishna, "Inhomogeneously filled, cylindrically anisotropic metamaterial optical fiber", *J. Nanophoton.* **12** (2018), no. 3, article no. 033002.

[67] D. Pratap, S. A. Ramakrishna, Nanoporous alumina microtubes for metamaterial and plasmonic applications, *preprint*, arXiv:1903.10296 (2018).

[68] W. Cai, V. Shalaev, *Optical Metamaterials: Fundamentals and Applications*, Springer, New York, 2009.

[69] M. J. Weber, *Handbook of Optical Materials*, CRC Press, Washington, D.C., 2003.

[70] C.-C. Lai, C.-Y. Lo, J.-Z. Huang, C.-C. F. Chiang, D. H. Nguyen, Y.-P. Chen, C.-D. Liao, "Architecting a nonlinear hybrid crystal–glass metamaterial fiber for all-optical photonic integration", *J. Mater. Chem. C* **6** (2018), no. 7, p. 1659-1669.

[71] C.-C. Lai, C.-Y. Lo, T.-H. Hsieh, W.-S. Tsai, D. H. Nguyen, Y.-R. Ma, "Ligand-driven and full-color-tunable fiber source: toward next-generation clinic fiber-endoscope tomography with cellular resolution", *ACS Omega* **1** (2016), no. 4, p. 552-565.

[72] C.-C. Lai, C.-Y. Lo, D. H. Nguyen, J.-Z. Huang, W.-S. Tsai, Y.-R. Ma, "Atomically smooth hybrid crystalline-core glass-clad fibers for low-loss broadband wave guiding", *Opt. Express* **24** (2016), no. 18, p. 20089-20106.

[73] A. Bhardwaj, K. V. Srivastava, S. A. Ramakrishna, "Hyperbolic metamaterial near-field coupler", in *2019 IEEE Asia-Pacific Microwave Conference (APMC)*, IEEE, 2019, p. 1736-1738.

[74] J. G. Pollock, A. K. Iyer, "Miniaturized circular-waveguide probe antennas using metamaterial liners", *IEEE Trans. Antennas Propag.* **63** (2014), no. 1, p. 428-433.

[75] J. G. Pollock, A. K. Iyer, "Effective-medium properties of cylindrical transmission-line metamaterials", *IEEE Antennas Wirel. Propag. Lett.* **10** (2011), p. 1491-1494.

[76] P. K. Choudhury, W. K. Soon, "On the tapered optical fibers with radially anisotropic liquid crystal clad", *Prog. Electromagn. Res.* **115** (2011), p. 461-475.

[77] M. M. Hasan, D. S. Kumar, M. R. C. Mahdy, D. N. Hasan, M. A. Matin, "Robust optical fiber using single negative metamaterial cladding", *IEEE Photon. Technol. Lett.* **25** (2013), no. 11, p. 1043-1046.

[78] S. Hou, S. Zhang, Y. Liu, D. Wang, J. Lei, "Investigation on characteristics of w-type fiber with an inner cladding made of negative refractive index materials", *Optik* **125** (2014), no. 20, p. 6127-6130.

[79] J. G. Pollock, A. K. Iyer, "Experimental verification of below-cutoff propagation in miniaturized circular waveguides using anisotropic ENNZ metamaterial liners", *IEEE Trans. Microw. Theory Tech.* **64** (2016), no. 4, p. 1297-1305.

[80] E. Baladi, J. G. Pollock, A. K. Iyer, "New approach for extraordinary transmission through an array of subwavelength apertures using thin ENNZ metamaterial liners", *Opt. Express* **23** (2015), no. 16, article no. 20356.

[81] H. A. Bethe, "Theory of diffraction by small holes", *Phys. Rev.* **66** (1944), p. 163-182.

[82] M. F. Limonov, M. V. Rybin, A. N. Poddubny, Y. S. Kivshar, "Fano resonances in photonics", *Nat. Photon.* **11** (2017), no. 9, p. 543-554.

[83] R. W. Ziolkowski, A. Erentok, "Metamaterial-based efficient electrically small antennas", *IEEE Trans. Antennas Propag.* **54** (2006), no. 7, p. 2113-2130.

[84] A. Alù, N. Engheta, "Polarizabilities and effective parameters for collections of spherical nanoparticles formed by pairs of concentric double-negative, single-negative, and/or double-positive metamaterial layers", *J. Appl. Phys.* **97** (2005), no. 9, article no. 094310.

[85] N. Engheta, "An idea for thin subwavelength cavity resonators using metamaterials with negative permittivity and permeability", *IEEE Antennas Wirel. Propag. Lett.* **1** (2002), p. 10-13.

[86] A. Alù, N. Engheta, "An overview of salient properties of planar guided-wave structures with Double-Negative (DNG) and Single-Negative (SNG) layers", in *Negative-Refraction Metamaterials*, John Wiley & Sons, Inc., Hoboken, NJ, USA, 2005, p. 339-380.

[87] A. Alu, N. Engheta, "Guided modes in a waveguide filled with a pair of Single-Negative (SNG), Double-Negative (DNG), and/or Double-Positive (DPS) layers", *IEEE Trans. Microw. Theory Tech.* **52** (2004), no. 1, p. 199-210.

[88] E. Baladi, A. K. Iyer, "Far-field magnification of subdiffraction conducting features using metamaterial-lined aperture arrays", *IEEE Trans. Antennas Propag.* **66** (2018), no. 7, p. 3482-3490.

[89] M. Semple, E. Baladi, A. K. Iyer, "Optical metasurface based on subwavelength nanoplasmonic metamaterial-lined apertures", *IEEE J. Sel. Top. Quantum Electron.* **25** (2019), no. 3, p. 1-8.

[90] A. Alu, N. Engheta, "Optical metamaterials based on optical nanocircuits", *Proc. IEEE* **99** (2011), no. 10, p. 1669-1681.

[91] N. Engheta, "From RF circuits to optical nanocircuits", *IEEE Microw. Mag.* **13** (2012), no. 4, p. 100-113.

[92] M. G. Silveirinha, A. Alù, J. Li, N. Engheta, "Nanoinsulators and nanoconnectors for optical nanocircuits", *J. Appl. Phys.* **103** (2008), no. 6, article no. 064305.

[93] H. Caglayan, S.-H. Hong, B. Edwards, C. R. Kagan, N. Engheta, "Near-infrared metatronic nanocircuits by design", *Phys. Rev. Lett.* **111** (2013), no. 7, article no. 073904.

[94] N. Engheta, "Circuits with light at nanoscales: optical nanocircuits inspired by metamaterials", *Science (New York, N.Y.)* **317** (2007), no. 5845, p. 1698-1702.

[95] T. W. Ebbesen, H. J. Lezec, H. F. Ghaemi, T. Thio, P. A. Wolff, "Extraordinary optical transmission through subwavelength hole arrays", *Nature* **391** (1998), no. 6668, p. 667-669.

[96] J. B. Pendry, L. Martín-Moreno, F. J. Garcia-Vidal, "Mimicking surface plasmons with structured surfaces", *Science (New York, N.Y.)* **305** (2004), no. 5685, p. 847-848.

[97] R. W. Wood, "On a remarkable case of uneven distribution of light in a diffraction grating spectrum", *Proc. Phys. Soc. Lond.* **18** (1902), no. 1, p. 269.

[98] A. Hessel, A. A. Oliner, "A new theory of wood's anomalies on optical gratings", *Appl. Opt.* **4** (1965), no. 10, p. 1275-1297.

[99] F. Medina, F. Mesa, R. Marques, "Extraordinary transmission through arrays of electrically small holes from a circuit theory perspective", *IEEE Trans. Microw. Theory Tech.* **56** (2008), no. 12, p. 3108-3120.

[100] S. Ghosh, K. V. Srivastava, "An equivalent circuit model of FSS-based metamaterial absorber using coupled line theory", *IEEE Antennas Wirel. Propag. Lett.* **14** (2015), p. 511-514.

[101] B. B. A. Munk, *Frequency Selective Surfaces: Theory and Design*, John Wiley & Sons, New York, USA, 2000.

[102] N. Liu, H. Liu, S. Zhu, H. Giessen, "Stereometamaterials", *Nat. Photon.* **3** (2009), no. 3, p. 157-162.

[103] M. Decker, R. Zhao, C. M. Soukoulis, S. Linden, M. Wegener, "Twisted split-ring-resonator photonic metamaterial with huge optical activity", *Opt. Lett.* **35** (2010), no. 10, article no. 1593.

[104] A. Arbabi, A. Faraon, "Fundamental limits of ultrathin metasurfaces", *Sci. Rep.* **7** (2017), no. 1, article no. 43722.

Comptes Rendus
Physique
2020, 21, nº 7-8, p. 713-749
`https://doi.org/10.5802/crphys.32`

Metamaterials 2 / *Métamatériaux 2*

Design of acoustic metamaterials made of Helmholtz resonators for perfect absorption by using the complex frequency plane

Conception de métamatériaux acoustiques constitués de résonateurs de Helmholtz pour l'absorption parfaite dans le plan des fréquences complexes

V. Romero-García[*, a], **N. Jiménez**[a], **G. Theocharis**[a], **V. Achilleos**[a], **A. Merkel**[a], **O. Richoux**[a], **V. Tournat**[a], **J.-P. Groby**[a] **and V. Pagneux**[a]

[a] Laboratoire d'Acoustique de l'Université du Mans (LAUM), UMR 6613, Institut d'Acoustique - Graduate School (IA-GS), CNRS, Le Mans Université, France

Current addresses: I3M, Instituto de Instrumetación para Imagen Molecular, CSIC - Universitat Politècnica de València, València, Spain (N. Jiménez), Université de Lorraine, CNRS, Institut Jean Lamour, F-54000 Nancy, France (A. Merkel)

E-mails: vicente.romero@univ-lemans.fr (V. Romero-García), nojigon@upv.es (N. Jiménez), Georgios.Theocharis@univ-lemans.fr (G. Theocharis), Achilleos.Vassos@univ-lemans.fr (V. Achilleos), aurelien.merkel@univ-lemans.fr (A. Merkel), olivier.richoux@univ-lemans.fr (O. Richoux), vincent.tournat@univ-lemans.fr (V. Tournat), Jean-Philippe.Groby@univ-lemans.fr (J.-P. Groby), Vincent.Pagneux@univ-lemans.fr (V. Pagneux)

Abstract. In this review, we present the results on sub-wavelength perfect acoustic absorption using acoustic metamaterials made of Helmholtz resonators with different setups. Low frequency perfect absorption requires to increase the number of states at low frequencies and finding the good conditions for impedance matching with the background medium. If, in addition, one wishes to reduce the geometric dimensions of the proposed structures for practical issues, one can use properly designed local resonators and achieve sub-wavelength perfect absorption. Helmholtz resonators have been shown good candidates due to their easy tunability of the geometry, so of the resonance frequency, the energy leakage and the intrinsic losses. When plugged to a waveguide or a surrounding medium they behave as open, lossy and resonant systems characterized by their energy leakage and intrinsic losses. The balance between these two represents the critical coupling condition and gives rise to maximum energy absorption. The critical coupling mechanism is represented here in the complex frequency plane in order to interpret the impedance matching condition. In this

---

[*] Corresponding author.

ISSN (electronic) : 1878-1535

review we discuss in detail the possibility to obtain perfect absorption by these critical coupling conditions in different systems such as reflection (one-port), transmission (two-ports) or three-ports systems.

Résumé. Dans cette revue, nous présentons des résultats sur l'absorption acoustique parfaite sub-longueur d'onde faisant appel à des métamatériaux acoustiques avec des résonateurs Helmholtz pour différentes configurations. L'absorption parfaite à basse fréquence nécessite une augmentation du nombre d'états aux basses fréquences ainsi que de trouver les bonnes conditions pour une adaptation d'impédance avec le milieu environnant. Si en outre, on souhaite réduire les dimensions géométriques des structures proposées pour des questions pratiques, on peut utiliser des résonateurs locaux judicieusement conçus afin d'attendre une absorption parfaite sub-longueur d'onde. Les résonateurs de Helmholtz se sont révélés de bons candidats en raison de leur accordabilité aisée de la géométrie, donc de la fréquence de résonance, de la fuite d'énergie et des pertes intrinsèques. Lorsqu'ils sont branchés à un guide d'ondes ou à un milieu environnant, ils se comportent comme des systèmes ouverts, avec pertes et résonances caractérisés par leur fuite d'énergie et leurs pertes intrinsèques. L'équilibre entre ces deux aspects représente la condition de couplage critique et donne lieu à un maximum d'absorption d'énergie. Le mécanisme de couplage critique est ici représenté dans le plan de fréquence complexe afin d'interpréter la condition d'adaptation d'impédance. Dans cette revue, nous discutons en détail la possibilité d'obtenir une absorption parfaite par ces conditions de couplage critiques dans différents systèmes tels que la réflexion (à un port), la transmission (à deux ports) ou les systèmes à trois ports.

Keywords. Acoustic metamaterials, Perfect absorption, Helmholtz resonators, Locally resonant materials, Critical coupling, Complex frequency plane.

Mots-clés. Métamatériaux acoustiques, Absorption parfaite, Résonateurs de Helmholtz, Résonateurs locaux, Couplage critique, Plan des fréquences complexes.

1. Introduction

The ability to perfectly absorb an incoming wave field in a sub-wavelength material is advantageous for several applications in wave physics as energy conversion [1], time reversal technology [2], coherent perfect absorbers [3] or soundproofing [4] among others. The solution of this challenge requires to solve a complex problem: reducing the geometric dimensions of the structure while increasing the number of states at low frequencies and finding the good conditions to match the impedance to the background medium.

A successful approach for increasing the number states at low frequencies with reduced dimensions is the use of metamaterials. Although the definition of metamaterial is still a source of discussion within the community, in this article, we will name metamaterial a structured system made of resonant elements with physical properties not usually encountered for wavelengths much larger than its dimensions. Exponentially increasing attention has been paid to these systems in all the fields of wave physics as electromagnetics [5], acoustics [6], elastodynamics [7, 8] and seismology [9], among others. In acoustics, the concept of metamaterial was introduced in the 2000s by Liu *et al.* [10] and Fang *et al.* [11]. Applications cover all frequency ranges from low-frequency vibrations to radio frequencies [6, 12]. Several possibilities based on these locally resonant systems have been recently proposed to design sound absorbing structures with simultaneous sub-wavelength dimensions and strong acoustic absorption [13–18]. Some strategies to design these sub-wavelength systems consist of using space-coiling structures [19–22], membranes [23], reconfigurable structures [24, 25] or Helmholtz resonators (HRs) [11, 26, 27]. However, all of these structures face the challenge of impedance mismatch to the background medium while they bring potentially solutions to reduce the geometric dimensions. Recently, several possibilities based on these systems made of open lossy resonant building blocks have been proposed to design sound absorbing structures with impedance match conditions, presenting simultaneously sub-wavelength dimensions and perfect acoustic absorption. Examples are acoustic metamaterials made of membranes [13, 28–31], quater wavelength resonators [32], bubbles in water [33], aerogel plates [34], split ring resonators [35] or HRs [20, 28, 36–51]. Among them, HRs have been shown as potential candidates to solve the problem due to the tunable possibilities they offer just by optimizing their geometry. In this work, the resonance frequency, the energy leakage and the intrinsic losses can be passively tuned by the geometry of the resonator. In fact, the energy leakage of the HRs can be controlled by the aperture of the neck and the inherent viscothermal losses in the neck and in the cavity. We also show an example of nonlinear absorption in which the losses are driven dynamically with the amplitude of the incident wave.

The interaction of an incoming wave with an open, lossy and resonant structure, in particular the impedance matching with the background field, is one of the most studied process in the field of wave physics [1–3]. These open systems, at the resonant frequency, are characterized by both the leakage rate of energy (i.e., the coupling of the resonant elements with the propagating medium), and the intrinsic losses of the resonator. The balance between the leakage and the losses activates the condition of critical coupling, trapping the energy around the resonant elements and generating a maximum of energy absorption [36, 52]. In the case of a reflecting system (one port systems), either symmetric or antisymmetric resonances that are critically coupled can be used to obtain perfect absorption (PA) of energy [28, 29, 33, 37]. In the case of transmission systems with N-ports [53], the problems becomes more difficult. In particular for the two port case, degenerate critically coupled resonators with symmetric and antisymmetric resonances [30, 51, 54] or systems with broken symmetry [39, 42] can be used to perfectly absorb the incoming energy. At this stage it is worth noting what we consider as symmetry. If either the geometry of the resonator or the profile of the wave field are mirror symmetric (antisymmetric) with respect to the middle plane of the resonator, then the system will be considered as symmetric (antisymmetric).

In this review we discuss the technique based on the analysis of the zeros and poles of the eigenvalues of the scattering matrix. In general these zeros and poles correspond to complex frequencies, then we introduce a representation in the complex frequency plane, i.e., real versus imaginary part of the complex frequency, applied to the case of acoustic metamaterials made of HRs for deep sub-wavelength PA. This methodology has been shown as an efficient tool to design broadband acoustic absorbers in the low frequency range. In our case, fine tuning of both the losses and of the geometric characteristics of the sub-wavelength resonators lead to the crossing of the complex zeros of the eigenvalues of the scattering matrix with the real frequency axis, i.e., they appear at purely real frequencies, which signifies the PA condition. This methodology has been also used to design efficient broadband absorbers in the low frequency regime. Different systems corresponding to different configurations are studied in this work: single port configuration in which corresponds to the pure reflection problem; two port systems in which the transmission problem with single side excitation can be analyzed; and multiport systems, in particular a 3-port system. Several examples of perfect and broadband absorption in all of these configurations are reviewed in detail in this work.

2. Scattering problem in 1D systems

2.1. *General problem*

Let us consider a two-port, one-dimensional and reciprocal scattering process. The relation between the amplitudes of the incoming (a, d), and outcoming (b, c) waves, on both sides of

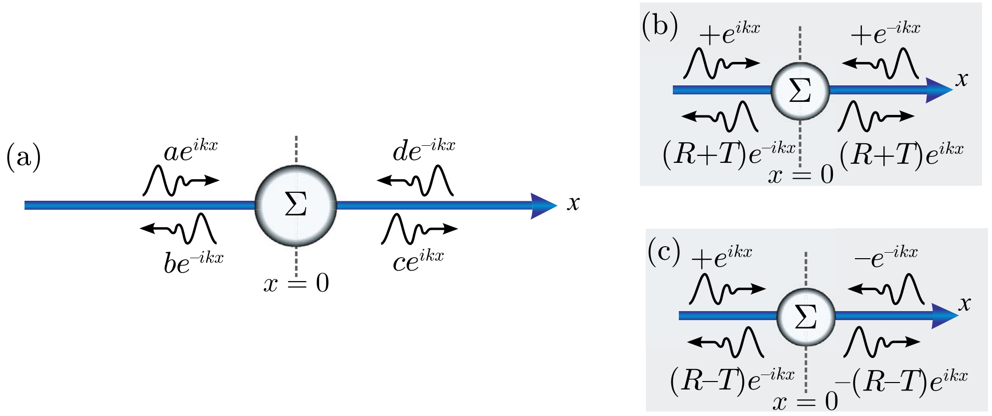

Figure 1. (a) Schematic of the two-port scattering process. (b) Symmetric and (c) antisymmetric uncoupled sub-problems for the case of a mirror-symmetric scatterer Σ. The time convention is $e^{-i\omega t}$. The weve number is $k = \omega/c$ with c the acoustic wave speed.

the scatterer Σ, as shown in Figure 1(a), is given by

$$\begin{pmatrix} c \\ b \end{pmatrix} = \mathbf{S}(f)\begin{pmatrix} a \\ d \end{pmatrix} = \begin{pmatrix} T & R^+ \\ R^- & T \end{pmatrix}\begin{pmatrix} a \\ d \end{pmatrix}, \tag{1}$$

where $\mathbf{S}(f)$ is the scattering matrix (S-matrix), f is the incident wave frequency, T is the complex amplitude transmission coefficient, R^- and R^+ are the complex amplitude reflection coefficients for left ($-$) and right ($+$) incidence, respectively. Note that the power scattering coefficients are, $|R^+|^2$, $|R^-|^2$ and $|T|^2$. In this work, the time dependence convention of the harmonic regime is $e^{-i\omega t}$, and it will be omitted in the following. The eigenvalues of the S-matrix are expressed as

$$\lambda_{1,2} = T \pm [R^- R^+]^{1/2} \tag{2}$$

and the eigenvectors of the system are

$$\begin{aligned} \mathbf{v_1} &= (v_{11}, v_{12}) = \left(R^+, -\sqrt{R^+R^-}\right) \\ \mathbf{v_2} &= (v_{21}, v_{22}) = \left(\sqrt{R^+R^-}, R^+\right). \end{aligned} \tag{3}$$

Therefore, the ratio of the eigenvector components v_{1i} and v_{2i} is $v_{2i}/v_{1i} = (-1)^i (R^-/R^+)^{1/2}$. A zero eigenvalue of the S-matrix corresponds to the case in which the incident waves corresponding to the eigenvectors of the S-matrix can be completely absorbed ($b = c = 0$). This, called coherent perfect absorption (CPA) [55], happens when $T = \pm[R^- R^+]^{1/2}$ and the incident waves a, d correspond to the relevant eigenvector.

Mirror symmetric scatterer

If the scatterer Σ is mirror symmetric with respect to the $x = 0$ plane, $R^+ = R^- \equiv R$ and the problem can be reduced to two uncoupled sub-problems by choosing incident waves that are symmetric (see Figure 1(b)) or antisymmetric (see Figure 1(c)) with the reflection coefficients $R_s = R + T$ and $R_a = R - T$. In particular, the reflection and transmission coefficients of the initial problem in Figure 1(a) can be expressed as $R = (R_s + R_a)/2$, and $T = (R_s - R_a)/2$ while the eigenvalues of the S-matrix can be written as $\lambda_1 = R_s$ and $\lambda_2 = -R_a$. For a one-sided incident wave, the absorption coefficient defined as $\alpha = 1 - |R|^2 - |T|^2$ becomes $\alpha = (\alpha_s + \alpha_a)/2$, where

$\alpha_s \equiv 1-|R_s|^2$ and $\alpha_a \equiv 1-|R_a|^2$. Achieving $\alpha(f_{\max}) = 1$ at a frequency $f_{\max}$, is equivalent to getting simultaneously the minima of the reflection coefficients of the two sub-problems, i.e., $R_a(f_{\max}) = R_s(f_{\max}) = 0$ $[\alpha_s(f_{\max}) = \alpha_a(f_{\max}) = 1]$. This has been achieved in Ref. [54] for a mirror symmetric slab made of graphene and a photonic crystal through intensive numerical calculations. In acoustics, these degenerate resonators have been analyzed and realized in Refs. [30, 51, 54].

Point symmetric scatterer

We now further consider that Σ is a point scatterer, i.e., its length is reduced to $x = 0$. In other words, the wavelength corresponding to the working frequency is much larger than the characteristic dimension of the resonator, which is the radius of the neck of a HR. This case is also relevant to the study of absorption by deep sub-wavelength scatterers. Imposing the continuity of the wave-field at this point [42] yields $1 + R = T$. This corresponds to $R_a = -1$, i.e., the scatterer Σ is transparent to antisymmetric incident waves, $\alpha_a = 0$, and thus $\alpha = \alpha_s/2 \le 1/2$. The maximum value of one-sided absorption, appears at $f_{\max}$, is $\alpha(f_{\max}) = 1/2$. It corresponds to $\alpha_s(f_{\max}) = 1$ which gives $R_s(f_{\max}) = \lambda_1(f_{\max}) = 0$, and $R(f_{\max}) = -T(f_{\max}) = 1/2$. Thus, $\alpha(f_{\max}) = 1/2$ corresponds to CPA to the two-incident waves problem for symmetric and in phase incoming waves at $f_{\max}$, i.e., $v_2(f_{\max})/v_1(f_{\max}) = 1$ [56].

Mirror asymmetric scatterer

In the most general case Σ could be asymmetric, such that $R^+ \neq R^-$. In this case two absorption coefficients can be defined, $\alpha^+ = 1 - |T|^2 - |R^+|^2$ and $\alpha^- = 1 - |T|^2 - |R^-|^2$. When the eigenvalues of the scattering matrix are zero, $T = \pm\sqrt{R^+R^-}$. Therefore as soon as one of the reflection coefficients reaches zero, $T = 0$ and the system can present unidirectional perfect one-side absorption (UNPOA). The eigenvectors of the system will be represented by $\mathbf{v_1} = (R^+, -\sqrt{R^+R^-})$ and $\mathbf{v_2} = (\sqrt{R^+R^-}, R^+)$. From the analysis of the eigenvectors, the direction from which PA is obtained corresponds to an eigenvector equal to $(0, 0)$. This situation has been exploited in acoustics to design UNPOA units [42, 45] and UNPOA panels [39].

2.2. *Complex frequency plane*

In the previous section we have highlighted the relevance of the eigenvalues and eigenvectors of the scattering matrix to identify the situations of PA in the system. A graphical procedure with rich information consists of representing these eigenvalues or the components of the eigenvectors in a complex frequency plane, in which the real part of the frequency is represented in the abscissas and the ordinates are used to represent the corresponding imaginary part [36, 57, 58].

In this section we analyze the reflection problems in order to introduce the concept of the zeros and the poles of the reflection coefficient representing the scattering of the problem, in the complex frequency plane. The information given by this representation will be exploited to interpret the PA in terms of the critical coupling conditions.

Consider the simple case of a slot with a quarter wavelength resonance plugged to a waveguide as shown in Figure 2(a). Since the interest is in the low frequency regime, only single-mode reflected waves are considered. In other words, attention is paid to the range of frequencies, f, smaller than the cutoff frequency of the waveguide; therefore the problem can be considered as 1D. This one-mode approximation allows us to illustrate with very simple analytic expressions the appearance of the zeros and poles of the reflection coefficient. The geometry of interest is displayed in Figure 2(a): it corresponds both to an incident wave on a slot of length L and section S_2 at the end of a waveguide of section S_1 or to a wave normally incident on a wall with periodic slots.

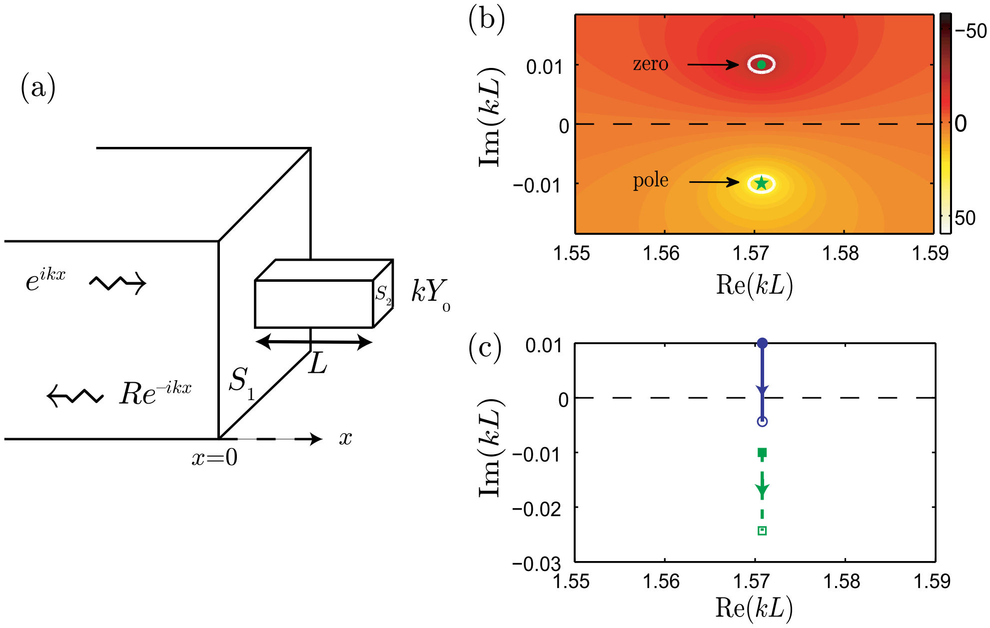

Figure 2. Analysis of the complex plane for the slot. (a) Scheme of the slot. (b) Representation of the 20 log($|R|$) in the complex frequency plane for the lossless case. The analyzed slot has the following parameters $L = 25$ cm, $S_2/S_1 = 0.1$. The dot and the star represent the zero and the pole respectively obtained considering the low frequency approximation (Equations (6) and (7)). (c) Dependence of the complex frequency of the zero (continuous line) and the pole (dashed line) on the losses added to the system. Arrows show the direction of the trajectory of the pole as the losses are increased. Filled symbols represent the lossless case and open symbols represent the last considered lossy case.

A plane wave is incident from the left such that a total wave of the form

$$p = \mathrm{e}^{\mathrm{i}kx} + R\mathrm{e}^{-\mathrm{i}kx} \tag{4}$$

is created in $x < 0$. The wavenumber is $k = \omega/c$ with c the acoustic wave speed.

2.2.1. *Lossless case*

For a rigid wall at the end of the slot $p'(L) = 0$ and thus $p'(0^+)/p(0^+) = k\tan(kL)$, with the prime denoting differentiation with respect to x. Then, assuming a one-mode approximation, the continuity conditions are $p(0^-) = p(0^+)$ and $S_1 p'(0^-) = S_2 p'(0+)$. That leads to the expression of the reflection coefficient

$$R = \frac{\cot(kL) + \mathrm{i}S_2/S_1}{\cot(kL) - \mathrm{i}S_2/S_1}. \tag{5}$$

For a real frequency (k real), $|R| = 1$ is recognized as dictated by energy conservation. Going to the complex frequency plane (complex k), Equation (5) shows that R satisfies $\overline{R(k)} = 1/R(\overline{k})$ where $\overline{r(k)}$ and $\overline{k}$ represent the complex conjugate of $R(k)$ and k respectively. The reflection coefficient has pairs of poles and zeros that are complex conjugate, where the poles have a negative imaginary part and the zeros have a positive imaginary part. These properties are general [59]; they come from the structure of the wave equation (Helmholtz equation) and are independent of the one-mode approximation used in this calculation.

From (5), the poles correspond to $\cot(kL) - \mathrm{i}S_2/S_1 = 0$ and the zeros to $\cot(kL) + \mathrm{i}S_2/S_1 = 0$. Assuming that the slot is thin ($S_2/S_1 \ll 1$), the expression of the first pole–zero pair is given by

$$(kL)_{\text{pole}} = \frac{\pi}{2} - \mathrm{i}\frac{S_2}{S_1}, \tag{6}$$

$$(kL)_{\text{zero}} = \frac{\pi}{2} + \mathrm{i}\frac{S_2}{S_1}. \tag{7}$$

Next pairs of pole–zero are just shifted by $m\pi$ ($m \geq 1$) and will not be regarded in the following. The complex pole of (6) corresponds to a complex resonance frequency of the slot with an open end at $x = 0$. The imaginary part (S_2/S_1) represents the leakage due to the radiation at the open end towards the exterior of the slot. With the convention of time dependence used in this work, the wave at the resonance frequency decreases as $\mathrm{e}^{\mathrm{Im}(\omega^{\text{pole}})t}$ (where $\omega^{\text{pole}} = (kL)_{\text{pole}}c/L$), thus the decay time, τ_{leak}, can be related with the quality factor due to the leakage as,

$$Q_{\text{leak}} = \frac{\mathrm{Re}(\omega_{\text{pole}})\tau_{\text{leak}}}{2} = \frac{\mathrm{Re}(\omega_{\text{pole}})}{2\mathrm{Im}(\omega_{\text{pole}})}, \tag{8}$$

where the leakage rate can be defined as $\Gamma_{\text{leak}} = 1/\tau_{\text{leak}} = \mathrm{Im}(\omega_{\text{pole}})$. The $|R|$ in the complex frequency plane is shown in Figure 2(b). According to the theory, there is a pole with negative imaginary part and a zero which is its complex conjugate (with an opposite imaginary part). In the neighborhood of the pole–zero pair, R is just given by $R = (kL - \pi/2 - \mathrm{i}S_2/S_1)/(kL - \pi/2 + \mathrm{i}S_2/S_1)$. Consequently, for real frequency (k real), although $|R| = 1$, the complex resonance frequency is seen as a rapid phase change of the reflection coefficient around $kL = \pi/2$. The imaginary part, which is related with the leakage rate of energy from the slot to the surrounding space, is equal to S_2/S_1, and it gives the quality factor of this rapid phase change.

2.2.2. *Lossy case*

Now a lossy coating at the end of the slot, such that $p'(L) = kY_0 p(L)$ where $\mathrm{Im}(Y_0) > 0$ is considered. The reduced admittance Y_0 has a positive imaginary part that corresponds to the loss of the coating. By using $p'(0^+)/p(0^+) = (k\tan(kL) + p'(L)/p(L))(1 - \tan(kL)/k \times p'(L)/p(L))$, the reflection coefficient is changed from (5) to

$$R = \frac{\cot(kL) - Y_0 + \mathrm{i}S_2/S_1(1 + Y_0\cot(kL))}{\cot(kL) - Y_0 - \mathrm{i}S_2/S_1(1 + Y_0\cot(kL))}. \tag{9}$$

Due to the loss ($\mathrm{Im}(Y_0) > 0$), $|R| < 1$ for real frequency k. Besides, the pole–zero pair is now shifted in the complex k plane. For thin slot and small coating ($Y_0 = O(S_2/S_1) \ll 1$), the pair is given analytically by

$$(kL)_{\text{pole}} = \frac{\pi}{2} - \mathrm{i}\frac{S_2}{S_1} - Y_0, \tag{10}$$

$$(kL)_{\text{zero}} = \frac{\pi}{2} + \mathrm{i}\frac{S_2}{S_1} - Y_0. \tag{11}$$

By comparing (6)–(7) and (10)–(11) the effect of the lossy coating is explicit: the pole and the zero are shifted downwards in the complex frequency plane by Y_0. This shift is illustrated in Figure 2(c) for a purely resistive admittance $Y_0 = \mathrm{i}A$ with $A > 0$.

From the point of view of absorption defined as $\alpha = 1 - |R|^2$, all that has decisive consequences: the zero of r coincides with the real frequency axis (k real) of the complex plane when

$$S_2/S_1 = \mathrm{Im}(Y_0). \tag{12}$$

Then, there is total absorption (for a real frequency) and it corresponds to the critical coupling where the leakage (S_2/S_1) is balanced by the loss ($\mathrm{Im}(Y_0)$). It is worthwhile to emphasize here that the narrowband or broadband character of this absorption peak is only governed by the radiation

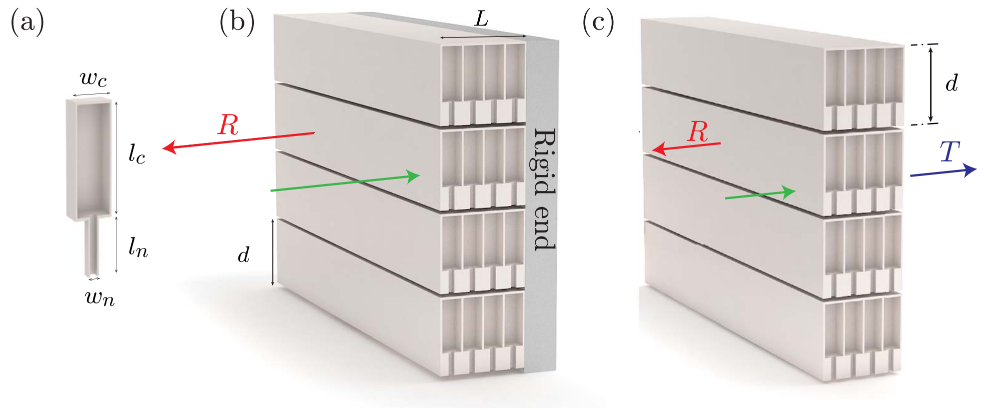

Figure 3. (a) Square cross-section HRs. (b) Conceptual view of the metamaterial panel placed on a rigid end with $N = 4$ layers of HRs. (c) Conceptual view of the metamaterial panel with $N = 4$ layers of HRs for the transmission problem.

leakage through the distance between the pole and the zero in the complex frequency plane. The loss just shifts the pole–zero pair (see (10)–(11)).

The situation of PA in the reflection problem in acoustics, described in this section with a toy model, has been exploited in real conditions to obtain deep sub-wavelength anechoic terminations by means of resonant building blocks made of slow sound metamaterials [32, 37], porous membranes [28], membranes [31], decorated membranes [29], bubble metascreens [33] and aerogel-like metamaterials [34], among other systems.

2.3. *Helmholtz resonators*

In this work we use HRs with either square or cylindrical cross-section. HRs with square (cylindrical) cross sections are characterized by a neck and cavity of width w_n and w_c (of radius r_n and r_c) and length l_n and l_c respectively (see Figure 3(a)). The HR is loaded in cylindrical waveguides (of radius r) or in two-dimensional slits (of height h). Two examples of HRs loaded in slits embedded in panels are shown in Figures 3(b) and (c) for the reflection and transmission problems. The visco-thermal losses in the system are considered in the resonators as well as in the slits or in the main waveguides by using its effective complex and frequency dependent parameters [60].

Using the effective parameters for the neck and cavity elements of a HR, the impedance can be written as

$$Z_{\mathrm{HR}} = \mathrm{i} Z_n \frac{A - \tan k_n l_n \tan k_c l_c}{A \tan k_n l_n + \tan k_c l_c}, \tag{13}$$

with $A = Z_c / Z_n$, l_n and l_c are the neck and cavity lengths, S_n and S_c are the neck and cavity surfaces and k_n and k_c, and Z_n and Z_c are the effective wavenumbers and effective characteristic impedance in the neck and cavity respectively. As we are using either square or cylindrical cross section HRs, the neck and cavity surfaces should be calculated corresponding to each case.

Equation (13) is not exact as long as correction due to the radiation should be included. The characteristic impedance accounting for the neck radiation can be expressed as [61]:

$$Z_{\mathrm{HR}} = -\mathrm{i} \frac{\cos(k_n l_n)\cos(k_c l_c) - Z_n k_n \Delta l \cos(k_n l_n)\sin(k_c l_c)/Z_c - Z_n \sin(k_n l_n)\sin(k_c l_c)/Z_c}{\sin(k_n l_n)\cos(k_c l_c)/Z_n - k_n \Delta l \sin(k_n l_n)\sin(k_c l_c)/Z_c + \cos(k_n l_n)\sin(k_c l_c)/Z_c}, \tag{14}$$

where the correction length is deduced from the addition of two correction lengths $\Delta l = \Delta l_1 + \Delta l_2$ as

$$\Delta l_1 = 0.82\left[1 - 1.35\frac{r_n}{r_c} + 0.31\left(\frac{r_n}{r_c}\right)^3\right] r_n, \tag{15}$$

$$\Delta l_2 = 0.82\left[1 - 0.235\frac{r_n}{r_s} - 1.32\left(\frac{r_n}{r_t}\right)^2\right. \tag{16}$$

$$\left. + 1.54\left(\frac{r_n}{r_t}\right)^3 - 0.86\left(\frac{r_n}{r_t}\right)^4\right] r_n. \tag{17}$$

The first length correction, Δl_1, is due to pressure radiation at the discontinuity from the neck duct to the cavity of the HR [62], while the second Δl_2 comes from the radiation at the discontinuity from the neck to the principal waveguide [63]. This correction only depends on the geometries of the waveguides (or slits), so it becomes important when the duct length is comparable to the radius, i.e., for small neck lengths and for frequencies where $kr_n \ll 1$.

2.4. *Transfer matrix method*

In this work we use the transfer matrix method (TMM) to analyze the wave propagation in the proposed systems. This method allows us to develop discrete models accounting for the finite number of resonators. The transfer matrix is written as:

$$\begin{pmatrix} P_\mathrm{i} \\ U_\mathrm{i} \end{pmatrix} = \mathbf{T}\begin{pmatrix} P_\mathrm{o} \\ U_\mathrm{o} \end{pmatrix}, \tag{18}$$

where P_i and P_o (U_i and U_o) are the incident and the output pressures (velocities) of the system. If the system is made of N resonators, as shown in Figure 3(c) for a single slit, the system can be represented by the following transmission matrix

$$\mathbf{T} = \begin{pmatrix} T_{11} & T_{12} \\ T_{21} & T_{22} \end{pmatrix} = \prod_{n=1}^{N}\left(\mathbf{M}_s \mathbf{M}_\mathrm{HR}^{(n)} \mathbf{M}_s\right).$$

In the case of identical resonators, $\mathbf{M}_\mathrm{HR}^{(n)} = \mathbf{M}_\mathrm{HR}\ \forall n$, and then

$$\mathbf{T} = (\mathbf{M}_s \mathbf{M}_\mathrm{HR} \mathbf{M}_s)^N, \tag{19}$$

where the transmission matrix for each lattice step, $\mathbf{M}_s$, is written as

$$\mathbf{M}_s = \begin{pmatrix} \cos\left(k_s \frac{a}{2}\right) & \mathrm{i} Z_s \sin\left(k_s \frac{a}{2}\right) \\ \frac{\mathrm{i}}{Z_s}\sin\left(k_s \frac{a}{2}\right) & \cos\left(k_s \frac{a}{2}\right) \end{pmatrix}, \tag{20}$$

with κ_s, ρ_s and S_s the effective bulk modulus, density (given by Ref. [60]) and the area of the waveguide where the resonators are loaded respectively. The resonators are introduced as punctual scatterers by a transmission matrix $\mathbf{M}_\mathrm{HR}^{(n)}$ as

$$\mathbf{M}_\mathrm{HR}^{(n)} = \begin{pmatrix} 1 & 0 \\ 1/Z_\mathrm{HR}^{(n)} & 1 \end{pmatrix}. \tag{21}$$

If the system is embedded in a panel of periodic slits with periodicity d, the radiation correction of the slit to the free space should be added to the (19) as

$$\mathbf{M}_{\Delta l_\mathrm{slit}} = \begin{pmatrix} 1 & Z_{\Delta l_\mathrm{slit}} \\ 0 & 1 \end{pmatrix}, \tag{22}$$

with the characteristic radiation impedance $Z_{\Delta l_\mathrm{slit}} = -\mathrm{i}\omega \Delta l_\mathrm{slit} \rho_0 / \phi_t S_0$, where S_0 is the area of exterior periodicity, ρ_0 the air density and Δl_slit the proper end correction coming from the radiation from the slits to the free air. The radiation correction for a periodic distribution of slits can be expressed as [64]:

$$\Delta l_{\text{slit}} = h\phi_t \sum_{n=1}^{\infty} \frac{\sin^2(n\pi\phi_t)}{(n\pi\phi_t)^3}. \tag{23}$$

Note that for $0.1 \le \phi_t \le 0.7$ this expression reduces to $\Delta l_{\text{slit}} \approx -\sqrt{2}\ln[\sin(\pi\phi_t/2)]/\pi$. Although (23) is appropriate for a periodic array of slits, it is not exact for slits loading HRs, therefore, we can evaluate a more realistic value for the end correction by reconstructing an equivalent impedance, $\tilde{Z}$, from the reflection coefficient of the zeroth order Bloch mode calculated with the full model and comparing it as [57]:

$$\tilde{Z} - \mathrm{i}Z_e \operatorname{cotan}(k_e L) = -\mathrm{i}\omega \frac{\rho_0}{\phi_t} \Delta l_{\text{slit}}, \tag{24}$$

where Z_e and k_e are the effective acoustic impedance and wave number of the acoustic metamaterial [38]. The end correction using this last approach gives a value that depends on the geometry of the HRs.

Then, in the reflection problem, the reflection coefficient is calculated using the elements of the transfer matrix as

$$R = \frac{T_{11} - Z_0 T_{21}}{T_{11} + Z_0 T_{21}}, \tag{25}$$

with $Z_0 = \rho_0 c_0 / S_0$, and finally the absorption as $\alpha = 1 - |R|^2$.

In the symmetric reciprocal transmission problem, the reflection and the transmission coefficients are calculated as

$$T = \frac{2\mathrm{e}^{-\mathrm{i}kL}}{T_{11} + T_{12}/Z_0 + Z_0 T_{21} + T_{22}}, \tag{26}$$

$$R = \frac{T_{11} + T_{12}/Z_0 - Z_0 T_{21} - T_{22}}{T_{11} + T_{12}/Z_0 + Z_0 T_{21} + T_{22}}. \tag{27}$$

In the antisymmetric reciprocal transmission problem, the reflection and the transmission coefficients are calculated as

$$T = \frac{2\mathrm{e}^{-\mathrm{i}kL}}{T_{11} + T_{12}/Z_0 + Z_0 T_{21} + T_{22}}, \tag{28}$$

$$R^+ = \frac{T_{11} + T_{12}/Z_0 - Z_0 T_{21} - T_{22}}{T_{11} + T_{12}/Z_0 + Z_0 T_{21} + T_{22}}, \tag{29}$$

$$R^- = \frac{-T_{11} + T_{12}/Z_0 - Z_0 T_{21} + T_{22}}{T_{11} + T_{12}/Z_0 + Z_0 T_{21} + T_{22}}. \tag{30}$$

3. Perfect absorption in one port systems (pure reflection problem)

In this section we experimentally and analytically report PA for audible sound, by the mechanism of critical coupling, with a sub-wavelength single resonant scatterer made of a HR with a closed waveguide structure [28]. The controlled balance between the energy leakage of the several resonances and the inherent losses of the system leads PA peaks.

The configurations analyzed in this section can be considered as equivalent to an asymmetric Fabry–Pérot cavity of length L with two different mirrors, i.e., the resonant scatterer, considered as a point-scatterer because it is sub-wavelength, and the rigid backing (as schematically shown in Figure 4(a)). The absorption of this system can be expressed as $\alpha = 1-|R|^2$, where R is the complex reflection coefficient obtained from the standard three-medium layer Fresnel equation [65],

$$R = R_R + \frac{T_R^2 R_t \mathrm{e}^{\mathrm{i}2kL}}{1 - R_R R_t \mathrm{e}^{\mathrm{i}2kL}}, \tag{31}$$

where R_R and R_t are the reflection coefficients of the resonant element and of the termination, respectively (in our case, $R_t = 1$). Considering inherent losses in this configuration, the PA is

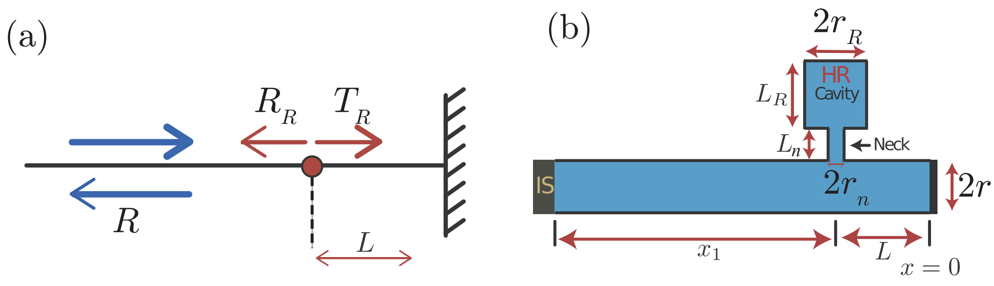

Figure 4. (a) Asymmetric Fabry–Pérot resonator made of a resonant element (red point) and a rigid backing at distance L from the resonator. (b) Shows the resonator set-up. In the set-up an Impedance Sensor (IS) [61] is used for the measurements.

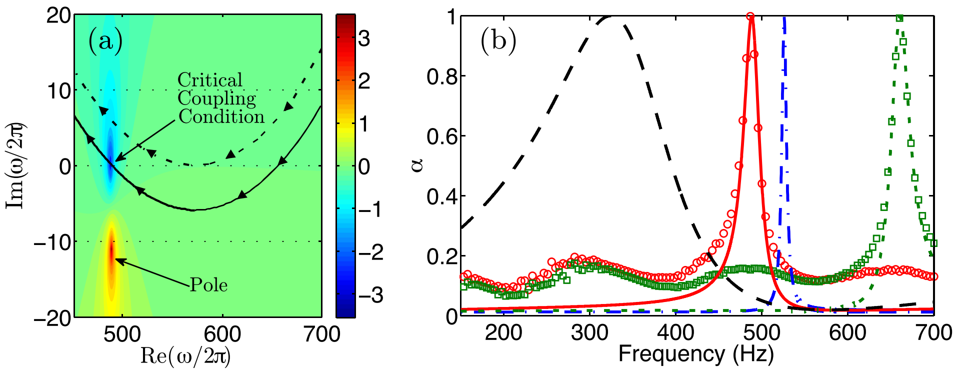

Figure 5. (a) Complex frequency map of $\log|r|$ for the resonant system with $L_R = 8.3$ cm. Black dashed (continuous) line represents the trajectory of the zero of $|r|$ for the lossless (lossy) case in the complex plane increasing L_R (sense of the increasing shown by arrows over the lines). (b) Red continuous and green dotted lines (open red circles and open green squares) represents the absorption coefficient α for the configurations $(L_R, f_{CC}) =$ (8.3 cm, 484.5 Hz) and $(L_R, f_{CC}) =$ (3.9 cm, 647 Hz). Blue dash-dotted line represents the absorption coefficient for the configuration $(L_R, f_{CC}) =$ (7 cm, 526 Hz) with half inherent losses of the experimental case. Black dashed line represents the absorption coefficient for the configuration $(L_R, f_{CC}) =$ (16 cm, 330 Hz) with 20 times the inherent losses of the experimental case. Figure reproduced from Ref. [28].

fulfilled when the reflection coefficient is zero, i.e., when the superposition of the multiple reflections in the cavity (second term in (31)) destructively interferes with the direct reflection from the resonant element (first term in (31)).

Figure 4(b) shows the set-up used for the system with the HR side-loaded to the closed waveguide. The HR is composed of a neck of length $L_n = 2$ cm with radius $R_n = 1$ cm, a cavity with tunable length, L_R, and radius $R_R = 2.15$ cm. The waveguide has a radius $R = 2.5$ cm and $L = 15$ cm. The viscothermal losses at the walls of the waveguide and of the resonator are characterized by both a complex wave vector and a complex impedance [60, 61, 66].

By changing L_R from 0 to 15 cm, i.e., by changing the resonant frequency of the HR, we study the trajectory of the zero of the reflection coefficient in the complex frequency plane for the lossless case. Figure 5(a) (black dashed line) shows the trajectory of the zero of the reflection coefficient that is produced by a hybridized resonance due to the interaction between the resonance of the HR and the resonance of the backing cavity. As shown by the arrows over the trajectory, the zero moves to lower real frequencies as L_R increases. The characteristics of the modes, i.e., the resonant frequency and the leakage rate are related to the real and imaginary part of the zero in the complex frequency plane respectively [28].

Now we consider the viscothermal losses in the system and we observe that the trajectory of the zero down-shifts (black continuous line) with respect to the lossless case. The critical coupling condition is satisfied at the frequency, f_{CC} at which the trajectory of the zero crosses the real frequency axis. For the analyzed system, one can clearly see two crossing points, i.e., two different configurations producing PA. These points correspond to $(L_R, f_{\mathrm{CC}}) = (8.3\text{ cm}, 484.5\text{ Hz})$ and $(L_R, f_{\mathrm{CC}}) = (3.9\text{ cm}, 647\text{ Hz})$. Figure 3(a) shows the reflection coefficient (31) in the complex frequency plane for the configuration $(L_R, f_{\mathrm{CC}}) = (8.3\text{ cm}, 484.5\text{ Hz})$. Similarly, a complex map for the configuration $(L_R, f_{\mathrm{CC}}) = (3.9\text{ cm}, 647\text{ Hz})$ with the zero in the real frequency axis can also be obtained [28]. We find analytically PA ($\alpha = 1$) for the two above mentioned configurations at 484.5 Hz and 647 Hz as shown in Figure 3(b), in agreement with the crossing points of the trajectory of the zero with the real frequency axis represented in Figure 5(a) (black continuous line). Experiments show also very good agreement with the theoretical predictions, producing 100% of absorption for these configurations at the corresponding frequencies with a relative narrow bandwidth of frequencies due to the small leakage of the resonance.

Generally, by changing the inherent losses of the system, we can move the trajectory of the zero in the complex plane, and we can always find a configuration with the good balance between the energy leakage and the inherent losses of the whole resonator to fulfill the critical coupling condition and activate the PA. In particular, increasing of inherent losses in the system produces two main effects: the critical coupling condition is shifted in frequencies and the PA peak becomes broadband because the critical coupled resonances are more leaky.

In order to show these effects, we theoretically analyze the cases of weak and large inherent losses. Dash-dotted blue line and dashed black line in Figure 5(b) represent the absorption coefficient for the configurations $(L_R, f_{\mathrm{CC}}) = (7\text{ cm}, 526\text{ Hz})$ and $(L_R, f_{\mathrm{CC}}) = (16\text{ cm}, 330\text{ Hz})$ each one with the right amount of inherent losses to accomplish the critical coupling. The first (second) one corresponds to a situation with 0.5 (20) times the inherent losses of the experimental case. With small amount of inherent losses, one can find a very narrow PA peak while with large amount of inherent losses the PA peak becomes broad. The broad character is due to the large energy leakage of the critically coupled resonance [28].

4. Perfect absorption in two port systems

In this section we review the main features of PA through the interplay of the inherent losses and transparent modes [67–71] with high Q factor as shown in [42]. These modes are generated in a two-port one-dimensional waveguide which is side-loaded by isolated resonators with moderate Q factor. This mode allows transparency in the lossless case, i.e., a perfectly transmitted wave, within a narrow spectral range. These modes are characterized by an extreme dispersion which leads to slow waves. In mirror symmetric structures, we show that in the presence of small inherent losses, these modes lead to coherent PA associated with one-sided absorption slightly larger than 0.5. In asymmetric structures, near perfect one-sided absorption is possible (96%) with a deep sub-wavelength sample ($\lambda/28$).

4.1. *Point symmetric*

A point symmetric scatterer made of two detuned HRs ($f_1^{\mathrm{HR}} \neq f_2^{\mathrm{HR}}$) located at the same axial position is analyzed in this section (see the sketch in Figure 6(b)). We define the detuning parameter as $(f_2^{\mathrm{HR}} - f_1^{\mathrm{HR}})/\Gamma_L$, where $\Gamma_L = 3.14$ Hz is the decay rate due to losses of the HRs [42].

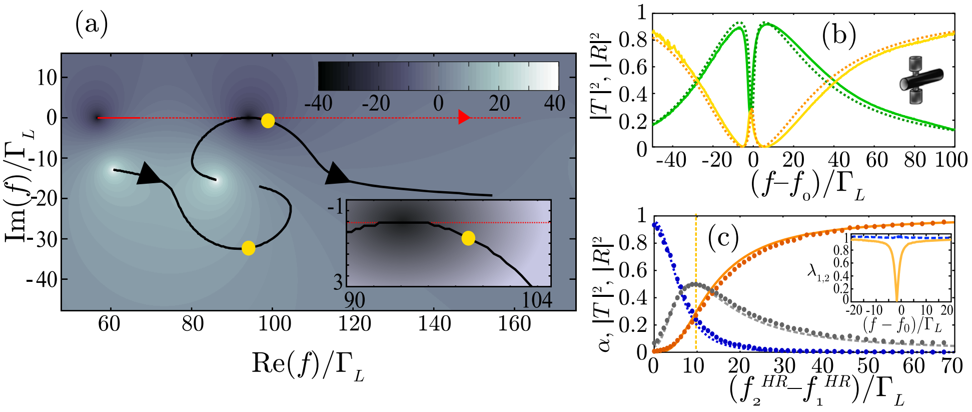

Figure 6. Point symmetric scatterer. (a) Theoretical lossless transmission coefficient (logscale) in the complex frequency plane with the trajectories of the poles (black lines) and of the zero (red dashed line) for $(f_2^{\mathrm{HR}} - f_1^{\mathrm{HR}})/\Gamma_L \in [-37;67]$. The positions of the poles are marked for $(f_2^{\mathrm{HR}} - f_1^{\mathrm{HR}})/\Gamma_L = 9.8$ (yellow dots) and the underlying colormap image corresponds to $(f_2^{\mathrm{HR}} - f_1^{\mathrm{HR}})/\Gamma_L = -37$. Inset: zoom around the critical coupling point. (b) Theoretical with losses (dashed curves), experimental (continuous curves) transmission (yellow curves) and reflection (green curves) coefficients versus frequency for $(f_2^{\mathrm{HR}} - f_1^{\mathrm{HR}})/\Gamma_L = 9.8$ with $f_0 = 311$ Hz. (c) Absorption (gray), transmission (orange) and reflection (blue) coefficients at $f_{\max}$ versus $(f_2^{\mathrm{HR}} - f_1^{\mathrm{HR}})/\Gamma_L$ (curves for theory and dots for experiments). Inset: eigenvalues of the experimental S-matrix for $(f_2^{\mathrm{HR}} - f_1^{\mathrm{HR}})/\Gamma_L = 9.8$.

Ignoring the losses, it has been shown that, for small values of the detuning parameter, the transmission coefficient presents an extraordinary induced transparent (EIT) like mode with unity transmission at $f_0 = (f_2^{\mathrm{HR}} + f_1^{\mathrm{HR}})/2$ [67–71]. The lossless transmission coefficient in the complex frequency plane is displayed in Figure 6(a); this reveals two poles which are hybridized resonances resulting from the two resonances of the HRs. As the detuning parameter changes, in our case by increasing the resonance frequency of one HR while keeping the other one fixed at $f_1^{\mathrm{HR}} = 294$ Hz, the poles move (sense of the arrows in Figure 6(a)), interact and repel each others. As $f_2^{\mathrm{HR}} - f_1^{\mathrm{HR}} \to 0$, one pole at f_{pole}, with $\mathrm{Re}(f_{\mathrm{pole}}) \simeq f_0$, approaches the real axis giving rise to an EIT-like mode with high Q factor. In other words, the interaction of the two resonances leads to a dark mode (the EIT-like mode) and a bright mode (with a corresponding pole far from the real axis).

We now analyze the experimental results and compare them with the theoretical predictions taking into account the losses [42] by looking at the scattering coefficients as a function of the frequency (corresponding to the real axis in the complex frequency plane). For small detuning parameter, the viscothermal losses importantly reduce the amplitude of the transparent peak associated with the EIT like mode: instead of the unity transmission in the lossless case, the peak can take values between 0 and 1. For each value of the detuning parameter, the transparent peak is associated with a peak of absorption found at $f_{\max}$ (slightly different from f_0 due to the losses). The maximum peak of absorption is found with $(f_2^{\mathrm{HR}} - f_1^{\mathrm{HR}})/\Gamma_L = 9.8$, highlighted with circles in Figure 6(a), at $f_{\max} = 306$ Hz. The relevant scattering coefficients are displayed in Figure 6(b). According to the theoretical considerations on point symmetric scatterers, $|T(f_{\max})| = |R(f_{\max})| = 0.5$ corresponds to $\alpha_s(f_{\max}) = 1$ and consequently to $\alpha(f_{\max}) = 0.5$. This one-sided incident wave maximum of absorption is found when the leakage of the EIT-like mode is tuned in order to balance the inherent losses, i.e., it is critically coupled [33, 42, 52, 72]. This is confirmed in

Figure 6(c) where the scattering coefficients and the absorption at $f_{\max}$ are plotted as a function of the detuning parameter. In addition, one experimental eigenvalue becomes zero at $f_{\max}$ as shown in Figure 6(c). As mentioned above, this is the symmetrical CPA [56]; the case at which the incident waves from the two sides of the sample, corresponding to the S-matrix eigenvector such as $v_2/v_1 = 1$, are completely absorbed.

4.2. *Mirror symmetric resonators*

We now pay attention to mirror symmetric scatterers. The interest of these scatterers, compared to the point symmetric scatterers, relies on the fact that the one-sided absorption α takes value larger than 0.5. This happens since α_a can be different from zero. Two tuned HRs ($f_1^{\mathrm{HR}} = f_2^{\mathrm{HR}} = f^{\mathrm{HR}}$) located at different axial positions and separated by the distance l forms the mirror symmetric resonator analyzed in this section (see the sketch in Figure 7(a)). Now, the detuning parameter is defined as $k^{\mathrm{HR}} l = 2\pi f^{\mathrm{HR}} l/c_0$ where c_0 is the sound velocity. As in the point symmetric scatterer case, we first inspect the behavior of the lossless transmission coefficient in the complex frequency plane. In addition to the two HR-related poles, multiple poles due to the Fabry–Pérot resonances of the waveguide appear. Once the resonance frequency of the HRs is close to a Fabry–Pérot frequency f^{FP} ($k^{\mathrm{HR}} l \sim n\pi$, where $n \in \mathbb{N}$ including $n = 0$), one of the poles approaches the real axis and gives rise to an EIT-like mode. In Figure 7(a), the case where $k^{\mathrm{HR}} l \to \pi$ is shown. As before, the viscothermal losses can subsequently reduce the amplitude of the transparent peak associated to the EIT-like mode, see Figures 7(b) and (c). The discrepancies between experimental results and theoretical predictions, larger than in the case of point symmetric scatterers, are attributed to a larger leakage outside the waveguide and to the difficulty to get $f_1^{\mathrm{HR}} = f_2^{\mathrm{HR}}$ in experiments. We continue our analysis by studying some particular detuning parameters values. For instance, we experimentally (theoretically) find that $R(f_{\mathrm{CPA}}) \simeq -T(f_{\mathrm{CPA}})$ for $k^{\mathrm{HR}} l/\pi = 0.82$ and 1.17 ($k^{\mathrm{HR}} l/\pi = 0.86$ and 1.14) at f_{CPA}.

According to the theory, these cases correspond to $\alpha_s(f_{\mathrm{CPA}}) = 1$, which is equivalent to a symmetrical CPA point, $\lambda_1(f_{\mathrm{CPA}}) = 0$. In Figure 7(b), we verify the existence of a symmetrical CPA point by plotting the scattering coefficients, as well as the eigenvalues of the experimental S-matrix, as a function of frequency for $k^{\mathrm{HR}} l/\pi = 1.17$. Importantly, at these detuning parameter values, both in theory and experiments, the one-sided absorption α takes a value larger than 0.5 around f_{CPA}. Indeed, as we mentioned above $\alpha_a \neq 0$, which is confirmed experimentally by the fact that $\lambda_2 \neq 1$, see inset of Figure 7(b). It is worth to comment here that, by using HRs of smaller Q factor, we observe a larger value of α. Overall, we find that the maximum peak of absorption is $\alpha(f_{\max}) = 0.55$ in theory ($\alpha(f_{\max}) = 0.6$ in experiments) for $k^{\mathrm{HR}} l/\pi = 0.86$ and 1.14 as shown in Figure 7(c); as before, we show that this corresponds to the critical coupling of the relevant EIT-like mode [42]. The maximum peak of absorption appears theoretically at the symmetrical CPA point, i.e., for the same detuning parameter and at $f_{\max} = f_{\mathrm{CPA}}$. This is explained by the experimentally observed nearly constant behavior of λ_2, and thus α_a, which is not the case of asymmetric scatterers as we will see below.

4.3. *Perfect absorption in asymmetric systems*

To enhance the one-side incident wave absorption, let us now turn to the case of asymmetric scatterers. We consider an additional degree of freedom in the setup: two detuned HRs ($f_1^{\mathrm{HR}} \neq f_2^{\mathrm{HR}}$) separated by the distance l (see the sketch in Figure 8(a)). The mirror symmetry is broken ($R^- \neq R^+$) and two detuning parameters are defined as $k_1^{\mathrm{HR}} l$ and $k_2^{\mathrm{HR}} l$. Figure 8(a) shows the maximum of one-sided absorption found at $f_{\max}$, which is defined with the left incoming wave $\alpha^- = 1 - |R^-|^2 - |T|^2$, as a function of the two detuning parameters, where the red dashed line

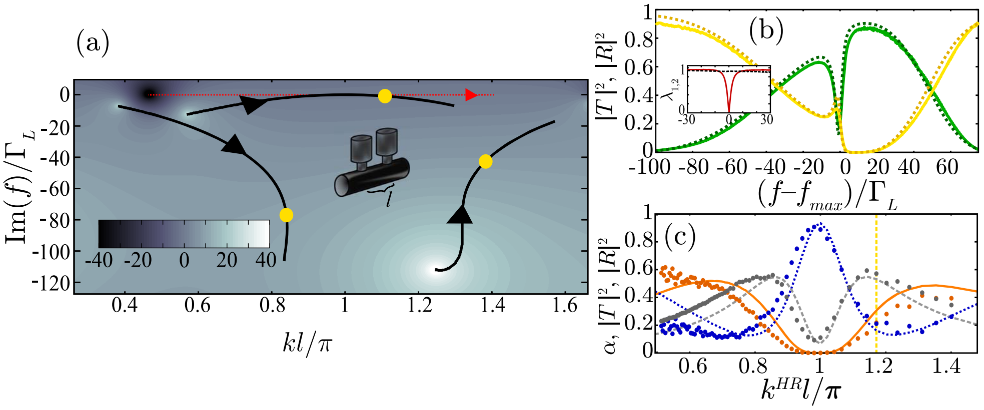

Figure 7. Mirror symmetric scatterer, $l = 30$ cm. (a) Theoretical lossless transmission coefficient (log-scale) in the complex frequency plane with the trajectories of the poles (black lines) and of the zeros (red dashed line) with $k^{\mathrm{HR}} l/\pi \in [0.35; 1.40]$ and $k = 2\pi f/c_0$. The positions of the poles are marked for $k^{\mathrm{HR}} l/\pi = 1.14$ (yellow dots) and the underlying colormap image corresponds to $k^{\mathrm{HR}} l/\pi = 0.35$. (b) Theoretical with losses (dashed curves), experimental (continuous curves) transmission (yellow curves) and reflection (blue curves) coefficients versus frequency for $k^{\mathrm{HR}} l/\pi = 1.17$ with $f_{\max} = 645$ Hz. Inset: eigenvalues of the experimental S-matrix for $k^{\mathrm{HR}} l/\pi = 1.17$. (c) Absorption (gray), transmission (orange) and reflection (blue) coefficients at $f_{\max}$ versus $k^{\mathrm{HR}} l$ (curves for theory and dots for experiments).

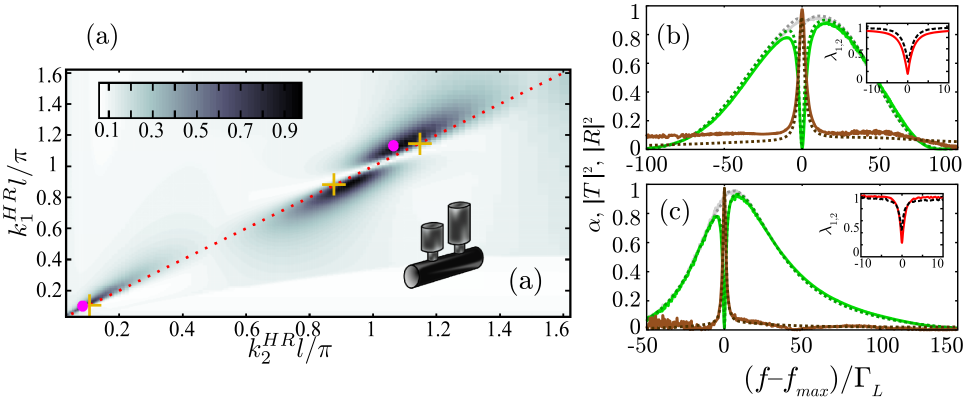

Figure 8. Asymmetric scaterrer. (a) Theoretical absorption versus $k_1^{\mathrm{HR}} l/\pi$ and $k_2^{\mathrm{HR}} l/\pi$. The red dashed line corresponds to the mirror symmetric scatterers. (b)–(c) Theoretical (dashed curves) and experimental (continuous curves) absorption (brown), reflection from left (green) and from right (gray) coefficients. Inset: eigenvalues of the experimental S-matrix. (b) $l = 30$ cm, $k_1^{\mathrm{HR}} l/\pi = 1.14$, $k_2^{\mathrm{HR}} l/\pi = 1.06$ and $f_{\max} = 618$ Hz. (c) $l = 5$ cm, $k_1^{\mathrm{HR}} l/\pi = 7.7.10^{-2}$, $k_2^{\mathrm{HR}} l/\pi = 7.2.10^{-2}$ and $f_{\max} = 244$ Hz.

corresponds to the mirror symmetric scatterer case. Close to the maximum peak of absorption for mirror symmetric scatterers (highlighted by crosses), there exist asymmetric scatterers presenting a Unidirectional Near Perfect One-sided Absorption (UNPOA). Figures 8(b) and (c) show the absorption, the right and left reflection coefficients as a function of frequency for two cases of UNPOA (highlighted by magenta points in Figure 8(a)). Figure 8(b) corresponds to the case

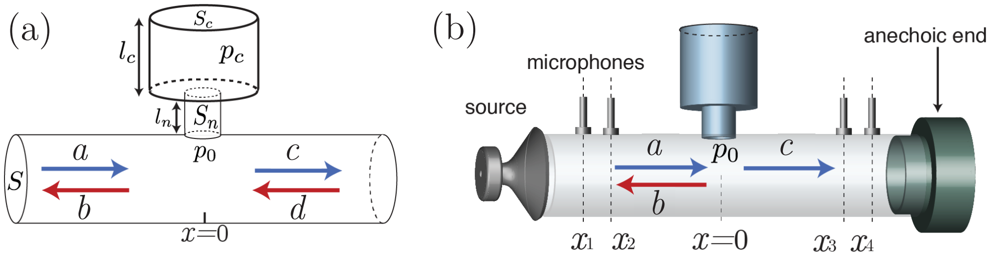

Figure 9. (a) Schematic representation of the system under study: a Helmholtz resonator side-loaded to a cylindrical waveguide. The two-port scattering process is also indicated by the arrows. (b) The experimental setup used for our measurements.

where the absorption reaches 0.98 with $k_1^{\mathrm{HR}} l/\pi = 1.14$ and $k_2^{\mathrm{HR}} l/\pi = 1.06$. More interestingly, the absorption is 0.96 for $k_1^{\mathrm{HR}} l/\pi = 0.08$ and $k_2^{\mathrm{HR}} l/\pi = 0.07$ in Figure 8(c). This latter case is particularly appealing because it reveals the possibility of UNPOA with a deep sub-wavelength structure (in the experiment, $f_{\max} = 244$ Hz and $l = 5$ cm corresponding to $\lambda/28$). Note also that $|R^+| > 0.9$ and $R^- \simeq 0$ near $f_{\max}$. This clearly demonstrates the unidirectional character of the absorber. Besides, it is observed that both eigenvalues of the scattering matrix λ_1 and λ_2 go to near zero values at $f_{\max}$ (see insets in Figures 8(b) and (c)). This differs importantly from the eigenvalues observed with the point symmetric and mirror symmetric scatterers where only one of them is going to zero.

4.4. *Nonlinear perfect absorption*

In the previous part, we have shown how the critical coupling condition (and consequently CPA) can be achieved either by tuning the losses of a single scatterer or by tuning the interaction between two different scatterers passively by changing the geometry. We now exploit the possibility that CPA can be induced only by changing the wave amplitude and the effects of nonlinearity. In particular, we study a two-port system composed of a cylindrical waveguide with section S side-loaded at $x = 0$ by a HR. In the case of two high pressure incident waves from each port of the system, we can derive simplified equations describing the dynamics of the system. For sufficiently low frequencies we assume incompressibility of the fluid in the HR's neck and uniform pressure field in its cavity.

By using the linearized mass and momentum conservation laws in the waveguide, continuity of the pressure at $x = 0$, and by considering boundary conditions for CPA (symmetric input waves), the dynamics of the pressure in the cavity of HR $p_c(t)$ side-loaded to the waveguide is found to be [43]

$$\ddot{p}_c + \omega_0^2 p_c + (r_L - \gamma + \beta|\dot{p}_c|)\dot{p}_c = 0. \qquad (32)$$

$(\dot{})$ denotes differentiation with respect to time, $\omega_0^2 = c_0^2 S_n / l'_n l_c S_c$ is the resonance frequency of the HR with c_0 the speed of sound. l_c and S_c are respectively the section and the length of the cavity while l'_n denotes the corrected length of the neck (see Figure 9(a)). The viscothermal losses in the resonator are quantified by the small parameter r_L. Finally, β is connected with flow separation and vorticity in the neck and quantifies the nonlinear losses in the HR. $\gamma = c_0^2 S_n / 2 l'_n S$ describes the coupling strength between the HR and the waveguide. The leakage rate of energy out of the HR is described by the additional dissipative term proportional to γ. In this representation, CPA is achieved when the leakage term analogous to $\dot{p}_c(t)$ (energy going away from the resonator) is vanishing. In consequence, we directly observe that, in the linear regime, the critical coupling

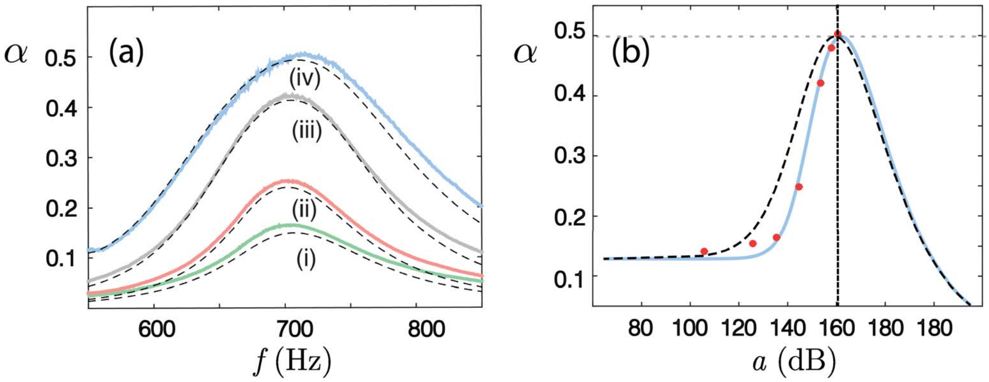

Figure 10. (a) Absorption as a function of frequency for different incident amplitudes $|a|$. Solid lines depict the measured absorption and dashed lines illustrate analytical results. (b) Absorption at the frequency $f_0' = 710$ Hz as a function of the amplitude of the incident wave $|a|$. Blue solid (dashed) line corresponds to the nonlinear impedance model using the fitting parameter $\Delta = 0.15$ ($\Delta = 0$). Dots indicate the corresponding experimental measurements. The vertical dashed line depicts the prediction of (33) for the CPA condition.

condition $r_L = \gamma$ is recovered. On the other hand, it can be found that the combined effects of the presence of losses and nonlinearity can be used to reach the critical coupling condition i.e.

$$\frac{4}{3\pi}\frac{|u_n|}{l_n} + r_L = \gamma, \tag{33}$$

where u_n is the acoustic particle velocity in the HR's neck. To obtain the last equation, a perturbation technique [26] up to first order, neglecting the contribution of higher harmonics is used, assuming a weak nonlinearity. Note that this particular nonlinearity does not introduce a frequency shift of the resonance. We perform one-sided incidence experiments (see Figure 9(b)) to confirm the nonlinear critical coupling by measuring the absorption for different amplitudes and frequencies of incident waves a. We want to verify that nonlinear losses can lead to an absorption $\alpha = 0.5$ (as in any two-port system with one-sided incident wave, see Section 2) when condition (33) is satisfied. To do so we use the 4 microphones method to measure the reflectance and the transmittance of the system and deduce the absorption (see Figure 9(b)).

The panel (a) of Figure 10 shows the absorption as a function of frequency where the solid lines depict the measured absorption for different incident wave amplitudes. We observe that by increasing the incident wave amplitudes $|a|$, the maximum of absorption increases and reaches the value of $\alpha = 0.5$ when $|a| = 160$ dB at the resonance frequency $f_0' = 710$ Hz. The dashed lines in Figure 10(a) show the theoretical predictions as obtained using the nonlinear impedance

$$Z_{HR}^{NL} = Z_{HR}^{L} + \frac{1}{1+\Delta St}\,\frac{4\rho_0|u_n|}{3\pi S_n C_{vc}^2},$$

where Z_{HR}^{L} is the linear impedance of the HRs (given by (14)), C_{vc}^2 is the vena-contracta coefficient having a value of ≈ 0.7 for a neck with hard edges and St is the Strouhal number. The fitting parameter Δ is chosen to take the value 0.15 and the velocity of the neck is calculated using the experimental values of the incident pressure. The theory and experiments are in good agreement demonstrating that the nonlinear response of the HR is adequately described by the nonlinear impedance.

To further illustrate the fact that the incident wave amplitude can be employed as a tuning parameter to obtain CPA, we show, in Figure 10(b), the absorption for the resonance frequency

f_0' as a function of incident amplitude wave $|a|$. The (red) dots depict the experimental values showing that $\alpha = 0.5$ is reached for $|a| = 160$ dB. This value is predicted by the (33) as indicated by the vertical dashed line and this verifies that critical coupling can be induced by nonlinear losses in addition of the linear ones. The blue and dashed lines are obtained using the theoretical nonlinear HR impedance with $\Delta = 0.15$ and $\Delta = 0$ respectively.

5. Perfect absorption in three-port systems

We now proceed by generalizing the results of the previous Section to a more complex structure, i.e., a 3-port system. In particular using (sub-wavelength) HRs, we theoretically and experimentally illustrate an acoustic perfect absorbing 3-port that operates at different frequencies and different intensities as well as relative phases of the input waves. The system under consideration is composed of three identical waveguides connected by a Y-shape connection. Each waveguide is side-loaded by an identical HR, with resonance frequency f_0, placed at the same distance d from the center of the device (Figure 11(b)–(c)).

5.1. *Scattering properties and CPA*

The 3-port acoustic system is reciprocal and symmetric and the corresponding scattering matrix is given by the following equation [53]

$$\begin{pmatrix} b \\ c \\ f \end{pmatrix} = \begin{pmatrix} R & T & T \\ T & R & T \\ T & T & R \end{pmatrix} \begin{pmatrix} a \\ d \\ g \end{pmatrix} = S \begin{pmatrix} a \\ d \\ g \end{pmatrix}, \tag{34}$$

where the frequency dependent coefficients R and T, correspond to the reflection and transmission when only one port is excited. Note that the definition of the S-matrix in (34) with the reflection coefficient in the diagonal is different from the one given in (1). The S-matrix is a *symmetric circulant* matrix due to the geometric symmetry of the 3-port and to the fact that we consider a reciprocal system. The matrix is symmetric due to reciprocity. An important property of the circulant matrix, is that its eigenvectors always remain the same and thus are independent of both the physical system (particular form of R and T) and the frequency. The vectors $(a,d,g)^T \equiv |\psi_{\text{in}}\rangle$ and $(b,c,f)^T \equiv |\psi_{\text{out}}\rangle$ describe the incoming and outgoing waves respectively as shown in Figure 11(a).

The eigenvalue problem associated to the scattering matrix is the following

$$\det(S - \lambda I) = 0, \tag{35}$$

where the eigenvalues are

$$\lambda_0 = R + 2T, \quad \text{and} \quad \lambda_1 = \lambda_2 = R - T, \tag{36}$$

and the corresponding orthonormal eigenvectors are given by

$$\begin{aligned} |u_0\rangle &= \tfrac{1}{\sqrt{3}}(1,1,1)^T, \\ |u_1\rangle &= \tfrac{1}{\sqrt{3}}(1,\mathrm{e}^{2\mathrm{i}\pi/3},\mathrm{e}^{-2\mathrm{i}\pi/3})^T, \\ |u_2\rangle &= \tfrac{1}{\sqrt{3}}(1,\mathrm{e}^{-2\mathrm{i}\pi/3},\mathrm{e}^{2\mathrm{i}\pi/3})^T. \end{aligned} \tag{37}$$

To quantify absorption, we use the parameter Θ defined as the ratio of total output to input power

$$\Theta = \frac{|b|^2 + |c|^2 + |f|^2}{|a|^2 + |d|^2 + |g|^2} = \frac{\sum_i \lambda_{i-1}^2 |c_{i-1}|^2}{\sum_i |c_{i-1}|^2} \quad i = 1,2,3, \tag{38}$$

where we use the fact that any input vector can be written as a sum of $|u_i\rangle$, i.e. $|\psi_{\text{in}}\rangle = \sum_i c_i |u_i\rangle$. By definition, CPA occurs when $\Theta = 0$ i.e. no output.

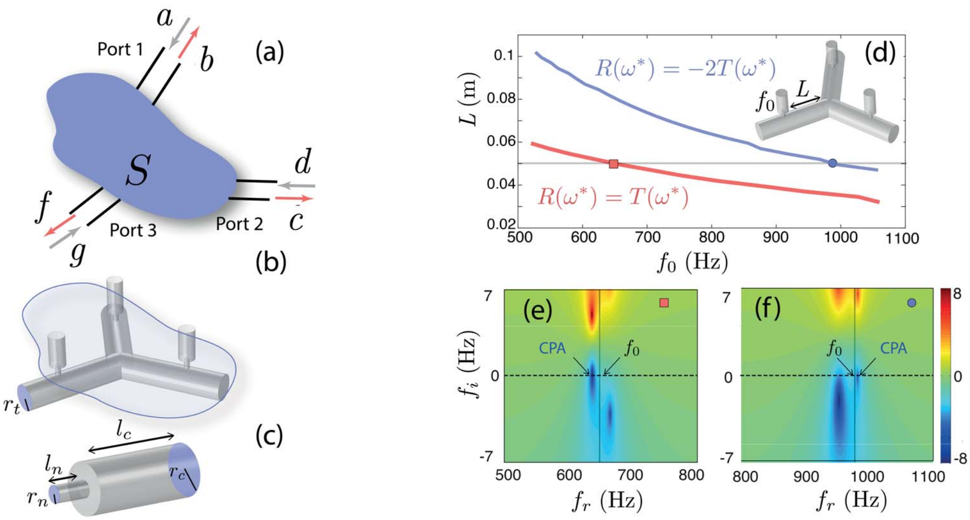

Figure 11. (a) A schematic illustration of a general three port system with incoming and outgoing waves at each port. The scattering matrix S of the system is assumed to be symmetric, at some frequency range, even if the geometry of the device may be not. (b) The symmetric network studied here (not in scale), which is composed by 3 identical cylindrical waveguides with radius $r_t = 2.5 \times 10^{-2}$ m, assembled by a Y-shape connection sideloaded with HRs at a distance d. (c) Details of the HRs composed by a neck with length $\ell_n = 2 \times 10^{-2}$ m, a radius $r_n = 0.45 \times 10^{-2}$ m branched to a cylindrical cavity with radius $r_c = 1.5 \times 10^{-2}$ m and varying length ℓ_c which is used in order to tune the resonance frequency f_0. (d) The upper (lower) curve depicts the symmetric (asymmetric) CPA solutions for varying resonant frequency f_0 and distance d. The horizontal line corresponds to the configurations with $L = 0.05$ m. (e), (f) The determinant $|\det(S)|$ in the complex frequency plane for the configurations corresponding to the two cases of panel (d) with a (red) square and a (blue) circle respectively.

A 3-port network exhibits CPA when the eigenvalues of its S-matrix given by (36) become zero at some particular frequency f^*. Requiring $\lambda_0 = 0$ leads to the following condition on the scattering coefficients $R = -2R \equiv R_s$ associated to a symmetric input of the form $|u_0\rangle$ (Equation (37)) which is completely absorbed (symmetric CPA). The zero value of the degenerate eigenvalues $\lambda_{1,2}$ gives a different CPA condition $R = T \equiv R_a$ with an input wave corresponding to the asymmetric vectors $|u_1\rangle$ or $|u_2\rangle$. In addition, any input in the form $|\psi_{\text{in}}\rangle = A|u_1\rangle + B|u_2\rangle$ will also be completely absorbed (asymmetric CPA).

To achieve CPA, the transmission and reflection coefficients have to be specifically tuned to fulfill the aforementioned CPA conditions. Due to the presence of HRs sided loaded to the waveguide, the strong interference around the resonance frequency greatly modifies both the transmission and the reflection coefficients and allows us to satisfy the CPA conditions. To treat the problem analytically, we assume that for sufficiently low frequencies, only the plane mode is considered in the waveguide and the HRs can be described as point scatterers. In this case, R and T are analytically obtained using the transfer matrix method and are given as a function of f_0 and L.

The CPA conditions are displayed in the parametric space (f_0, L) using the analytical expressions of R and T as shown in Figure 11(d) where the red (lower) curve corresponds to the

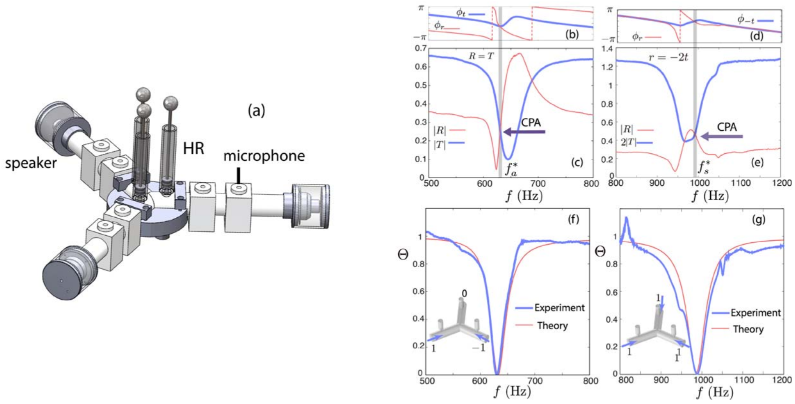

Figure 12. (a) View of the experimental device. (b)–(c) The phase and absolute value of the experimentally measured reflection and transmission coefficients T and R, as a function of frequency, for the configuration which exhibits an asymmetric CPA at $f_a^* = 630$ Hz. The resonance frequency of the HRs is $f_0 = 645$ Hz corresponding to a cavity length $l_c = 0.02$ m. CPA is ensured since both the real and the imaginary parts of r and t are equal for this frequency (vertical gray line). (d)–(e) The phase and absolute value of the experimentally measured reflection and transmission coefficients R and $-2T$, as a function of frequency, for the configuration which exhibits a symmetric CPA at $f_s^* = 988$ Hz. The resonance frequency of the HRs is $f_0 = 975$ Hz corresponding to a cavity length $l_c = 0.89 \times 10^{-2}$ m. CPA appears when the two the curves of both the real and imaginary part become equal, indicated by the vertical gray line. (f)–(g) The output to input power ratio Θ as a function of frequency for the asymmetric and the symmetric CPA respectively. The thick (thin) line corresponds to the experimental (theoretical) measurement. The insets depict the eigenvector used in order to obtain the curves in each case.

asymmetric and the blue (upper) line depicts the symmetric CPA. The occurence of the CPA can also be illustrated in another way; through the complex frequency plane of the determinant of the S-matrix. By scanning the space (f_0, L), the zeros of the determinant move and cross the real axis when CPA occurs fixing the geometry of the system. This is illustrated in Figure 11(e)–(f) where two different configurations, symmetric and asymmetric CPA, are shown respectively. Note that the operating frequency f^* for the CPA is close but not the same as f_0 due to the interaction of the resonances through the waveguides.

5.2. *Experimental demonstration of CPA*

We now experimentally study the scattering of the 3-port network to verify the analytical results of Figure 11(d) with $L = 0.05$ m. The experimental device is illustrated in Figure 12(a). The reflexion and transmission coefficients are determined using a pair of microphones connected to each branch allowing the measurement of the forward and backward waves in each waveguide. With the help of the definition of scattering matrix, the measured incoming and outgoing waves give R and T. Two sets of HRs with different resonance frequencies f_0 are used corresponding to asymmetric and symmetric CPA configurations as indicated respectively by the square and the circle in Figure 11(d). The asymmetric CPA is illustrated in Figure 12(b)–(c) where the CPA condition $R = T$ is fulfilled for $f_a^* = 630$ Hz as indicated by the vertical gray lines. The configuration corresponding to the symmetric case is shown in Figure 12(d)–(e) and the required condition is achieved for $f_s^* = 988$ Hz (vertical gray line).

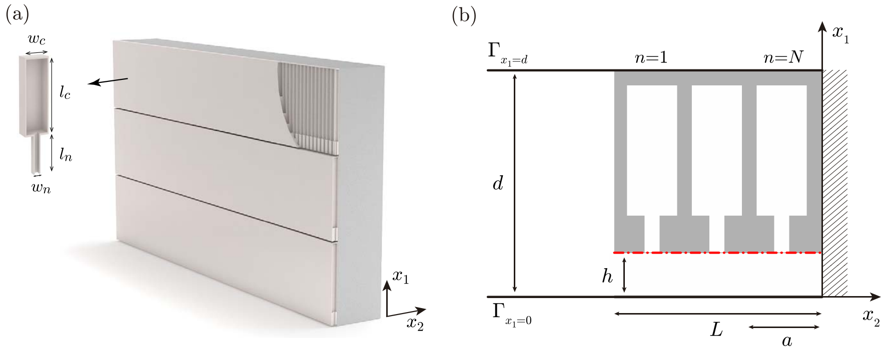

Figure 13. (a) Conceptual view of the thin panel placed on a rigid wall with one layer of square cross-section HRs, $N = 1$. (b) Scheme of the unit cell of the panel composed of a set of N HRs. Symmetry boundary conditions are applied at boundaries $\Gamma_{x_1=d}$ and $\Gamma_{x_1=0}$.

The measurement of r and t allows to experimentally determine the scattering matrix of the 3-port for the two different configurations and for the frequency range of interest. Then the ability of the network to completely absorb an incoming wave can be quantified by considering an input vector $(a,d,g)^T = (1,-1,0)^T$ (inset of Figure 12(f)) and the experimental scattering matrix. With the corresponding output, we determine Θ as shown in Figure 12(f) with the thick solid line, where at the CPA frequency f_a^*, an almost PA is obtained with $\Theta \approx 5\times 10^{-4}$. The same analysis is performed for the symmetric CPA, considering $(a,d,g)^T = (1,1,1)^T$ (inset of Figure 12(g)). The result on Θ is shown with the thick solid line in Figure 12(g) where the system reaches a value of $\Theta \approx 10^{-3}$ at f_s^*.

6. Perfect absorption from panels in reflection

In this section we theoretically and experimentally report a perfect and omnidirectional absorbing metamaterial panel with deep sub-wavelength thickness by using the concepts of slow sound and critical coupling [37]. As shown in Figure 13, the system consists of a thin panel perforated with a periodic arrangement of slits, of thickness h, with periodicity d along the x_1 direction. The upper wall of the slit is loaded by N identical HRs arranged in a square array of side a. The HRs, of square cross-section, are characterized by a neck and a cavity widths w_n and w_c, and lengths l_n and l_c respectively. The presence of the HRs introduces a strong dispersion in the slit producing slow propagation, in such a way that the resonance of the slit is down shifted: the slit becomes a deep sub-wavelength resonator. The visco-thermal losses in the system are considered in both the resonators and in the slit by using effective complex and frequency dependent parameters [60] as described in Section 2.3. Therefore, by modifying the geometry, the intrinsic losses of the system can be efficiently tuned and the critical coupling condition can be fulfilled to solve the impedance matching to the exterior medium.

We start by analyzing the dispersion properties inside the slit in order to inspect the slow sound behavior. Periodic boundary conditions are assumed at boundaries $\Gamma_{x_1=0}$ and $\Gamma_{x_1=d}$. At this stage we have to notice that several theoretical models are used to analyze the structure: an approach based on the TMM and the finite element method (FEM) (see Ref. [37] for more details of the models). Figure 14(a) shows the real part of the phase velocity in the slit, calculated both in the lossless and lossy cases, for a metamaterial with parameters $h = 1.2$ mm, $a = 1.2$ cm, $w_n = a/6$, $w_c = a/2$, $d = 7$ cm, $l_n = d/3$, and $l_c = d-h-l_n$. Figure 14(b) shows the corresponding dispersion relation, where a band gap can be observed above the resonant frequency of the HRs, f_{HR}. Due to

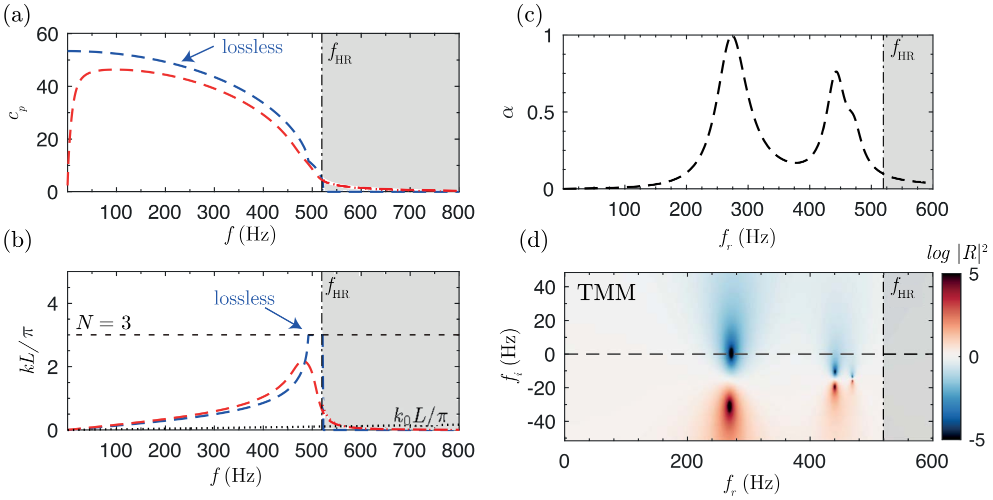

Figure 14. (a) Phase speed for a panel of $N = 3$ resonators calculated by TMM (dashed) for the lossless case (blue) and including thermo-viscous losses (red). (b) Corresponding wavenumber, where k_0 is the wavenumber in air. (c) Absorption of the panel. The dashed-dotted line marks the resonant frequency of the HRs and the shaded area corresponds to the band-gap. (d) Complex-frequency planes of the reflection coefficient calculated by TMM where f_r and f_i are the real and imaginary part of the complex frequency respectively.

the presence of this band gap, slow propagation conditions are achieved in the dispersive band below $f_{\rm HR}$. In the lossless case, zero phase velocity can be observed for frequencies just below $f_{\rm HR}$. Note also that the maximum wavenumber inside the slit is limited by the discreteness to the value $k_{\max} = \pi N/L$, as shown by the TMM calculations (dashed blue curve in Figure 14(b)). In the lossy case, the losses limit the minimum value of group velocity [61], but in our system slow sound velocity can be achieved in the dispersive band below $f_{\rm HR}$. The average sound speed in the low frequency range is much lower (50 m/s) than the speed of sound in air.

Consider now the geometry shown in Figure 13(b) where the array is bounded. In that case the frequency of the quarter wavelength resonance, which is $c/4L$ is dictated by the sound velocity of the metamaterial made by the waveguide loaded with the HRs, so by an slow sound velocity. In that case, the resonance frequency is therefore shifted to the low frequencies. Figure 14(c) shows the absorption when the geometry made by $N = 3$ HRs has been tuned to present the exact amount of intrinsic losses that exactly compensates the energy leakage of the system at 275 Hz. In this situation, as shown in Figure 14(d), the lower frequency zero is located on the real axis, leading to a peak of PA. In addition, as we have $N = 3$ resonators, two other secondary peaks of absorption are observed at higher frequencies, e.g. 442 Hz and 471 Hz. Their corresponding zeros are located close to the real axis and, although the critical coupling condition is not exactly fulfilled, high absorption values can be observed at these frequencies.

The previous sample, with $N = 3$ HRs, provides PA for a thickness of $L = 3a = \lambda/34.5$. Using an optimization method (sequential quadratic programming (SQP) method [73]) the geometry of the system can be tuned in order to minimize the thickness of the material, providing structures with PA and deep sub-wavelength dimensions. The TMM was employed in the optimization to consider the discreteness effects on the reflection coefficient. The resulting structure from the optimization procedure is shown in Figure 15(a): a sample with a single layer of resonators, $N = 1$ with $h = 2.63$ mm, $d = 14.9$ cm, $a = L = d/13 = 1.1$ cm, $w_n = 2.25$ mm, $w_c = 4.98$ mm, $l_n = 2.31$ cm, $l_c = 12.33$ cm. The width of the impedance tube used for measurements, d, allows to

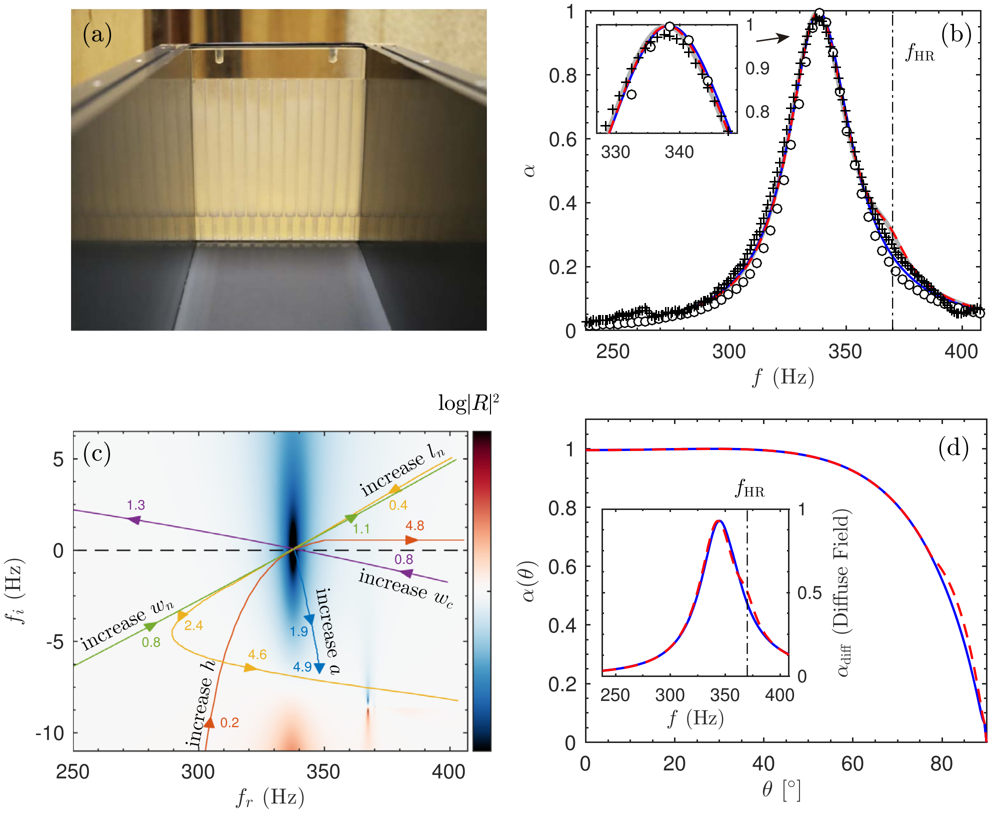

Figure 15. (a) Photograph of the experimental setup with a vertical unit cell, $N = 1$, in the interior of the impedance tube. The translucent resin allows to see the array of HRs. Picture shows the tube open, but it was closed for the experiments. (b) Absorption of the system measured experimentally (crosses), calculated by the full modal expansion (thick continuous gray), effective parameters (dashed red), transfer matrix method (continuous blue) and finite element method (circles). (c) Representation of the reflection coefficient in the complex frequency plane for the optimized sample. Each line shows the trajectory of its zero by changing a geometry parameter. (d) Absorption peak as a function of the angle of incidence calculated by the effective parameters (dashed red), transfer matrix method (continuous blue). The inset in (d) shows the absorption coefficient in diffuse field as a function of frequency. Figure reproduced from Ref. [37].

fit 13 resonators in the transversal dimension as shown Figure 15(a). The sample was built using stereolithography techniques using a photosensitive epoxy polymer.[1] The structure presents a peak of PA at $f = 338.5$ Hz (different than that of the HR, $f_{\mathrm{HR}} = 370$ Hz) with a thickness $L = \lambda/88$.

Figure 15(b) shows the absorption coefficient at normal incidence calculated with the different semi-analytical methods, predicted numerically by FEM and measured experimentally. At $f = 338.5$ Hz, PA can be observed. The maximum absorption measured experimentally is $\alpha = 0.97$, as shown in the inset of Figure 15(b). This small discrepancy between the measurements and the models can be caused by experimental reasons including the non perfect fitting of the slit on

---

[1] (Accura 60®, 3D Systems Corporation, Rock Hill, SC 29730, USA), where the acoustic properties of the solid phase are $\rho_{\mathrm{accura}} = 1210\ \mathrm{kg/m^3}$, $c_{\mathrm{accura}} = [1570, 1690]$ m/s.

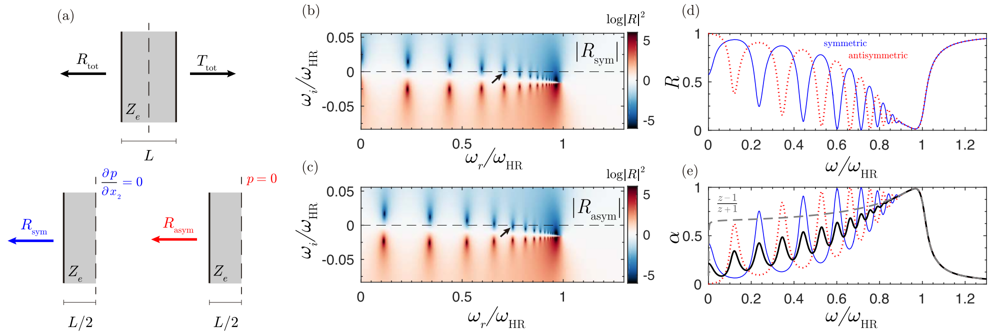

Figure 16. (a) Symmetric and antisymmetric problem decomposition for an homogeneous layer of material with effective parameters. (b–c) Complex frequency representation of the reflection coefficient for the symmetric and antisymmetric problem respectively. (d) Reflection coefficient at the real axis for symmetric (blue) and antisymmetric (dotted red). (e) Absorption for symmetric (blue), antisymmetric (dotted red), total (thick black) and impedance matching condition (dashed gray). Figure reproduced from Ref. [38].

the impedance tube and the excitation of plate modes of the solid medium that composes the metamaterial.

Figure 15(c) also shows the corresponding reflection coefficient in the complex frequency plane. The color map corresponds to the case in which the critical coupling condition is fulfilled, i.e., the zero of the reflection coefficient is exactly located on the real frequency axis. As long as the intrinsic losses depend on the geometry of the resonators and the thickness of the slits, we also represent in Figure 15(c) the trajectory of this zero as the geometry of the system is modified. The crossing of the trajectories with the real frequency axis implies that PA can be achieved with this geometry at this particular frequency. It can be seen that the trajectories linked to the resonators geometry, w_n, w_c, l_n have a strong effect in the real part of the complex frequency of the zero, as they modify the HRs resonant frequency.

Finally, Figure 15(d) shows the absorption of the metamaterial panel as a function of the angle of incidence. It can be observed that almost PA is obtained for a broad range of angles, being $\alpha > 0.90$ for incident waves with $\theta < 60°$. The inset of Figure 15(d) shows the absorption in diffuse field [74] calculated as $\alpha_{\text{diff}} = 2\int_0^{\pi/2} \alpha(\theta)\cos(\theta)\sin(\theta)\,\mathrm{d}\theta$, where at the working frequency it reaches a value of $\alpha_{\text{diff}} = 0.93$, showing the omnidirectional behavior of the absorption in this sub-wavelength structure.

7. Perfect absorption from panels in transmission

In this section we discuss the several possibilities to obtain quasi-PA or PA in the transmission problem, i.e. in the case in which the metamaterial is excited from one side and the wave is either transmitted, reflected or absorbed by the metamaterial. When transmission is introduced, the problem of PA becomes more complicated because the eigenvalues of both the symmetric and the antisymmetric problem must be on the real frequency axis at the same frequency (see Section 4). Depending on the symmetry of the resonator used as building block of the metamaterial, several solutions to the problem are discussed in this section.

7.1. *Quasi-perfect absorption in the symmetric problem by accumulation of resonances*

In this section we theoretically and experimentally report sub-wavelength resonant panels for low-frequency quasi-perfect sound absorption including transmission by using the accumulation of cavity resonances due to the slow sound phenomenon [38]. The sub-wavelength panel is composed of periodic horizontal slits loaded by identical HRs. Due to the presence of the HRs, the propagation inside each slit is strongly dispersive, with near-zero phase velocity close to the resonance of the HRs. In this slow sound regime, the frequencies of the cavity modes inside the slit are down-shifted and the slit behaves as a sub-wavelength resonator. Moreover, due to strong dispersion, the cavity resonances accumulate at the limit of the bandgap below the resonance frequency of the HRs. Near this accumulation frequency, simultaneously symmetric and anti-symmetric quasi-critical coupling can be achieved. In this way, using only monopolar resonators quasi-PA can be obtained in a material including transmission.

7.1.1. *Asymptotic behavior, large number of resonators*

Let us first consider N sufficiently large to accurately describe the system as a slab of material with the effective parameters. Figures 16(b–c) show the corresponding reflection coefficient in the complex frequency plane. It is obtained with the TMM, of the symmetric and antisymmetric problems for $N = 30$ resonators considering a complex frequency $\omega = \omega_r + \mathrm{i}\omega_i$, with ω_r and ω_i the real and imaginary frequencies. First, it can be observed that a series of zero-pole pairs appear in the frequency complex plane [36]. The poles correspond to the cavity modes inside the slab of effective material [59]. Due to dispersion, these cavity modes accumulate below the resonance frequency of the HRs. It can be also seen that the cavity modes of the symmetric problem (see R_s) appear at frequencies different from the frequencies of the antisymmetric one (see R_a). This effect is clearly seen in Figure 16(d), where the reflection coefficients for each problem are plotted at the real axis of frequencies.

In addition, it can be seen that for some particular frequencies, as those marked with the arrows in Figures 16(b–c), the zeros of the reflection coefficient are located on the real axis of frequencies. At these frequencies, shown by arrows in Figures 16 (b–c), the reflection coefficient of the (anti)symmetric vanishes and the structure is critically coupled. This condition is enough to achieve PA for, e.g., the symmetric problem, as was demonstrated in rigid-backed materials [28, 37, 57]. However, in order to obtain PA of the full transmission problem, both symmetric and antisymmetric reflection coefficients must simultaneously vanish [42, 54], as the following relations hold: $R = (R_s + R_a)/2$ and $T = (R_s - R_a)/2$ as explained in Section 4 and depicted in Figure 16(a).

In general, for a homogeneous slab of material the cavity resonances of the symmetric and antisymmetric problems, i.e., its Fabry–Pérot modes, are staggered in frequency and PA is not possible. However, in our system the cavity modes are accumulated below the limit of the band-gap because of the strong dispersion introduced by the presence of the resonators. Then, the zeros of the reflection coefficient for the symmetric and antisymmetric problems can be close one to another in frequency and quasi-PA can be obtained at the edge of the band-gap. Figure 16(e) shows the corresponding absorption of the full problem (black line), where the absorption due to accumulation of resonances around ω_{HR} is observed. It is interesting to show that, in the limit of a semi-infinite panel, both the reflection coefficient of the symmetric and antisymmetric problems collapse to the impedance matching condition, $\lim_{L\to\infty} R_s = \lim_{L\to\infty} R_a = (Z_e - 1)/(Z_e + 1)$, and then, only in this limit, PA can be achieved, as shown in Figure 16(e). However, for a finite layer $R_s \neq R_a$ and only quasi-PA can be reached with a single homogenized slab of material. Moreover, Z_e is generally complex and no perfect matching can be achieved.

7.1.2. *Finite number of resonators*

Figure 17 shows the scattering of the system in the lossless case for $N = 3$ resonators with the same parameters as in the Section 7.1.1. Figure 17(a–b) shows the complex frequency representation of the reflection coefficient obtained by using the TMM. The TMM correctly accounts for

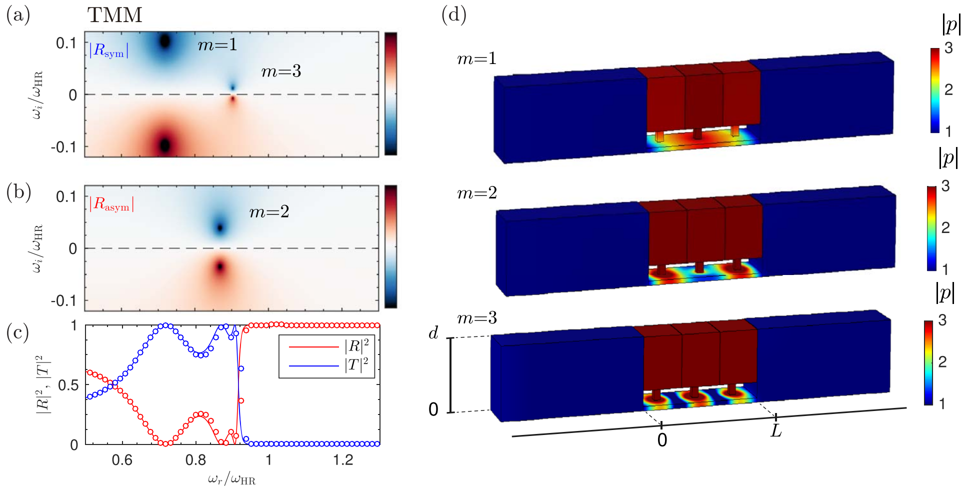

Figure 17. Complex frequency plane representation of the reflection coefficient for a panel of $N = 3$ resonators. (a) Symmetric and (b) asymmetric reflection obtained using the transfer matrix method (TMM). Colorbar in $\log|R|^2$ units. (c) Total transmission (blue) and reflection (red) using TMM, symbols correspond to the FEM simulations. (d) Acoustic field obtained using finite element method (FEM) at frequencies corresponding to the resonances $m = 1, 2, 3$, colorbar in normalized pressure units.

the finite number of resonances, in this case $N = 3$, in agreement with FEM simulations. It is also worth noting here that these cavity resonances are in fact the collective modes of the HRs and there exist only N different collective modes. Figure 17(c) shows the total reflection and transmission in the real frequency axis calculated with TMM and FEM. We note that the finite number of HRs limits the accumulation of resonances near the band-gap: as N decreases the condition to have symmetric and antisymmetric resonances close to one another in frequency becomes more difficult to achieve. Therefore, the number of (identical) HRs is a critical parameter to obtain quasi-PA in metamaterials made of identical resonators considering transmission by means of the accumulation of resonances.

Once losses are introduced in the system, the zero-pole structure is down shifted in the complex frequency plane and the system starts to absorb energy [36]. Figure 18(a) presents the absorption of a panel as a function of the number of resonators, N, and frequency. First, it can be observed that for a relatively large number of resonators quasi-PA can be achieved even when the discreteness is retained, e.g. for $N = 50$ resonators as shown in the Figure 18(b). The material is almost impedance matched with the exterior medium.

For most sound absorption applications it is desirable to use panels with reduced thickness, and of special interest is the design of panels with sub-wavelength dimensions. Then, when reducing the panel thickness, the number of resonators must also be reduced and, therefore, the accumulation of resonances becomes limited. Figure 18(c) shows the absorption of a panel with $N = 15$ ($L \approx \lambda_{\alpha_{\max}}/2$), while Figure 18(d) shows the absorption of a panel with $N = 5$ ($L = \lambda_{\alpha_{\max}}/6.6$). In both cases, a peak of absorption is still observed, but its amplitude falls to $\alpha_{\max} = 0.96$ and $\alpha_{\max} = 0.92$ respectively for each case. The corresponding reflection coefficient in complex frequency plane for $N = 5$ is shown in Figure 18(f) for the symmetric and antisymmetric problems. By tuning the geometry of the system, high acoustic absorption can be achieved by locating one zero of the reflection coefficient of the symmetric problem on the real frequency axis and, simultaneously, locate another zero of the antisymmetric problem as close as possible

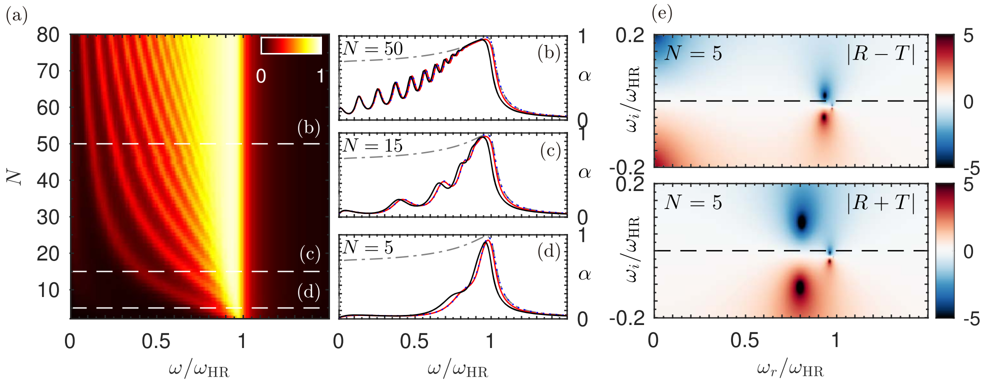

Figure 18. (a) Absorption of the material as a function of the number of resonators and frequency. (b–d) Absorption for $N = 50, 15$ and 5 resonators, obtained using MEM (red), effective parameters (dotted blue) and TMM (black). Dashed-dotted gray line shows the impedance matching condition. (e) Complex frequency representation of the reflection coefficient for $N = 5$ resonators. Colormap in $\log|R|^2$ units. Figure reproduced from Ref. [38].

to the real axis at a different but nearly frequency. Therefore, the maximum value of absorption is directly dependent on the number of HRs and inversely dependent on the panel thickness. Using an array of identical resonators the design of the panel is a compromise between the peak acoustic absorption and the parameter $\lambda_{\max}/L$.

7.1.3. *Experimental results*

A sub-wavelength thickness sample with $N = 10$ resonators is built using stereolithography techniques using a photosensitive epoxy polymer.[2] The geometry of the structure was tuned using an optimization method (sequential quadratic programming (SQP) method [73]) in order to maximize the absorption at a given frequency (350 Hz), while the panel thickness was constrained to $L = \lambda/10$. The resulting parameters were $h = 4.3$ mm, $a = 9.8$ mm, $w_n = 5.3$ mm, $w_{c,1} = 11.4$ mm, $w_{c,2} = 9.3$ mm, $d =$ cm, $l_n = 25.2$ mm, and $l_c = 139.6$ mm. It is worth noting here that we use the coiling of the HRs in order to save space. The amplitude of the acoustic source is low enough to consider negligible the contribution of the nonlinearity of the HRs. Figure 19 summarizes the experimental results. First, Figure 19(a) shows a photograph of the panel, composed by 3 unit cells with $N = 10$ for each one, allowing the measurement of reflection and transmission coefficients at normal incidence (white arrow in Figure 19), which are shown in Figure 19(b). A good agreement between the experimental results, theoretical predictions and FEM simulations is observed. The results show the band-gap generated by the resonance of the HRs, where the low-cutoff frequency of the band-gap is just below the resonance frequency of the HRs, $f_{\mathrm{HR}} = 364$ Hz. In this frequency range, transmission almost vanishes and the total reflection does not, as shown in Figure 19(b), as a consequence of the staggered structure of zero-pole structure. The corresponding absorption is plotted in Figure 19(c), where again good agreement can be observed between theory and experiments. Here, at 350 Hz the absorption peak obtained from the experiments was $\alpha = 0.87$, while $\alpha = 0.91$ was obtained from TMM predictions. In addition, small differences can be observed around 300 Hz. These small discrepancies can be associated to imperfections on the fitting of the structure to the impedance tube and due to the coiling of the HRs.

---

[2] (Accura 60®, 3D Systems Corporation, Rock Hill, SC 29730, USA), where the acoustic properties of the solid phase are $\rho_0 = 1210$ kg/m^3, $c_0 = 1630 \pm 60$ m/s.

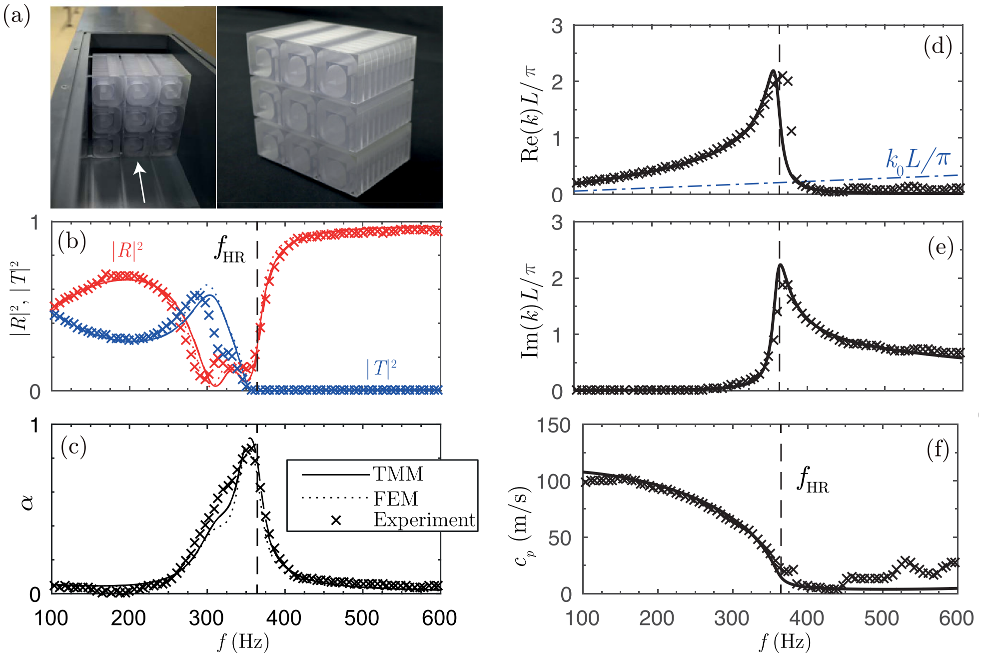

Figure 19. (a) Photographs of the experimental setup, where the semitransparent resin allows to see the coiled HRs inside the material. The arrow shows the incidence direction. (b) Corresponding reflection (red) and transmission (blue) coefficients of the sample measured experimentally (markers), TMM (continuous), and finite element simulation (dotted). The vertical dashed line marks the resonance of the HRs. (c) Corresponding absorption. (d) Real part of the wavenumber (thick gray), and its reconstruction using the experimental data (markers) and analytic data (continuous line). (e) Corresponding imaginary part. (f) Quantity $\tilde{c_p} = \mathrm{Re}(\omega/k)$, closely related to the speed of sound.

The effective wavenumber inside the slits was reconstructed using an inversion method [75]. Figure 19(d,e) shows the experimental and theoretical reconstruction of the real and imaginary part of the wavenumber respectively. It can be observed that the experimental reconstruction agrees with the theoretical prediction. Here, at $f = 350$ Hz where the peak absorption is observed, the real part of the wavenumber is greatly increased compared to the wavenumber in air, k_0. Moreover, the imaginary part of the wavenumber is also increased, leading to the damping of the acoustic waves inside the material. Finally, the quantity $\tilde{c}_p = \mathrm{Re}(\omega/k)$, is shown in Figure 19(f). It can be seen that slow sound conditions are achieved by the experiment and the speed of sound inside the material is reduced to $\tilde{c}_p = 34$ m/s at the peak absorption frequency, $f = 350$ Hz. Finally, it is important to note that the effect of the evanescent coupling between adjacent resonators is negligible. This coupling is implicitly included in FEM simulations and inherently present in the experiments. The good agreement between FEM simulations and experiments, and theoretical models shows the evanescent coupling can be considered negligible.

7.2. *Perfect absorption in asymmetric panels*

In this section we address the problem of the PA in asymmetric panels for a single frequency [39]. The analyzed structure, namely *sub-wavelength asymmetric panel* (SAP) is composed of $N = 2$ HRs and it is shown in Figure 20(a). The SAP is designed to produce a single-frequency peak of PA

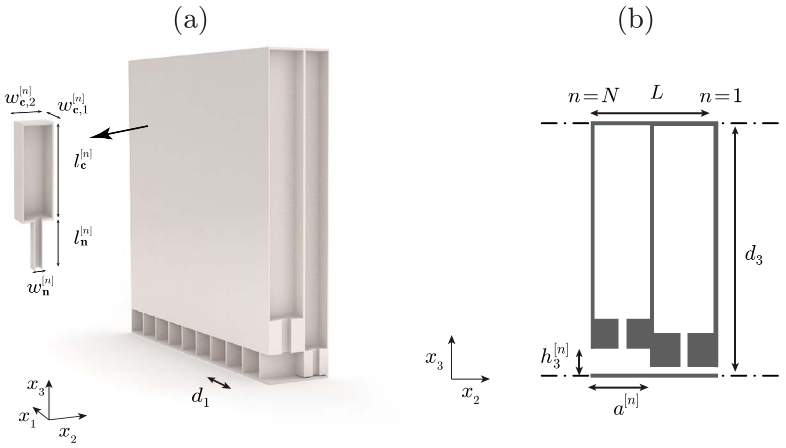

Figure 20. (a) Conceptual view of a sub-wavelength asymmetric panel (SAP) ($N = 2$ resonators), where cross-section shows the waveguide and the loading HRs. (b) Scheme showing the geometrical variables for the SAP.

Table 1. Geometrical parameters for the SAP ($N = 2$)

n	$a^{[n]}$ (mm)	$h_3^{[n]}$ (mm)	$h_1^{[n]}$ (mm)	$l_{\mathbf{n}}^{[n]}$ (mm)	$l_{\mathbf{c}}^{[n]}$ (mm)	$w_{\mathbf{n}}^{[n]}$ (mm)	$w_{\mathbf{c},1}^{[n]}$ (mm)	$w_{\mathbf{c},2}^{[n]}$ (mm)
2	16.8	12.7	13.8	15.4	119.1	4.5	13.8	15.7
1	11.8	1.0	13.8	12.0	134.1	3.2	13.8	10.8

Table reproduced from Ref. [39].

at 300 Hz. The geometrical parameters of both structures were tuned using optimization methods (sequential quadratic programming (SQP) [73]). In the case of the SAP the cost function minimized during the optimization process was $\varepsilon_{\text{SAP}} = |R^-|^2 + |T|^2$, i.e., to maximize the absorption at a given frequency, in this case we selected 300 Hz. The length of the SAP was constrained to $L = 2.64$ cm, i.e., a panel 40 times thinner than the incoming wavelength. The geometrical parameters for the SAP, corresponding to Figure 21, are listed in Table 1 (more details in Ref. [39]). The total structure thickness is $L = \sum a^{[n]} = 28.6$ mm, and its height and width of the unit cell are $d_3 = 148.1$ mm and $d_1 = 14.8$ mm respectively.

We start analyzing the behavior of the designed SAP, considering the two directions of incidence, namely *forward* and *backward*, as depicted in Figures 21(a,b). Figures 21(c–f) show the corresponding absorption, reflection and transmission coefficients for each case. The results are calculated analytically using the transfer matrix method (TMM) in which the thermoviscous losses are accounted for, numerically using finite element method (FEM) and experimentally validated by impedance tube measurements (see Ref. [39] for more details).

First, in the forward configuration, shown in Figure 21(a), the resonator $n = 1$ of the waveguide presents a resonance frequency at $f_1 = 285$ Hz. As a consequence, above f_1, a band gap is introduced and the transmission is strongly reduced, the HR acting effectively as a rigidly-backed wall for the right ingoing waves. Then, the resonator $n = 2$, with a superior resonance frequency at $f_2 = 310$ Hz, is tuned by the optimization process to critically couple the system with the exterior medium, matching the impedance of the waveguide to that of the surrounding medium. This is achieved at 300 Hz. As a consequence, no reflected waves are produced at this particular frequency and therefore, $\alpha = 1 - |R^-|^2 - |T|^2 = 1$ holds. In this situation, PA is observed in a panel

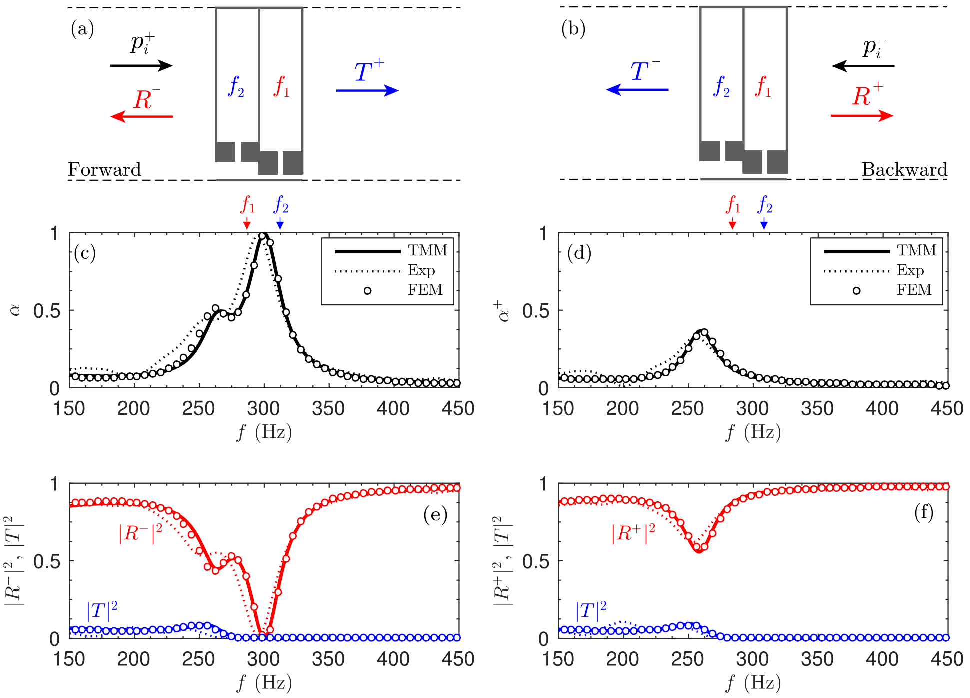

Figure 21. Scheme of the sub-wavelength asymmetric panel in (a) forward and (b) reverse configuration. (c) Absorption for the forward configuration obtained using TMM (continuous line), FEM (circles), and experiment (dotted line). Corresponding reflection and transmission coefficients. (d) Absorption for the backward configuration. (f) Corresponding reflection and transmission coefficients. The arrows mark the resonance frequencies of the HRs, f_1 and f_2. Figure reproduced from Ref. [39].

with a thickness 40 times smaller that the wavelength, i.e., a panel of thickness $L = 2.64$ cm. It is worth noting here that the change of section in the main waveguide helps to achieve the impedance matching, specially for very thin SAPs as the one presented here. We will see later on that this steeped change in the cross-section is analogous to the graded profile of the main waveguide for the broadband structure.

Second, in the backward propagation shown in Figure 21(b), the wave impinges first the lowest resonance frequency resonator, f_1. Now at 300 Hz the wave almost no transmission is allowed in the waveguide. As the waveguide is not impedance matched at 300 Hz in backward direction, reflection is high and absorption is poor ($\alpha^+ = 0.05$). For frequencies below f_2, propagation is allowed in the main waveguide and the effect of the second HR may be visible inducing a decrease of the reflection coefficient. However, the impedance matching in the backward direction is not fully achieved and only a small amount of absorption is observed near the resonance frequency of the first resonator. Therefore, the absorption in this configuration is different from each incidence side.

7.3. *Rainbow absorbers*

The concept of the SAP can be applied to design broadband perfect absorbers. The idea is to create a frequency-cascade of band-gaps and critically coupled resonators in order to generate a rainbow-trapping effect as described in Ref. [39]. By using this approach we address the problem

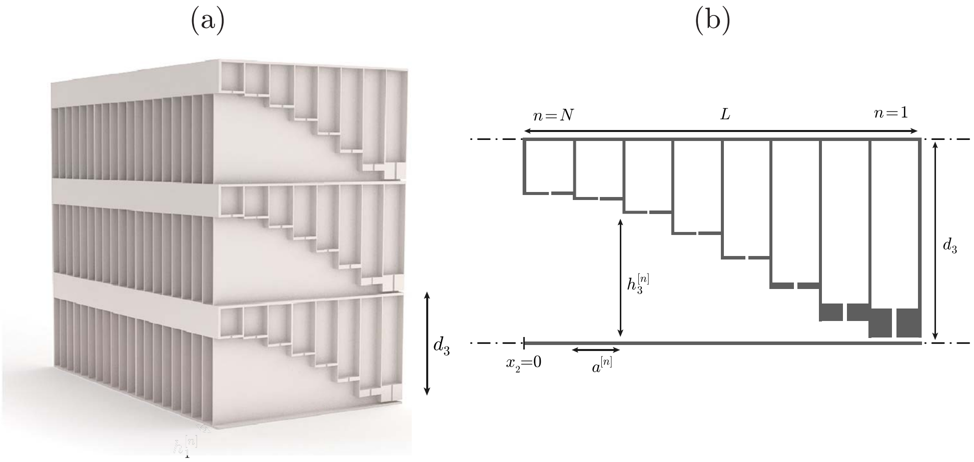

Figure 22. (a) Conceptual view of a sub-wavelength rainbow trapping absorber (RTA) with $N = 8$ HRs, where cross-section shows the waveguide and the loading HRs. (b) Scheme showing the geometrical variables for RTA panels.

of perfect and broadband acoustic absorption using deep-sub-wavelength panels. Rainbow trapping phenomenon, i.e., the localization of energy due to a gradual reduction of the group velocity in graded structures, has been observed in optics [76], acoustics [77–79] or elastodynamics [80]. However, losses were not accounted for and, therefore, absorption was not studied in these works. In the present configuration, a set of graded HRs is used, allowing to reduce, in addition to the thickness of the panels, the dimension of the unit cell to the deep-sub-wavelength regime.

We design panels composed of monopolar resonators with graded dimensions, namely *rainbow-trapping absorbers* (RTA). The designed panels present broadband, perfect and asymmetric sound absorption, and, due to slow sound [32,38,39,57,81], their thickness is reduced to the deep-sub-wavelength regime. In practice, the resonance frequency of a waveguide in which slow sound propagates is strongly reduced and eventually shifted to the sub-wavelength regime, because it is proportional to the sound velocity. In particular, the structures are composed of a rigid panel, of thickness L, periodically perforated with series of identical waveguides of variable square cross-section loaded by an array of N HRs of different dimensions, as shown in Figures 22(a,b). Each waveguide is therefore divided in N segments of length $a^{[n]}$, width $h_1^{[n]}$ and height $h_3^{[n]}$. The HRs are located in the middle of each waveguide section.

The geometrical parameters are tuned using optimization methods SQP [73]. For the rainbow trapping absorber ($N = 9$), the cost function is $\varepsilon_{\mathrm{RTA}} = \int_{f_1}^{f_N} |R^-|^2 + |T|^2 \,\mathrm{d}f$, i.e., to maximize the absorption in a broad frequency bandwidth, that is chosen from $f_1 = 300$ Hz to $f_N = 1000$ Hz. In the case of the RTA the length of the panel is constrained to $L = 11.3$ cm, i.e. a panel 10 times thinner than the wavelength at 300 Hz. The geometrical parameters for the RTA ($N = 9$), measured experimentally, corresponding to Figure 23, are listed in Table 2 (more details in Ref. [39]). The total structure thickness is $L = \sum a^{[n]} = 113$ mm, and its height and width of the unit cell are $d_3 = 48.7$ mm and $d_1 = 14.6$ mm respectively.

The process is as follows. First, we tune the deepest resonator ($n = 1$) in the waveguide to reduce the transmission above a frequency f_1. Second, in the same way as previously done in the SAP, a second resonator with slightly higher resonance frequency, f_2, is placed in the preceding segment of the waveguide. The geometry of this resonator and the section of the waveguide are tuned to impedance match the system at this frequency. Therefore, the reflection vanishes and a peak of PA is achieved in the same way as in the SAPs. Note this latter HR also reduces the

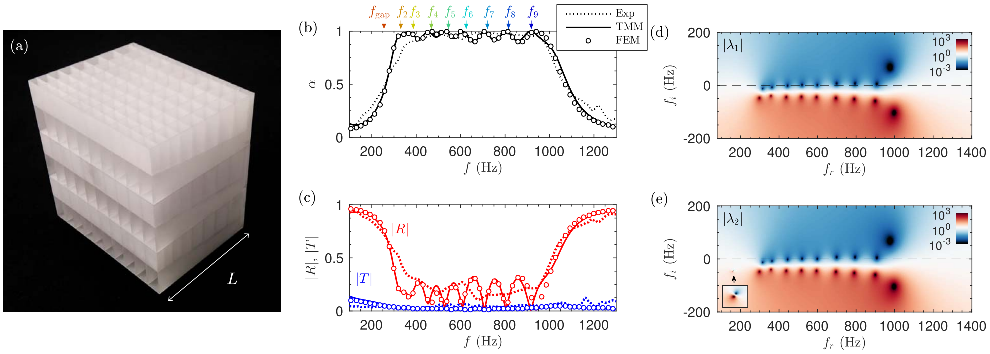

Figure 23. (a) Photograph of the sample containing 10 × 3 unit cells. (b) Absorption obtained by using the TMM (continuous line), FEM simulations (circles) and measured experimentally (dotted line). (b) Corresponding reflection (red curves) and transmission (blue curves) coefficients in amplitude. (d–e) Complex frequency representation of the eigenvalues of the scattering matrix, $\lambda_{1,2}$. Colormap in $10\log_{10}|\lambda|^2$ scale. Figure reproduced from Ref. [39].

Table 2. Geometrical parameters for the RTA ($N = 9$)

n	$a^{[n]}$ (mm)	$h_3^{[n]}$ (mm)	$h_1^{[n]}$ (mm)	$l_{\mathbf{n}}^{[n]}$ (mm)	$l_{\mathbf{c}}^{[n]}$ (mm)	$w_{\mathbf{n}}^{[n]}$ (mm)	$w_{\mathbf{c},1}^{[n]}$ (mm)	$w_{\mathbf{c},2}^{[n]}$ (mm)
9	7.9	25.6	14.0	1.1	21.4	1.2	14.0	7.2
8	9.5	24.2	14.0	1.0	22.8	1.2	14.0	9.0
7	11.0	22.8	14.0	1.7	23.6	1.4	14.0	10.6
6	12.6	21.6	14.0	0.7	25.9	1.0	14.0	12.0
5	14.1	20.2	14.0	1.5	26.5	1.2	14.0	13.6
4	15.7	18.8	14.0	1.1	28.3	1.0	14.0	15.2
3	17.3	17.4	14.0	1.6	29.2	1.0	14.0	16.8
2	18.8	16.0	14.0	1.1	31.2	0.8	14.0	18.4
1	6.4	1.0	1.0	3.0	44.7	0.6	14.0	5.6

Table reproduced from Ref. [39].

transmission at even higher frequencies. Then, the process can be repeated by extending the waveguide with more segments, each one with a tuned HR being its resonance frequency higher than the preceding one.

Due to machine precision of the available 3D printing system (the minimum step was 0.1 mm), the design of the RTA should be constrained to accomplish this precision. The main limitation is related to the loss of accuracy of the diameters of the small necks that compose the HRs. Under this technological constraint we design the RTA using $N = 9$ HRs and quantizing the dimensions of all the geometrical elements that compose the structure to the machine precision. The manufactured sample is shown in Figure 23(a) and the quantized geometrical parameters are listed in Table 2 (see Ref. [39]). Figures 23(b–c) show the absorption, reflection and transmission of the device calculated with the TMM, FEM and measured experimentally. Note that both reflection and transmission coefficients are plotted in terms of amplitude and not in terms of energy in order to emphasize the fact that the transmission does not vanish apart from the PA frequency band. The deepest resonator ($n = 1$) presents a resonance frequency of $f_1 = f_{gap} =$ 259 Hz, causing the transmission to drop. A set of 9 resonators are tuned following the process

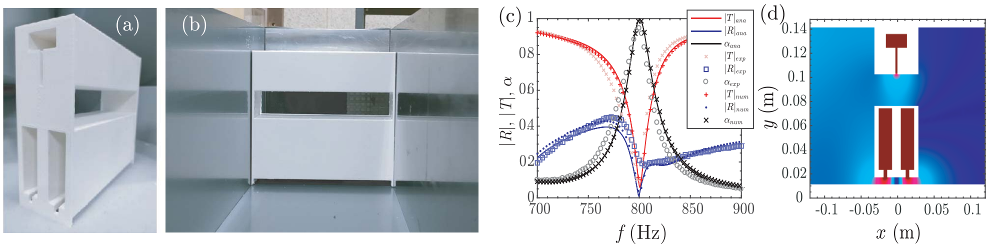

Figure 24. (a,b) Images of the metamaterial with degenerated resonators. (c) Reflection, absorption and transmission coefficients of the metamaterial. (d) Pressure field $|p|$ at the perfect absorption frequency.

previously described, with increasing resonance frequencies ranging from 300 to 1000 Hz. As a result of the frequency-cascade process, the impedance of the structure in the working frequency range is matched with the exterior medium while the transmission vanishes. As a consequence, the RTA presents a flat and quasi-PA coefficient in this frequency range (see Figure 23(b)). Excellent agreement is found between the TMM predictions and FEM simulations, while good agreement is observed between the experimental measurements and both models. It can be observed that at low frequencies there are small differences between the measurements and the models. These disagreements are mainly caused by imperfections in the sample manufacturing, by imperfect fitting of the structure to the impedance tube, by the possible evanescent coupling between adjacent waveguides and adjacent HRs, and/or by the limitations of the visco-thermal model used at the joints between waveguide sections.

The corresponding representation of the two eigenvalues of the **S**-matrix in the complex frequency plane is shown in Figures 23(d–e). We can see that even under the constraints imposed by the metamaterial construction process, all the $N-1$ zeros of the eigenvalues that produce the critical coupling of the structure are located very close to the real axis being the zeros of λ_1 at the same frequencies as λ_2. Note in the manufactured system, not all the zeros are located exactly on the real axis, but the quality factor of the resonances is very low (note the logarithmic color scale in Figure 23(c–d)). Therefore they overlap producing quasi-perfect sound absorption in a frequency band from 300 to 1000 Hz for a panel 10 times thinner than the wavelength at 300 Hz in air.

7.4. *Perfect absorption with mirror symmetric resonators with degenerate resonances*

As previously discussed in Section 4, when the metamaterial is mirror symmetric with respect to its center, degenerated resonators must be used [30, 51, 54] to achieve perfect absorption. In this section, we show the possibility to design resonant building blocks with different slits supporting each one symmetric and antisymmetric resonances as described in Ref. [51]. Figures 24(a,b) show a mirror-symmetric metamaterial with two slits loaded by one and two HRs. While the slit with a single resonator supports only one single resonance corresponding to the first symmetric Fabry–Pérot resonance, the slit loaded with two HRs supports the first Fabry–Pérot resonances, the first one being symmetric and the second one being antisymmetric. The challenge consists in tuning the symmetric resonance of the slit with a single HR and the antisymmetric resonance of the slit with two HRs at the same frequency with the good amount of inherent losses that compensates the energy leakage. In this case PA can be obtained when a plane wave excites the system independently of the side of the metamaterial, thus producing two-sided PA at the same frequency.

Figure 24(c) shows the scattering coefficients of the full transmission problem. A PA peak is observed at 800 Hz. Figure 24(d) shows the sound field distribution of the complete problem at the perfect absorption frequency. The upper slit, loaded by a single HR, shows a symmetric Fabry–Pérot mode while the lower slit, loaded by two HRs, shows the antisymmetric Fabry–Pérot mode. Both modes are excited at the same frequency, i.e. the structure has a degenerate mode. It should be noted here that perfect absorption is very sensitive to the geometry of the resonators, which explains the slight discrepancies between the analytical or numerical predictions and the experimental results as shown in detail in Ref. [51].

8. Conclusions and perspectives

Finite size acoustic metamaterials made of Helmholtz resonators, or in general, local resonators can be considered as open lossy resonant systems. Due to this open and lossy features, the system can be characterized by both the energy leakage and the inherent losses at the resonance frequency. In this work, only geometries involving the sole propagation of plane waves far from the absorbing system are considered. Then, a scattering matrix of low dimension (1×1 for reflection problems (one port system), 2×2 for transmission problems (two port systems) or 3×3 for the three port system) can be used to represent the scattering properties of the system. The frequencies at which its eigenvalues are zero and the system is excited with the corresponding eigenvector, represent the cases in which the outgoing waves present zero amplitude, and as consequence PA is obtained. We have connected this specific feature situation with the critical coupling condition by means of the representation of the eigenvalues of the scattering matrix in the complex frequency plane [36]. The balance between the energy leakage and the inherent losses of the system, i.e., the critical coupling condition, is graphically represented in the complex frequency plane by the crossing of the zeros of the complex eigenvalues with the real frequency axis, representing the PA configuration. We have used this technique to analyze the reflection problem, where the PA have been obtained in 1-port systems [28] and in reflecting panels [37,57]. The transmission problem becomes more complicated as the zeros of the two eigenvalues should be simultaneously placed on real frequency axis. This situation can be obtained by breaking the symmetry of the system in 2-port systems [42] or in transmission panels [39]. The nonlinear absorption can also be used to fulfill the critical coupling conditions [43, 46]. An intermediate situation can be obtained by using the strong dispersion introduced by the local resonators, producing an accumulation point [38] with quasi-perfect absorption in the transmission problem. The N-port system have been analyzed [53], showing the possibility to obtain the critical coupling conditions for each channel in the system.

The challenge of acoustic absorption and insulation represents a major issue, the solution of which could benefit several industrial sectors such as building, civil or transport ones. Noise reduction and control are major societal and industrial issues, particularly in the low frequency range and require the development of new materials as well as innovative approaches both in terms of process and target properties. Everyday life and industrial standards impose lighter, thinner and long life structures that are needed to mitigate and absorb lower and lower frequency acoustic noises. This work intends to motivate new research lines in the field of acoustic absorption with sub-wavelength structures.

Acknowledgements

The authors gratefully acknowledge the ANR-RGC METARoom (ANR-18-CE08-0021) project and the project HYPERMETA funded under the program Étoiles Montantes of the Région Pays de la Loire. NJ acknowledges financial support from the Spanish Ministry of Science, Innovation and Universities (MICINN) through grant "Juan de la Cierva-Incorporación" (IJC2018-037897-I). This article is based upon work from COST Action DENORMS CA15125, supported by COST (European Cooperation in Science and Technology).

References

[1] M. Law, L. E. Greene, J. C. Johnson, R. Saykally, P. Yang, "Nanowire dye-sensitized solar cells", *Nat. Mater.* **4** (2005), no. 6, p. 455-459.

[2] A. Derode, P. Roux, M. Fink, "Robust acoustic time reversal with high-order multiple scattering", *Phys. Rev. Lett.* **75** (1995), no. 23, p. 4206-4209.

[3] Y. Chong, L. Ge, H. Cao, A. D. Stone, "Coherent perfect absorbers: time-reversed lasers", *Phys. Rev. Lett.* **105** (2010), no. 5, article no. 053901.

[4] J. Mei, G. Ma, M. Yang, Z. Yang, W. Wen, P. Sheng, "Dark acoustic metamaterials as super absorbers for low-frequency sound", *Nat. Commun.* **3** (2012), article no. 756.

[5] N. Engheta, R. W. Ziolkowski, *Metamaterials: Physics and Engineering Explorations*, John Wiley & Sons, 2006.

[6] V. Romero-García, A. Hladky-Hennion, *Fundamentals and Applications of Acoustic Metamaterials: From Seismic to Radio Frequency*, ISTE Willey, 2019.

[7] R. Craster, S. Guenneau, *Acoustic Metamaterials*, Springer Series in Materials Science, vol. 166, Spinger, 2013.

[8] X. Yu, J. Zhou, H. Liang, Z. Jiang, L. Wu, "Mechanical metamaterials associated with stiffness, rigidity and compressibility: A brief review", *Prog. Mater. Sci.* **94** (2018), p. 114-173.

[9] D. Mu, H. Shu, L. Zhao, S. An, "A review of research on seismic metamaterials", *Adv. Eng. Mater.* **22** (2020), no. 4, article no. 1901148.

[10] Z. Liu, X. Zhang, Y. Mao, Y. Y. Zhu, Z. Yang, C. T. Chan, P. Sheng, "Locally resonant sonic materials", *Science* **289** (2000), no. 5485, p. 1734-1736.

[11] N. Fang, D. Xi, J. Xu, M. Ambati, W. Srituravanich, C. Sun, X. Zhang, "Ultrasonic metamaterials with negative modulus", *Nat. Mater.* **5** (2006), no. 6, p. 452-456.

[12] P. Deymier (ed.), *Acoustic Metamaterials and Phononic Crystals*, Springer-Verlag, Berlin, Heidelberg, 2013.

[13] G. Ma, P. Sheng, "Acoustic metamaterials: From local resonances to broad horizons", *Sci. Adv.* **2** (2016), no. 2, article no. e1501595.

[14] M. Yang, P. Sheng, "Sound absorption structures: From porous media to acoustic metamaterials", *Annu. Rev. Mater. Res.* **47** (2017), p. 83-114.

[15] Y. I. Bobrovnitskii, T. Tomilina, "Sound absorption and metamaterials: A review", *Acoust. Phys.* **64** (2018), no. 5, p. 519-526.

[16] C. Lagarrigue, J.-P. Groby, V. Tournat, O. Dazel, O. Umnova, "Absorption of sound by porous layers with embedded periodic array of resonant inclusions", *J. Acoust. Soc. Am.* **134** (2013), p. 4670-4680.

[17] J.-P. Groby, B. Nennig, C. Lagarrigue, B. Brouard, O. Dazel, V. Tournat, "Enhancing the absorption properties of acoustic porous plates by periodically embedding Helmholtz resonators", *J. Acoust. Soc. Am.* **137** (2015), no. 1, p. 273-280.

[18] C. Lagarrigue, J.-P. Groby, O. Dazel, V. Tournat, "Design of metaporous supercells by genetic algorithm for absorption optimization on a wide frequency band", *Appl. Acoust.* **102** (2016), p. 49-54.

[19] X. Cai, Q. Guo, G. Hu, J. Yang, "Ultrathin low-frequency sound absorbing panels based on coplanar spiral tubes or coplanar Helmholtz resonators", *Appl. Phys. Lett.* **105** (2014), no. 12, article no. 121901.

[20] Y. Li, B. M. Assouar, "Acoustic metasurface-based perfect absorber with deep subwavelength thickness", *Appl. Phys. Lett.* **108** (2016), no. 6, article no. 063502.

[21] Y. Wang, H. Zhao, H. Yang, J. Zhong, J. Wen, "A space-coiled acoustic metamaterial with tunable low-frequency sound absorption", *Europhys. Lett.* **120** (2018), no. 5, article no. 54001.

[22] C. Shen, S. A. Cummer, "Harnessing multiple internal reflections to design highly absorptive acoustic metasurfaces", *Phys. Rev. Appl.* **9** (2018), no. 5, article no. 054009.

[23] Z. Yang, J. Mei, M. Yang, N. Chan, P. Sheng, "Membrane-type acoustic metamaterial with negative dynamic mass", *Phys. Rev. Lett.* **101** (2008), no. 20, article no. 204301.

[24] X. Guo, V. Gusev, K. Bertoldi, V. Tournat, "Manipulating acoustic wave reflexion by a nonlinear elastic metasurface", *J. Appl. Phys.* **123** (2018), no. 12, article no. 124901.

[25] X. Guo, V. Gusev, V. Tournat, B. Deng, K. Bertoldi, "Frequency-doubling effect in acoustic reflection by a nonlinear, architected rotating-square metasurface", *Phys. Rev. E* **99** (2019), article no. 052209.

[26] C. E. Bradley, "Acoustic bloch wave propagation in a periodic waveguide", Tech. rep., Technical Report of Applied Research Laboratories, Report No. ARL-TR-91-19 (July), The University of Texas at Austin (1991).

[27] N. Sugimoto, T. Horioka, "Dispersion characteristics of sound waves in a tunnel with an array of Helmholtz resonators", *J. Acoust. Soc. Am.* **97** (1995), no. 3, p. 1446-1459.

[28] V. Romero-García, G. Theocharis, O. Richoux, A. Merkel, V. Tournat, V. Pagneux, "Perfect and broadband acoustic absorption by critically coupled sub-wavelength resonators", *Sci. Rep.* **6** (2016), article no. 19519.

[29] G. Ma, M. Yang, S. Xiao, Z. Yang, P. Sheng, "Acoustic metasurface with hybrid resonances", *Nat. Mater.* **13** (2014), no. 9, p. 873-878.

[30] M. Yang, C. Meng, C. Fu, Y. Li, Z. Yang, P. Sheng, "Subwavelength total acoustic absorption with degenerate resonators", *Appl. Phys. Lett.* **107** (2015), no. 10, article no. 104104.

[31] Y. Aurégan, "Ultra-thin low frequency perfect sound absorber with high ratio of active area", *Appl. Phys. Lett.* **113** (2018), article no. 201904.

[32] J.-P. Groby, W. Huang, A. Lardeau, Y. Aurégan, "The use of slow waves to design simple sound absorbing materials", *J. Appl. Phys.* **117** (2015), no. 12, article no. 124903.

[33] V. Leroy, A. Strybulevych, M. Lanoy, F. Lemoult, A. Tourin, J. H. Page, "Superabsorption of acoustic waves with bubble metascreens", *Phys. Rev. B* **91** (2015), article no. 020301.

[34] A. A. Fernández-Marín, N. Jiménez, J.-P. Groby, J. Sánchez-Dehesa, V. Romero-García, "Aerogel-based metasurfaces for perfect acoustic energy absorption", *Appl. Phys. Lett.* **115** (2019), article no. 061901.

[35] H. Long, Y. Cheng, J. Tao, X. Liu, "Perfect absorption of low-frequency sound waves by critically coupled subwavelength resonant system", *Appl. Phys. Lett.* **110** (2017), no. 2, article no. 023502.

[36] V. Romero-García, G. Theocharis, O. Richoux, V. Pagneux, "Use of complex frequency plane to design broadband and sub-wavelength absorbers", *J. Acoust. Soc. Am.* **139** (2016), no. 6, p. 3395-3403.

[37] N. Jiménez, W. Huang, V. Romero-García, V. Pagneux, J.-P. Groby, "Ultra-thin metamaterial for perfect and quasi-omnidirectional sound absorption", *Appl. Phys. Lett.* **109** (2016), no. 12, article no. 121902.

[38] N. Jiménez, V. Romero-García, V. Pagneux, J.-P. Groby, "Quasiperfect absorption by subwavelength acoustic panels in transmission using accumulation of resonances due to slow sound", *Phys. Rev. B* **95** (2017), article no. 014205.

[39] N. Jiménez, V. Romero-García, V. Pagneux, J.-P. Groby, "Rainbow-trapping absorbers: Broadband, perfect and asymmetric sound absorption by subwavelength panels for transmission problems", *Sci. Rep.* **7** (2017), no. 1, article no. 13595.

[40] N. Jiménez, T. J. Cox, V. Romero-García, J.-P. Groby, "Metadiffusers: Deep-subwavelength sound diffusers", *Sci. Rep.* **7** (2017), no. 1, article no. 5389.

[41] N. Jiménez, V. Romero-García, J.-P. Groby, "Perfect absorption of sound by rigidly-backed high-porous materials", *Acta Acust. United Acust.* **104** (2018), no. 3, p. 396-409.

[42] A. Merkel, G. Theocharis, O. Richoux, V. Romero-García, V. Pagneux, "Control of acoustic absorption in one-dimensional scattering by resonant scatterers", *Appl. Phys. Lett.* **107** (2015), no. 24, article no. 244102.

[43] V. Achilleos, O. Richoux, G. Theocharis, "Coherent perfect absorption induced by the nonlinearity of a Helmholtz resonator", *J. Acoust. Soc. Am.* **140** (2016), article no. EL94.

[44] H. Long, Y. Cheng, X. Liu, "Asymmetric absorber with multiband and broadband for low-frequency sound", *Appl. Phys. Lett.* **111** (2017), no. 14, article no. 143502.

[45] A. Merkel, V. Romero-García, J.-P. Groby, J. Li, J. Christensen, "Unidirectional zero sonic reflection in passive pt-symmetric willis media", *Phys. Rev. B* **98** (2018), article no. 201102(R).

[46] E. Monsalve, A. Maurel, P. Petitjeans, V. Pagneux, "Perfect absorption of water waves by linearor nonlinear critical coupling", *Appl. Phys. Lett.* **114** (2018), article no. 013901.

[47] L. Schwan, O. Umnova, C. Boutin, "Sound absorption and reflection from a resonant metasurface: Homogenisation model with experimental validation", *Wave Motion* **72** (2017), p. 154-172.

[48] S. Huang, X. Fang, X. Wang, B. Assouar, Q. Cheng, Y. Li, "Acoustic perfect absorbers via spiral metasurfaces with embedded apertures", *Appl. Phys. Lett.* **113** (2018), no. 23, article no. 233501.

[49] A. Elayouch, M. Addouche, A. Khelif, "Extensive tailorability of sound absorption using acoustic metamaterials", *J. Appl. Phys.* **124** (2018), no. 15, article no. 155103.

[50] A. Maurel, J.-F. Mercier, K. Pham, J.-J. Marigo, A. Ourir, "Enhanced resonance of sparse arrays of Helmholtz resonators—application to perfect absorption", *J. Acoust. Soc. Am.* **145** (2019), no. 4, p. 2552-2560.

[51] V. Romero-García, N. Jiménez, J.-P. Groby, A. Merkel, V. Tournat, G. Theocharis, O. Richoux, V. Pagneux, "Perfect absorption in mirror-symmetric acoustic metascreens", *Phys. Rev. Appl.* (2020), article no. 054055.

[52] K. Y. Bliokh, Y. P. Bliokh, V. Freilikher, S. Savel'ev, F. Nori, "Colloquium: Unusual resonators: Plasmonics, metamaterials, and random media", *Rev. Mod. Phys.* **80** (2008), no. 4, p. 1201-1213.

[53] O. Richoux, V. Achilleos, G. Theocharis, I. Brouzos, "Subwavelength interferometric control of absorption in three-port acoustic network", *Sci. Rep.* **8** (2018), no. 1, article no. 12328.

[54] J. R. Piper, V. Liu, S. Fan, "Total absorption by degenrate critical coupling", *Appl. Phys. Lett.* **104** (2014), article no. 251110.

[55] Y. Chong, L. Ge, H. Cao, A. Stone, "Coherent perfect absorbers: Time-reversed lasers", *Phys. Rev. Lett.* **105** (2010), article no. 053901.

[56] P. Wei, C. Croënne, S. T. Chu, J. Li, "Symmetrical and anti-symmetrical coherent prefect absorption for acoustic waves", *Appl. Phys. Lett.* **104** (2014), article no. 121902.

[57] J.-P. Groby, R. Pommier, Y. Aurégan, "Use of slow sound to design perfect and broadband passive sound absorbing materials", *J. Acoust. Soc. Am.* **139** (2016), no. 4, p. 1660-1671.

[58] T. Luk, S. Campione, I. Kim, S. Feng, Y. Jun, S. Liu, J. Wright, I. Brener, P. Catrysse, S. Fan, M. Sinclair, "Directional perfect absorption using deep subwavelength lowpermittivity films", *Phys. Rev. B* **90** (2014), article no. 085411.

[59] V. Pagneux, "Trapped modes and edge resonances in acoustics and elasticity", in *Dynamic Localization Phenomena in Elasticity, Acoustics and Electromagnetism*, CISM International Centre for Mechanical Sciences, vol. 547, Springer, Vienna, 2013, p. 181-223.

[60] M. R. Stinson, "The propagation of plane sound waves in narrow and wide circular tubes, and generalization to uniform tubes of arbitrary cross-sectional shape", *J. Acoust. Soc. Am.* **89** (1991), no. 2, p. 550-558.

[61] G. Theocharis, O. Richoux, V. Romero-Garcìa, A. Merkel, V. Tournat, "Limits of slow sound and transparency in lossy locally resonant periodic structures", *New J. Phys.* **16** (2014), article no. 093017.

[62] J. Kergomard, A. Garcia, "Simple discontinuities in acoustic waveguides at low frequencies: critical analysis and formulae", *J. Sound Vib.* **114** (1987), no. 3, p. 465-479.

[63] V. Dubos, J. Kergomard, A. Khettabi, J.-P. Dalmont, D. Keefe, C. Nederveen, "Theory of sound propagation in a duct with a branched tube using modal decomposition", *Acta Acust. United Acust.* **85** (1999), no. 2, p. 153-169.

[64] F. P. Mechel, *Formulas of Acoustics*, 2nd ed., Springer Science & Business Media, Springer-Verlag, Heidelberg, 2008.

[65] M. Born, E. Wolf, *Principles of Optics: Electromagnetic Theory of Propagation, Interference and Diffraction of Ligth*, Cambridge University Press, UK, 1999.

[66] C. Zwikker, C. Kosten, *Sound Absorbing Materials*, Elsevier Publishing Company, Amsterdam, 1949.

[67] Q. Xu, S. Sandhu, M. L. Povinelli, J. Shakya, S. Fan, M. Lipson, "Experimental realization of an on-chip all-optical analogue to electromagnetically induced transparency", *Phys. Rev. Lett.* **96** (2006), article no. 123901.

[68] X. Yang, M. Yu, D.-L. Kwong, C. W. Wong, "All-optical analog to electromagnetically induced transparency in multiple coupled photonic crystal cavities", *Phys. Rev. Lett.* **102** (2009), article no. 173902.

[69] E. H. E. Boudouti, T. Mrabti, H. Al-Wahsh, B. Djafari-Rouhani, A. Akjouj, L. Dobrzynski, "Transmission gaps and Fano resonances in an acoustic waveguide: analytical model", *J. Phys.: Condens. Matter* **20** (2008), article no. 255212.

[70] A. Santillan, S. I. Bozhevolnyi, "Acoustic transparency and slow sound using detuned acoustic resonators", *Phys. Rev. B* **84** (2011), article no. 064394.

[71] A. Mouadili, E. H. E. Boudouti, A. Soltani, A. Talbi, B. Djafari-Rouhani, A. Akjouj, K. Haddadi, "Electromagnetically induced absorption in detuned stub waveguides: a simple analytical and experimental model", *J. Phys.: Condens. Matter* **26** (2014), article no. 505901.

[72] Y. Xu, Y. Li, R. K. Lee, A. Yariv, "Scattering-theory analysis of waveguide–resonator coupling", *Phys. Rev. E* **62** (2000), p. 7389-7404.

[73] M. J. Powell, "A fast algorithm for nonlinearly constrained optimization calculations", in *Numerical Analysis*, Springer, 1978, p. 144-157.

[74] T. J. Cox, P. D'Antonio, *Acoustic Absorbers and Diffusers: Theory, Design and Application*, 3rd ed., CRC Press, 2016.

[75] J.-P. Groby, E. Ogam, L. De Ryck, N. Sebaa, W. Lauriks, "Analytical method for the ultrasonic characterization of homogeneous rigid porous materials from transmitted and reflected coefficients", *J. Acoust. Soc. Am.* **127** (2010), no. 2, p. 764-772.

[76] K. L. Tsakmakidis, A. D. Boardman, O. Hess, "Trapped rainbow storage of light in metamaterials", *Nature* **450** (2007), no. 7168, p. 397-401.

[77] J. Zhu, Y. Chen, X. Zhu, F. J. Garcia-Vidal, X. Yin, W. Zhang, X. Zhang, "Acoustic rainbow trapping", *Sci. Rep.* **3** (2013), article no. 1728.

[78] V. Romero-Garcia, R. Picó, A. Cebrecos, V. Sanchez-Morcillo, K. Staliunas, "Enhancement of sound in chirped sonic crystals", *Appl. Phys. Lett.* **102** (2013), no. 9, article no. 091906.

[79] X. Ni, Y. Wu, Z.-G. Chen, L.-Y. Zheng, Y.-L. Xu, P. Nayar, X.-P. Liu, M.-H. Lu, Y.-F. Chen, "Acoustic rainbow trapping by coiling up space", *Sci. Rep.* **4** (2014), article no. 7038.

[80] A. Colombi, D. Colquitt, P. Roux, S. Guenneau, R. V. Craster, "A seismic metamaterial: The resonant metawedge", *Sci. Rep.* **6** (2016), article no. 27717.

[81] A. U. Jan, R. Porter, "Transmission and absorption in a waveguide with a metamaterial cavity", *J. Acoust. Soc. Am.* **144** (2018), no. 6, p. 3172-3180.

Comptes Rendus
Physique
2020, 21, nº 7-8, p. 751-765
`https://doi.org/10.5802/crphys.30`

Metamaterials 2 / *Métamatériaux 2*

Introduction to mechanical metamaterials and their effective properties

Introduction aux métamatériaux mécaniques et à leurs propriétés effectives

Xueyan Chen [a, b], **Nicolas Laforge** [a], **Qingxiang Ji** *, [a, b], **Huifeng Tan** [b],
Jun Liang [b, c], **Gwenn Ulliac** [a], **Johnny Moughames** [a], **Samia Adrar** [a],
Vincent Laude [a] **and Muamer Kadic** [a]

[a] Institut FEMTO-ST, UMR 6174, CNRS, Université de Bourgogne Franche-Comté, 25000 Besançon, France

[b] National Key Laboratory of Science and Technology on Advanced Composites in Special Environments, Harbin Institute of Technology; 92 Xidazhi Street, Harbin, 150001, PR China

[c] Institute of Advanced Structure Technology, Beijing Institute of Technology, No. 5 South Zhongguancun Street, Haidian District, Beijing, 100081, PR China

E-mails: chenxueyan@hit.edu.cn (X. Chen), nicolas.laforge@femto-st.fr (N. Laforge), jiqingxiang@hit.edu.cn (Q. Ji), tanhf@hit.edu.cn (H. Tan), liangjun@bit.edu.cn (J. Liang), gwenn.ulliac@femto-st.fr (G. Ulliac), johnny.moughames@femto-st.fr (J. Moughames), samia.adrar@femto-st.fr (S. Adrar), vincent.laude@femto-st.fr (V. Laude), muamer.kadic@femto-st.fr (M. Kadic)

Abstract. Metamaterials are rationally designed composites made of building blocks which are composed of one or more constituent materials. Metamaterial properties can go beyond those of the ingredient materials, both qualitatively and quantitatively. In addition, their properties can be mapped on some generalized continuum model. We present the general procedure of designing elastic metamaterials based on masses and springs. We show that using this simple approach we can design any set of effective properties including linear elastic metamaterials,—defined by bulk modulus, shear modulus, mass density—and nonlinear metamaterials,—with instabilities or programmable parts. We present designs and corresponding numerical calculations to illustrate their constitutive behavior. Finally, we discuss the addition of a thermal stimulus to mechanical metamaterials.

Résumé. Les métamatériaux sont des composites de conception rationnelle constitués de briques élémentaires qui sont composées d'un ou plusieurs matériaux constitutifs. Les propriétés des métamatériaux peuvent aller au-delà de celles des matériaux constitutifs, à la fois qualitativement et quantitativement. En outre, leurs propriétés peuvent être mises en correspondance avec certains modèles de milieux continus généralisés. Nous présentons une procédure générale de conception de métamatériaux élastiques à base de

---

* Corresponding author.

systèmes de type masses et de ressorts. Nous montrons quavec cette approche simple, nous pouvons concevoir tout un ensemble de propriétés effectives, y compris celles de métamatériaux élastiques non linéaires avec instabilités ou parties programmables — définis par un module de masse, de cisaillement et une masse volumique. Nous présentons des designs et calculs numériques afin dillustrer les lois de comportement. Enfin, nous discutons de l'apport d'un stimulus thermique aux métamatériaux mécaniques.

Keywords. Metamaterials, Effective parameters, Elasticity, Anisotropy, Waves, Cauchy elasticity, Navier equation.

Mots-clés. Métamatériaux, Paramètres effectifs, Élasticité, Anisotropie, Ondes, Élasticité de Cauchy, Équation de Navier.

2020 Mathematics Subject Classification. 00-01,99-00.

1. Introduction

For the last 50 years, a huge deal of effort has been made to design novel materials by chemical synthesis (graphene [1–3], carbon nanotubes [4, 5]), by structuration (composites, fibrous materials, multilayers) [6–8], or by topology optimization in quasi-static conditions [9] or for dynamical Bloch waves (phononic crystals) [10]. The ultimate goal has been to reach an improvement in stiffness or toughness, increase or decrease in the mass density, or to absorb/reflect or transmit energy [9, 11, 12]. Indeed, in aeronautics and the automotive industry for instance, it was necessary to decrease the weight of all parts leading to a fundamental change from metals to only aluminum, alloys and composites. It is, for example, almost impossible to find a car bumper made of metal today thanks to composites (mainly fibrous). The quest for a dynamical design response (sound and vibration absorption), firstly questioned by Brillouin, was deeply expanded after pioneering works by Yablonovitch [13, 14], Monkhorst [15], and Bloch [16]. Later, the introduction of functionalities designed by transformational elastodynamics and the wish of mapping more complex media onto generalized continua motivated the expansion from Cauchy elasticity to micropolar, micromorphic or Cosserat models (an effort started in the sixties by Eringen, Maugin and other precursors [17, 18]) led to the higher order gradient theories of elasticity [19] and to the modification of the Newton's second law by Willis and Milton [20].

In this paper, we revisit these innovations from the perspective of metamaterial designs taken from the literature. First, we summarize for newcomers the different models used in elasticity. Second, we focus on linear elasticity and show that using masses and spring all mechanical properties can be independently designed. Third, we present an extension of linear metamaterials toward their use for non-linear wave absorption.

2. Elasticity equations

In this section we review the complexity of the description of mechanical materials and of their constitutive laws [21].

2.1. *Hooke's spring law*

In the seventeenth century, Robert Hooke formulated the first constitutive law in mechanics that states that the force, F, needed to extend or compress a spring by a distance d is given by $F = k\,d$, where k is a constant (the stiffness). This law can obviously be generalized to a vectorial force $\mathbf{F}$ connecting a general vector elongation in 3D space $\mathbf{d} = (d_1, d_2, d_3)$ by a matrix of spring constants $\mathbf{k}$ as $\mathbf{F} = \mathbf{k}\mathbf{d}$. It is well known that in the general case, the spring constant is a constant scalar (or

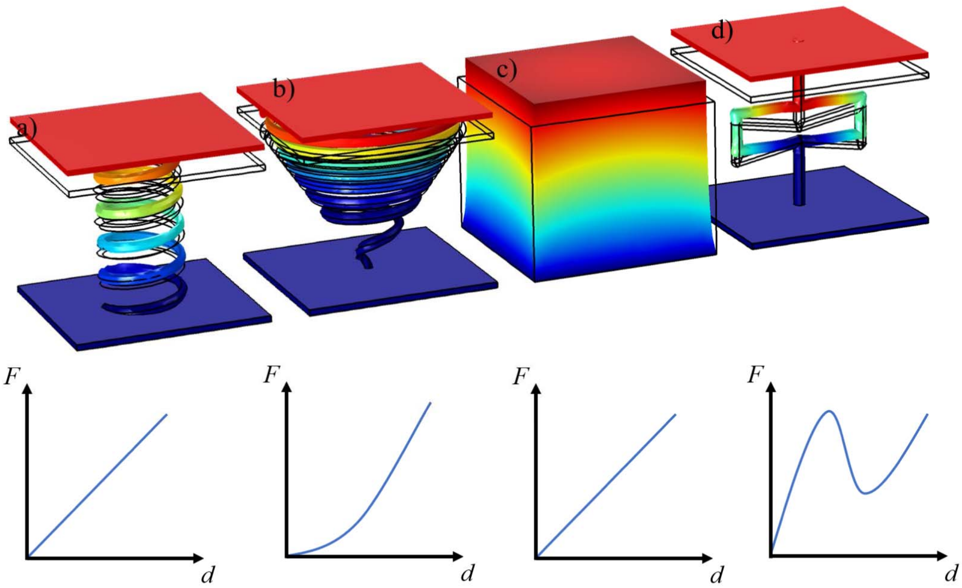

Figure 1. Under uniaxial tension, the deformations of (a) a linear spring, (b) a nonlinear spring, (c) an homogeneous cube, and (d) a geometrically nonlinear spring are depicted, respectively. The color scale measures the vertical displacement, from blue (no displacement) to red (maximum displacement). For the finite element computations, the bottom surface is clamped and a force F directed upward is applied at the top surface. The thin lines are for the structures at rest. Under each panel, a schematic force-elongation curve is displayed.

a constant matrix), but that its magnitude can change depending on the load in a nonlinear way (either monotonically or not; see the section on nonlinear mechanics). In Figure 1 we illustrate the principles of linear and nonlinear springs and continua, a concept that we will more clearly describe later on. The scalar Hooke's law primarily relates linearly the tension of an homogeneous spring to its elongation (Figure 1(a)). If the spring is made inhomogeneous along its length, such as in Figure 1(b), then the relationship becomes nonlinear. Similarly, the homogeneous cube of Figure 1(c) can often be modelled with the linear Hooke's law, but a structural spring such as depicted in Figure 1(d) must be described using a nonlinear stiffness under large deformations. In the figure, the color scale represents the local vertical displacement with respect to the static equilibrium position under zero tension. The elongation d is the difference of the top displacement and the bottom displacement. Whereas in the first three cases the displacement field is basically a simple vertical gradient, in the structural spring case the displacement field varies in a more complex fashion.

Clearly, Hooke's approach can be justified only for simple spring-like geometries and for long bars. When all dimensions (pushing and lateral) of a material are comparable then this approach does not reflect properly the deformation of the body. Thus, a more general theory is required. It is called Cauchy elasticity from the contribution of Louis Cauchy to the definition of the stress tensor replacing the simple applied force by a quantity homogeneous to a force per surface area (thus with the units of pressure). Figure 2 illustrates the different components of the Cauchy stress tensor exerted on an infinitesimal cubic volume.

The stress tensor defined graphically in Figure 2 obeys the fundamental law of conservation of linear momentum. Combined with the conservation of angular momentum, the stress tensor

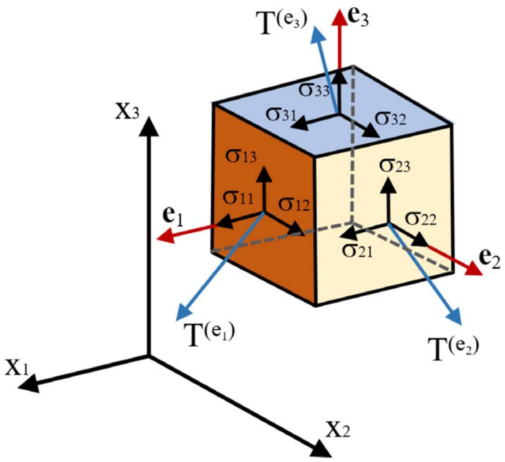

Figure 2. Illustration of the elements of the Cauchy tensor and of the orientation convention. In a Cartesian coordinate system, the stress vectors applying on each elemental plane, $T^{(e_1)}$, $T^{(e_2)}$, and $T^{(e_3)}$ can be decomposed into a normal component and two shear components measured along the three principal axes.

takes a symmetric form with only six independent parameters, rather than nine, and may thus be written:

$$\begin{bmatrix}\sigma_{11} & \sigma_{12} & \sigma_{13}\\ \sigma_{21} & \sigma_{22} & \sigma_{23}\\ \sigma_{31} & \sigma_{32} & \sigma_{33}\end{bmatrix} = \begin{bmatrix}\sigma_1 & \sigma_6 & \sigma_5\\ \sigma_6 & \sigma_2 & \sigma_4\\ \sigma_5 & \sigma_4 & \sigma_3\end{bmatrix} \tag{1}$$

where the diagonal entries σ_1, σ_2 and σ_3 are the normal stresses, and the off-diagonal entries $\sigma_{12} = \sigma_6$, $\sigma_{13} = \sigma_5$ and $\sigma_{23} = \sigma_4$ are the orthogonal shear stresses.

Next, the infinitesimal strain tensor for a displacement field $\mathbf{u}$ is defined by:

$$\boldsymbol{\varepsilon} = \tfrac{1}{2}[\nabla\mathbf{u} + (\nabla\mathbf{u})^T].$$

By construction this tensor is also symmetric. In component form, it writes as

$$\varepsilon_{ij} = \tfrac{1}{2}(u_{i,j} + u_{j,i}), \quad i,j = 1,2,3,$$

and the notation $u_{i,j} = \partial u_i/\partial x_j$. Therefore, the displacement gradient can alternatively be expressed as

$$\nabla\mathbf{u} = \boldsymbol{\varepsilon} + \boldsymbol{\gamma}$$

with a skew symmetric tensor $\boldsymbol{\gamma}$ also called the rotation tensor:

$$\boldsymbol{\gamma} = \tfrac{1}{2}[\nabla\mathbf{u} - (\nabla\mathbf{u})^T].$$

Finally the constitutive equation between stress and stain tensors is given by the generalized Hooke's law as

$$\boldsymbol{\sigma} = \mathsf{C} : \boldsymbol{\varepsilon},$$

with $\boldsymbol{\sigma}$ Cauchy's stress tensor, $\boldsymbol{\varepsilon}$ the infinitesimal strain tensor, and C a fourth-order elasticity tensor. The latter must obey certain properties of tensors such as symmetries and positive definiteness.

Sometimes it is difficult to model lattice metamaterials with continuum mechanics, especially if bars get very thin and numerous. For this purpose, it is important to note that simplified theories exist, e.g. Timoshenko's and Euler–Bernouilli beam theories. However, in the quest of an efficient implementation they are not practical compared to finite element models. Anyway, an extensive and specific literature exists and has been used for the design of metamaterials [22–26].

2.2. *Navier's equation*

Once a rigid or deformable body is in motion, Newton's second law can be written as follows (omitting possible external forces):

$$\nabla \cdot \boldsymbol{\sigma} = \rho \frac{\partial^2 \mathbf{u}}{\partial t^2} \tag{2}$$

with $\boldsymbol{\rho}$ the mass density and t the time variable. If the elastic body is isotropic, then

$$\mathsf{C}_{ijkl} = \lambda \delta_{ij} \delta_{kl} + 2\mu \delta_{ij}, \tag{3}$$

where Lamé's parameters λ and μ can be expressed in terms of Poisson's ratio ν and Young's modulus E as

$$\lambda = \frac{E\nu}{(1+\nu)(1-2\nu)}, \quad \mu = \frac{E(1-\nu)}{(1+\nu)(1-2\nu)}. \tag{4}$$

In the time-harmonic regime Navier's equation at angular frequency ω is

$$\nabla \cdot \boldsymbol{\sigma} = -\rho \omega^2 \mathbf{u}. \tag{5}$$

3. Linear mechanical metamaterials

3.1. *Isotropic metamaterials*

In the isotropic case, the effective elasticity tensor that describes the elastic properties of a solid metamaterial is very simple and in fact can be decomposed in a form with only two eigenvalues (see Milton [27] and Banerjee [28]). Here, we describe how to design the most simple isotropic mechanical metamaterial (as a remark, isotropy in mechanics is not as simple as in crystallography, since space groups must be considered instead of point groups in order to describe symmetry). We start from the ideal pentamode metamaterials introduced by Milton and Cherkaev [27], as shown in Figure 3. Pentamodes are expected to avoid the coupling of compression and shear waves due to their extremely large bulk modulus, B, in comparison with the shear modulus, G [27,29]. However, it is almost impossible to fabricate such ideal pentamodes due to infinitely small connections between cones. In 2012, Kadic *et al.* realized pentamodes experimentally by modifying the diameter of thin and thick ends of double cones [29]. They investigated the effect of the overlap volume on the ratio B/G. They found that increasing the overlap volume stabilizes the structures, yet at the same time decreasing the ratio.

Figures 3(b) and (c) show 3D view and magnified front view electron micrographs of an optimal pentamode truss micro-lattice metamaterial fabricated by dip-in three-dimensional direct-laser-writing (DLW) optical lithography. These structures are experimentally validated to possess an extremely large B/G ratio which can be also observed in Figure 5(a). Figure 4 and Figure 5(b) illustrate how to independently control the bulk modulus B by connecting the middle part of double cones with soft loose springs. One can also fulfill the goal to control density by using parallel springs while enlarging the diameter d. By replacing loose springs with dense springs, it is easy to keep the bulk modulus B and to enhance the capacity to resist shear loading.

Actually, we can make pentamode metamaterials isotropic by adapting the optimal method presented by Buckmann *et al.* [31]. We can relate the elastic modulus, the shear modulus and Poisson's ratio to three phase velocities v of the pentamode material, which are chosen either purely longitudinally or transversely polarized, in the M direction or [110] direction. We thus get

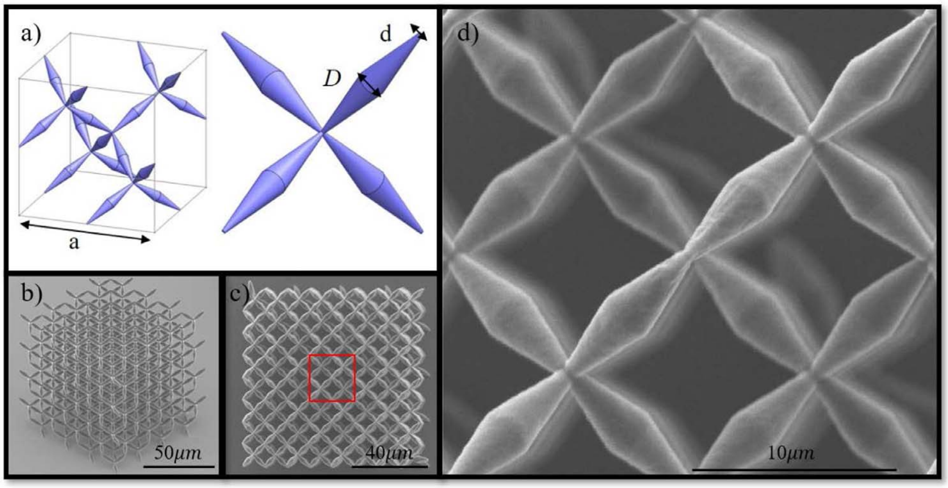

Figure 3. (a) An ideal periodic unit cell of a pentamode metamaterial with constant length a and a modified pentamode with a smaller diameter, d, at connecting parts of the double-cone strut, and a bigger diameter, D, of the middle part. 3D view (b) and magnified front view (c) electron micrograph of a pentamode truss micro-lattice metamaterial fabricated by dip-in three-dimensional direct-laser-writing (DLW) optical lithography. Front view electron micrograph (d) of an unit cell of the metamaterial part which is highlighted with a red square in (c). The samples chosen reproduce those discussed originally in Ref. [29].

a sufficient condition for isotropy as $v_{110}^{L} = v_{110}^{T,xy}$. This condition can be undertood as follows: the phase velocity of the longitudinal wave along the crystallographic direction [110] equals the phase velocity of the transverse wave along the same direction. The condition can be achieved by adjusting geometrical parameters or by adding additional springs. All in all, we obtain a possible way to control the 3 independent mechanical parameters and to make pentamodes isotropic by adjusting different parts of the periodic unit cell.

4. Nonlinear mechanical metamaterials

In the regime of large deformations, the stress–strain response of mechanical metamaterials [32–34] always goes through a sequence of increases [35, 36] or decreases [37, 38], and steady [39–41] or damping [42,43] variations. Globally, the part of the graph extending beyond the initial elastic region describes the mechanical nonlinearity. Scientists usually pay much attention to the elastic region for load-bearing mechanical metamaterials [38, 43], whereas nonlinearity is important for energy absorption mechanical metamaterials [39,43] and programmable metamaterials [11, 44]. Nonlinearity arises from two aspects, either geometrical (structural) nonlinearity or the nonlinearity of the parent materials used for building the metamaterial [45]. Geometrical nonlinearity, which is mainly determined by the topological structure and geometrical parameters, exists in systems that sustain large deformations. Geometrical structures, such as truss lattices [35, 40], shell lattices [42, 43] and plate lattices [46, 47] have to abide by two different deformation criteria: stretching dominated or bending dominated [48]. Different geometrical parameters will yield different failure modes, including stiffening or softening plastic yield [38], plastic collapse [35], linear and nonlinear buckling [39, 43], and so on. In a similar way, the mechanical properties, especially in the nonlinear region, of the parent materials also affect the failure modes

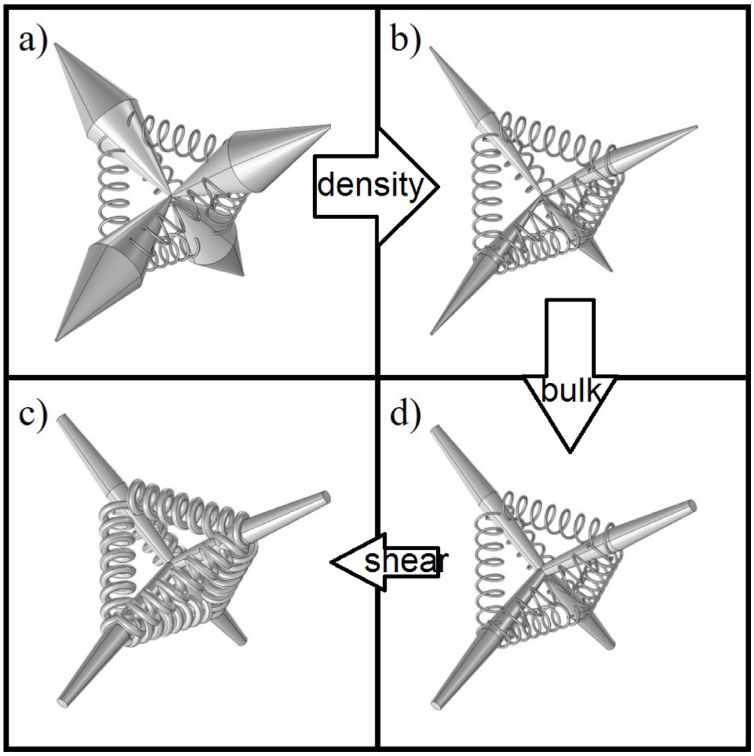

Figure 4. Illustration of optimal pentamodes with (a) a larger diameter D and additional loose springs, (b) additional loose springs, (c) a larger diameter d and additional dense springs and (d) a larger diameter d and additional loose springs.

of mechanical metamaterials. Material nonlinearity works only after the deformation of the parent materials has gone beyond the elastic region. Plastic yield will dominate the failure of most metals and polymers. However, brittle failure will be most common for ceramics, composite materials, and other ceramic-like materials. Material properties and the topological structure together with geometrical parameters decide the failure models, that is the nonlinear response, of mechanical metamaterials.

Viscous materials, for which the relationship between stress and strain depends on time, provide another possibility to design energy absorption, energy dissipation, and vibration suppression metamaterials. Their energy dissipation capacity highly depends on the angular frequency. Several mathematical models have been proposed to describe such dispersive relationships. The Maxwell loss model [49, 50] is probably the oldest viscoelastic model and can be represented by a purely viscous damper and a purely elastic spring connected in series, as shown in Figure 6(a). The dynamic modulus $E^*(\omega) = E' + \mathrm{i}E''$ is obtained following the rules for admittance in equivalent circuits. In the case of the Maxwell model,

$$\frac{1}{E^*} = \frac{1}{E} + \frac{1}{\mathrm{i}\omega\eta} \tag{6}$$

which yields

$$E' = \frac{\tau^2\omega^2}{\tau^2\omega^2+1}E, \quad E'' = \frac{\tau\omega}{\tau^2\omega^2+1}E, \tag{7}$$

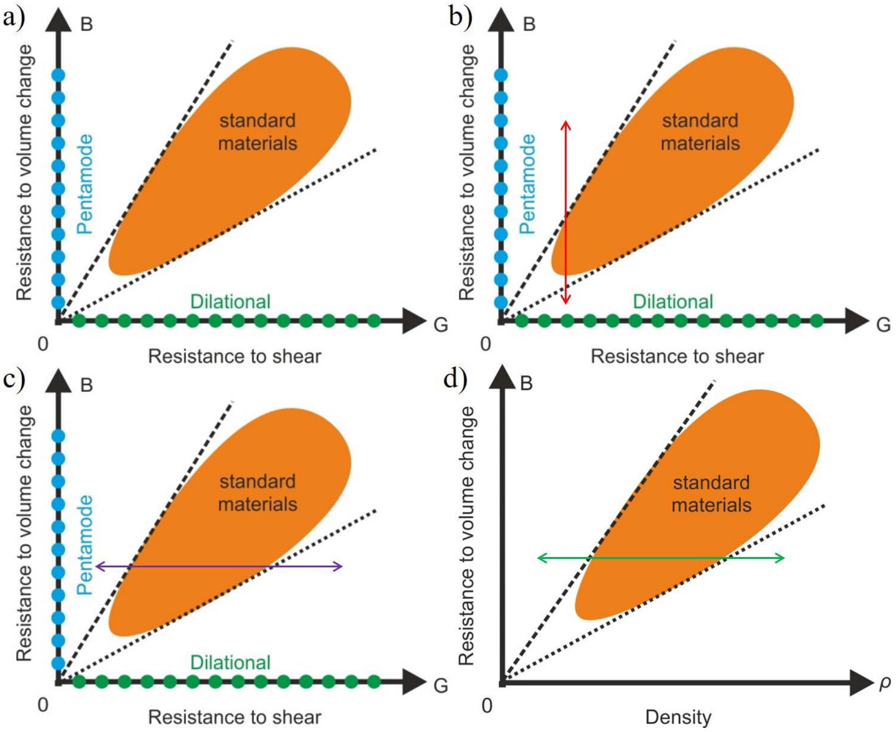

Figure 5. Milton's maps of (a) pentamode metamaterials and (b), (c) optimal pentamode metamaterials with different geometrical parameters. Ashby's map (d) of optimal pentamode metamaterials. This figure is inspired by Ref. [30].

with $\tau = \eta/E$. If we connect elastic and viscous elements in parallel, as in Figure 6(b), we get the generalized Kelvin–Voigt model [49, 50]

$$E^* = E + \mathrm{i}\omega\eta. \tag{8}$$

Then obviously $E' = E$ and $E'' = \omega\eta$. Combining a serial Maxwell branch in parallel with a purely elastic branch, the more realistic model of the standard linear solid is obtained, as depicted in Figure 6(c). The model contains two independent elastic elements, E_1 and E_2, and a viscous element η, and is also known as the Zener model [49–51]. The complex dynamic modulus is

$$E^*(\omega) = \left(\frac{1}{E_1} + \frac{1}{\mathrm{i}\omega\eta}\right)^{-1} + E_2, \tag{9}$$

leading to

$$E'(\omega) = \frac{\tau^2\omega^2}{\tau^2\omega^2+1}E_1 + E_2, \tag{10}$$

$$E''(\omega) = \frac{\tau\omega}{\tau^2\omega^2+1}E_1. \tag{11}$$

Figure 6 depicts the three previous elastic-viscous models and the corresponding relationships between dynamics modulus and vibration frequency. The equations are simple enough but often prove insufficient. For instance, the Maxwell model successfully captures the evolution of the imaginary dynamic modulus as a function of vibration frequency, but fails to describe the dependence of the real part on frequency. It should be noted that any solid material must have a non zero elastic modulus in the absence of vibrations, i.e. at the zero frequency. Hence, the

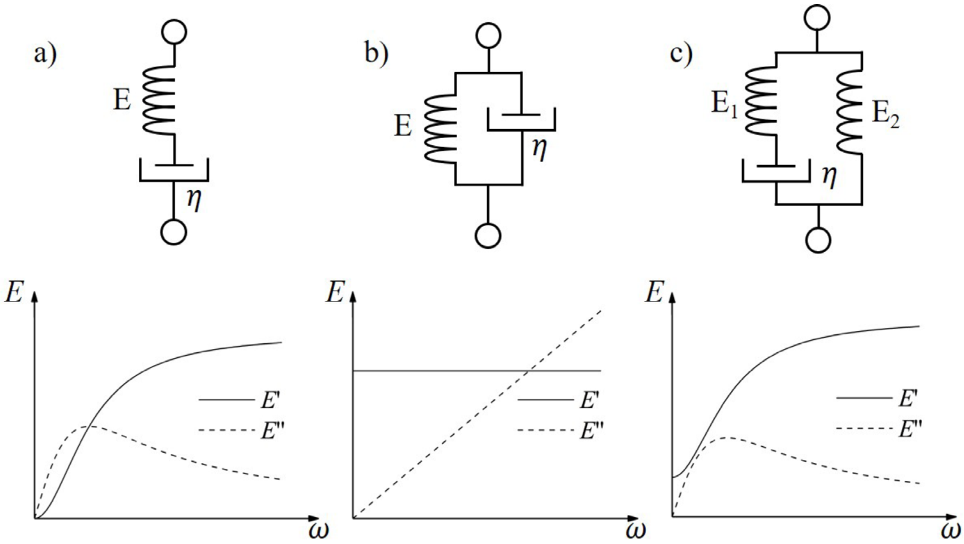

Figure 6. (a) Maxwell, (b) Voigt and (c) the standard linear solid simplified elastic-viscous models are depicted in analogy with equivalent electrical circuits. Young's modulus E is analogous to a real-valued admittance, whereas viscosity contributes a $\mathrm{i}\omega\eta$ admittance similar to a capacitance. The resulting relationship between dynamic modulus and angular frequency is depicted below each equivalent circuit model (see text for their expressions).

Maxwell loss model is not physical in the limit of low frequencies. Finally, the Kelvin–Voigt model is too ideal to describe nonlinear variations of the dynamic modulus.

4.1. *Tailoring the stress–strain curve*

A central issue of mechanical metamaterial design is indeed to tailor the stress–strain curve to follow given shapes chosen in order to meet given requirements [35, 39, 46]. As outlined in the previous section, the geometrical structure is one of most important factors in metamaterial design. Here, we will give three examples to illustrate how to tailor the stress–strain curve by optimizing the structure.

Let us start from a conventional spring which is the most basic elastic element in a mechanical metamaterial. When a conventional spring is compressed or stretched from its rest position (strained), a stress distribution appears along the length. Figure 1(a) illustrates the force versus elongation curve. The spring constant is almost a constant as long as deformation does not go beyond spring stoke. Under certain circumstances, however, a spring constant increasing with applied strain is needed. In this case, replacing the constant spacing spring coils with graded spacing spring coils, or replacing the constant major radius with an increasing major radius, a progressive rate spring can be obtained, as Figure 1(b) depicts.

Second, the simple cubic solid structure, that is a base element in 3D mechanical metamaterials, can be used to implement any geometrical structure by periodic repetition of a unit cell. Figure 1(c) shows the deformation and the corresponding stress–strain curve of an homogeneous cubic unit cell under tension. Clearly, Poisson's ratio is positive and a conventional elastic–plastic tensile response is obtained. However, the structure [32] shown in Figure 1(d), which is composed of several relatively small simple cubic elements, has a totally different deformation behavior: it

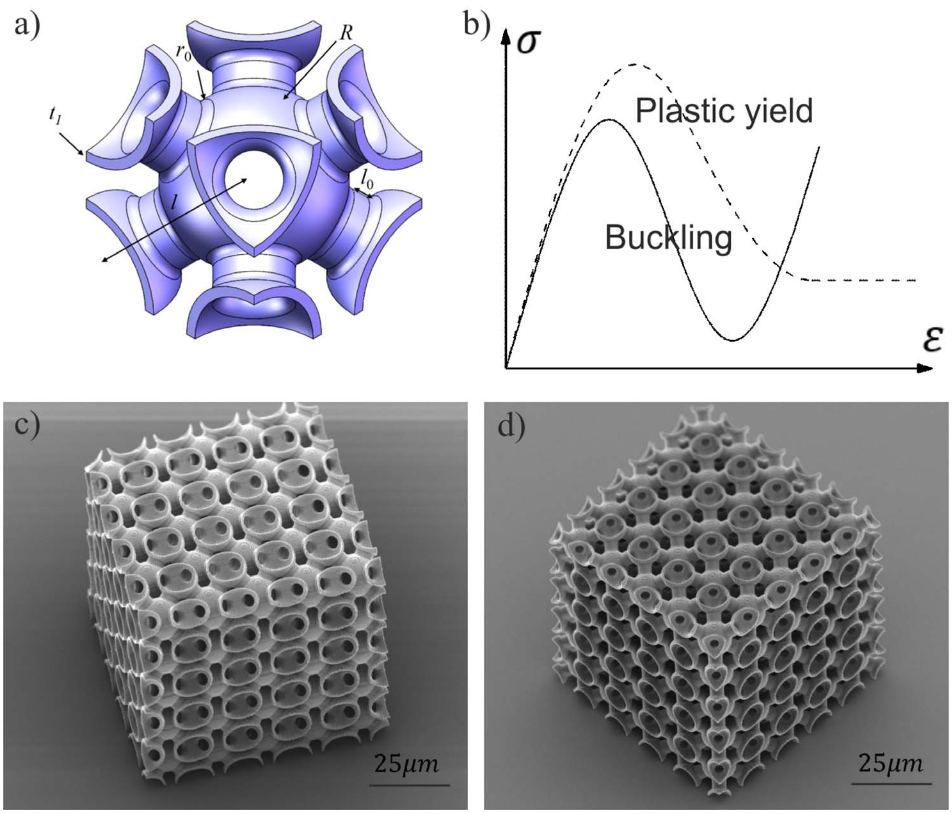

Figure 7. Body centered cubic (BCC) shell-lattice metamaterial. (a) A unit cell is depicted along with its geometrical parameters. (b) Two different failure models can be observed for the shell-lattice material, either plastic yield or buckling. The optimal designs obtained for (c) energy absorption and (d) bearing load were fabricated by two-photon lithography.

is auxetic (Poisson's ratio is negative). Moreover, the failure mode changes from elastic–plastic to plastic bending. Note that such mechanical behavior is unusual in natural materials.

Third, we consider the control of the failure mode of mechanical metamaterials. The body centered cubic (BCC) shell-lattice metamaterial depicted in Figure 7 has high stiffness, high strength, and large specific energy absorption at low relative density [52]. The compressive failure mode of the metamaterial, either dominated by plastic yield or buckling, is affected by the geometrical parameters defining the structure, including the spherical node radius R, the cylindrical strut radius r, the smooth connecting shell radius r_0, the cylindrical strut length l_0, the total length l, and thickness t_1. These geometrical parameters are not independent: we have $r_0 = 2R - r$ and $l = l_0 + 2\sqrt{3}(R - r)$. Further fixing the total length of the shell strut and setting the relative density to 0.05, only two independent parameters are left, for instance the spherical node radius R and the smooth connecting shell radius r_0. After topology optimization, we obtained two different functional shell metamaterials: a buckling dominated metamaterial ($R/r = 2.3$ and $l_0/(l - l_0) = 0.1$) and a yield dominated metamaterial ($R/r = 2.5$ and $l_0/(l - l_0) = 0.2$). The buckling dominated metamaterial can almost recover 92% of its original shape after compressions in excess of 60% strain, which makes it a good candidate for energy absorption. The yield dominated metamaterial has higher stiffness, higher strength and better load bearing capacity. These examples encourage one to make possible the impossible.

4.2. *Material nonlinearities and their use for energy absorption*

Nonlinear metamaterials are widely used in our daily life for energy absorption [53–56]. Aiming at absorbing as much energy as possible, nonlinear metamaterials were usually designed to obtain a relatively large peak force with large deformation [35, 55, 57]. Most metamaterials utilize plastic deformation or brittle fracture of micro-struts [37], shell [43] or plate [46, 47] to dissipate a large amount of energy. Stretching dominated metamaterials [43, 46, 47], which are maybe the most famous plastic yield metamaterials, have been proven to possess extraordinary loading bear capacity and energy absorption at high relative density. In contrast, bending dominated metamaterials [35, 41], which make use of plastic bending joint, allow for large deformation and provide relatively large and nearly constant stress area in the nonlinear region at low relative density. In addition, reusable energy metamaterials [39, 58, 59] were proposed to extend their life span. By utilizing elastic buckling of shell, straight strut and curved beam, reusable energy metamaterials were shown to present unusual features including mechanical multi-stability [60, 61], close to 100 percent recovery after unloading [39, 55, 58], and controllable mechanical response [44].

5. Thermomechanical metamaterials

Systems placed in a thermal environment are sensitive to temperature changes of their surroundings. An ambient temperature change ΔT will cause a thermal strain $\alpha_{ij}\Delta T$ in an elastic solid due to thermal expansion. Generally, thermal expansion is described by a symmetric tensor of rank two

$$\alpha_{ij} = \begin{bmatrix} \alpha_{11} & \alpha_{12} & \alpha_{13} \\ \alpha_{12} & \alpha_{22} & \alpha_{23} \\ \alpha_{13} & \alpha_{23} & \alpha_{33} \end{bmatrix}. \tag{12}$$

For isotropic solids, the thermal expansion tensor is proportional to the identity matrix, $\alpha_{ij} = \alpha \boldsymbol{I}$, where $\boldsymbol{I}$ is the rank-two identity matrix and α is the thermal length expansion defined by

$$\alpha = \frac{1}{L}\frac{\partial L}{\partial T}. \tag{13}$$

In the elastic stress–strain relation, thermal strain has to be subtracted from total strain, leading to the relation

$$\sigma_{ij} = C_{ijkl}(\varepsilon_{kl} - \alpha_{kl}\Delta T) \tag{14}$$

or, in the case of isotropic solids,

$$\sigma_{ij} = 2\mu\varepsilon_{ij} + \lambda\varepsilon_{ij}\delta_{ij} - (2\mu + 3\lambda)\alpha\Delta T\delta_{ij}. \tag{15}$$

Note that the temperature dependence of the elastic constants was neglected in the above equations.

Temperature variations can result both in thermal expansion and in geometry changes, which can be problematic in temperature-sensitive applications that require thermal stability like space frame trusses, satellite antennas and space crafts [62, 63]. Alternatively, thermal expansion can also be tailored to achieve some required thermal deformation and behavior. Material systems and structures can be deliberately designed to deform in a controllable manner in response to a temperature stimulus. Applications based on this principle include morphing structures [64], large reversible shape changing components [65], micro-actuators [66], self-assembly systems [67], grippers for soft micro-robotics [68], biology devices [69], and so on.

Generally, those applications bring in demands on controllable coefficients of thermal expansion (CTE), e.g. large, positive, negative or zero thermal expansion materials and structures. Many efforts have been made to create architectured materials with tunable CTE using two constituents with widely different thermal expansion combined in space. Different concepts were proposed under this approach and each has its working principle and specific advantages. One major concept is utilizing the bending-dominated bi-material strip, based on which some researchers proposed cellular solid structures with unbounded thermal expansion [70, 71]. Other concepts include stretch-dominated structures composed of nested double-parallel units with large stiffness [71], flexure blade structures with high CTE tunability [72], and tetrahedron structure combined with sizable CTE tunability and large stiffness [73, 74]. Another major approach is to generate CTE tunability via topology optimization [75–77]. Structures obtained following this method are generally more complicated. Finally, using 3D printing technologies, researchers have managed to directly print metamaterials with controllable thermal expansion and have achieved rather high but negative thermal expansion coefficients [72, 78, 79].

6. Conclusion

In this paper, we have presented general procedures to design mechanical metamaterials in both the linear and the nonlinear regimes using an effective medium approach based on simple mechanical models. We have emphasized the complexity and the opportunities in the nonlinear case if one uses viscosity or plasticity. Finally, we have summarized proposals aiming at using an external stimulus (variation of temperature) to change the shape of designed metamaterials.

Acknowledgments

We thank Graeme W. Milton (Utah Univ., USA) and Martin Wegener (KIT, Germany) for stimulating discussions. We acknowledge Marina Raschetti, Roland Salut, and Jean-Marc Cote for technical help. This work was partly supported by the french RENATECH network and its FEMTO-ST technological facility. We acknowledge support by the EIPHI Graduate School (contract "ANR-17-EURE-0002") and the French Investissements d'Avenir program, project ISITE-BFC (contract ANR-15-IDEX-03). This work was partly supported by the french RENATECH network and its FEMTO-ST technological facility. This work was supported in part by the Foundation for Innovative Research Groups of the National Natural Science Foundation of China (grant numbers 11421091 and 11732002) and by the Fundamental Research Funds for the Central Universities (grant number HIT.MKSTISP.2016 09).

References

[1] M. J. Allen, V. C. Tung, R. B. Kaner, "Honeycomb carbon: a review of graphene", *Chem. Rev.* **110** (2009), no. 1, p. 132-145.

[2] Y. Shao, J. Wang, H. Wu, J. Liu, I. A. Aksay, Y. Lin, "Graphene based electrochemical sensors and biosensors: a review", *Electroanalysis* **22** (2010), no. 10, p. 1027-1036.

[3] M. Yi, Z. Shen, "A review on mechanical exfoliation for the scalable production of graphene", *J. Mater. Chem. A* **3** (2015), no. 22, p. 11700-11715.

[4] G. Mittal, V. Dhand, K. Y. Rhee, S.-J. Park, W. R. Lee, "A review on carbon nanotubes and graphene as fillers in reinforced polymer nanocomposites", *J. Ind. Eng. Chem.* **21** (2015), p. 11-25.

[5] A. D. Moghadam, E. Omrani, P. L. Menezes, P. K. Rohatgi, "Mechanical and tribological properties of self-lubricating metal matrix nanocomposites reinforced by carbon nanotubes (CNTs) and graphene–a review", *Composites B* **77** (2015), p. 402-420.

[6] J. J. Carruthers, A. Kettle, A. Robinson, "Energy absorption capability and crashworthiness of composite material structures: a review", *Appl. Mech. Rev.* **51** (1998), no. 10, p. 635-649.

[7] D. Liu, Y. Tang, W. Cong, "A review of mechanical drilling for composite laminates", *Compos. Struct.* **94** (2012), no. 4, p. 1265-1279.

[8] R. F. Gibson, “A review of recent research on mechanics of multifunctional composite materials and structures”, *Compos. Struct.* **92** (2010), no. 12, p. 2793-2810.

[9] X. Yu, J. Zhou, H. Liang, Z. Jiang, L. Wu, “Mechanical metamaterials associated with stiffness, rigidity and compressibility: A brief review”, *Prog. Mater. Sci.* **94** (2018), p. 114-173.

[10] A. Srivastava, “Elastic metamaterials and dynamic homogenization: a review”, *Int. J. Smart Nano Mater.* **6** (2015), no. 1, p. 41-60.

[11] K. Bertoldi, V. Vitelli, J. Christensen, M. van Hecke, “Flexible mechanical metamaterials”, *Nat. Rev. Mater.* **2** (2017), no. 11, p. 17066.

[12] J.-H. Lee, J. P. Singer, E. L. Thomas, “Micro-/nanostructured mechanical metamaterials”, *Adv. Mater.* **24** (2012), no. 36, p. 4782-4810.

[13] E. Yablonovitch, “Photonic band-gap structures”, *J. Opt. Soc. Am. B* **10** (1993), no. 2, p. 283-295.

[14] E. Yablonovitch, T. Gmitter, K.-M. Leung, “Photonic band structure: The face-centered-cubic case employing nonspherical atoms”, *Phys. Rev. Lett.* **67** (1991), no. 17, p. 2295.

[15] H. J. Monkhorst, J. D. Pack, “Special points for Brillouin-zone integrations”, *Phys. Rev. B* **13** (1976), no. 12, p. 5188.

[16] P. E. Blöchl, O. Jepsen, O. K. Andersen, “Improved tetrahedron method for Brillouin-zone integrations”, *Phys. Rev. B* **49** (1994), no. 23, p. 16223.

[17] A. C. Eringen, E. S. Suhubi, S. Cowin, “Elastodynamics (volume 1, finite motions)”, *J. Appl. Mech.* **42** (1975), p. 748.

[18] G. A. Maugin, “Applications of an energy-momentum tensor in nonlinear elastodynamics: Pseudomomentum and eshelby stress in solitonic elastic systems”, *J. Mech. Phys. Solids* **40** (1992), no. 7, p. 1543-1558.

[19] J. Achenbach, *Wave Propagation in Elastic Solids, Vol. 16*, Elsevier, Amsterdam, The Netherlands, 2012.

[20] G. W. Milton, J. R. Willis, “On modifications of Newton’s second law and linear continuum elastodynamics”, *Proc. R. Soc. A* **463** (2007), no. 2079, p. 855-880.

[21] M. Kadic, G. W. Milton, M. van Hecke, M. Wegener, “3D metamaterials”, *Nat. Rev. Phys.* **1** (2019), no. 3, p. 198-210.

[22] P. Martinsson, A. Movchan, “Vibrations of lattice structures and phononic band gaps”, *Q. J. Mech. Appl. Math.* **56** (2003), no. 1, p. 45-64.

[23] D. Colquitt, I. Jones, N. Movchan, A. Movchan, “Dispersion and localization of elastic waves in materials with microstructure”, *Proc. R. Soc. A* **467** (2011), no. 2134, p. 2874-2895.

[24] A. Piccolroaz, A. Movchan, “Dispersion and localisation in structured Rayleigh beams”, *Int. J. Solids Struct.* **51** (2014), no. 25-26, p. 4452-4461.

[25] A. N. Norris, “Low-frequency dispersion and attenuation in partially saturated rocks”, *J. Acoust. Soc. Am.* **94** (1993), no. 1, p. 359-370.

[26] C. Findeisen, J. Hohe, M. Kadic, P. Gumbsch, “Characteristics of mechanical metamaterials based on buckling elements”, *J. Mech. Phys. Solids* **102** (2017), p. 151-164.

[27] G. W. Milton, A. V. Cherkaev, “Which elasticity tensors are realizable?”, *J. Eng. Mater. Technol.* **117** (1995), no. 4, p. 483-493.

[28] B. Banerjee, *An Introduction to Metamaterials and Waves in Composites*, CRC Press, Boca Raton, Florida, USA, 2011.

[29] M. Kadic, T. Bückmann, N. Stenger, M. Thiel, M. Wegener, “On the practicability of pentamode mechanical metamaterials”, *Appl. Phys. Lett.* **100** (2012), no. 19, article no. 191901.

[30] M. Kadic, T. Bückmann, R. Schittny, M. Wegener, “Metamaterials beyond electromagnetism”, *Rep. Prog. Phys.* **76** (2013), no. 12, article no. 126501.

[31] T. Bückmann, R. Schittny, M. Thiel, M. Kadic, G. W. Milton, M. Wegener, “On three-dimensional dilational elastic metamaterials”, *New J. Phys.* **16** (2014), no. 3, article no. 033032.

[32] T. Bückmann, N. Stenger, M. Kadic, J. Kaschke, A. Frölich, T. Kennerknecht, C. Eberl, M. Thiel, M. Wegener, “Tailored 3D mechanical metamaterials made by dip-in direct-laser-writing optical lithography”, *Adv. Mater.* **24** (2012), no. 20, p. 2710-2714.

[33] T. Frenzel, M. Kadic, M. Wegener, “Three-dimensional mechanical metamaterials with a twist”, *Science* **358** (2017), no. 6366, p. 1072-1074.

[34] I. Fernandez-Corbaton, C. Rockstuhl, P. Ziemke, P. Gumbsch, A. Albiez, R. Schwaiger, T. Frenzel, M. Kadic, M. Wegener, “New twists of 3D chiral metamaterials”, *Adv. Mater.* **31** (2019), no. 26, article no. 1807742.

[35] R. Gümrük, R. Mines, “Compressive behaviour of stainless steel micro-lattice structures”, *Int. J. Mech. Sci.* **68** (2013), p. 125-139.

[36] T. Tancogne-Dejean, D. Mohr, “Elastically-isotropic truss lattice materials of reduced plastic anisotropy”, *Int. J. Solids Struct.* **138** (2018), p. 24-39.

[37] T. Tancogne-Dejean, D. Mohr, “Stiffness and specific energy absorption of additively-manufactured metallic bcc metamaterials composed of tapered beams”, *Int. J. Mech. Sci.* **141** (2018), p. 101-116.

[38] V. S. Deshpande, N. A. Fleck, M. F. Ashby, “Effective properties of the octet-truss lattice material”, *J. Mech. Phys. Solids* **49** (2001), no. 8, p. 1747-1769.

[39] T. Frenzel, C. Findeisen, M. Kadic, P. Gumbsch, M. Wegener, “Tailored buckling microlattices as reusable light-weight shock absorbers”, *Adv. Mater.* **28** (2016), no. 28, p. 5865-5870.

[40] T. Tancogne-Dejean, A. B. Spierings, D. Mohr, "Additively-manufactured metallic micro-lattice materials for high specific energy absorption under static and dynamic loading", *Acta Mater.* **116** (2016), p. 14-28.

[41] X. Cao, S. Duan, J. Liang, W. Wen, D. Fang, "Mechanical properties of an improved 3D-printed rhombic dodecahedron stainless steel lattice structure of variable cross section", *Int. J. Mech. Sci.* **145** (2018), p. 53-63.

[42] S. C. Han, J. W. Lee, K. Kang, "A new type of low density material: Shellular", *Adv. Mater.* **27** (2015), no. 37, p. 5506-5511.

[43] C. Bonatti, D. Mohr, "Smooth-shell metamaterials of cubic symmetry: Anisotropic elasticity, yield strength and specific energy absorption", *Acta Mater.* **164** (2019), p. 301-321.

[44] B. Florijn, C. Coulais, M. van Hecke, "Programmable mechanical metamaterials", *Phys. Rev. Lett.* **113** (2014), no. 17, article no. 175503.

[45] L. J. Gibson, M. F. Ashby, *Cellular Solids: Structure and Properties*, Cambridge University Press, Cambridge, UK, 1999.

[46] T. Tancogne-Dejean, M. Diamantopoulou, M. B. Gorji, C. Bonatti, D. Mohr, "3D plate-lattices: An emerging class of low-density metamaterial exhibiting optimal isotropic stiffness", *Adv. Mater.* **30** (2018), no. 45, article no. 1803334.

[47] J. Berger, H. Wadley, R. McMeeking, "Mechanical metamaterials at the theoretical limit of isotropic elastic stiffness", *Nature* **543** (2017), no. 7646, p. 533.

[48] V. Deshpande, M. Ashby, N. Fleck, "Foam topology: bending versus stretching dominated architectures", *Acta Mater.* **49** (2001), no. 6, p. 1035-1040.

[49] R. S. Lakes, *Viscoelastic Solids, Vol. 9*, CRC Press, Boca Raton, Florida, USA, 1998.

[50] R. Christensen, *Theory of Viscoelasticity: An Introduction*, Academic Press Inc., New York, USA, 2012.

[51] C. M. Zener, S. Siegel, "Elasticity and anelasticity of metals", *J. Phys. Chem.* **53** (1949), no. 9, p. 1468-1468.

[52] X. Chen, Q. Ji, J. Wei, H. Tan, J. Yu, P. Zhang, V. Laude, M. Kadic, "Light-weight shell-lattice metamaterials for mechanical shock absorption", *Int. J. Mech. Sci.* **169** (2020), article no. 105288.

[53] G. Lu, T. Yu, *Energy Absorption of Structures and Materials*, Woodhead Publishing Limited, Cambridge, UK, 2003.

[54] L. Salari-Sharif, T. A. Schaedler, L. Valdevit, "Energy dissipation mechanisms in hollow metallic microlattices", *J. Mater. Res.* **29** (2014), no. 16, p. 1755-1770.

[55] L. R. Meza, S. Das, J. R. Greer, "Strong, lightweight, and recoverable three-dimensional ceramic nanolattices", *Science* **345** (2014), no. 6202, p. 1322-1326.

[56] J. Ma, Z. You, "Energy absorption of thin-walled square tubes with a prefolded origami pattern part I: geometry and numerical simulation", *J. Appl. Mech.* **81** (2014), no. 1, article no. 011003.

[57] S. Li, H. Fang, S. Sadeghi, P. Bhovad, K.-W. Wang, "Architected origami materials: How folding creates sophisticated mechanical properties", *Adv. Mater.* **31** (2019), no. 5, article no. 1805282.

[58] T. A. Schaedler, A. J. Jacobsen, A. Torrents, A. E. Sorensen, J. Lian, J. R. Greer, L. Valdevit, W. B. Carter, "Ultralight metallic microlattices", *Science* **334** (2011), no. 6058, p. 962-965.

[59] J. L. Silverberg, A. A. Evans, L. McLeod, R. C. Hayward, T. Hull, C. D. Santangelo, I. Cohen, "Using origami design principles to fold reprogrammable mechanical metamaterials", *Science* **345** (2014), no. 6197, p. 647-650.

[60] S. Shan, S. H. Kang, J. R. Raney, P. Wang, L. Fang, F. Candido, J. A. Lewis, K. Bertoldi, "Multistable architected materials for trapping elastic strain energy", *Adv. Mater.* **27** (2015), no. 29, p. 4296-4301.

[61] K. Bertoldi, "Harnessing instabilities to design tunable architected cellular materials", *Annu. Rev. Mater. Res.* **47** (2017), p. 51-61.

[62] T.-C. Lim, "Negative thermal expansion in transversely isotropic space frame trusses", *Phys. Status Solidi B* **250** (2013), no. 10, p. 2062-2069.

[63] D. G. Gilmore, *Spacecraft Thermal Control Handbook*, Fundamental Technologies, vol. 1, American Institute of Aeronautics and Astronautics, Reston, Virginia, USA, 2002, Online version available at: http://www.knovel.com/knovel2/Toc.jsp, 373-403 pages.

[64] Q. Zhang, J. Wommer, C. ORourke, J. Teitelman, Y. Tang, J. Robison, G. Lin, J. Yin, "Origami and kirigami inspired self-folding for programming three-dimensional shape shifting of polymer sheets with light", *Extreme Mech. Lett.* **11** (2017), p. 111-120.

[65] Y. Mao, Z. Ding, C. Yuan, S. Ai, M. Isakov, J. Wu, T. Wang, M. L. Dunn, H. J. Qi, "3D printed reversible shape changing components with stimuli responsive materials", *Sci. Rep.* **6** (2016), p. 24761.

[66] J. B. Hopkins, K. J. Lange, C. M. Spadaccini, "Designing microstructural architectures with thermally actuated properties using freedom, actuation, and constraint topologies", *J. Mech. Design* **135** (2013), no. 6, article no. 061004.

[67] S. Tibbits, "Design to self-assembly", *Archit. Design* **82** (2012), no. 2, p. 68-73.

[68] J. C. Breger, C. Yoon, R. Xiao, H. R. Kwag, M. O. Wang, J. P. Fisher, T. D. Nguyen, D. H. Gracias, "Self-folding thermo-magnetically responsive soft microgrippers", *ACS Appl. Mater. Interfaces* **7** (2015), no. 5, p. 3398-3405.

[69] G. Stoychev, N. Puretskiy, L. Ionov, "Self-folding all-polymer thermoresponsive microcapsules", *Soft Matter* **7** (2011), no. 7, p. 3277-3279.

[70] R. Lakes, "Dense solid microstructures with unbounded thermal expansion", *J. Mech. Behav. Mater.* **7** (1996), no. 2, p. 85-92.

[71] J. Lehman, R. S. Lakes, "Stiff, strong, zero thermal expansion lattices via material hierarchy", *Compos. Struct.* **107** (2014), p. 654-663.

[72] Q. Wang, J. A. Jackson, Q. Ge, J. B. Hopkins, C. M. Spadaccini, N. X. Fang, "Lightweight mechanical metamaterials with tunable negative thermal expansion", *Phys. Rev. Lett.* **117** (2016), no. 17, article no. 175901.

[73] C. A. Steeves, S. L. d. S. e Lucato, M. He, E. Antinucci, J. W. Hutchinson, A. G. Evans, "Concepts for structurally robust materials that combine low thermal expansion with high stiffness", *J. Mech. Phys. Solids* **55** (2007), no. 9, p. 1803-1822.

[74] G. Jefferson, T. A. Parthasarathy, R. J. Kerans, "Tailorable thermal expansion hybrid structures", *Int. J. Solids Struct.* **46** (2009), no. 11-12, p. 2372-2387.

[75] O. Sigmund, S. Torquato, "Composites with extremal thermal expansion coefficients", *Appl. Phys. Lett.* **69** (1996), no. 21, p. 3203-3205.

[76] O. Sigmund, S. Torquato, "Design of materials with extreme thermal expansion using a three-phase topology optimization method", *J. Mech. Phys. Solids* **45** (1997), no. 6, p. 1037-1067.

[77] S. Watts, D. A. Tortorelli, "Optimality of thermal expansion bounds in three dimensions", *Extreme Mech. Lett.* **12** (2017), p. 97-100.

[78] J. Qu, M. Kadic, M. Wegener, "Poroelastic metamaterials with negative effective static compressibility", *Appl. Phys. Lett.* **110** (2017), no. 17, article no. 171901.

[79] J. Qu, M. Kadic, A. Naber, M. Wegener, "Micro-structured two-component 3D metamaterials with negative thermal-expansion coefficient from positive constituents", *Sci. Rep.* **7** (2017), p. 40643.

Comptes Rendus
Physique
2020, 21, nº 7-8, p. 767-785
`https://doi.org/10.5802/crphys.39`

Metamaterials 2 / *Métamatériaux 2*

Past, present and future of seismic metamaterials: experiments on soil dynamics, cloaking, large scale analogue computer and space–time modulations

Passé, présent et futur des métamatériaux sismiques : expériences sur la dynamique des sols, camouflage, calculateur analogique à grande échelle et modulations spatio–temporelles

Stéphane Brûlé[*, a] **and Sébastien Guenneau**[b]

[a] Aix Marseille Univ, CNRS, Centrale Marseille, Institut Fresnel, Marseille, France

[b] UMI 2004 Abraham de Moivre-CNRS, Imperial College London, London SW7 2AZ, UK

E-mails: stephane.brule@menard-mail.com (S. Brûlé), s.guenneau@imperial.ac.uk (S. Guenneau)

Abstract. Some properties of electromagnetic metamaterials have been translated, using some wave analogies, to surface seismic wave control in sedimentary soils structured at the meter scale. Two large scale experiments performed in 2012 near the French cities of Grenoble [1] and Lyon [2] have confirmed the usefulness of this methodology and its potential influence on soil-structure interaction. We present here a new perspective on the in-situ experiment near Lyon, which unveils energy corridors in the seismic lens. We further introduce a concept of time-modulated seismic metamaterial underpined by an effective model based on Willis's equations. As a first application, we propose that ambient seismic noise time-modulates structured soils that can be viewed as moving media. In the same spirit, a design of an analogous seismic computer is proposed making use of ambient seismic noise. We recall that ancient Roman theaters and forests of trees are two examples of large scale structures that behave in a way similar to electromagnetic metamaterials: invisibility cloaks and rainbows, respectively. Seismic metamaterials can thus not only be implemented for shielding, lensing and cloaking of potentially deleterious Rayleigh waves, but they also have potential applications in energy harvesting and analogous computations using ambient seismic noise, and this opens new vistas in seismic energy harvesting and conversion through the use of natural or artificial soil structuring.

---

[*] Corresponding author.

ISSN (electronic) : 1878-1535 `https://comptes-rendus.academie-sciences.fr/physique/`

Résumé. Certaines propriétés des métamatériaux électromagnétiques ont été traduites, en utilisant certaines analogies d'ondes, en contrôle des ondes sismiques de surface dans des sols sédimentaires structurés à l'échelle du mètre. Deux expériences à grande échelle réalisées en 2012 près des villes françaises de Grenoble [1] et Lyon [2] ont confirmé l'utilité de cette méthodologie et son influence potentielle sur l'interaction sol-structure. Nous présentons ici une nouvelle perspective sur l'expérience in-situ menée près de Lyon, qui dévoile des couloirs d'énergie dans la lentille sismique. Nous introduisons en outre un concept de métamatériau sismique modulé dans le temps sous-tendu par un modèle effectif s'appuyant sur les équations de Willis. Dans une première application, nous proposons que le bruit sismique ambiant module dans le temps les sols structurés pouvant être considérés comme des milieux en mouvement. Dans le même esprit, il est proposé de concevoir un calculateur analogique sismique utilisant le bruit sismique ambiant. Nous rappelons que les anciens théâtres romains et les forêts d'arbres sont deux exemples de structures à grande échelle qui se comportent de manière similaire aux métamatériaux électromagnétiques : capes d'invisibilité et rainbows (anglicisme d'arcs-en-ciel), respectivement. Les métamatériaux sismiques peuvent donc non seulement être mis en œuvre pour des murailles, lentilles et capes pour ondes de Rayleigh potentiellement délétères, mais ils ont également des applications potentielles dans la récupération d'énergie et des ordinateurs analogiques utilisant le bruit sismique ambiant, ce qui ouvre de nouvelles perspectives dans la récupération et la conversion d'énergie sismique grâce à l'exploitation de structuration naturelle ou artificielle des sols.

Keywords. Seismic metamaterial, Transformational physics, Time-modulated medium, Homogenization, Analogue computer, Ambient seismic energy.

Mots-clés. Métamatériaux sismiques, Physique transformationnelle, Milieux modulés en temps, Homogénéisation, Calculateur analogique, Energie sismique ambiante.

1. Introduction

In earthquake engineering, the trapping of seismic waves in natural u-shaped basin filled with very soft sediments remains a major issue such as for Mexico City downtown built on a former drought lake [3]. Independently of the path taken by the body waves coming from the earthquakes focus located in the crust a few tens of kilometers deep, essential wave transformations occur in the last tens of meters below the free surface. Main effects are interaction between different components of body waves at the Earth's surface generating Rayleigh surface waves, strong wave magnitude amplification at the free surface (e.g. site effects), wave trapping prolonging the duration of the signal, and so forth. At the scale of the Earth, there is a clear differentiation of the seismic motion at the surface because of local and superficial geological features (shape of sediment layers, density contrasts, anisotropy, viscoelasticity effect, etc.). That is exactly what scientific research on wave physics and more precisely, on seismic metamaterials tries to anticipate, asserting that the creation of a small-volume of anisotropic ground, made of a 2D mesh of inclusions inside the bulk, can also induce seismic wave-matter interactions [1, 2, 4] with civil engineering purposes. The influence of such inclusions in the ground can be characterized in different, complementary, ways by numerical models and site-experiments: wave mode conversion, redistribution of energy within the network with focusing effects, wave reflection, frequency filtering, reduction of the amplitude of seismic signal energy, etc. In this article, we browse the main tools to design the smart deep infrastructure of tomorrow, presenting an introduction to the field of seismic metamaterials (Section 1), pointing out some analogous phenomena observed in the field of electromagnetic metamaterials, not only the now well established negative refraction, (Section 2) and cloaking (Section 3), but also large scale metamaterials analogues of computers solving integral equations making use of ambient seismic noise (Section 4) and finally some prediction of non-reciprocal effects for surface seismic waves akin to those in electromagnetic time-modulated media (Section 5) and bridging the two fields via the unifying concept of transformational optics and acoustics. Since the first in-situ experiment carried out in 2012 [1], many research groupings worldwide have started to work on this topic, and although this field of seismic metamaterials is still in its infancy, we believe it has a bright future. One of the future perspectives we propose to initiate is an outline of a two-scale homogenization theory based on [5], that shows exotic effective elastodynamic media that can be achieved with soils structured with boreholes and concrete (or steel) columns. Indeed, we stress that Willis's equations [6], which have an additional term in the constitutive equation related to the gradient of pre-stresses, compared to classical constitutive equation of linear elasticity for homogeneous media, are a natural framework when a seismic wave passes through such structured soils. Interestingly, Willis's equations have a counterpart in electromagnetics, so-called bi-anisotropic equations with a magneto-optic coupling tensor [7], which have been recently shown to mimic moving media [8]. We finally propose to translate the concept of electromagnetic metamaterial analog computing [9, 10], based on suitably designed metamaterial cells that can perform mathematical operations (such as spatial differentiation, integration, or convolution) on the profile of an impinging wave as it propagates through these cells, to the realm of seismology. We will finally propose some new types of seismic metamaterials, that we coin as seismic computers. This bold idea is to make use of mechanical energy of small earthquakes which occur daily, to perform mathematical operations on a large scale at a minimum cost. We think this theoretical proposal of a kind of Türing machine at a geophysical scale can be a green contribution for our planet, since apart from the human-seismic machine interface, it does not require any energy consuming device to work. We further believe that using ambient noise at the Earth scale, a new type of world wide web could emerge, connecting seismic computers from various parts of the world. Finally, as a twist of epistemology, it looks like seismic metamaterials were already present in the ancient world, and we will say more about that in the sequel.

2. Revisiting the 2012 site-experiment in Saint-Priest

The wave trapping in a sedimentary basin may be the cause of phenomena of amplification of the seismic motion and prolongation of the duration of the shaking. The full-scale vibration experiments carried out in France during the year 2012 on two arrays of holes [1, 2] have shown the reality of the elastic wave-matter interaction for the case of artificial structured soils, just beneath the Earth's surface. Inside the grid of holes and for the near field, the distribution of the mechanical energy has been significantly modified. In this article, we propose to revisit the experience of Saint Priest (a small town located nearby the French city of Lyon) conducted in 2012 by presenting original results. So far we wanted to show the remarkable effective properties that could be obtained by structuring the soils (reflexion, negative refractive index, etc.) and try to identify what could be the link with earthquake engineering [11].

2.1. *Energetic seismic metamaterials*

However, we propose to open a complementary research track based on some observations on the turbulence of the velocity field inside a structured fluid, known as an invisibility carpet and demonstrated for water waves at a meter scale [12]. In this experimental study on the control of water waves within a 17 m long water channel, it was found that the velocity field was very disturbed inside the corridors of the water wave cloak. Similar observation was made twelve years ago on numerical simulations performed for a small scale experiment on a water wave invisibility cloak [13], see Figure 1. We have already pointed out the analogous behaviour of water waves in structured fluids, and Rayleigh waves in soft structured soils [14]. It seems thus possible that similar enhancement for the velocity field of the elastodynamic waves within the structured soil in Saint-Priest might occur, as this seismic metamaterial can be viewed as a transformed

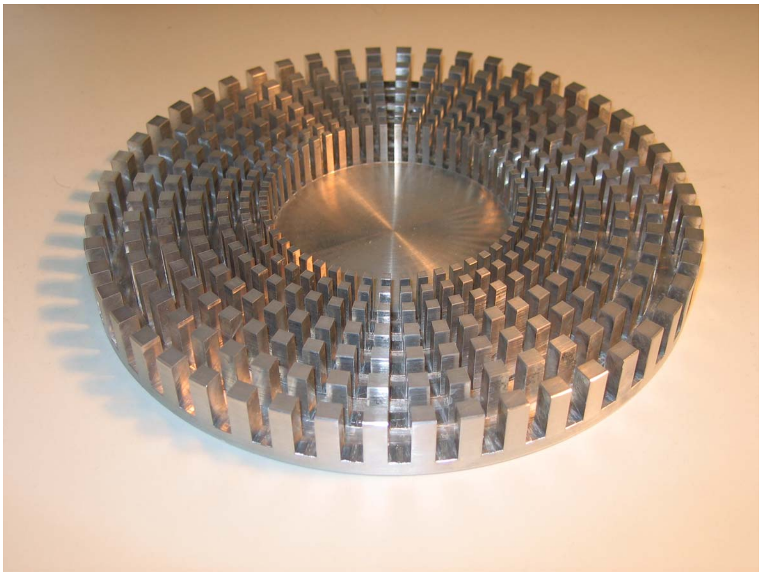

Figure 1. Photo (credit: S. Enoch) of the multi-wave metamaterial cloak (made of aluminium) designed, simulated, and experimentally tested at Institut Fresnel in 2008: this cloak which is 20 cm in diameter and 1 cm in height smoothly detours water waves around its center from 8 to 15 Hz. Cloaking is also achieved for micro waves from 3 to 7 GHz and for airborne pressure waves from 4 to 8 kHz. A single governing equation (Helmholtz equation) models all three types of waves propagating though this cloak [15]. The same geometry works for cloaking of flexural waves in a thin plate [16]. A scaled-up version of this cloak serves as an inspiration for designs of seismic cloaks at the meter scale.

medium [11], just like the carpet in [12] and the cloak in [13], and so all these metamaterials should share similar features.

Thus, one wonders whether the mechanical energy inside the seismic metamaterial is not a potential resource to exploit. The peak of particle velocity is a few mm·s^{-1} for the vibrations generated by urban work site—The amplitude of urban seismic noise ranges from 10^{-6} to 10^{-4} m·s^{-1}.

For the largest amplitudes of this range, with a mechanical energy conversion with calibrated buried oscillators, we can hope to light a bulb of a few tens of Watt. The answer is positive as we now show making use of existing data with measurements acquired inside the corridors of the Saint-Priest grid of holes, see Figure 2. We would like to coin such large scale structured seismic energetic metamaterials, since they have a purpose in energy harvesting [17]. We believe this subfield of seismic metamaterials might have a bright future.

This large scale experiment, which took place near the French city of Lyon in September 2012, is a large scale phononic crystal, made of five rows of self-stable boreholes 2 m in diameter, 5 m in depth with a center-to-center spacing of 7 m, see Figure 2. To capture the ground motion's field, a set of 15 three-component velocimeters (V_x, V_y, V_z) has been implemented on site. The sensors were used simultaneously with a common time base and were densely set on half of the grid. For the purposes of the study, here we present only the sensors inside the grid. The artificial source consisted this time of the fall of a 17 ton steel pounder from a height of about 12 m to generate clear transient vibrations pulses. We checked that most of the energy of the source was converted into energetic surface waves. The typical waveform of the source in time-domain looked like a

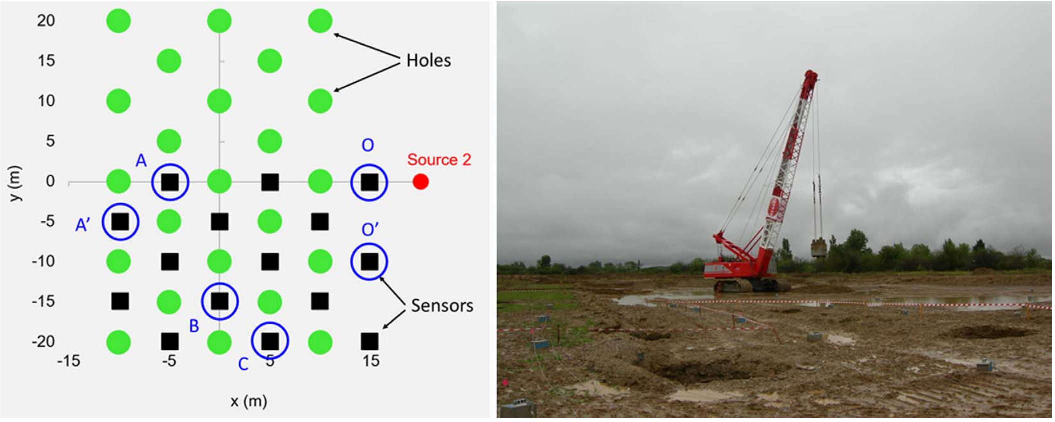

Figure 2. Experiment on a flat seismic lens: (Left) Plan view of field-site layout with 23 boreholes (green disks), 2 m in diameter, 5 m in depth, with hole spacing of 5 m. Sensors (black squares) are located midway between the holes, with 5 m spacing. The source (red disk) is located 10 m in horizontal distance from the first row of holes. Points A, A′, O, O′, B, C are sensors selected for the study of energy or frequency filtering effect, see Figures 4–5. (Right) Photo (credit: S. Brûlé) of the field experiment near the French city of Lyon in September 2012, with some boreholes in the foreground and a crane carrying a 17 ton mass (the seismic source) in the background.

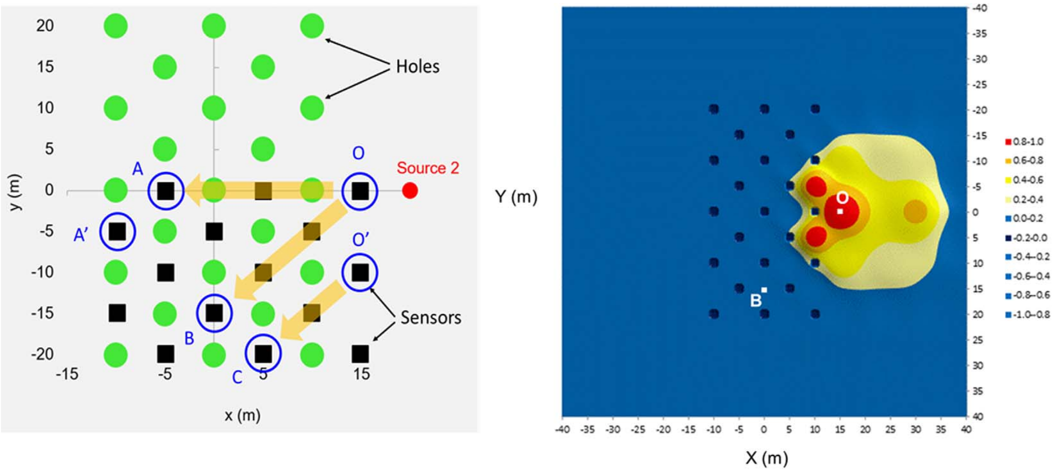

Figure 3. (Left) Selected corridors for the experimental study on frequency filtering and energy distribution: line 1 from point O to A, line 2 from point O to B and line 3 from O′ to C. (Right) Snapshot illustrating the recorded energy distribution in the soil structured with 23 holes after an impact (17 ton mass dropped for the crane shown in Figure 2) at the Earth's surface. Source is located at $(x = 20, y = 0)$.

second order Ricker wavelet (or "Mexican hat wavelet"). The signal was characterized by a mean frequency value at 8.15 Hz ($\lambda_{P\text{-wave}} \sim 74$ m) with a range of frequencies going from 3 Hz to 20 Hz ($30 < \lambda_{P\text{-wave}} < 200$ m). A preliminary test was performed on the ground without holes with sensors arranged in a single row. Thereafter, we compare the measurements acquired on a soil without holes with those acquired inside the grid of holes.

The diagrams in Figure 5 show the decrease in energy with the distance from the source. The energy is defined as the sum of the squared value of each component (V_x, V_y, V_z) of the seismogram. With or without holes in the ground, the energy decreases very quickly with the distance. On the total energy diagram (Figure 5(a)), the energy decreases for the three profiles, but much less quickly on the first 15 m for OB (black dotted line) and O′C (grey dotted line). For the profile OA (solid black curve) passing through the holes, the decay is linear. We can advance two explanations to this observation. The first is a strong reflection of the seismic signal coming on the long side of the array. The second is a channelization of energy in the soil bridges between the holes. This phenomenon can be seen on a snapshot in time domain, showing the energy map inside the grid (Figure 3) and along the corridor OB.

Now, if we study the energy diagrams by components (V_x^2, V_y^2, V_z^2), we observe that the energy ratio between the different components is changing with the offset and with the corridor considered (Figure 3(b) and (c)). The OA profile shows an apparent regularity by component, but the ordinate scale being logarithmic the differences between components are nevertheless marked. At 15 m, there is an inversion of importance between the X and Z components (profile OA). These rapid changes seem to reflect changes in polarization of the seismic signal [18]. Let's see if we can explain this in the spectral domain. We have calculated the magnitude in dB of three transfer functions $|T_x(\omega)|$, $|T_y(\omega)|$ and $|T_z(\omega)|$ as the spectral ratio of the ground particle velocity for a couple of sensors (O, A) and (O, B). Basically we considered the grid of holes as a filter without any consideration of initial soil properties (wave velocity, pattern of the grid, etc.).

$$|T_{\mathrm{A/O}}(\omega)| = |\mathscr{A}(\omega)/\mathscr{O}(\omega)| \tag{1}$$

with $\mathscr{A}(\omega)$ and $\mathscr{O}(\omega)$ the Fourier transforms of signal recorded with sensor A and O.

The transfer function represents information relating to the signal entering in the grid of holes (point A or B) from the right-hand side of the Figure (point O or O′). We have calculated the magnitude in dB of the transfer function for the initial soil (solid blue line) and for the structured soil with holes (solid red line). We have also drawn the magnitude of the original soil transfer function minus 3 dB (gray dotted line) to illustrate the efficiency of the holey-ground. We consider that results acquired with the land streamer (solid blue line) make the benchmark curve to compare with the others. It is the spectral signature of the soil with its initial peculiarities. $T_{\mathrm{A/O}}$ and $T_{\mathrm{B/O}}$ curves are significantly different. For $T_{\mathrm{A/O}}$ in the left hand side of Figure 4, we observe an horizontal amplification of the particle's velocity (solid red line), compared to the ground without hole (blue solid line), from 1 to 10 Hz. For the vertical component, the amplification is identified between 1 and 2 Hz and 4 and 10 Hz. Between 2 and 4 Hz, there is a de-amplification of the magnitude around 3 dB (grey dotted line).

In regards to $T_{\mathrm{B/O}}$ curves, only de-amplification from 1 to 10 Hz is observed for x-component, after completion of the holes. Same observation up to 2.3 Hz for the y-component but then, there is amplification unlike what was described for x-component. For the y-component, there is only amplification between 4.6 and 10 Hz with a peak at 6.5 Hz. Overall, there is a larger frequency bandwidth regarding de-amplification for the profile passing between the holes (OB) than for the line crossing the holes (OA). Roughly speaking, the signal is much more attenuated horizontally in x and vertically in z and for a broader range of frequency for the profile passing between the holes (OB) than for the line crossing the holes (OA). However, there is amplification according to y. These contrasts between $T_{\mathrm{A/O}}$ and $T_{\mathrm{B/O}}$ result in polarization changes for the seismic waves, as further discussed in terms of dynamic effective properties akin to auxetic media (with a negative Poisson ratio) in [3]. We believe that the realization of holes and the associated densification of soils might be the cause of the 6.5 Hz peak in z-component. Also worth mentioning is that we have proposed here a viewpoint in the context of linearized elastic wave equations, but some

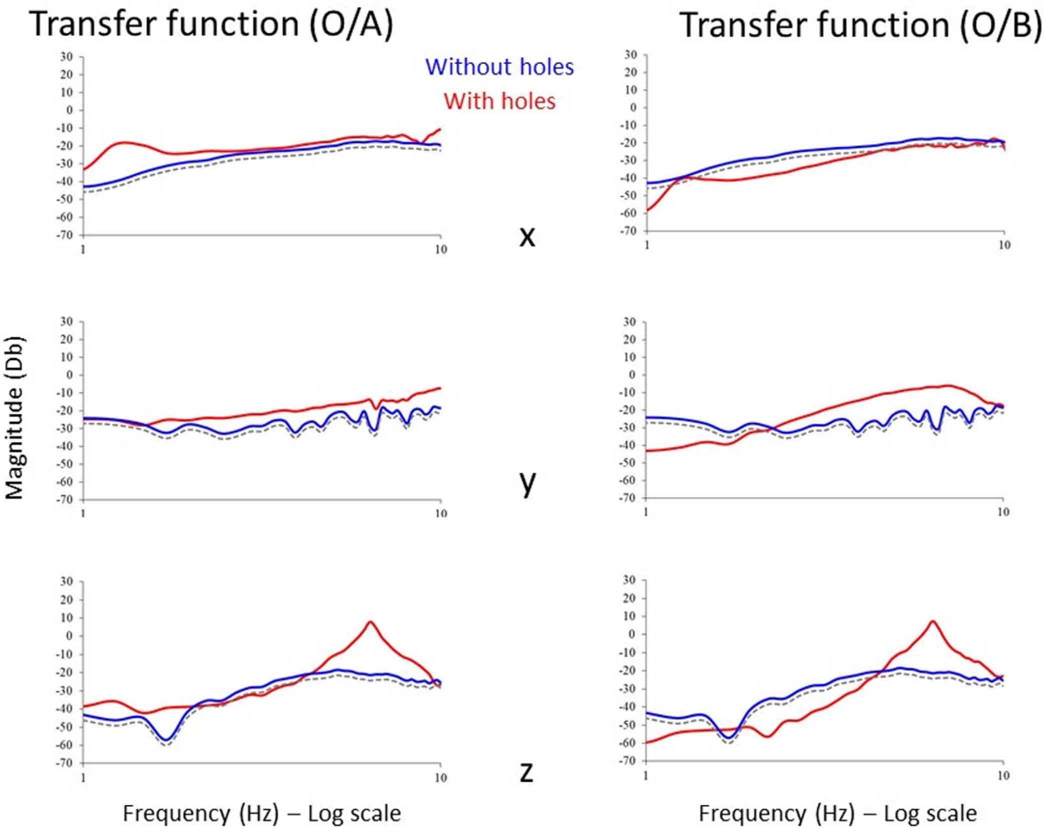

Figure 4. Transfer functions O/A and O/B for x (upper panel), y (middle panel) and z (lower panel) component of two velocimeters located inside the array of boreholes, compared to those of a velocimter placed in between the source and the array, as shown in Figure 1(left). (OA) is for the line passing through the source and the two circled sensors. (OB) is for the line passing through a corridor without boreholes, see Figure 3. Light blue curves are for soil without holes and red curves for structured soil.

interesting non-linear effects would be also woth studying such as the possibility of rogue waves in soft soils that one could counteract with the array of boreholes [19].

3. Seismic cloaks, Roman theaters and forests of trees

On the basis of these results, we extend the theoretical analysis to ancient structures, made up of many elements of symmetries such as the foundations of Roman amphitheatres [4].

3.1. *Seismic metamaterials from the ancient world*

Built of travertine, tuff, and brick-faced concrete, the Coliseum in Roma is the largest amphitheatre ever built. Construction began under the emperor Vespasian in AD 72 and was completed in AD 80 under his successor and heir, Titus. A numerical simulation was conducted on a structured soil reproducing the geometry of the foundations of an ancient amphitheater (see Figure 6(b)), with a source inside (see Figure 6(c)) and outside (see Figure 6(d)) of the structure. The similarity

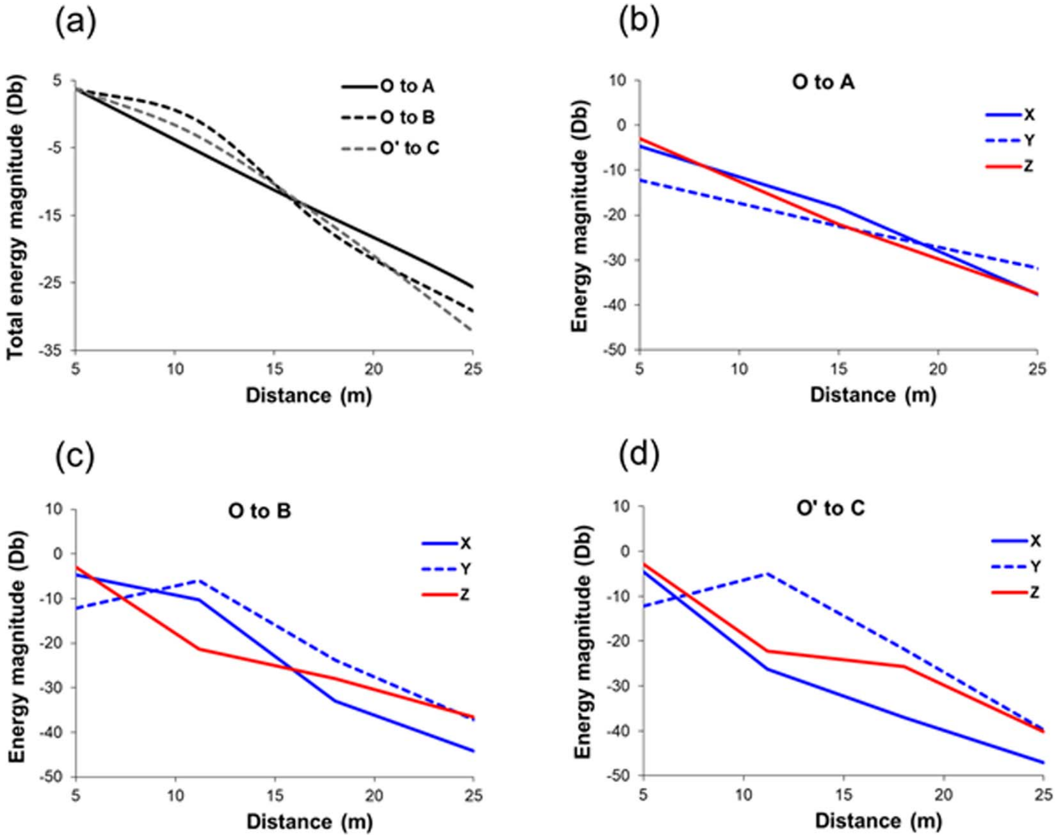

Figure 5. Mechanical energy magnitude versus offset, according to the studied corridor. (a) Total energy mesured for the three selected corridors (O to A, O to B and O′ to C). Diagrams (b), (c) and (d) show respectively the energy by component X, Y, Z versus offset, for corridors OA, OB et O′C shown in Figure 3.

between the foundations of the Coliseum in Figure 6(b) and the design of the invisibility cloak in Figure 1 can be seen in Figure 6(a). We note that such fortuitous seismic metamaterials could inspire seismic cloak designs at the scale of cities [20].

3.2. *Forests as seismic metamaterials*

There is currently a renewed interest in site-city interactions as slender bodies such as medium size buildings placed atop of soft soil may have a strong interaction with surface seismic waves in the 1 to 10 Hz frequency range. This has been further explored in a recent work [4]. It has been recently proposed that other types of locally resonant large scale structures such as forest of trees can shield [21] and convert [22] surface Rayleigh waves. The latter can be viewed as an elastic counterpart of graded metamaterial surfaces in electromagnetics, that make possible a rainbow effect whereby the colors of light are filtered by resonant elements of varying sizes [23]. This type of rainbow effect has been also noted for Love waves propagating in soils with a soft guiding layer surmounted by a forest of trees, see Figure 7 in which case a complete correspondence with spoof plasmon polaritons has been mathematically established [24]. Interestingly, it has

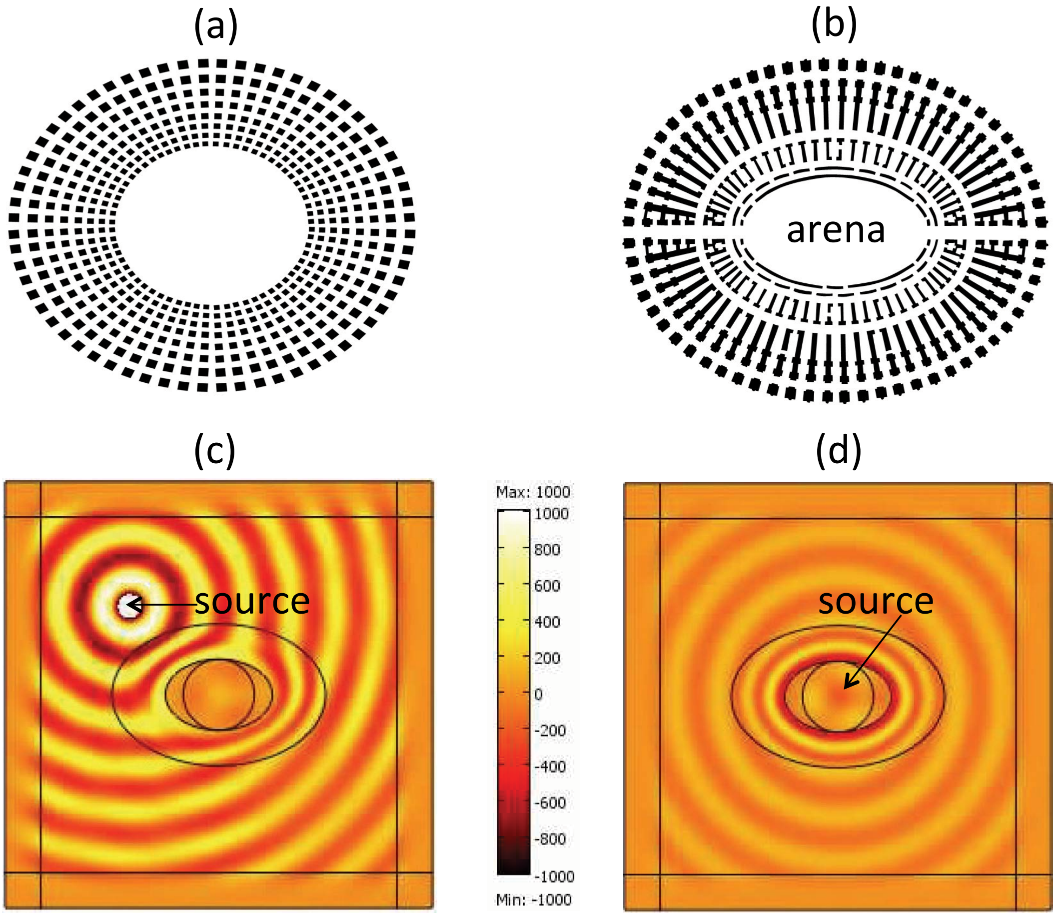

Figure 6. The Coliseum: an unexpected seismic metamaterial from the ancient world. (a) Geometry of the cloak in Figure 1 mapped onto an ellipsis. (b) Geometry of the Coliseum Main axes of arena are 86 m by 54 m (height of 4.5 m) and outer dimensions are 187.75 m by 155.60 m (height of 50.75 m). (c) Finite element (Comsol) simulation for a flexural wave, emitted by a point source of wavelength 35 m, propagating in an elastic plate (of thickness 3 m) with an elliptical cloak with similar dimensions to the Coliseum. (d) Same for a source located inside the arena. One notes the reduced amplitude of field in arena in (c) and its enhancement at the boundary of arena in (d).

been demonstrated in [25] that one can design special types of elastic rainbows that can harvest Rayleigh waves and we believe a similar design can be applied to harvest Love waves.

After this review of seismic metamaterials from the past and the present, we would like to turn our mind to seismic metamaterials of the future.

4. Proposal for an analogue computer with a seismic metamaterial

Before we detail our proposal for a seismic computer, we need to recall the main difference between analogue and digital computers. An analogue computer is a type of computer that relies on the continuously changeable aspects of physical phenomena such as electrical, mechanical,

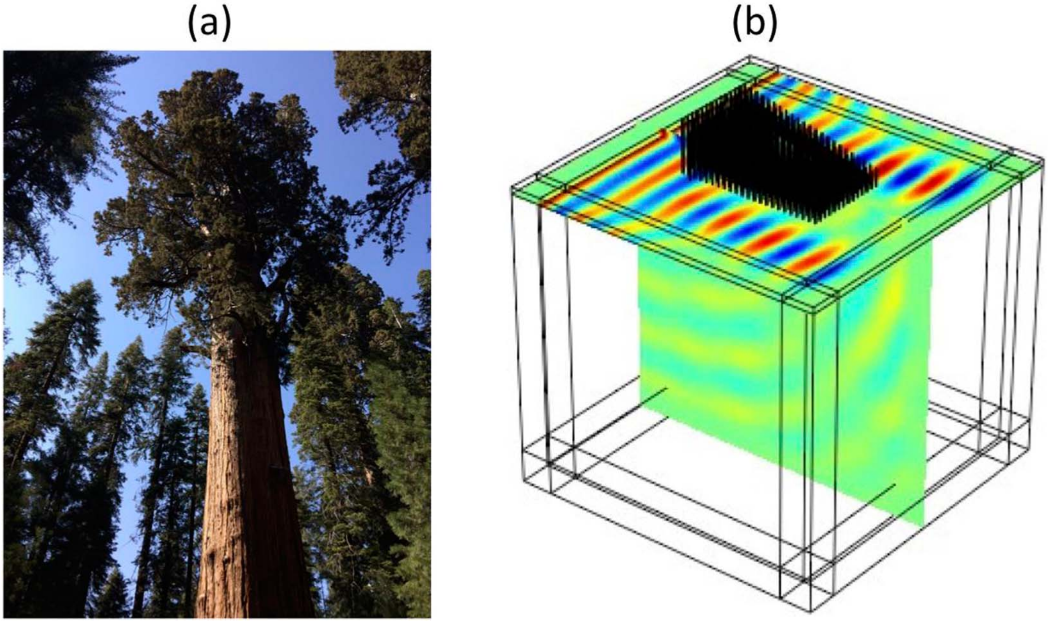

Figure 7. Forests as seismic metamaterials: (a) Photo (S. Brule) of the General Sherman (height of 83.7 m, diameter of 7.7 m) which is located in California's Sequoia National Park. (b) Finite element (Comsol) simulation of a Love wave of frequency 10 Hz propagating through a forest of tree trunks (without foliage) of heights ranging from 80 m to 4 m. When adding foliage to the tree trunks, same effect can occur for a Love wave of frequency 5 Hz (or alternatively at 10 Hz for trees twice as small), according to a theory developed in [24].

or hydraulic quantities to model the problem being solved. In contrast, digital computers represent varying quantities symbolically, as their numerical values change. As an analogue computer does not use discrete values, but rather continuous values, processes cannot be reliably repeated with exact equivalence, as they can with Türing machines. Unlike machines used for digital signal processing, analogue computers do not suffer from the discrete error caused by quantisation noise. Instead, results from analog computers are subject to continuous error caused by electronic noise. We now wish to propose an analogue computer that would use the energy of ambient seismic noise in structured sedimentary soils. Mechanical analogue computing devices date back at least to the Roman author, architect civil and military engineer Marcus Vitruvius Pollio who lived in the first century BC, who is known for his multi-volume work entitled De architectura [26]. His discussion of perfect proportion in architecture and the human body led to the famous Renaissance drawing by Leonardo da Vinci of Vitruvian Man which describes the use of a wheel for measuring an arc length along a curve i.e. the most simple integral in space. Many other elementary analogue devices were described until now, see for instance [27].

We shall only recall here that James Clerk Maxwell described a ball type of integrating device while he was an undergraduate: it was incorporated in a planimeter design, which is a measuring instrument used to determine the area of an arbitrary two-dimensional shape.

We propose that metastructures hold the potential to bring a new twist to the field of spatial-domain optical analogue computing: migrating from conceptually wavelength-sized elements for electromagnetic waves to seismic waves. We show in Figure 8 the principle of a metamaterial soil capable of solving integral equations using ambient seismic noise. For an arbitrary seismic wave as the input function to an equation associated with a prescribed integral operator, the solution of such an equation is generated as a complex-valued output seismic field. Our approach is based on analogies drawn with the seminal work [10] which experimentally demonstrated the concept of an analogue optical computer at microwave frequencies through solving a generic integral equation and using a set of waveguides as the input and output to the designed metastructures. By exploiting subwavelength-scale light-matter interactions in a metamaterial platform, the analogue computer may provide a route to achieve chip-scale, fast, and integrable computing elements. The researchers believed metamaterials could offer several important advantages over this conventional digital process. One benefit is that the computational process could be extremely fast because electromagnetic waves pass through metamaterials at the speed of light. Also, the same metamaterial can process multiple waves simultaneously. In the present case, the emphasis is on decameter scale seismic analogue computers that could solve complex mathematical equations using natural resources (ambient seismic noise). The seismic metamaterial analogue computer should be based on metamaterial blocks that can perform mathematical operations (such as spatial differentiation, integration, or convolution) on the profile of a surface (Rayleigh and Love) and bulk (shear and pressure) seismic waves as they propagate through these blocks. Two types of seismic metamaterials can achieve such functionality: (i) subwavelength structured metascreens combined with graded-index seismic waveguides such as forest of trees in Figure 7 and multilayered soils designed to achieve a desired spatial Green's function such as in Figure 8. Our proposal for these two types of seismic computers will require further theoretical and experimental efforts to become a tangible reality, but we are confident that at least one of the two routes towards of seismic computer can be tested in the near future.

5. Seismic metamaterials versus space–time modulated media

There is currently a keen interest in space–time modulated media in optics, as these can be mapped onto bi-anisotropic equations in the long wavelength limit, which present interesting features such as non-reciprocity of light propagation in moving media [8]. We propose here to adapt these results to surface seismic waves propagating in a vibrating soil, which can then be modelled as Willis' equations in the long wavelength limit as we will now show using the approach of [5]. We further note that homogenization results derived in [5] for the elastic wave equation, are an extension of results obtained in [28] for the acoustic wave equation. The latter is a very comprehensive, and landmark, textbook on the topic of dynamic materials, which are nothing but consecrated space–time mdulated media. We stress that the time-modulated system studied in [5] is a good model for the seismic computer that we study here.

5.1. *Two-scale homogenization of the modulated vector Navier system*

We consider the two-scale homogenization of the vector Navier system of a time-modulated layered medium. For this we need a fixed space–time Cartesian coordinate system $(\mathbf{x}, t) = (x_1, x_2, x_3, t)$ and a time modulated layered periodic medium. The propagation is assumed along the direction x_1 of stacking of layers. In what follows, the subscript denotes dependence of the field upon the periodicity η in the space–time variable $x_1 - c_1 t$, where c_1 is the modulation speed along x_1. We mostly follow the same lines as the derivation of Nassar et al. [5]. One considers a displacement field $\mathbf{A}_\eta$ which is a function on $\mathbb{R}^3 \times [0, T]$ solution of

$$(\mathscr{P}_\eta^{\mathbf{A}}) \begin{cases} \nabla \cdot \left[\tilde{\mathbf{C}}\left(\mathbf{x}, t, \dfrac{x_1 - c_1 t}{\eta}\right) : \nabla \mathbf{A}_\eta \right] = \dfrac{1}{c^2} \dfrac{\partial}{\partial t} \left[\tilde{\rho}\left(\mathbf{x}, t, \dfrac{x_1 - c_1 t}{\eta}\right) \dfrac{\partial}{\partial t} \mathbf{A}_\eta \right] , \\ \mathbf{A}_\eta(\mathbf{x}, 0) = \overline{\mathbf{A}}_\eta(\mathbf{x}), \end{cases}$$

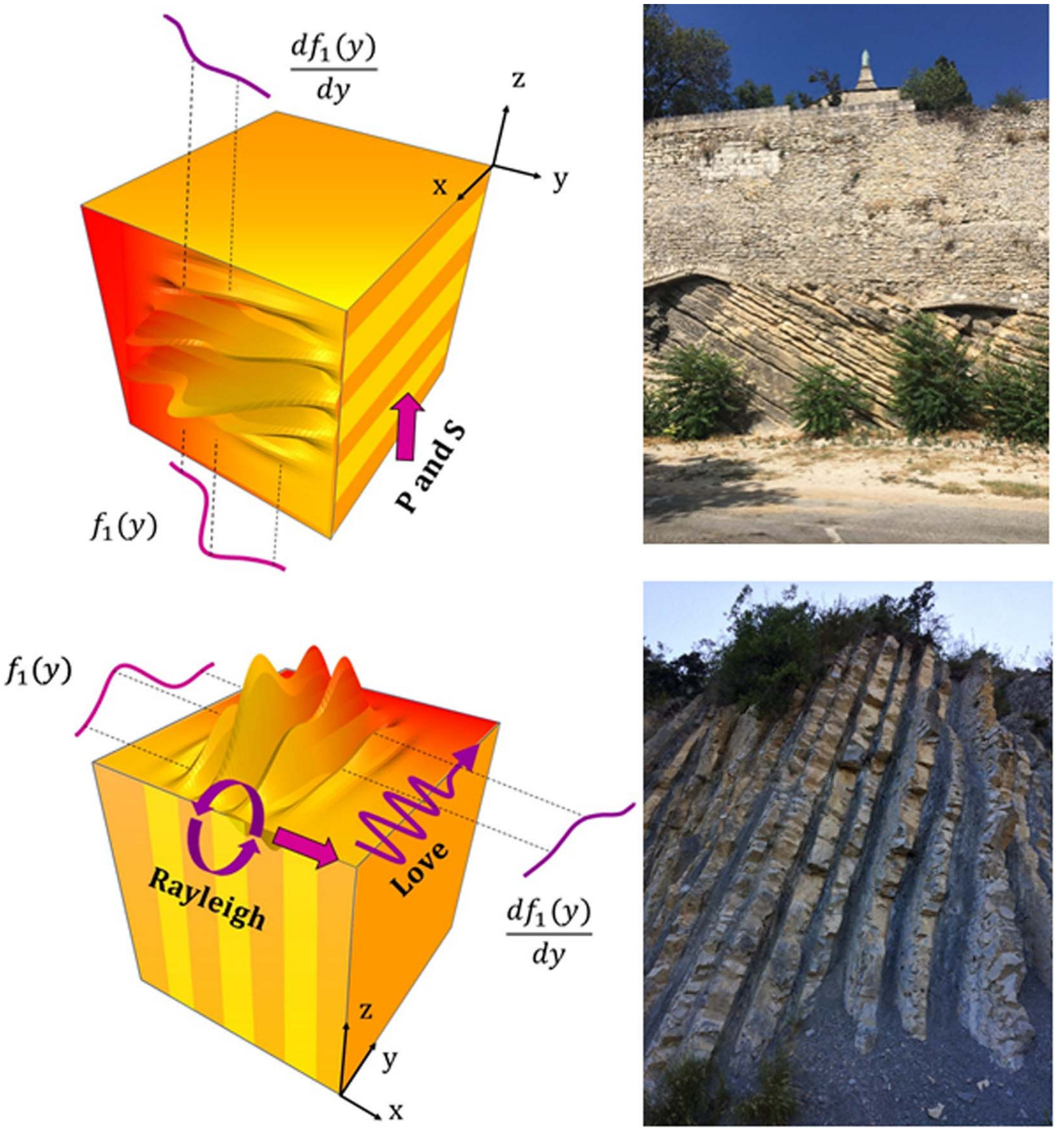

Figure 8. Principle of the seismic computer: sketch of suitably designed (Left) and naturally occuring (Right) layered soils that may perform a desired mathematical operation (e.g. integration and differentiation) on arbitrary seismic wave signals (ambient noise) in the case of volume pressure (P) and shear (S) waves (Top), and surface Love and Rayleigh waves (Bottom), as they propagate through it (adapted from [10]). (Upper left) Photo of inclined geologic layers with horizontal rows of stone walls in Arles, France (credit: S. Brûlé). (Lower right) Photo of subvertical geological layers with a regular alternation (with periodicity of about 1 m) of limestones (yellow) and marl (dark) in La Charce, France (credit: S. Brûlé).

where $\tilde{\mathbf{C}}(\mathbf{x}, t, (x_1 - c_1 t)/\eta)$ and $\tilde{\rho}(\mathbf{x}, t, (x_1 - c_1 t)/\eta)$ respectively denote the rank-4 elasticity tensor and density which are equal to $\mathbf{C}((x_1 - c_1 t)/\eta)$ and $\rho((x_1 - c_1 t)/\eta)$ in the modulated layered medium that is in the interval $x_1 \in [0, h]$ and $\mathbf{C}_0$ and ρ_0 outside the layered time-modulated soil. These parameters are 1 periodic functions of x_1 and $1/c_1$ periodic functions of t.

From now on we assume that $\mathbf{C}_0 = \mathbf{I}$ and $\rho_0 = 1$ using the linearity of the Navier system, and we consider the following ansatz for the vector displacement field

$$\begin{aligned}\mathbf{A}_\eta(\mathbf{x},t) &= \mathbf{A}_0\left(\mathbf{x},t,\frac{x_1-c_1t}{\eta}\right)+\eta\mathbf{A}_1\left(\mathbf{x},t,\frac{x_1-c_1t}{\eta}\right)\\ &\quad+\eta^2\mathbf{A}_2\left(\mathbf{x},t,\frac{x-c_1t}{\eta}\right)+\cdots\end{aligned}\tag{2}$$

where $\mathbf{A}_i : [0,h]\times\mathbb{R}\times\mathbb{R}\times[0,T]\times Y \longmapsto \mathbb{C}^3$ is a smooth vector valued function of 5 variables, independent of η, such that $\forall(\mathbf{x},t)\in[0,h]\times\mathbb{R}\times\mathbb{R}\times[0,T]$, $\mathbf{A}_i(\mathbf{x},t,\cdot)$ is 1-periodic in $\mathbb{R}$.

We consider the coordinate system $(y,t) = (x_1-c_1t,t)$, in the moving frame attached to the modulated medium. We note that the partial derivatives in the moving frame can be expressed as $(\partial_{x_1},\partial_t) = (\partial_y,-c_1\partial_y+\partial_t)$. In a way similar to what is usually done for homogenization of unmodulated periodic media we replace the partial differential operator acting on the space variable x_1 by the two-scale operator $\partial/\partial x_1 := \partial/\partial x_1 + (1/\eta)(\partial/\partial y)$, and thus the rescaled curl operator can be expressed as

$$\nabla = \nabla+\left(\frac{\partial}{\eta\partial y},0,0\right)^T = \left(\nabla+\frac{\mathbf{n}}{\eta}\frac{\partial}{\partial y}\right),\tag{3}$$

where $\nabla = (\partial/\partial x_1,\partial/\partial x_2,\partial/\partial x_3)^T$ and $\mathbf{n}$ is the unit outward normal to the layers's interfaces. Moreover we do the same for the partial differential operator acting on the time variable t, so that $\partial/\partial t := \partial/\partial t - (c_1/\eta)(\partial/\partial y)$. These two-scale operators are combined with the asymptotic expansion of the potential field $\mathbf{A}_\eta$.

Assuming that the terms of the development of the powers higher than 2 are bounded in (2), we can write:

$$\begin{aligned}&\left[\nabla+\frac{\mathbf{n}}{\eta}\frac{\partial}{\partial y}\right]\cdot\left(\tilde{\mathbf{C}}(\mathbf{x},t,y):\left[\nabla+\frac{\mathbf{n}}{\eta}\frac{\partial}{\partial y}\right]\left(\mathbf{A}_0+\eta\mathbf{A}_1+\eta^2\mathbf{A}_2\right)\right)\\
&\quad=\nabla\cdot\left(\tilde{\mathbf{C}}:\nabla\left(\mathbf{A}_0+\eta\mathbf{A}_1+\eta^2\mathbf{A}_2\right)\right)+\nabla\cdot\left(\tilde{\mathbf{C}}:\frac{\mathbf{n}}{\eta}\frac{\partial}{\partial y}\left(\mathbf{A}_0+\eta\mathbf{A}_1+\eta^2\mathbf{A}_2\right)\right)\\
&\qquad+\frac{\mathbf{n}}{\eta}\frac{\partial}{\partial y}\left(\tilde{\mathbf{C}}:\nabla\left(\mathbf{A}_0+\eta\mathbf{A}_1+\eta^2\mathbf{A}_2\right)\right)\\
&\qquad+\frac{\mathbf{n}}{\eta}\frac{\partial}{\partial y}\cdot\left(\tilde{\mathbf{C}}:\frac{\mathbf{n}}{\eta}\frac{\partial}{\partial y}\left(\mathbf{A}_0+\eta\mathbf{A}_1+\eta^2\mathbf{A}_2\right)\right)+o(\eta)\\
&\quad=\left(\frac{\partial}{\partial t}-\frac{c_1}{\eta}\frac{\partial}{\partial y}\right)\left[\tilde{\rho}(\mathbf{x},t,y)\left(\frac{\partial}{\partial t}-\frac{c_1}{\eta}\frac{\partial}{\partial y}\right)\left(\mathbf{A}_0+\eta\mathbf{A}_1+\eta^2\mathbf{A}_2\right)\right]+o(\eta)\\
&\quad=\frac{\partial}{\partial t}\left[\tilde{\rho}\frac{\partial}{\partial t}\left(\mathbf{A}_0+\eta\mathbf{A}_1+\eta^2\mathbf{A}_2\right)\right]-\frac{c_1}{\eta}\frac{\partial}{\partial t}\left[\tilde{\rho}\frac{\partial}{\partial y}\left(\mathbf{A}_0+\eta\mathbf{A}_1+\eta^2\mathbf{A}_2\right)\right]\\
&\qquad-\frac{c_1}{\eta}\frac{\partial}{\partial y}\left[\tilde{\rho}\frac{\partial}{\partial t}\left(\mathbf{A}_0+\eta\mathbf{A}_1+\eta^2\mathbf{A}_2\right)\right]+\frac{c_1^2}{\eta^2}\frac{\partial}{\partial y}\left[\tilde{\rho}\frac{\partial}{\partial y}\left(\mathbf{A}_0+\eta\mathbf{A}_1+\eta^2\mathbf{A}_2\right)\right]+o(\eta)\end{aligned}\tag{4}$$

which leads to

$$\begin{aligned}&\eta^{-2}\left[\mathbf{n}\frac{\partial}{\partial y}\cdot\left(\tilde{\mathbf{C}}:\mathbf{n}\frac{\partial}{\partial y}\mathbf{A}_0\right)-c_1^2\frac{\partial}{\partial y}\tilde{\rho}\frac{\partial}{\partial y}\mathbf{A}_0\right]\\
&\quad+\eta^{-1}\left[\mathbf{n}\frac{\partial}{\partial y}\cdot\left(\tilde{\mathbf{C}}:\nabla\mathbf{A}_0\right)+\nabla\cdot\left(\tilde{\mathbf{C}}:\mathbf{n}\frac{\partial}{\partial y}\mathbf{A}_0\right)+\mathbf{n}\frac{\partial}{\partial y}\cdot\left(\tilde{\mathbf{C}}:\mathbf{n}\frac{\partial}{\partial y}\mathbf{A}_1\right)\right.\\
&\quad\left.-c_1^2\frac{\partial}{\partial y}\tilde{\rho}\frac{\partial}{\partial y}\mathbf{A}_1+c_1\frac{\partial}{\partial y}\tilde{\rho}\frac{\partial}{\partial t}\mathbf{A}_0+c_1\frac{\partial}{\partial t}\tilde{\rho}\frac{\partial}{\partial y}\mathbf{A}_0\right]\\
&\quad+\eta^0\left[\nabla\cdot\left(\tilde{\mathbf{C}}:\nabla\mathbf{A}_0\right)+\nabla\cdot\left(\tilde{\mathbf{C}}:\mathbf{n}\frac{\partial}{\partial y}\mathbf{A}_1\right)+\mathbf{n}\frac{\partial}{\partial y}\cdot\left(\tilde{\mathbf{C}}:\nabla\mathbf{A}_1\right)\right.\\
&\quad\left.+\mathbf{n}\frac{\partial}{\partial y}\cdot\left(\tilde{\mathbf{C}}:\mathbf{n}\frac{\partial}{\partial y}\mathbf{A}_2\right)-\frac{\partial}{\partial t}\tilde{\rho}\frac{\partial}{\partial t}\mathbf{A}_0-c_1^2\frac{\partial}{\partial y}\tilde{\rho}\frac{\partial}{\partial y}\mathbf{A}_2+c_1\frac{\partial}{\partial y}\tilde{\rho}\frac{\partial}{\partial t}\mathbf{A}_1+c_1\frac{\partial}{\partial t}\tilde{\rho}\frac{\partial}{\partial y}\mathbf{A}_1\right]=o(\eta).\end{aligned}\tag{5}$$

In a neighborhood of $\eta = 0$, we express the vanishing of the coefficients of successive powers of $1/\eta$ which leads to three equations.

5.2. *What we learn from the order* η^{-2}

Let us start by the expression factor of η^{-2}, we obtain

$$\mathbf{n}\frac{\partial}{\partial y}\cdot\left(\tilde{\mathbf{C}}(\mathbf{x},t,y):\mathbf{n}\frac{\partial}{\partial y}\mathbf{A}_0\right) = c_1^2\frac{\partial}{\partial y}\tilde{\rho}(\mathbf{x},t,y)\frac{\partial}{\partial y}\mathbf{A}_0. \tag{6}$$

By integration over the periodic cell Y, we get

$$\left(\mathbf{n}\cdot\tilde{\mathbf{C}}(\mathbf{x},t,y)\cdot\mathbf{n} - c_1^2\tilde{\rho}(\mathbf{x},t,y)\mathbf{I}\right)\frac{\partial}{\partial y}\mathbf{A}_0(\mathbf{x},t,y) = \mathbf{m}(\mathbf{x},t) \tag{7}$$

where $\mathbf{I}$ is the rank-2 identity tensor and $\mathbf{m}$ is an integration (vector valued) function, so that integrating again over the periodic cell and taking into account that $\mathbf{A}_0$, $\tilde{\mathbf{C}}(\mathbf{x},t,y)$ and $\tilde{\rho}(\mathbf{x},t,y)$ are 1-periodic in y, we get

$$\mathbf{m}(\mathbf{x},t)\int_0^1 \mathrm{d}y = \mathbf{0} = \int_0^1 \left(\mathbf{n}\cdot\tilde{\mathbf{C}}(\mathbf{x},t,y)\cdot\mathbf{n} - c_1^2\tilde{\rho}(\mathbf{x},t,y)\mathbf{I}\right)\frac{\partial}{\partial y}\mathbf{A}_0(\mathbf{x},t,y)\,\mathrm{d}y. \tag{8}$$

Assuming that $\mathbf{n}\cdot\tilde{\mathbf{C}}\cdot\mathbf{n} - c_1^2\tilde{\rho}\mathbf{I}$, is a rank-2 tensor which is always definite positive or definite negative for $y \in [0,1]$, we deduce that

$$\frac{\partial}{\partial y}\mathbf{A}_0(\mathbf{x},t,y) = \mathbf{0} \tag{9}$$

which is just like the modulated elastic case in [5] for which one has that the leading order term in the asymptotic expansion of the displacement field (2), does not depend upon y.

5.3. *What we learn from the order* η^{-1}

Let us now look at the expression factor of η^{-1}, we have

$$\begin{aligned}\mathbf{n}\frac{\partial}{\partial y}\cdot\left(\tilde{\mathbf{C}}:\nabla\mathbf{A}_0\right) + \nabla\cdot\left(\tilde{\mathbf{C}}:\mathbf{n}\frac{\partial}{\partial y}\mathbf{A}_0\right) + \mathbf{n}\frac{\partial}{\partial y}\cdot\left(\tilde{\mathbf{C}}:\mathbf{n}\frac{\partial}{\partial y}\mathbf{A}_1\right)\\ - c_1^2\frac{\partial}{\partial y}\tilde{\rho}\frac{\partial}{\partial y}\mathbf{A}_1 + c_1\frac{\partial}{\partial y}\tilde{\rho}\frac{\partial}{\partial t}\mathbf{A}_0 + c_1\frac{\partial}{\partial t}\tilde{\rho}\frac{\partial}{\partial y}\mathbf{A}_0 = \mathbf{0}.\end{aligned} \tag{10}$$

Using that $\mathbf{A}_0$ is independent of y, and assuming that we are at all times in the layered modulated medium $\tilde{\mathbf{C}}(\mathbf{x},t,y) = \mathbf{C}(y)$ and $\tilde{\rho}(\mathbf{x},t,y) = \rho(y)$, we obtain

$$\begin{aligned}\mathbf{n}\frac{\partial}{\partial y}\cdot\left(\mathbf{C}(y):\nabla\mathbf{A}_0\right) + \mathbf{n}\frac{\partial}{\partial y}\cdot\left(\mathbf{C}(y):\mathbf{n}\frac{\partial}{\partial y}\mathbf{A}_1\right)\\ + c_1^2\frac{\partial}{\partial y}\rho(y)\frac{\partial}{\partial y}\mathbf{A}_1 - c_1\frac{\partial}{\partial y}\rho(y)\frac{\partial}{\partial t}\mathbf{A}_0 = \mathbf{0}.\end{aligned} \tag{11}$$

Let us integrate over the periodic cell Y, we get

$$\frac{\partial}{\partial y}\mathbf{A}_1 = \mathbf{M}(y)\left(-\mathbf{n}\cdot\mathbf{C}(y):\nabla\mathbf{A}_0 - c_1\rho(y)\frac{\partial}{\partial t}\mathbf{A}_0 + \mathbf{p}\right), \tag{12}$$

where $\mathbf{p}$ is an integration vector and $\mathbf{M}(y) = (\mathbf{n}\cdot\mathbf{C}\cdot\mathbf{n} - c_1^2\mathbf{I})^{-1}$ is a symmetric, definite positive or negative rank-2 tensor.

Integrating once again over the periodic cell, we get

$$\begin{aligned}\int_0^1 \frac{\partial}{\partial y}\mathbf{A}_1\,\mathrm{d}y = \mathbf{0} \;=\; \int_0^1 (-\mathbf{M}(y)\otimes\mathbf{n}:\mathbf{C}(y)\,\mathrm{d}y):\nabla\mathbf{A}_0\\ + c_1\int_0^1 (\mathbf{M}(y)\rho(y)\,\mathrm{d}y)\frac{\partial}{\partial t}\mathbf{A}_0 + \int_0^1 \mathbf{M}(y)\mathbf{p}\,\mathrm{d}y.\end{aligned} \tag{13}$$

Combining (12) and (13), we get the following annex problem on the periodic cell

$$\frac{\partial}{\partial y}\mathbf{A}_1 = \mathbf{N}(y) : \nabla \mathbf{A}_0 + \mathbf{P}(y) \cdot \frac{\partial}{\partial t}\mathbf{A}_0, \tag{14}$$

where the tensors $\mathbf{N}(y)$ and $\mathbf{P}(y)$ are given by

$$\begin{aligned} \mathbf{N}(y) &= \mathbf{M}(y)\left(\left(\int_0^1 \mathbf{M}(y)\,\mathrm{d}y\right)^{-1}\left(\int_0^1 (\mathbf{M}(y)\otimes\mathbf{n} : \mathbf{C}(y))\,\mathrm{d}y\right) - \mathbf{n}\cdot\mathbf{C}\right) \\ \mathbf{P}(y) &= c_1\mathbf{M}(y)\left(\left(\int_0^1 \mathbf{M}(y)\,\mathrm{d}y\right)^{-1}\int_0^1 (\mathbf{M}(y)\rho(y))\,\mathrm{d}y - \rho(y)\mathbf{I}\right). \end{aligned} \tag{15}$$

5.4. *What we learn from the order* η^0

Finally, we look at the expression factor of η^0, performing an integration over the periodic cell, we obtain the homogenized equation of motion

$$\begin{aligned} &\nabla\cdot\left(\int_0^1 \tilde{\mathbf{C}} : \left(\mathbf{n}\frac{\partial}{\partial y}\,\mathrm{d}y\mathbf{A}_1 + \nabla\mathbf{A}_0\right)\right) \\ &\quad = \frac{\partial}{\partial t}\int_0^1 \tilde{\rho}\frac{\partial}{\partial t}\mathbf{A}_0\,\mathrm{d}y - c_1\int_0^1 \frac{\partial}{\partial y}\tilde{\rho}\frac{\partial}{\partial t}\mathbf{A}_1\,\mathrm{d}y \end{aligned} \tag{16}$$

which has the form of the equation $\nabla\cdot\Sigma = \partial_t\Pi$ where Σ is the macroscopic stress field and Π is the macroscopic momentum field.

The homogenized constitutive equations are, as first derived in [5],

$$\begin{aligned} \Sigma &= \mathbf{C}_{\text{eff}} : \nabla\mathbf{A}_0 + \mathbf{S}^1_{\text{eff}}\cdot\frac{\partial}{\partial t}\mathbf{A}_0 \\ \Pi &= \mathbf{S}^2_{\text{eff}} : \nabla\mathbf{A}_0 + \rho_{\text{eff}}\cdot\frac{\partial}{\partial t}\mathbf{A}_0 \end{aligned} \tag{17}$$

where the rank-4 homogenized elasticity tensor $\mathbf{C}_{\text{eff}}$, the rank-3 homogenized coupling Willis tensors $\mathbf{S}^1_{\text{eff}}$ and $\mathbf{S}^2_{\text{eff}}$ and the rank-2 homogenized density tensor are given by:

$$\begin{aligned} \mathbf{C}_{\text{eff}} &= \langle\mathbf{C}\rangle + \langle\mathbf{C} : \mathbf{n}\otimes\mathbf{M}\rangle\cdot\langle\mathbf{M}\rangle^{-1}\cdot\langle\mathbf{M}\otimes\mathbf{n} : \mathbf{C}\rangle - \langle\mathbf{C} : \mathbf{n}\otimes\mathbf{M}\otimes\mathbf{n} : \mathbf{C}\rangle, \\ \mathbf{S}^1_{\text{eff}} &= c_1\langle\mathbf{C} : \mathbf{n}\otimes\mathbf{M}\rangle\cdot\langle\mathbf{M}\rangle^{-1}\cdot\langle\rho\mathbf{M}\rangle - c_1\langle\rho\mathbf{C} : \mathbf{n}\otimes\mathbf{M}\rangle, \\ \mathbf{S}^2_{\text{eff}} &= -c_1\langle\rho\mathbf{M}\rangle\cdot\langle\mathbf{M}\rangle^{-1}\cdot\langle\mathbf{M}\otimes\mathbf{n} : \mathbf{C}\rangle + c_1\langle\rho\mathbf{M}\otimes\mathbf{n} : \mathbf{C}\rangle, \\ \rho_{\text{eff}} &= \langle\rho\rangle\mathbf{I} - c_1^2\langle\rho\mathbf{M}\rangle\cdot\langle\mathbf{M}\rangle^{-1}\cdot\langle\rho\mathbf{M}\rangle + c_1^2\langle\rho^2\mathbf{M}\rangle, \end{aligned} \tag{18}$$

which couple stress to velocity and momemtum to strain, when $c_1 > 0$.

We note that such coupling is the counterpart of opto-magnetic coupling in time-modulated electromagnetic media within which light experiences a Fresnel drag [8]. Fresnel drag after Augustin Fresnel, who in 1818 put forward the aether drag hypothesis: a moving fluid appears to drag light along so that light traveling in opposite directions to the fluid flow would have different velocities [29]. Its extra velocity was related to, but not equal to, the velocity of the fluid. Although Fresnel's derivation was flawed, Hippolyte Fizeau measured the drag effect and published in 1851 in the Proceedings of the French Academy of Sciences, nowadays called the Comptes Rendus Physique, an article confirming Fresnel's formula [30]. We thus believe seismic waves propagating in layered soils such as in Figure 8 should experience some similar drag phenomenon due to the ambient noise which acts as a source of time-modulation of the soil. In this case, the Fresnel drag underpins the mechanism of the seismic computer, since this non-reciprocity is an essential ingredient for logical operations, making possible seismic diodes akin electrical diodes, which let electrical currents pass in one direction only and play an essential role in computers. We note in passing some small scale experiments on asymmetric acoustic wave propagation in unconsolidated granular medium via a nonlinear self demodulation mechanism [31] which could be revisited in light of the effective description using the above equations.

6. Conclusion

We have made a survey of seismic metamaterials, which is an emergent topic beyond electromagnetic metamaterials [32,33], spanning the scales from hundredths of nanometers to tenths of meters [34]. We have revisited some earlier work [1,2], which initiated this fast growing field, and we further described some fortuitous seismic metamaterials from the past (Roman theaters), some natural seismic metamaterials (forest of trees) of present days and some seismic metamaterial computer that might become a reality in the near future. We have stressed that Willis's equations are a good framework for seismic metamaterials, which can be viewed as a mechanical counterpart of time modulated electromagnetic media experiencing some Fresnel drag [8] induced in the present case by seismic ambient noise. This non reciprocity associated with the Fresnel drag can serve to achieve some seismic diodes, and so some logical operations with seismic computers.

Before we conclude this perspective article, we would like to point out an earlier work [35] that unveiled theoretically and experimentally for kHz Rayleigh waves in the Bragg regime some elastic stop bands properties: attenuation of Rayleigh waves was observed in a marble quarry by drilling cylindrical holes arranged in honeycomb and triangular lattices. We further note the theoretical and experimental observation of subwavelength stop bands for MHz Rayleigh waves propagating within an array of nickel pillars grown on a lithium niobate substrate [36]. In our opinion, these two seminal works that predate the area of seismic metamaterials have touched upon the essence of the wave physics at work in large scale mechanical metamaterials: control of surface seismic waves in the Bragg [1,35,37,38] and subwavelength [2,21,36,39–41] regimes. In all fairness, seismologists and earthquake engineers had already noted 40 years ago the effect of soil roughness on the propagation of seismic waves [42]. Of course, shielding and damping of surface seismic waves thanks to stop band properties does not tell all the story of seismic metamaterials, as our team has theoretically and experimentally demonstrated that one can actually focus such waves via negative refraction [2] through a tilted array of boreholes in a sedimentary soil. In fact, the earthquake engineer could arrange boreholes or concrete columns in soil in many ways, for instance in a concentric fashion to achieve a seismic cloak, and some numerical simulations show encouraging results in this direction [43], using some effective medium approach based on Willis's equations. This work takes a new dimension thanks to the concept of time-modulated media. Our group has actually proposed to scale up further the design of seismic cloaks in order to achieve some self-protection for cities [44]. This might seem like a far-fetched concept, but we recall here that geophysicists and civil engineers have already observed theoretically and numerically site-city interactions [20,45–50].

Finally, we would like to conclude this review and perspective article on seismic metamaterials by the proposal that one might be able to further extend ideas rooted in the physics of electromagnetic metamaterials to control, harvest and redirect not only seismic ambient noise but also the powerful energy released near seismic faults during metric sliding mechanism along fault plan. The Figure 9 shows the cumulative displacement (130 m) at San Andreas fault after several earthquakes occured during the last millennia. For an illustrative example of an earthquake of magnitude 4, seismic energy radiated at a fault with similar characteristics can be estimated to be in the order of $M_0 = 2.6 \times 10^{10}$ J (i.e. 26,000 MJ) for a surface of the fault about 1.2×10^6 m $\times 3.5 \times 10^{-2}$ m $= 4.2 \times 10^4$ m^2 (so 42,000 m^2), in a rock of shear modulus $G = 30{,}000$ MPa. However, a word of caution would be in order as the propagated seismic energy computed from the Gutenberg–Richter formulas [51] would be much smaller. Last, but not least, this article benefited from scientific interactions with colleagues.

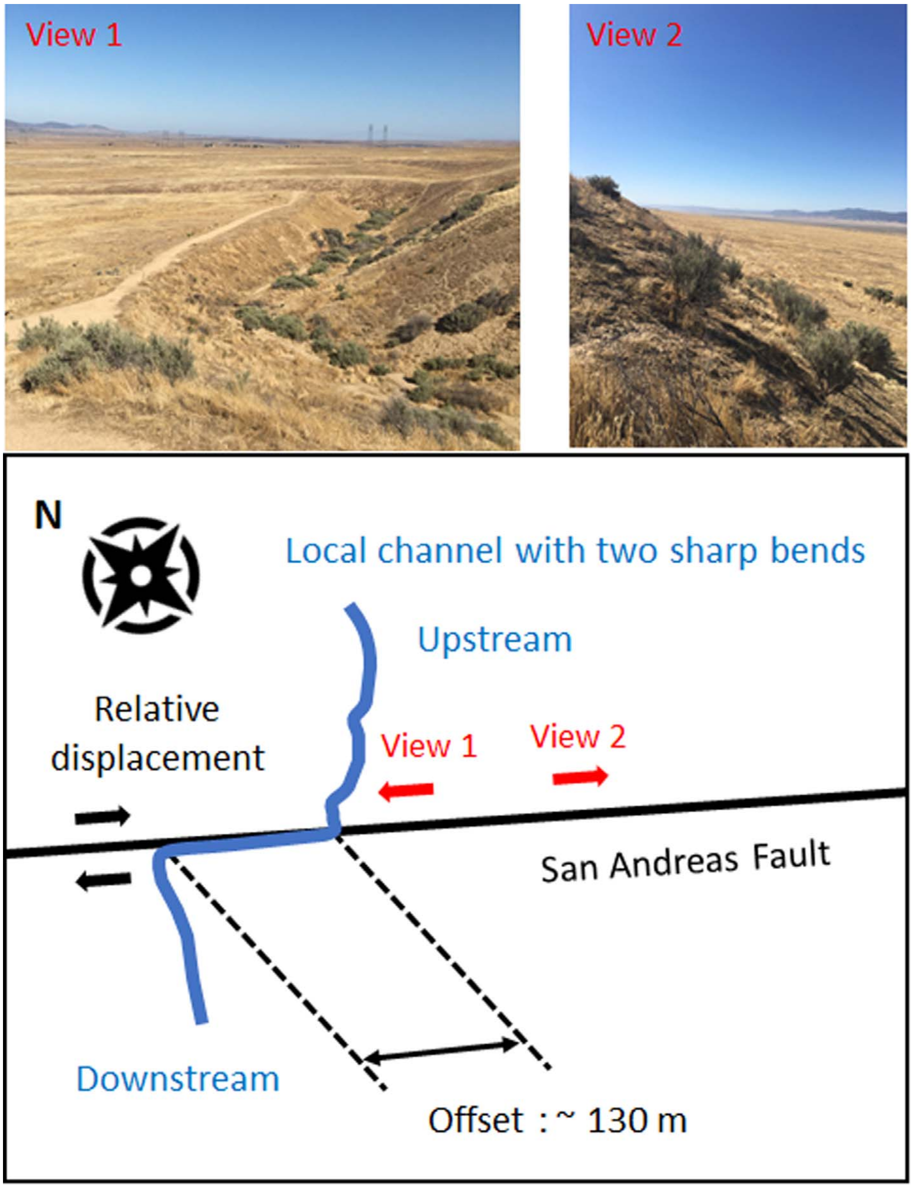

Figure 9. Wallace Creek, Carizo Plain (California, USA). Channel with sharp bends. The upstream half of the channel doesn't line up with its downstream half (upper left panel) because the San Andreas strike-slip fault has been slided (sismo-geological top-view figure). The two tectonic blocks slide past one another. The San Andreas Fault is a right lateral fault (upper right panel). Photo credits: S. Brûlé. From Wallace Creek Interpretive Trail-A geological guide to the San Andreas Fault at Wallace Creek (Southern California Earthquake Center, U.S. Geological Survey, California Institute of Technology and Bureau of Land Management).

Acknowledgements

The authors would like to particularly acknowledge stimulating discussions with (in alphabetical order) Yves Aurégan, Richard Craster, Stéphane Enoch, Mohamed Farhat, Emanuele Galiffi, Boris Gralak, Paloma Huidobro, Muamer Kadic, Konstantin Lurie, Jean-Jacques Marigo, Graeme Milton, Marco Miniacci, John Pendry, Kim Pham, Agnes Maurel, Vincent Pagneux, Jean-François Semblat, Bogdan Ungureanu, Martin Wegener and John Willis.

References

[1] S. Brûlé, E. Javelaud, S. Enoch, S. Guenneau, "Experiments on seismic metamaterials: molding surface waves", *Phys. Rev. Lett.* **112** (2014), article no. 133901.

[2] S. Brûlé, E. Javelaud, S. Enoch, S. Guenneau, "Flat lens for seismic waves", *Sci. Rep.* **7** (2017), article no. 18066.

[3] S. Brûlé, C. Deprez, C. Fernandez, M. Givry, K. Manchuel, G. Mendoza, B. Richard, C. Taylor, "Report of the post-seismic mission on the mexico earthquake of september 19th, 20017", Tech. report, Association Française du Génie Parasismique (AFPS), 2017.

[4] S. Brûlé, S. Enoch, S. Guenneau, "Role of nanophotonics in the birth of seismic megastructures", *Nanophotonics* **8** (2019), p. 1591-1605.

[5] H. Nassar, X. Xu, A. Norris, G. Huang, "Modulated phononic crystals: non-reciprocal wave propagation and willis materials", *J. Mech. Phys. Solids* **101** (2017), p. 10-29.

[6] J. Willis, "Variational principles for dynamic problems in inhomogeneous elastic media", *Wave Motion* **3** (1981), p. 1-11.

[7] Y. Liu, S. Guenneau, B. Gralak, "Artificial dispersion via high-order homogenization: magnetoelectric coupling and magnetism from dielectric layers", *Proc. R. Soc. Lond. A* **469** (2013), article no. 20130240.

[8] P. Huidobro, E. Galiffi, S. Guenneau, R. Craster, J. Pendry, "Fresnel drag in space-time modulated metamaterials", *Proc. Natl Acad. Sci. USA* **116** (2019), p. 24943-24948.

[9] A. Silva, F. Monticone, G. Castaldi, V. Galdi, A. Alu, N. Engheta, "Performing mathematical operations with metamaterials", *Science* **343** (2014), p. 160-163.

[10] N. Estakhri, B. Edwards, N. Engheta, "Inverse-designed metastructures that solve equations", *Science* **22** (2019), p. 1333-1338.

[11] S. Brûlé, S. Enoch, S. Guenneau, "Sols structurés sous sollicitation dynamique : des métamatériaux en géotechnique", *Rev. Fr. Geotech.* **151** (2017), p. 4.

[12] G. Dupont, O. Kimmoun, B. Molin, S. Guenneau, S. Enoch, "Numerical and experimental study of an invisibility carpet in a water channel", *Phys. Rev. E* **91** (2015), article no. 023010.

[13] M. Farhat, S. Enoch, S. Guenneau, A. Movchan, "Broadband cylindrical acoustic cloak for linear surface waves in a fluid", *Phys. Rev. Lett.* **101** (2008), article no. 134501.

[14] S. Brûlé, S. Enoch, S. Guenneau, "Emergence of seismic metamaterials: current state and future perspectives", *Phys. Lett. A* **384** (2020), article no. 126034.

[15] J. Xu, X. Jiang, N. Fang, E. Georget, R. Abdeddaim, J. Geffrin, M. Farhat, P. Sabouroux, S. Enoch, S. Guenneau, "Molding acoustic, electromagnetic and water waves with a single cloak", *Sci. Rep.* **5** (2015), article no. 10678.

[16] M. Farhat, S. Guenneau, S. Enoch, "Broadband cloaking of bending waves via homogenization of multiply perforated radially symmetric and isotropic thin elastic plates", *Phys. Rev. B* **85** (2012), article no. 020301.

[17] N. Stephen, "On energy harvesting from ambient noise", *J. Sound Vib.* **293** (2006), p. 413-425.

[18] S. Brûlé, S. Enoch, S. Guenneau, "Experimental evidence of auxetic features in seismic metamaterials: Ellipticity of seismic rayleigh waves for subsurface architectured ground with holes", https://arxiv.org/abs/1809.05841, 2018.

[19] S. Brûlé, S. Enoch, S. Guenneau, "On the possibility of seismic rogue waves in very soft soils", 2020, https://arxiv.org/abs/2004.07037.

[20] B. Ungureanu, S. Guenneau, Y. Achaoui, A. Diatta, M. Farhat, H. Hutridurga, R. Craster, S. Enoch, S. Brûlé, "The influence of building interactions on seismic and elastic body waves", *EPJ Appl. Metamater.* **6** (2019), p. 18.

[21] A. Colombi, P. Roux, S. Guenneau, P. Gueguen, R. Craster, "Forests as a natural seismic metamaterial: Rayleigh wave bandgaps induced by local resonances", *Sci. Rep.* **6** (2016), article no. 19238.

[22] A. Colombi, D. Colquitt, P. Roux, S. Guenneau, R. Craster, "A seismic metamaterial: the resonant metawedge", *Sci. Rep.* **6** (2016), article no. 27717.

[23] K. Tsakmakidis, A. Boardman, O. Hess, "Trapped rainbow storage of light in metamaterials", *Nature* **450** (2007), p. 397.

[24] A. Maurel, J. Marigo, K. Pham, S. Guenneau, "Conversion of love waves in a forest of trees", *Phys. Rev. B* **98** (2018), article no. 134311.

[25] J. D. Ponti, A. Colombi, R. Ardito, F. Braghin, A. Corigliano, R. Craster, "Graded metasurface for enhanced sensing and energy harvesting", *New J. Phys.* **22** (2020), article no. 013013.

[26] P. Vitruvius, *Ten Books on Architecture. Vol. 15*, Cambridge University Press, New York, 1999.

[27] A. B. Clymer, "The mechanical analog computers of Hannibal Ford and William Newell", *IEEE Ann. Hist. Comput.* **15** (1993), p. 19-34.

[28] K. Lurie, *An Introduction to the Mathematical Theory of Dynamic Materials*, Springer, New York, 2007.

[29] A. Fresnel, "Lettre d'augustin fresnel a francois arago sur l'influence du mouvement terrestre dans quelques phenomenes d'optique", *Ann. Chem. Phys.* **9** (1818), p. 57-67.

[30] H. Fizeau, "Sur les hypotheses relatives a l'ether lumineux", *C. R. Acad. Sci.* **33** (1851), p. 349-355.

[31] T. Devaux, V. Tournat, O. Richoux, V. Pagneux, "Asymmetric acoustic propagation of wave packets via the self-demodulation effect", *Phys. Rev. Lett.* **115** (2015), article no. 234301.

[32] M. Kadic, T. Buckmann, R. Schittny, M. Wegener, "Metamaterials beyond electromagnetism", *Rep. Prog. Phys.* **76** (2013), article no. 126501.

[33] B. Ungureanu, Y. Achaoui, S. Enoch, S. Brûlé, S. Guenneau, "Auxetic-like metamaterials as novel earthquake protections", *EPJ Appl. Metamater.* **2015** (2016), p. 17.

[34] R. Aznavourian, T. Puvirajesinghe, S. Brûlé, S. Enoch, S. Guenneau, "Spanning the scales of mechanical metamaterials using time domain simulations in transformed crystals, graphene flakes and structured soils", *J. Phys. Condens. Matter* **29** (2017), article no. 433004.

[35] F. Meseguer, M. Holgado, D. Caballero, N. Benaches, J. Sanchez-Dehesa, C. Lopez, J. Llinares, "Rayleigh-wave attenuation by a semi-infinite two-dimensional elastic-bandgap", *Phys. Rev. B* **59** (1999), article no. 12169.

[36] Y. Achaoui, A. Khelif, S. Benchabane, L. Robert, V. Laude, "Experimental observation of locally-resonant and bragg band gaps for surface guided waves in a phononic crystal of pillars", *Phys. Rev. B* **83** (2011), article no. 104201.

[37] M. Miniaci, A. Krushynska, F. Bosia, N. Pugno, "Large scale mechanical metamaterials as seismic shields", *New J. Phys.* **18** (2016), article no. 083041.

[38] Y. Achaoui, T. Antonakakis, S. Brûlé, R. Craster, S. Enoch, S. Guenneau, "Clamped seismic metamaterials: ultra-low frequency stop bands", *New J. Phys.* **19** (2017), article no. 063022.

[39] A. Palermo, S. Krödel, K. H. Matlack, R. Zaccherini, V. K. Dertimanis, E. N. Chatzi, A. Marzani, C. Daraio, "Hybridization of guided surface acoustic modes in unconsolidated granular media by a resonant metasurface", *Phys. Rev. Appl.* **9** (2018), article no. 054026.

[40] M. Lott, P. Roux, S. Garambois, P. Gueguen, A. Colombi, "Evidence of metamaterial physics at the geophysics scale: the metaforet experiment", *Geophys. J. Int.* **220** (2020), p. 1330-1339.

[41] D. Mu, H. Shu, L. Zhao, S. An, "A review of research on seismic metamaterials", *Adv. Eng. Mater.* **22** (2020), article no. e1901148.

[42] H. Wong, M. Trifunac, B. Westermo, "Effects of surface and subsurface irregularities on the amplitude of monochromatic waves", *Bull. Seismol. Soc. Am.* **67** (1977), p. 353-368.

[43] A. Diatta, Y. Achaoui, S. Brûlé, S. Enoch, S. Guenneau, "Control of Rayleigh-like waves in thick plate willis metamaterials", *AIP Adv.* **6** (2016), article no. 121707.

[44] S. Brûlé, B. Ungureanu, Y. Achaoui, R. Aznavourian, T. Antonakakis, R. Craster, S. Enoch, S. Guenneau, "Metamaterial-like transformed urbanism", *Innov. Infrastruct. Solut.* **2** (2017), p. 20.

[45] A. Wirgin, P. Bard, "Effects of buildings on the duration and amplitude of ground motion in mexico city", *Bull. Seismol. Soc. Am.* **86** (1996), p. 914-920.

[46] J. Semblat, A. Duval, P. Dangla, "Numerical analysis of seismic wave amplification in nice (france) and comparisons with experiments", *Soil Dyn. Earthq. Eng.* **19** (2000), p. 347-362.

[47] D. Clouteau, D. Aubry, "Modification of the ground motion in dense urban areas", *J. Comput. Acoust.* **9** (2001), p. 1659-1675.

[48] P. Gueguen, P. Bard, F. Chavez-Garcia, "Site-city seismic interaction in mexico city-like environments: an analytical study", *Bull. Seismol. Soc. Am.* **92** (2002), p. 794-811.

[49] C. Boutin, P. Roussillon, "Assessment of the urbanization effect on seismic response", *Bull. Seismol. Soc. Am.* **94** (2004), p. 251-268.

[50] M. Kham, J. Semblat, P. Bard, P. Dangla, "Seismic site-city interaction: main governing phenomena through simplified numerical models", *Bull. Seismol. Soc. Am.* **96** (2006), p. 1934-1951.

[51] B. Gutenberg, C. Richter, "Magnitude and energy of earthquakes", *Ann. Geofis.* **9** (1956), p. 1-15.

Comptes Rendus
Physique

Objet de la revue

Les *Comptes Rendus Physique* sont une revue électronique évaluée par les pairs de niveau international, qui couvre l'ensemble des domaines de la physique et de l'astrophysique. Ils publient principalement des numéros thématiques, mais également des articles originaux de recherche, des annonces préliminaires, des articles de revue, des mises en perspective historiques, des textes à visée pédagogique ou encore des actes de colloque, sans limite de longueur, en anglais ou en français. Ils proposent également des numéros spéciaux consacrés à certains aspects récents et/ou significatifs de la discipline, dont les auteurs sont choisis parmi les chercheurs les plus actifs sur le sujet et dont la coordination est assurée par des rédacteurs en chef invités.

Les *Comptes Rendus Physique* sont diffusés selon une politique vertueuse de libre accès diamant, gratuit pour les auteurs (pas de frais de publications) comme pour les lecteurs (libre accès immédiat et pérenne).

À propos de la revue

Toutes les informations concernant la revue, y compris le texte des articles publiés qui est en accès libre intégral, figurent sur le site https://comptes-rendus.academie-sciences.fr/physique/.

Informations à l'attention des auteurs

Pour toute question relative à la soumission des articles, les auteurs peuvent consulter le site https://comptes-rendus.academie-sciences.fr/physique/.

Contact

Académie des sciences
23, quai de Conti, 75006 Paris, France
Tél. : (+33) (0)1 44 41 43 72
CR-Physique@academie-sciences.fr

COMPTES RENDUS
DE L'ACADÉMIE DES SCIENCES

Physique

Volume 21, nº 7-8, 2020

Special issue / *Numéro thématique*
Metamaterials 2 / *Métamatériaux 2*

Guest editors / *Rédacteurs en chef invités*
Boris Gralak (CNRS, Institut Fresnel, Marseille, France)
Sébastien Guenneau (UMI2004 Abraham de Moivre, CNRS-Imperial College, London, UK)

Cover illustration / *Illustration de couverture*
© 123rf.com

1878-1535 (electronic)

Académie des sciences — Paris

Comptes Rendus
de l'Académie des sciences

Physique

Volume 21, n° 7-8, 2020